



HAL
open science

Interfacial stability and degradation in organic photovoltaic solar cells

William Greenbank

► **To cite this version:**

William Greenbank. Interfacial stability and degradation in organic photovoltaic solar cells. Other. Université de Bordeaux, 2016. English. NNT : 2016BORD0338 . tel-01552294v2

HAL Id: tel-01552294

<https://theses.hal.science/tel-01552294v2>

Submitted on 3 Jul 2017

HAL is a multi-disciplinary open access archive for the deposit and dissemination of scientific research documents, whether they are published or not. The documents may come from teaching and research institutions in France or abroad, or from public or private research centers.

L'archive ouverte pluridisciplinaire **HAL**, est destinée au dépôt et à la diffusion de documents scientifiques de niveau recherche, publiés ou non, émanant des établissements d'enseignement et de recherche français ou étrangers, des laboratoires publics ou privés.

MANUSCRIT DE THÈSE PRÉSENTÉ

POUR OBTENIR LE GRADE DE

DOCTEUR DE
L'UNIVERSITÉ DE BORDEAUX

ÉCOLE DOCTORALE DES SCIENCES PHYSIQUES ET DE L'INGENIEUR

SPÉCIALITÉ : Électronique

Par **William GREENBANK**

**Interfacial stability and degradation in organic photovoltaic
solar cells**

Sous la direction de : Sylvain CHAMBON et Lionel HIRSCH

Soutenance le 18 novembre 2016

Membres du jury :

M. HOPPE Harald
M. DYAKONOV Vladimir
Mme. REVAUX Amélie
M. RATIER Bernard
M. CHAMBON Sylvain
M. HIRSCH Lionel

Professeur à l'Université de Jena
Professeur à l'Université de Würzburg
Chef de Laboratoire à CEA, Grenoble
Professeur à l'Université de Limoges
Chargé de recherche CNRS, Bordeaux
Directeur de recherche CNRS, Bordeaux

Rapporteur
Rapporteur
Examinatrice
Examineur
Encadrant de thèse
Directeur de thèse

Abstract/Résumé

Interfacial stability and degradation in organic photovoltaic solar cells

Keywords: Organic, Photovoltaic, Stability, Interfaces, Degradation, Diffusion, Electrode

Organic photovoltaic (OPV) solar cells show great promise but suffer from short operating lifetimes. This study examines the role that the selection of materials for the hole extraction interface in inverted OPV devices plays in determining the lifetime of a device. In the first part of the study, the effects of thermal degradation were examined. It was found that devices containing MoO₃ HTLs and silver top electrodes exhibit an open-circuit voltage (V_{oc})/fill factor (FF)-driven mechanism. Physical characterisation experiments showed that, with heating, the silver electrode undergoes de-wetting. With thin electrodes this can result in the catastrophic failure of the device. A fracture analysis study found that silver-containing devices experience an increase in adhesion of their top layers to the active layer due to interdiffusion between the layers. This interdiffusion may be related to the loss of V_{oc} and FF in Ag/MoO₃ devices through diffused species forming charge traps in the active layer. In the second part of the study, the effects of photodegradation in different atmospheres were studied. Some material-dependent effects were observed when the devices were aged in an inert atmosphere, including variations in projected lifetime. The effect of oxygen was to greatly accelerate degradation, and remove any of the material-dependence observed in the inert experiment, while humidity led to a substantial increase in the degradation rate of devices containing PEDOT:PSS (poly(3,4-ethylenedioxythiophene) polystyrene sulfonate). This study underlines the importance of considering device lifetime in device design, and choosing materials to minimise degradation.

La stabilité et le vieillissement aux interfaces des cellules solaires organiques photovoltaïques

Mots-clés : Organique, Photovoltaïque, Stabilité, Interface, Vieillessement, Diffusion, Electrode

Les durées de vie des cellules solaires photovoltaïques organiques (OPV) doivent être améliorées afin que cette technologie puisse être commercialisée sur une grande échelle. Ce travail étudie l'influence de la sélection des matériaux pour l'interface supérieure sur la dégradation des OPV inversées. La première partie de cette étude s'occupe des effets de la dégradation thermique. Il a été constaté que la tension de circuit-ouvert (V_{oc}) et le facteur de forme (FF) diminuent lors du vieillissement des OPVs ayant une HTL de MoO₃ et une électrode d'argent. Des expériences de caractérisation physique ont mis en évidence que les électrodes d'argent démouillent lors du vieillissement thermique ce qui peut conduire à la mort rapide des cellules avec des électrodes minces. Des analyses de rupture ont également faites. Il a été constaté que l'adhésion d'interface supérieure augmente fortement dans les échantillons avec électrode en argent due à la diffusion de matière, et il est possible qu'il y ait une relation entre cette diffusion et la perte de V_{oc} et FF . Dans la deuxième partie, les effets de la lumière sur la dégradation et l'influence de la présence d'oxygène ou d'humidité ont été étudiés. Quelques effets des matériaux ont été notés, en particulier sur la durée de vie. L'oxygène a eu l'effet d'accélérer notablement la dégradation, et aucune différence n'a été notée selon les matériaux utilisés. En revanche, l'humidité a eu un effet prononcé sur les échantillons avec certains HTLs. Ce travail souligne l'importance de penser à la durée de vie quand on désigne les dispositifs OPV, en particulier pour sélectionner des matériaux appropriés afin d'optimiser la durée de vie.

Résumé de thèse français

Les émissions de gaz à effet de serre représentent un risque important pour notre civilisation à cause du changement climatique. Une grande partie de nos émissions proviennent de la génération d'électricité, il est donc nécessaire de trouver et d'utiliser des sources d'énergie moins polluantes. Les cellules photovoltaïques organiques (OPV) sont une technologie de génération d'énergie solaire de troisième génération, et pourraient représenter une solution viable pour générer de l'énergie sans émission de gaz à effet de serre. De plus, il est possible d'imprimer les OPVs sur des substrats flexibles de grande surface ce qui ouvrirait les panneaux solaires à de nouvelles applications. Cependant, si on compare les OPVs aux panneaux en silicium, leurs rendements et durées de vie sont inférieurs. Concernant le rendement, si les coûts des modules OPVs sont suffisamment bas, le faible rendement pourrait ne pas représenter un grand obstacle. En revanche, il est primordial que les durées de vie soient améliorées afin que cette technologie puisse être commercialisée sur une grande échelle.

Ce travail étudie l'influence de la sélection des matériaux pour la couche de transport de trous (HTL) et pour l'électrode supérieure sur la dégradation des OPVs inversées et la façon dont les matériaux interagissent avec les stimuli de vieillissement. La dégradation des OPVs est difficile à étudier à cause du grand nombre de mécanismes de dégradation qui peuvent être présents pendant le vieillissement d'une cellule. Il est donc impératif que le vieillissement des cellules OPV soit étudié dans les conditions très contrôlées où les effets de chaque stimulus peuvent être observés individuellement, et conjointement. Pour se faire, les expériences de vieillissement dans cette étude étaient réalisées avec ou sans la présence de lumière, de chaleur, d'oxygène, et d'humidité.

La première partie de cette étude traite des effets de la dégradation thermique sur les OPV à base de P3HT:PC₆₁BM (poly(3-hexylthiophène):[6,6]-phényl-C₆₁-butanoate de méthyle) et avec des HTLs et électrodes supérieures différentes. L'étude du vieillissement thermique des OPVs est importante parce qu'il représente un type de dégradation intrinsèque, c'est-à-dire une dégradation observable dans l'utilisation normale d'une cellule. Comme la plupart des radiations absorbées par un dispositif OPV ne contribuent pas à la génération de porteur de charge et sont donc convertis en chaleur, les stimuli thermiques sont toujours présents dans l'opération d'un OPV. Les expériences de vieillissement sont réalisées sur une plaque chauffant à 85°C, sans lumière, et sous une atmosphère inerte (<0.1 ppm d'oxygène et d'humidité). Ces conditions expérimentales permettent d'éviter la possibilité que d'autres stimuli de dégradation interviennent en plus de la chaleur. Pendant l'étude, il a été constaté que la tension de circuit-

ouvert (V_{OC}) et le facteur de forme (FF) diminuent lors du vieillissement des OPVs possédant une combinaison spécifique de matériaux à l'interface de l'extraction des trous : le MoO_3 en tant que HTL et l'argent en tant qu'électrode. En plus de cette dégradation, une perte de courant de court-circuit (J_{SC}) est observée avec toutes les combinaisons de matériaux. Cette perte est attribuée aux changements induits thermiquement dans la couche active.

La perte de J_{SC} avec la dégradation thermique des OPVs est connue et très bien documentée dans la littérature : ce comportement est généralement attribué à l'augmentation de la taille des domaines accepteur et donneur dans la couche active. Dans les OPVs, l'absorption d'un photon par une couche active organique n'aboutit pas à la formation de charges libres, en revanche un couple électron trou lié est formé : il s'agit d'un exciton. Ces excitons sont métastables, et se recombinent rapidement (la recombinaison géminât). Pour une extraction réussie des charges, l'exciton doit être capable de migrer à l'interface donneur-accepteur avant qu'il ne se recombine. Donc, si la taille des domaines dans la couche active est plus grande que la longueur de diffusion des excitons, le taux de recombinaison géminât augmentera, et le J_{SC} diminuera.

Néanmoins, la diminution de V_{OC} et de FF observé avec les échantillons contenant de l'argent et de l'oxyde de molybdène n'a pas encore été observée dans la littérature scientifique. Ce comportement peut être attribué à la formation d'états électroniques dans la bande interdite de la couche active près d'une interface d'extraction des charges (souvent à cause d'une imperfection structurale, comme une impureté). Ces états s'appellent des pièges de charges, et peuvent contribuer à faire écran la tension interne du dispositif ce qui entraîne une diminution de V_{OC} et FF . Par ailleurs, quand le P3HT dans la couche active a été remplacé par un polymère ayant une température de transition vitreuse plus élevée, la diminution de V_{OC} a été beaucoup plus lente. Cela suggère qu'il existe une relation entre la diminution de V_{OC} et le taux de diffusion de matière dans la couche active. Une explication de ses observations serait que la matière provenant de la HTL ou de l'électrode diffuserait dans la couche active et que des pièges de charges se seraient formés à cause de ces impuretés.

Des expériences de caractérisation physique ont été faites afin de trouver une origine physique de la diminution de V_{OC} et FF . La première technique utilisée pour ces expériences était la spectroscopie de rétrodiffusion de Rutherford (RBS) – un technique de caractérisation nucléaire qui donne des informations sur la composition et le profil élémentaire d'un échantillon. Il a été constaté que le profil élémentaire des échantillons avec des électrodes en argent change fortement avec un traitement thermique. Ce changement de profil peut provenir de la diffusion de l'argent, ou d'une augmentation de la rugosité de la surface de l'électrode. Avec la microscopie à force atomique (AFM) il a été possible de démontrer que la plupart de ces

observations était une conséquence de modification morphologique à la surface des échantillons. Les deux analyses ont indiqué que l'effet est plus prononcé avec des échantillons contenant un HTL d'oxyde de tungstène, même s'il est aussi observé quand l'oxyde de molybdène est utilisé.

Ces observations n'expliquent pas les changements des paramètres photovoltaïques observées dans les cellules OPV, néanmoins l'augmentation de la rugosité peut avoir des conséquences pour les cellules avec des électrodes minces. Pour mettre cela en évidence, une expérience a été faite pour étudier les effets de l'épaisseur d'une électrode en argent sur la stabilité thermique d'un dispositif OPV. Il a été constaté que la résistance série des dispositifs avec des électrodes plus minces de 60 nm augmente significativement avec le vieillissement thermique, par ailleurs les échantillons avec les électrodes les plus minces s'arrêtent complètement de fonctionner à cause de cette augmentation. Comme observé dans les expériences de RBS, la défaillance des dispositifs arrive plus rapidement avec un HTL d'oxyde de tungstène. L'étude de ces échantillons avec AFM a mis en évidence que les électrodes minces d'argent démouillent lors du vieillissement thermique ce qui peut conduire à la formation d'îlots d'argent avec les électrodes minces, et la mort rapide de la cellule. Ce mécanisme de défaillance n'avait pas encore été relevé dans la littérature scientifique, et pourrait être important pour l'application des électrodes minces d'argent comme des électrodes transparentes.

Des analyses de rupture ont également été faites pour suivre les effets du recuit sur la stabilité mécanique des cellules. Ces analyses suivent la propagation d'une rupture dans un échantillon d'une couche mince et donnent des informations sur le chemin de fracture (c'est-à-dire le point plus faible dans l'échantillon), sur l'énergie de rupture – l'énergie d'adhésion si l'échantillon rompt à l'interface de deux matériaux - ou bien sur l'énergie de cohésion - si il fracture au milieu d'une couche. Il a été constaté que l'adhésion des couches supérieures sur la couche active augmente fortement avec le vieillissement thermique, et la cohésion de la couche active diminue (probablement à cause de la séparation de phase donneur et accepteur). Ces effets conduisent le chemin de fracture à migrer de l'interface HTL-couche active au milieu de la couche active.

Des mesures de profil élémentaire avec spectrométrie photoélectronique X (XPS) ont été faites sur les surfaces fracturées des échantillons qui avait fracturé à l'interface HTL-couche active. Ces mesures ont démontré la diffusion de matière entre les couches supérieures et la couche active dans les échantillons avec électrode en argent. Contrairement aux expériences de RBS où des observations similaires étaient attribuées aux changements de la morphologie de surface des échantillons, il n'y a pas une grande différence de rugosité de la surface fracturée entre les échantillons de référence et les échantillons vieillis. Ceci indique que les observations d'XPS

représentent une vraie diffusion de matière. Notre hypothèse est que l'augmentation de l'adhésion est due à la diffusion de matière entre les couches supérieures et la couche active, ce qui serait cohérent avec des observations relevées dans la littérature scientifique. Par ailleurs, il est possible qu'il y ait une relation entre cette diffusion et la perte de V_{OC} et FF observée pour les cellules avec une HTL en MoO_3 et une électrode en argent, cependant il n'y a pas une corrélation directe.

Dans la deuxième partie de ce travail, une chambre de vieillissement a été fabriquée pour analyser les effets de la lumière sur la dégradation des OPVs inversées de P3HT:PC₆₁BM, selon les matériaux utilisés pour l'HTL et l'électrode et l'influence de la présence d'oxygène ou d'humidité. Cette chambre a la capacité de mesurer automatiquement 64 cellules solaires OPV avec un simulateur solaire HMI. Il y a également plusieurs capteurs pour suivre les conditions dans la chambre, en particulier l'intensité de la radiation, la température, et le taux d'humidité. Toutes les mesures sont faites avec un 'source measure unit' (Keithley 2400) contrôlé par un logiciel développé spécialement pour cette étude qui enregistre les données dans un fichier personnalisé et qui peut être contrôlé à distance avec une application smartphone. Chaque expérience génère un grand volume de données, et pour les traiter il était devenu nécessaire de faire un deuxième logiciel. En plus de tracer l'évolution des statistiques photovoltaïques des groupes d'échantillons, ce logiciel est capable d'estimer la durée de vie et les statistiques de 'burn-in' (la première partie exponentielle de la courbe de dégradation) des cellules en utilisant des modèles exponentielles et un algorithme personnalisé pour cette tâche.

Quelques effets des matériaux ont été notés quand les cellules étaient dégradées sous azote, en particulier la perte de V_{OC} n'est pas la même selon les HTLs et les électrodes utilisées, et par conséquent il y a de grandes différences de 'burn-in' et de durée de vie estimée. Les échantillons avec WO_3 et aluminium ont eu les durées de vies les plus longues, 97.7 ± 7.7 jours, soit le double de la durée de vie des autres échantillons. L'oxygène a eu pour effet d'accélérer notablement la dégradation, et aucune différence n'a été notée selon les matériaux utilisés pour l'HTL et l'électrode à cause des diminutions rapides des paramètres PV. En revanche, l'humidité a eu un effet prononcé sur les échantillons avec les HTLs de PEDOT:PSS (poly(3,4-éthylènedioxythiophène) poly(styrène sulfonate) de sodium), la résistance série a fortement augmentée entraînant une diminution du FF , et donc de rendement des cellules. Après avoir comparé ces résultats avec ceux publiés dans la littérature scientifique, il a été possible de proposer des mécanismes expliquant ces observations.

Ce travail souligne l'importance de penser à la durée de vie quand on désigne les dispositifs OPV, en particulier à faire attention à l'environnement dans lequel l'OPV va être utilisée pour sélectionner des matériaux appropriés afin d'optimiser la durée de vie.

Acknowledgements

In many ways, a thesis is a bit like a baby. It seems to be something people in their late 20s make that consumes an enormous amount of their social lives, causes loss of sleep, and you end up liking it no matter how ugly it looks. However, in the same way that it takes a village to raise a child, you are only reading this thesis today because of a large number of people who helped me over the last three years.

First and foremost, I need to thank my supervisors, Lionel Hirsch and Sylvain Chambon. Your guidance and knowledge on this project was instrumental in keeping me on-track, and helping me find answers to the questions that my research threw up... even if those answers were more questions! I will forever be grateful that you decided to offer this position to the guy with the funny accent from the other side of the world.

Throughout this project, I have been privileged to be able to collaborate with some amazing people. Among these are Professor Dauskaradt and his group at Stanford University, who very kindly hosted me last year and welcomed me into their laboratory to carry out fracture analysis work. In particular, I would like to thank Nick Rolston for all the work he has done with me on this project and his help in getting me up to speed with both the practical aspects of fracture analysis and American football. I would also like to thank Dr Stéphanie Sorieul at CENBG for her help with the RBS measurements, Dr Gilles Pecastaings at LCPO for his help with the AFM measurements, Philippe Barboteau at CRPP for the fabrication of the sample holder for the ageing chamber, and Franck Delalée at CENBG for fabrication of the ageing chamber lid.

Much of this project has been made easier by having great colleagues around me while working, both with respect to the science, and navigating some of the trickier aspects of life as a foreigner here in France. In particular, I would like to thank: Uyxing, Thérèse, Aurélien, Giorgio, Fred, Gildas, Léo, Maxime, Lionel D, Geoffroy, Mylène, Ashwin, Yu-Tong, Yan-Fang, Guillaume G, Elodie, Yolande, Marcin, Marco, Frank, Damien, Florence, Pierre-Henri, and Gilles for their help, advice, and friendship over the years. It has been great working with you all, and it will be sad to say goodbye. I know I will leave here with fond memories of each and every one of you. I would especially like to thank Marcin Kielar for both his advice with LabVIEW and his photography skills, Marco Pereira for his help with the 3D printing, and Elodie Destousse for her help with the doctor blade. I would also be remiss if I did not thank our excellent intern Thibaud Marazano, who did much of the early programming work for the ageing chamber control program.

I am fortunate in my life to have a large number of friends from all over the world. Since moving to France, I have made many more. My ability to finish this work was, in no small part, due to the support I have received from my friends here in Bordeaux, elsewhere in Europe, and further afield. I particularly want to thank my dear friend Maria Mattera who, although far away, has been there for me at every stage of my PhD and very kindly agreed to proofread this thesis.

The majority of this work has been funded by the French National Research Agency (*Agence Nationale de la Recherche*) in the frame of the project number ANR-13-JS09- 0014-01 "IN-STEP". My travel to the United States for the fracture analysis experiments was funded by LabEx AMADEus

(ANR-10-LABX-42) in the framework of IdEx Bordeaux (ANR-10-IDEX-03-02) - the *Investissements d'Avenir* programme of the French Government, managed by the French National Research Agency (*Agence Nationale de la Recherche*). I would like to thank the University of Bordeaux, the Bordeaux-Gradignan Centre for Nuclear Research (*Centre Etudes Nucléaires de Bordeaux Gradignan - CENBG*), and Stanford University for the roles they played in this project. I would also like to thank the IMS laboratory (*Laboratoire de l'Intégration du Matériau au Système*) for recruiting me to this position.

Finally, but most importantly, I would like to thank my father Ian Greenbank, my mother Christine Greenbank, my sister Emma Greenbank, and my brother Richard Greenbank for their love and support over the last three years. Although it hasn't been easy being separated by such a great distance from you all, the Skype calls every Tuesday morning certainly helped to make it all seem not so far. The world is growing smaller every year, and even though I ended up living on the other side of the planet from home, if there's one thing this experience has taught me, it is that such a distance is only far if you imagine it to be so.

This work was carried out at the IMS Laboratory, at the University of Bordeaux in the Organic Electronics Group. Ce travail a été fait dans le laboratoire d'IMS à l'Université de Bordeaux, dans le groupe d'Electronique Organique.



Laboratoire de l'Intégration du Matériau au Système CNRS UMR 5218
351 Cours de la libération, 33405 Talence cedex, France.

Dedicated to the memory of Albert Ernest Black

1923 – 2014

Table of contents

ABSTRACT/RÉSUMÉ	I
RESUME DE THESE FRANÇAIS	III
ACKNOWLEDGEMENTS	VII
TABLE OF CONTENTS	IX
TABLE OF ABBREVIATIONS	XV
CHAPTER 1 - INTRODUCTION	1
1.1. Why pursue solar energy?	1
1.2. The development of photovoltaic technology	2
1.3. Organic photovoltaic solar cells	3
1.4. Research aims of this study	4
CHAPTER 2 - DEGRADATION OF OPV SOLAR CELLS	7
2.1. Introduction	7
2.2. The photovoltaic parameters	8
2.3. Origins and Mechanisms of Degradation	10
2.3.1. OPV device design and the photovoltaic effect	10
2.3.2. Degradative effects on absorption	13
2.3.3. Degradative effects on exciton separation	16
2.3.4. Degradative effects on charge migration	20
2.3.5. Degradative effects on charge extraction	26
2.4. Studying OPV Device Degradation	31
2.4.1. The ISOS protocols	31
2.4.2. OPV degradation behaviour under working conditions	32
2.5. Strategies to minimise device degradation	38
CHAPTER 3 - EXPERIMENTAL DETAILS	41
3.1. Thermal degradation study of inverted OPV devices	41
3.1.1. Fabrication of OPV devices	41

3.1.2. IV characterisation of OPV devices	43
3.1.3. Thermal ageing of the OPV devices	44
3.2. Rutherford backscatter spectrometry and atomic force microscopy (AFM) experiments	45
3.2.1. Preparation of samples for RBS	45
3.2.2. Instrument settings and parameters	45
3.3. Fracture analysis experiment	46
3.3.1. Sample fabrication	46
3.3.2. Sample transportation	46
3.3.3. Sample preparation for fracture analysis and measurement	46
3.3.4. Fracture analysis data processing	47
3.3.5. X-ray photoelectron spectroscopy (XPS) and Kelvin probe analysis	47
3.4. Photodegradation experiments	47
3.4.1. Sample fabrication and experiment design	47
3.4.2. External quantum efficiency measurements	48
3.4.3. Construction and use of the ageing chamber	48
3.4.4. Ageing chamber control and data processing applications	53
CHAPTER 4 - THERMAL AGEING MECHANISMS IN OPV SOLAR CELLS	57
<hr/>	
4.1. Introduction	57
4.2. OPV Device Studies	58
4.2.1. P3HT Study Outline	58
4.2.2. Results Overview	59
4.2.3. J_{SC} -driven thermal degradation	64
4.2.4. V_{OC} and FF-driven degradation	66
4.2.5. Thermal degradation of PCDTBT:PC ₇₁ BM devices	69
4.3. RBS and AFM Studies	72
4.3.1. Overview of the studies	72
4.3.2. Rutherford backscattering spectrometry analysis	73
4.3.3. AFM experiments	79
4.3.4. Variations in thermal ageing with electrode thickness	83
4.4. Fracture analysis	87
4.4.1. Introduction to fracture analysis	87
4.4.2. Experiment design and optimisation	90
4.4.3. Fracture analysis of unaged samples	93
4.4.4. Fracture analysis trends with thermal ageing	94
4.5. XPS depth profiling and Kelvin probe analysis	98
4.5.1. Overview	98
4.5.2. Sample structure	99
4.5.3. XPS elemental depth profile measurements	99
4.5.4. Kelvin probe measurements	102
4.6. Summary	103

CHAPTER 5 - DEGRADATION OF OPV SOLAR CELLS UNDER SIMULATED WORKING CONDITIONS	107
<hr/>	
5.1. Introduction	107
5.2. Photo-degradation studies under an inert atmosphere	109
5.2.1. Analytical modelling of PCE loss	109
5.2.2. Material-dependence of PCE ageing parameters	113
5.2.3. Analysis of the burn-in	117
5.2.4. Post-burn-in degradation	123
5.3. Effects of atmospheric composition on photodegradation	127
5.3.1. Degradation in dry synthetic air	127
5.3.2. Degradation in humid nitrogen	132
5.4. Summary	135
CHAPTER 6 - CONCLUSIONS AND FUTURE WORK	139
<hr/>	
6.1. General conclusions	139
6.2. Avenues for future research	142
REFERENCES	145
APPENDIX A - TRANSPORTATION OF FRACTURE ANALYSIS SAMPLES	159
APPENDIX B - XPS SURVEY SCANS OF FRACTURED SAMPLES	161
<hr/>	
B.1. Unaged control samples	161
B.2. Samples aged one week	162

Table of abbreviations

Abbreviation	Definition
AES	<i>Auger electron spectroscopy</i>
AFM	<i>Atomic force microscopy</i>
AM1.5	<i>Air-mass 1.5</i>
BHJ	<i>Bulk heterojunction</i>
DCB	<i>Double cantilever beam</i>
DIO	<i>1,8-diiodooctane</i>
EQE	<i>External quantum efficiency</i>
ETL	<i>Electron transport layer</i>
FF	<i>Fill factor</i>
HMI	<i>Hydrargyrum medium-arc iodide</i>
HTL	<i>Hole transport layer</i>
IQE	<i>Internal quantum efficiency</i>
IR	<i>Infrared</i>
ISOS	<i>International Summit on Hybrid and Organic PV Stability</i>
ITO	<i>Indium-tin oxide</i>
IV	<i>Current-voltage</i>
KP	<i>Kelvin probe</i>
KPFM	<i>Kelvin probe force microscopy</i>
NREL	<i>National renewable energy laboratory</i>
OFET	<i>Organic field-effect transistor</i>
OLED	<i>Organic light-emitting diode</i>
OPD	<i>Organic photodetector</i>
OPV	<i>Organic photovoltaic</i>
P3HT	<i>Poly(3-hexyl thiophene)</i>
PC _{61/71} BM	<i>[6,6]-phenyl-C_{61/71}-butyric acid methyl ester</i>
PCDTBT	<i>poly(carbazole-dithiophene-benzothiadiazole</i>
PCE	<i>Power conversion efficiency</i>
PCPDTBT	<i>Poly[2,6-(4,4-bis-(2-ethylhexyl)-4H-cyclopenta [2,1-b;3,4-b']dithiophene)-alt-4,7(2,1,3-benzothiadiazole)]</i>
PEDOT	<i>Poly(3,4-ethylenedioxythiophene)</i>
PPV	<i>Poly(p-phenylene vinylene)</i>
PSS	<i>Polystyrene sulfonate</i>
PV	<i>Photovoltaic</i>
RBS	<i>Rutherford backscatter spectrometry</i>
RH	<i>Relative humidity</i>
TOF-SIMS	<i>Time of flight secondary ion mass spectrometry</i>
UV	<i>Ultraviolet</i>
XPS	<i>X-ray photoelectron spectroscopy</i>



Chapter 1

Introduction

1.1. Why pursue solar energy?

In the latter half of the 20th century a number of different scientific disciplines were beginning to show that the extremely rapid industrialisation and urbanisation of humanity were having a destructive impact on the planet's climate.¹ Over the last two centuries, the atmosphere's CO₂ content has dramatically increased to over 400 ppm and global average temperatures have followed, as a result of emissions from the burning of fossil fuels. This level has not occurred naturally in over 15 million years.² Furthermore, when CO₂ levels were last this high, the oceans were between 25 m and 40 m higher than their current levels, and global temperatures were between 3°C and 6°C higher than current averages.² If climate change is allowed to continue to accelerate at its current rate, even the best case scenario outcomes are potentially catastrophic for hundreds of millions of people,¹ and it is likely that climate change is already contributing to natural disasters and geopolitical instability around the world.³

Despite initial political resistance, there is now significant momentum behind initiatives to reduce carbon emissions to avert the worst-possible consequences of anthropogenic climate change. This was signified by the signing of the Paris Agreement at the COP21 conference in December 2015, in which all participant nations agree to reduce CO₂ emissions and pursue strategies to mitigate the impact of climate change.⁴ Achieving the targets laid out in the agreement will require a concerted effort to reduce emissions in many economic sectors, but of these the energy sector is the single largest contributor to global CO₂ emissions, with electricity generation alone being responsible for 25% of all global emissions.¹ This is mostly due to the significant role that fossil-fuel-based generation plays in global generation capacity, supplying approximately 57% of the world's installed electricity generation capacity in 2015.⁵

A further complication is the rising global demand for energy. Despite efficiency gains in the design of "smart-grids" and the push towards energy efficiency in urban design and architecture, global generation capacity is projected to double in the next 25 years to meet rising demand.⁵ This means that a significant portion of this added capacity must come from renewable energy if economic growth is to continue while reducing emissions. Fortunately, this is exactly the trend being observed in the energy industry. By 2040 it is expected that zero-emission energy sources will account for 60% of installed global generation capacity, representing an investment of USD\$11.4 trillion in new renewable energy generation.⁵ Of the added generation capacity, it is projected that 43% will come from photovoltaic (PV) solar energy, representing an investment of USD\$3 trillion.⁵ While no doubt public policy will play a role, this trend is predominantly market-driven, in particular by the decline in the cost of wind and solar energy.⁵ With the latter, a significant portion is predicted to be the result of technological developments.⁵ It is therefore evident that in the coming years there will be a growing demand for cheap solar energy, and that technological innovation is required to meet this demand.

Solar energy also presents a number of benefits beyond being a zero-carbon energy source. Although probably not likely to run out in the near future, fossil fuels (particularly oil) are subject to significant amounts of price volatility and regional scarcity.^{6,7} While fossil fuels are certainly a significant factor in the economic development that has occurred over the last two centuries, the supply of oil has driven conflict in many parts of the world for over half a century, and continues to determine the foreign policies of many developed nations.⁷ Solar energy is unlikely to suffer from any such scarcities. Moreover, solar energy is highly scalable, and while it is frequently used in large scale power plants, it can also be used for distributed generation, allowing access to electricity in many parts of the world where centralised electricity infrastructure is inadequate or non-existent.⁸

1.2. The development of photovoltaic technology

The photovoltaic effect was first demonstrated by the French physicist Alexandre-Edmond Becquerel in 1839 when, while working with certain metal electrodes and electrolytes, he noted a slight increase in current when the electrodes were exposed to light.⁹ At the time he could not explain his discovery, and the photovoltaic effect remained little more than a curiosity until April 25, 1954 when Bell Labs demonstrated the first practical silicon solar cell.¹⁰ These were of great interest to both the public, and to NASA who began immediately incorporating solar panels into their satellites and spacecraft.

These first solar cells were fabricated from doped monocrystalline silicon, and had an efficiency of just 6%.¹⁰ Over time, the efficiency of these monocrystalline devices improved, and the current record efficiency for a single junction silicon-based device is 25.0% (blue circles in Figure 1.2.1).¹¹ These devices and some variations are collectively referred to as “first generation” photovoltaic solar cells. Despite the name, first generation solar cells are the constituent technology for the majority of commercially available photovoltaic modules today.¹²

First generation PV devices have been widely adopted and could be considered a mature technology, but they have significant drawbacks in terms of the resources and energy required to fabricate them, and therefore have long energy payback times.¹² These drawbacks were the reason for the development of second generation technologies which included a number of different thin-film, inorganic designs (shown in green in Figure 1.2.1). While an improvement on first generation devices, second generation devices suffered from stability issues (unlike first generation devices which are extremely stable), and commercialisation of the technology was very slow.¹²

Finally there is the broad class of photovoltaic technologies referred to as third generation photovoltaics. The definition of what constitutes a third generation PV technology vs. a second generation technology is nebulous; however the term “third generation” generally encompasses multi-junction devices (purple in Figure 1.2.1), and devices using organic or inorganic/organic hybrid active layers (orange in Figure 1.2.1).¹² The latter category can include: dye-sensitised solar cells, perovskite solar cells, and organic photovoltaic (OPV) solar cells. Although they differ significantly in materials, efficiency, and stability, the unifying feature of these technologies is that they can be printed and are not reliant on vacuum deposition or single crystal growth.¹²

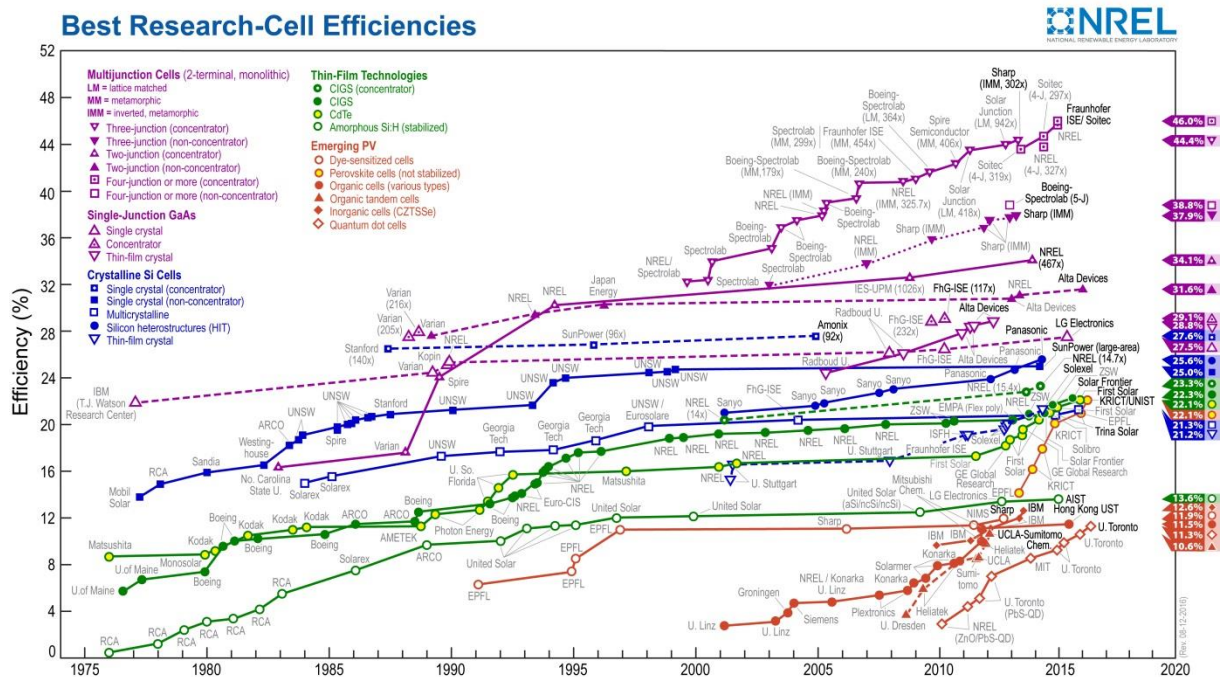


Figure 1.2.1: The United States National Renewable Energy Laboratory (NREL) chart of device efficiency records from 1976 to present. This chart was downloaded on 26/09/2016 from the NREL website at: http://www.nrel.gov/ncpv/images/efficiency_chart.jpg

These third generation technologies, particularly OPV and perovskites, represent a dramatic shift in the design of photovoltaics towards low-cost, mass-production technologies. While both technologies have significant barriers to their wide-scale commercialisation, both have generated significant interest in the research community and have the potential to significantly change the solar energy industry if these barriers are overcome.

1.3. Organic photovoltaic solar cells

OPV, and organic electronics in general have their origins in the work of Shirakawa *et al.* in the mid-1970s who discovered the conductive properties of doped polyacetylene.¹³ Their work was the beginning of the entire organic electronics field, which now encompasses a wide range of devices including organic light-emitting diodes (OLEDs), organic field-effect transistors (OFETs), organic photodetectors (OPDs), and of course OPV solar cells. For this discovery, Professors MacDiarmid, Shirakawa, and Heeger were jointly awarded the Nobel Prize in Chemistry in 2000.¹⁴

What defines an OPV solar cell is that it is fabricated with an organic (carbon-based) active layer. This distinguishes it from other types of solar cells which incorporate inorganic (or hybrid) active layers – most commonly silicon. The various components and structure of an OPV device will be discussed in more detail in Chapter 2, but in general, one of the key strengths of OPV solar cells is that they can be much cheaper, and require less energy to fabricate than inorganic solar cells.¹⁵ This is because their active layers are typically fabricated using either semiconducting polymers or small molecules which do not require processing at high temperatures.¹⁵ Furthermore, OPV solar cells can be deposited by printing techniques instead of vacuum deposition or single crystal growth which allows for scaling to high volume manufacturing, and the fabrication of mechanically flexible devices.¹⁵ This

has the potential to greatly expand the range of applications of photovoltaic solar energy,¹⁶ as well as to greatly lower its cost.

Whenever a new solar energy technology is being considered, there are several factors that determine its market viability. They are:

- production, transportation and installation costs,
- efficiency,
- lifetime,
- scalability, and
- environmental impact.

With respect to cost, scalability, and environmental impact, OPV solar cells typically perform favourably when compared to other PV technologies.^{17,18} This is particularly promising with respect to cost and environmental impact as these metrics typically improve when production is scaled up.¹⁹ Where OPV do not perform as well is in efficiency and lifetime. The current power conversion efficiency (PCE) record for an OPV device is 11.5% (Figure 1.2.1 – cf. 25% for a lab-scale silicon device), and although little progress has been made in recent years in improving upon this figure, there are a number of avenues open to researchers to improve on this record.²⁰ Besides, if the costs of an OPV system are sufficiently low, this can offset the lower efficiency.

The other area where OPV fail to perform is in their operational lifetime. Despite significant improvements in recent years,²¹ progress is still needed to reach the generally accepted target of 10 years operational lifetime.¹⁹ Much of this is because the topic of operational stability has received less research interest than efficiency, although this is slowly changing.²¹ However, it is estimated that if the operational lifetime of OPV could be increased to (or beyond) 10 years, this would make OPV technology competitive with established PV technologies at the commercial scale, despite the lower efficiency,¹⁹ suggesting that understanding OPV degradation deserves much more attention than it currently receives.

1.4. Research aims of this study

As was noted in section 1.3, one of the principal barriers to the wide-scale commercialisation of OPV solar cell technology is the lifetime of the devices. While the price advantage of OPV can compensate for their lower efficiencies, lifetimes need to reach at least 10 years in order for OPV to be competitive with established technologies.¹⁹ Although interest in OPV degradation research has increased in recent years,²¹ there is still much left to understand about how and why OPV degrade, and how they can be designed to be more resilient to degradation.

The ageing of OPV solar cells is a complex topic. This is because in operating conditions there are several different degradation stimuli all interacting simultaneously with different parts of a device while it ages. This is exacerbated by the number of different materials and device architectures that may be employed in the design of an OPV solar cell. A further complication is that although standard protocols exist for testing OPV lifetimes in conditions that range from simple laboratory experiments up to large-scale outdoor experiments,²² many studies of ageing have not followed these protocols, or do not provide key information about the protocol that they are following.

The purpose of this work is to gain understanding of the interactions between different ageing stimuli and the different materials in an OPV device in a controlled setting. In particular, the aim of the study is to examine the role that the choice of materials at the hole extraction interface plays in determining the lifetime of an inverted OPV device under different ageing conditions. There are two parts to this study. The first part examines the thermal ageing in the dark of OPV devices (ISOS-D-2)²² fabricated with a range of hole transport layer (HTL) and metal electrode materials. This is because heat is an intrinsic degradation stimulus that will always be present in the normal operation of a solar cell, and so the design of long-lifetime OPV must take thermal stability into account. This part of the study incorporates a device study to examine the evolution of the photovoltaic parameters with thermal ageing when different materials are used in the fabrication of the device. This is followed by a physical characterisation study to understand how thermal ageing can physically alter the top electrode of a device and the impact that this can have on the operation of the device. Finally, a fracture analysis study is detailed which examines the effects that thermal ageing has on the mechanical stability of the devices. These changes in mechanical stability are then correlated to physical changes in the devices, which in turn can be related to changes in the photovoltaic parameters. The findings from this part of the study illustrate a number of key considerations in device design that can greatly enhance the thermal stability of inverted OPV devices.

The second part of the study examined the ageing of OPV devices under illumination in controlled atmospheric conditions (ISOS-L-1).²² As with the first half of the study, devices incorporating a range of materials at the hole extraction interface were fabricated for the experiments. The aim of this part of the study is to understand the role that the different materials play in determining the lifetime of the device and how this is affected by exposure to either oxygen or humidity. Doing so requires that the ageing be carried out in highly controlled conditions, and that large numbers of devices can be examined to ensure that there are statistically significant numbers of devices with the different combinations of materials. This was done by constructing a purpose-built photovoltaic ageing chamber that conformed to standard OPV stability testing protocols, and writing customised software to automatically carry out measurements during an experiment and process the large volume of data generated by an experiment. Data from this apparatus gives information about the role that certain materials can play in decreasing the severity of photodegradation in an OPV device, and in lengthening the devices' lifetime under illumination, as well as the vulnerabilities to particular ageing stimuli that devices can exhibit if certain materials are used in their fabrication.

All parts of this study were carried out in accordance with accepted standard testing protocols for OPV ageing in a laboratory setting²² to ensure comparability to other studies.

I

Chapter 2

Degradation of OPV solar cells

2.1. Introduction

In addressing the challenges simultaneously posed by both anthropogenic climate change and the continually rising global demand for energy, solar energy presents an attractive option. The main obstacle to widespread adoption of photovoltaic technology has been, and continues to be, the ratio of the required financial investment to device efficiency, energy payback time and device lifetime. Organic photovoltaic solar cells (OPV) approach this problem by dramatically decreasing the fabrication cost and energy payback time of devices,¹⁷ but often at the expense of lifetime and efficiency.²³ It follows, therefore, that researchers must focus on improving the efficiency and lifetime of OPV technology. In recent years, a series of breakthroughs in polymer design have resulted in devices with efficiencies exceeding 10%,^{24–26} a long-held target of researchers.¹⁵ Although these values fall well short of the efficiencies achieved by their inorganic counterparts,²⁵ the substantially lower fabrication costs and shorter energy payback time¹⁵ of OPV devices mean that achieving parity in efficiency is not a prerequisite for large-scale commercialisation.

Progress in improving device lifetime has often lagged behind the advances made in device efficiency.²¹ This is likely due in part to greater focus being given to efficiency, but also reflects the relative complexity of OPV degradation. Broadly-speaking, degradation mechanisms can be divided into two categories: extrinsic mechanisms which occur due stimuli that can be removed without impeding the function of the device, and intrinsic mechanisms that can only be prevented by altering the design of the device. There are four main external stimuli that give rise to extrinsic degradation in OPV: light, heat, oxygen and water (depending on the application, one might also consider mechanical stress). Each of these stimuli can act individually, such as in the case of thermally-driven variation of the morphology of the active layer,²⁷ or in concert, such as in the case of photo-oxidative bleaching of the active layer.²⁸

Determining the role of each degradation stimulus and the corresponding mechanism of action in the ageing of a device requires careful study to decorrelate the different effects. This typically involves the use of environmental chambers at the lab scale with controlled atmospheres, temperatures and light levels in addition to long-term outdoor testing for industrial purposes.²¹ To ensure comparability between tests carried out in different laboratories in different parts of the world, a number of standards for OPV testing have been agreed upon,²² which will be discussed in detail later in this chapter (section 2.4.1), and form the basis for the procedures followed in later chapters.

The state of the art of OPV degradation research will be summarised in this chapter, in particular the degradation trends followed by OPV devices and the proposed origins of their behaviour. Next, the mechanistic origins of the degradation behaviour of OPV will be discussed in detail with reference to the four degradation stimuli stated above. The section will conclude by describing the state of progress in finding strategies to extend device lifetime by limiting the action of degradation stimuli. It

should be noted that as the subject of this work is the degradation of polymer-based OPV, the majority of this chapter will focus on their degradation, although there will be a limited examination of the degradation behaviour of small molecule OPV.

2.2. The photovoltaic parameters

Efficiency alone is poor metric to use when describing the function of a solar cell, and even worse when trying to understand the effects that the use of different materials, or ageing have on the function of a device. For this reason, researchers typically study the evolution of several different characteristics of a device, which will be outlined in this section.

An ideal solar cell can be represented by the equivalent circuit shown in Figure 2.2.1.²⁹

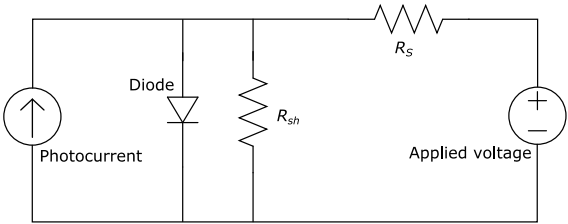


Figure 2.2.1: The equivalent circuit of a photovoltaic solar cell. In the diagram, R_s and R_{sh} represent the series and shunt resistances respectively.

The shunt and series resistances (R_{sh} and R_s respectively) are the first two important parameters to calculate when characterising a solar cell. The shunt resistance describes how close to a perfect diode the device is, i.e. the lower shunt resistance, the less perfect the diode. The series resistance can be considered as the sum of all the ohmic resistances in a device, and should be minimised in an optimal device.²⁹ Both of these parameters can be determined from the current-voltage (IV) curve of a device when the device is measured in the dark. In the dark, the photocurrent component of the circuit is removed, leaving only the diode and two resistive components. When the device is forward-biased, the contribution of the shunt resistance is negligible, while when the device is reverse biased, the shunt resistance dominates as it is typically many orders of magnitude greater than the series resistance (see Figure 2.2.2). Current that flows when the device is reverse-biased (in the dark) is also referred to as “leakage current”.²⁹ A typical IV curve obtained from an OPV solar cell in the dark is shown in Figure 2.2.2, with the shunt and series resistances annotated.

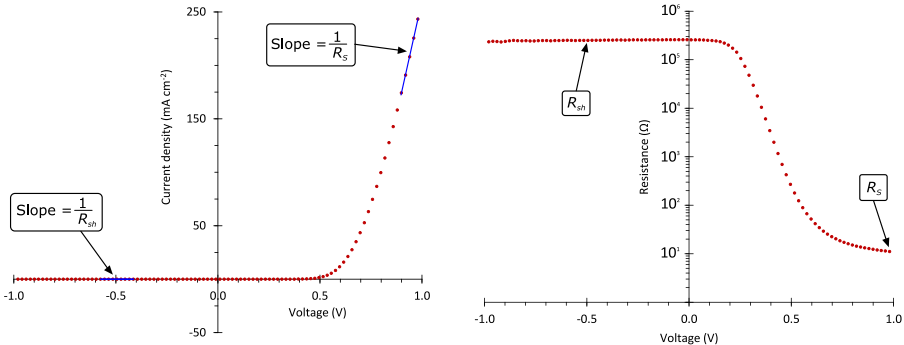


Figure 2.2.2: (left) a typical IV curve obtained from an OPV device in the dark, with the points corresponding to the series and shunt resistances, and (right) a resistance-voltage curve of the same device in the dark with the shunt and series resistances annotated.

The remaining parameters are determined from an IV curve when measured under illumination, i.e. with the photocurrent portion of the equivalent circuit included (Figure 2.2.1). The effect of adding the photocurrent is shown in Figure 2.2.3.

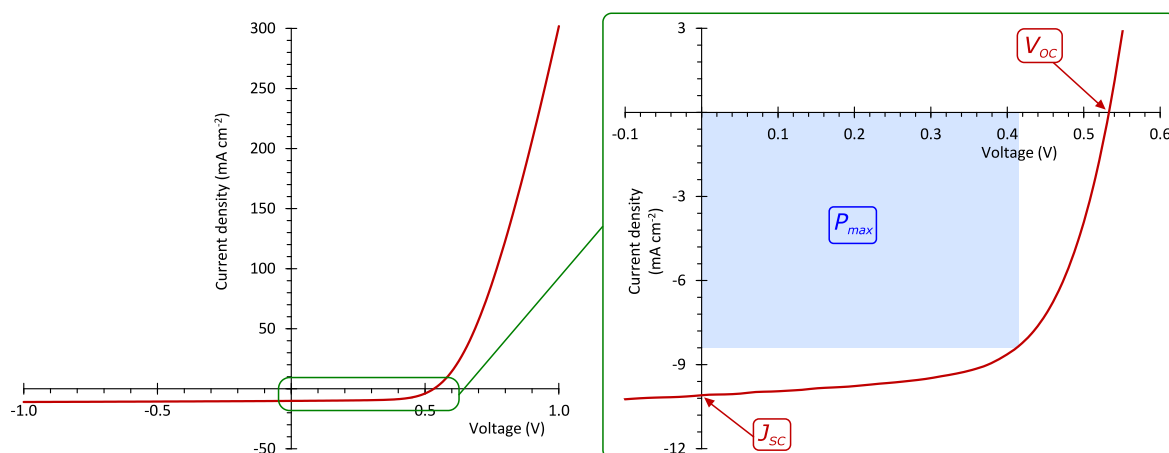


Figure 2.2.3: (left) a typical IV curve obtained from an OPV device under illumination, and (right) a magnification of the power generating portion of the curve with the V_{OC} , J_{SC} , and P_{max} annotated.

The two easiest terms to determine from the illuminated IV curve are the open-circuit voltage (V_{OC}) and the short-circuit current density (J_{SC}) (see Figure 2.2.3). The V_{OC} is effectively the largest voltage that the device can produce, and in OPV is related to the difference in energy between the lowest unoccupied molecular orbital (LUMO) of the acceptor species and the highest occupied molecular orbital (HOMO) of the donor species (section 2.3.1). The J_{SC} is the highest current that the device can produce (itself) and is related to the ability of a device to absorb light and extract the photo-generated charges. It is also possible to find the maximum power generation point (P_{max}) from the IV curve (Figure 2.2.3 and Figure 3.1.2), which is the point at which the device would be held under operating conditions. From these three parameters it is possible to calculate the fill factor (FF):

$$FF = \frac{P_{max}}{J_{SC} \times V_{OC}} \quad 2.2.1$$

The FF is a measure of the “squareness” of the IV curve, and therefore is closely related to the shunt and series resistances.²⁹ These parameters can, in turn, be used to calculate the power conversion efficiency (PCE):

$$\eta = \frac{P_{max}}{P_{rad}} = \frac{FF \times J_{SC} \times V_{OC}}{P_{rad}} \quad 2.2.2$$

in which η is the PCE and P_{rad} is the radiation intensity. The PCE is the most widely quoted metric for device efficiency, as it directly relates the radiation intensity to the maximum power the device can produce, and is therefore the easiest to measure.²⁹ Another efficiency measurement frequently quoted is the external quantum efficiency (EQE), which is the ratio of the number incident photons on a device at a given wavelength to the number of electrons collected at the electron-collecting electrode (not determined from an IV curve). This a complementary measurement to internal quantum efficiency (IQE) which measures the ratio of the number of photons absorbed by the device at a given wavelength to the number of electrons collected at the electron-collecting electrode.

Of these parameters, the most commonly quoted are J_{SC} , V_{OC} , FF , and PCE.²⁹ The variation of each of these parameters can reveal information about specific changes in a PV device, and their optimisation frequently requires specific synthesis and fabrication considerations.

2.3. Origins and Mechanisms of Degradation

Degradation can occur in every part of an OPV device, and can affect any or every stage of photocurrent generation.³⁰ This can be due to the action of any, or all, of: light, heat, oxygen and humidity. This section will describe the process of photocurrent generation in OPV and the way in which each stage of photocurrent generation is vulnerable to attack by degradation stimuli.

2.3.1. OPV device design and the photovoltaic effect

The different stages of photocurrent generation in OPV devices and their typical architectures are illustrated in Figure 2.3.1.

In the first stage (Figure 2.3.1), light is absorbed by the active layer. Absorption can occur in either the donor or acceptor species in the active layer; however, in practise the donor species is normally designed to achieve maximal absorption across the visible spectrum (although increasing focus is being given to acceptor design to increase its contribution in the generated photocurrent).³¹ The absorption of a photon excites an electron from the highest occupied molecular orbital (HOMO) to the lowest unoccupied molecular orbital (LUMO) of the absorbing species. The analogous process in a silicon-based device would be excitation of an electron from the valence band to the conduction band.

In a silicon device, at this point the generated free hole and free electron can be easily extracted. However, in organic devices the hole and electron do not fully separate upon excitation by the photon, instead forming a quasi-particle called an exciton. This exciton has a characteristic “binding energy” that must be overcome to separate the charges so charge extraction can occur.³² Exciton binding energies in organic materials are typically on the order of 0.1 – 1.4 eV, compared to only a few millielectron volts in inorganic materials.^{33,34} This is because organic semiconductors, having molecular orbitals rather than bands, do not undergo the same degree of orbital delocalisation that crystalline inorganic semiconductors do. This localises the hole and electron wave functions, increasing their mutual attraction (enhanced by the relatively low dielectric constants of organic materials).³³ This type of highly localised exciton is known as a Frenkel excitation (see section 2.3.3). As kT is 25.7 meV at 298 K, thermal energy is insufficient to separate excitons in an organic active layer at room temperature (as it is in inorganic devices). In OPV, this problem is overcome by having a “donor” and “acceptor” species present in the active layer.³⁵ The exciton migrates to an interface between the donor and acceptor species where a potential gradient exists that is large enough to separate the charges through transfer of the photo-excited electron from the donor to the acceptor.³²

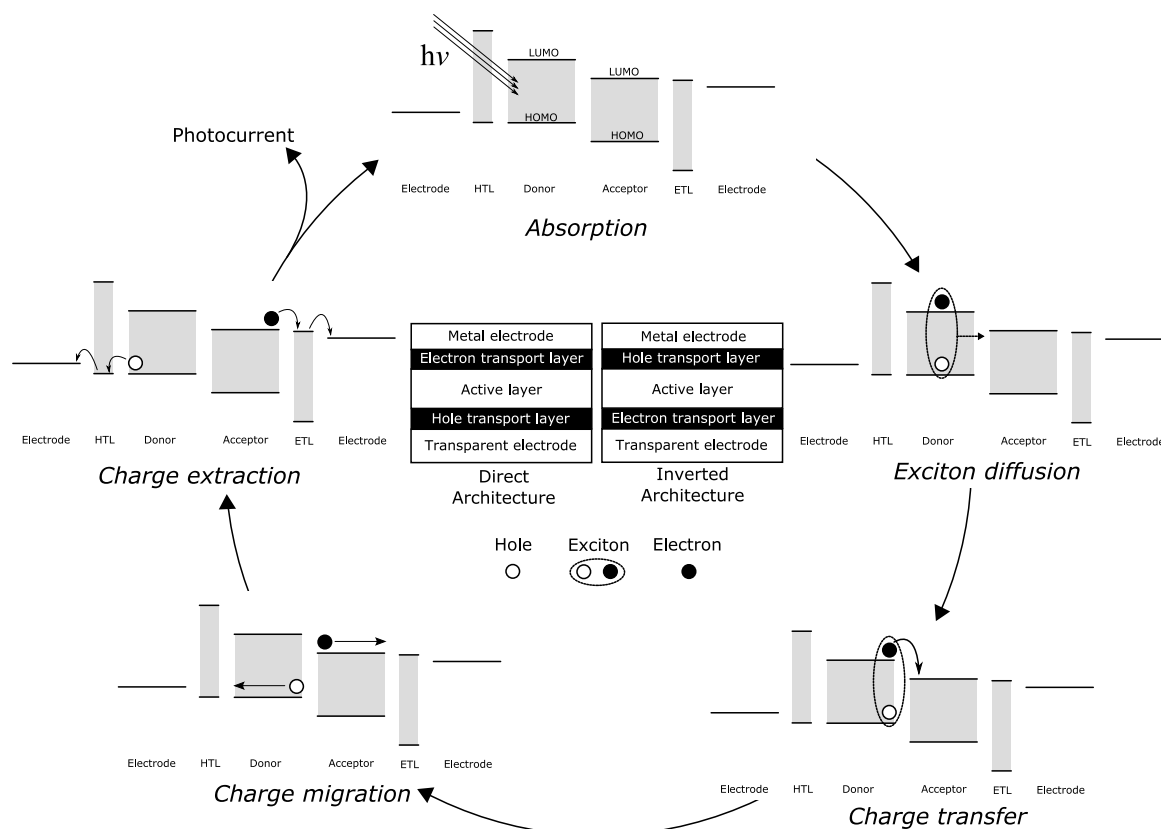


Figure 2.3.1: An outline of the photovoltaic process in OPV devices and the two main device architectures

This touches on a critical aspect of active layer design: morphology. Early OPV devices utilised a bilayer design similar to the design of p-n junctions in classical silicon devices (Figure 2.2.2 left).³⁵ These devices are easier to reliably fabricate; however, they have the significant drawback that only excitons near the donor-acceptor boundary will undergo charge transfer as exciton diffusion length is generally evaluated around 10 nm^{36–38} and any excitons generated elsewhere in the device will recombine (*vide infra*).³² To overcome this limitation, it became necessary to redesign the active layer, moving away from bilayer structures towards more intermixed designs. With this in mind, Yu *et al.* proposed the “bulk heterojunction” (BHJ).³⁹ In a BHJ the donor and acceptor phases are highly intermixed, maximising contact between them and therefore maximizing the volume of space within an active layer in which photo-generated excitons are able to diffuse to a donor-acceptor interface and undergo charge transfer (Figure 2.3.2 right). Key to the design of BHJ active layers is morphology optimisation, i.e. ensuring that domains of donor and acceptor are smaller than the exciton diffusion length but still have continuity in order to ensure the charge collection. This can be achieved via a number of strategies, including careful selection of solvent and solvent additives,⁴⁰ using thermal annealing to promote phase segregation,⁴¹ and annealing the active layer in solvent vapour.⁴²

Typical materials used for the donor are semiconducting polymers like poly(3-hexyl)thiophene (P3HT) and poly[N-9'-heptadecanyl-2,7-carbazole-alt-5,5-(4',7'-di-2-thienyl-2',1',3'-benzothiadiazole)] (PCDTBT), or semiconducting small molecules like phthalocyanine, subphthalocyanine and merocyanine derivatives.⁴³ Acceptor materials are typically fullerene derivatives like phenyl-C₆₁-butyric acid methyl-ester (strictly PC₆₁BM, but frequently referred to as PCBM), and its C₇₁ derivative PC₇₁BM, but there are some notable exceptions³⁸ that show great potential for pushing device efficiency beyond

the 10% limit for fullerene-based acceptors described by Scharber *et al.*⁴⁴ This limit is largely a consequence of the energy losses upon charge transfer between donor and acceptor, resulting in the V_{oc} of the device (which is directly related to the difference in energies between the donor HOMO and acceptor LUMO) being lower than it might otherwise be.^{38,45} An example of the benefit of non-fullerene acceptors was reported this year in *Nature Communications*, in which the authors demonstrate efficiencies exceeding 6% and improved resilience to oxygen when a non-fullerene acceptor is paired with P3HT in an OPV device.⁴⁶

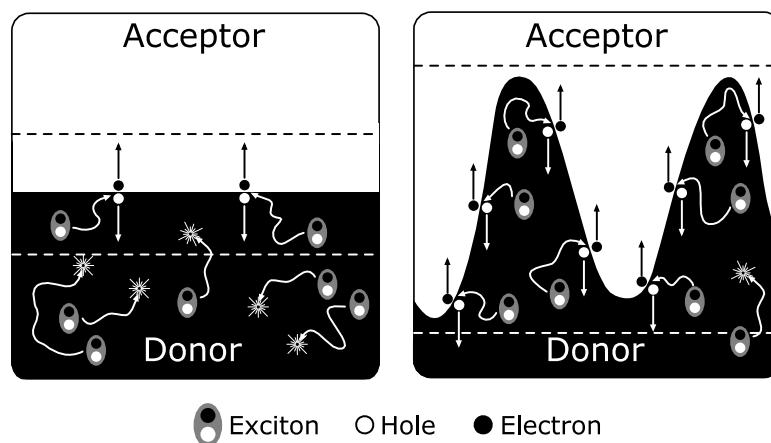


Figure 2.3.2: An illustration of a (left) bilayer and (right) BHJ active layer. The dashed lines represent the volume of space in which a photo-generated exciton is likely to diffuse to an interface and separate, which is larger with a BHJ.

After charge transfer, the two charge carriers must migrate to the correct interfaces for charge extraction. Due to the relatively low charge carrier mobility in organic semiconductors, this migration is slow and the charges are vulnerable to recombination.⁴⁷ This is typically taken into account in the design of devices, particularly with respect to the thickness of the active layer. The thinner an active layer is, the greater number of photo-generated charges are able to reach their respective electrodes.⁴⁸ Conversely, however, a thinner active layer has a lower absorption cross-section, meaning that it is less likely that radiation is absorbed by the device in the first place.⁴⁹ Determining the optimal thickness of an active layer is largely a balancing act between these considerations and ultimately determined by the mobility of the active layer blend.⁴⁹

In the final step, the charges are extracted at their respective electrodes, typically in the presence of hole/electron transport interlayers. These interlayers have energy levels that are optimised for the transportation of one charge carrier over another. For instance, a hole transport layer would have a HOMO that is close in energy to the HOMO of the donor species to facilitate the extraction of holes and a high energy LUMO to serve as a barrier to electrons (see Figure 2.3.1), and *vice versa* for an ETL.^{50,51} Typical materials used for HTL materials are MoO_3 , WO_3 , V_2O_5 , and Poly(3,4-ethylenedioxythiophene)-poly(styrenesulfonate) (PEDOT:PSS), deposited by either solution processing or evaporation as appropriate.⁵¹ The ETL layer in direct devices is typically a low work function metal like calcium; in inverted devices, ZnO , TiO_x , or organic interlayers like polyethylenimine (PEI) and ethoxylated-polyethylenimine (PEIE) are frequently used.^{51,52}

The electrodes themselves have a number of different configurations, depending on the application of the device. At least one of the electrodes is typically a metallic electrode (usually either silver or aluminium), while the other must be transparent to allow light to enter the device.⁵³ The most

common material used for a transparent electrode in either the inverted or direct configuration is tin-doped indium (III) oxide (ITO) on a glass substrate.⁵⁴ The continued use of this material faces some significant challenges owing to the high cost and relative scarcity of indium⁵⁵ and the unsuitability of ITO to applications involving flexible substrates or roll-to-roll manufacturing.⁵³ A number of alternatives to ITO are being pursued, such as silver nanowire meshes,⁵⁶ monolayer and/or doped graphene,⁵⁷ carbon nanotubes,⁵⁸ and highly conductive PEDOT:PSS.⁵⁹ These new electrode materials can also be used to replace the metallic electrode, enabling the fabrication of semi-transparent devices.⁶⁰

2.3.2. Degradative effects on absorption

The harvesting of light for energy in a photovoltaic device begins with absorption of a photon, forming an exciton via photoexcitation of an electron in the HOMO of (usually) the donor molecule. The compounds used in the active layer are designed to have as wide an absorption band and as high an extinction coefficient as possible across the solar spectrum to maximise photocurrent generation capacity. It therefore follows that any chemical degradation of these carefully designed compounds has the potential to interfere with their ability to absorb radiation, severely limiting their capability to function in an OPV device.

The most common way in which the absorption spectrum of an active layer component is negatively affected is through oxidative photo-bleaching.³⁰ This is a problem that has plagued researchers since the earliest days of OPV research; in their seminal article in *Synthetic Metals*, Weinberger, Akhter, and Gau note the extreme oxygen sensitivity of their polyacetylene photovoltaic junctions.⁶¹ These issues persisted as researchers moved on to using polyphenylenevinylene (PPV) derivatives²³ and continued through study of polythiophene derivatives.²⁸ As the OPV research community has been aware of photooxidation of semiconducting polymers for some time, there have been a number of studies into the mechanistic details of this process. This effort is also aided by the fact that there is no need to fabricate a complete device when studying it, as oxidative photo-bleaching is a fundamental property of a material and can be studied in isolation from the other device components. This is frequently done via ultraviolet-visible (UV-vis) studies of thin films of the organic semiconductors, like the one shown in Figure 2.3.3. It should be noted that this phenomenon is also observed in small molecule-based devices,⁶² but as the bulk of OPV stability research has focussed on polymer-based OPV³⁰ that is the focus of this section.

Deducing the exact chemical pathways for the photooxidation can prove challenging when working with polymers, so frequently model compounds (oligomers) are used instead as they can be purified and characterised to a much greater degree of precision. One such study was reported by Norrman, *et al.* in *Surface and Interface Analysis*, in which they deposit films of a PPV-type oligomer, subject it to 20 hours of accelerated photo-ageing, and analyse the degradation products using X-ray photoelectron spectroscopy (XPS) and time of flight secondary ion mass spectrometry (TOF-SIMS).⁶³ Under these conditions it was found that the model compound fragments into numerous smaller molecules (Figure 2.3.4), which would undoubtedly lead to bleaching in a PPV-derivative polymer. With respect to polymer studies, Chambon *et al.* worked on the elucidation of the degradation mechanisms in MDMO-PPV.⁶⁴ Combining infrared spectroscopy and chemical derivatisation treatments, they proposed a two-step degradation mechanism based on radical attack of several

expected to contribute to device-level performance loss. Moreover, studies have shown that the cleavage of the side chain is a likely initiator of the break-up of the thiophene ring through the action of hydroxyl radicals that form during side chain cleavage.⁶⁷ This is further confirmed by the fact that un-substituted polythiophene does not undergo photooxidation.^{28,67} Unlike the side chains, any disruption to the conjugated backbone of the polythiophene would be expected to have a significant effect on the absorption of the polymer.

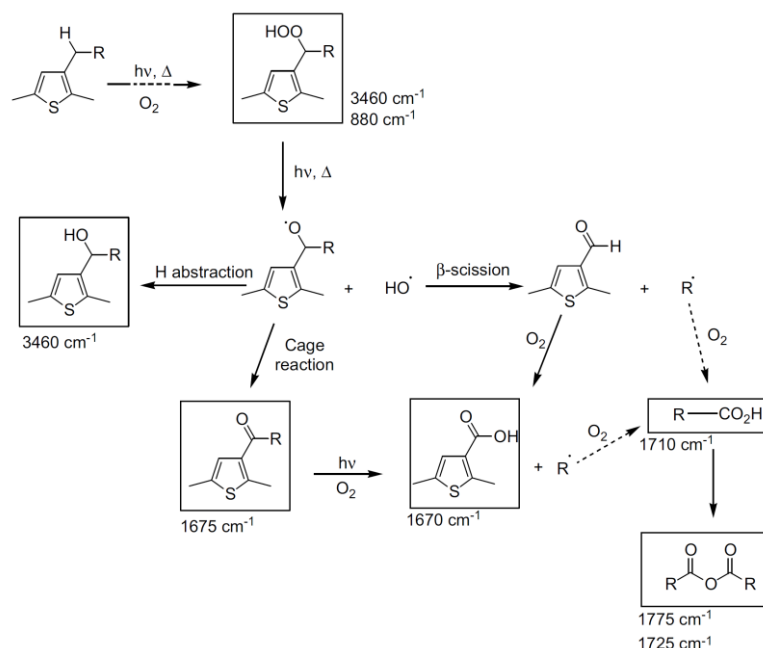


Figure 2.3.5: Thermal and photooxidative cleavage mechanisms of side chains in polythiophene derivatives with key IR absorption bands noted. Figure reproduced from Manceau, M., et al., *Polym. Degrad. Stab.* 94, 898–907 (2009).

In recent years, much of the research into novel semiconducting polymers has centred on “push-pull” architectures. These are copolymers of electron-rich and electron-poor units in which the level of the HOMO of the polymer can be controlled by tuning the electron-poor unit and the level of the LUMO, the electron-rich unit.⁷⁰ This formalism has allowed the development of increasingly high efficiency polymers, including PCPDTBT (poly[2,6-(4,4-bis-(2-ethylhexyl)-4H-cyclopenta[2,1-b;3,4-b']-dithiophene)-alt-4,7-(2,1,3-benzothiadiazole)]),⁷¹ and PCDTBT (poly[N-9''-hepta-decanyl-2,7-carbazole-alt-5,5-(4',7'-di-2-thienyl-2',1',3'-benzothiadiazole)]),⁷² the structures of which are shown in Figure 2.3.6. While still vulnerable to photooxidation (Figure 2.3.3), some of these push-pull polymers show improved stability against photooxidation as compared to polythiophene derivatives.⁶⁵ When photooxidation of the polymer backbone does occur, it has been shown in both PCDTBT⁶⁵ and PCPDTBT⁷³ to occur at the sulfur-containing units (Figure 2.3.6).

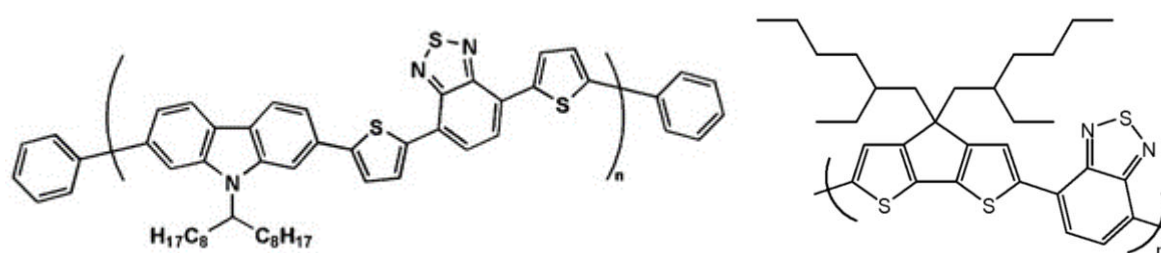


Figure 2.3.6: The chemical structures of PCDTBT (left) and PCPDTBT (right).

It should be noted throughout this discussion that while material studies of polymer materials can be useful in identifying degradation mechanisms and in deconvoluting degradation phenomenon, in any device application at either lab or commercial scale, the polymer is not typically present in an active layer alone. As discussed in section 2.3.1, the polymer is commonly mixed with an acceptor compound, usually a fullerene derivative and typically in a BHJ. Studies have shown that the presence of a fullerene-based acceptor has a net benefit on the photooxidative stability of an active layer.²⁸ One reason for this is that photooxidation is partially caused by the UV portion of the spectrum, and fullerenes and their derivatives are strong UV absorbers;²⁸ this is similar to the effect observed when UV absorbing compounds are added as a part of a ternary BHJ blend, significantly increasing the photostability of the device.⁷⁴ The other reason relates to the way the polymers break down, which typically involves the proliferation of photo-generated radicals.²⁸ Due to fast electron transfer between the donor and acceptor,⁷⁵ and the radical scavenging properties of fullerenes,⁷⁶ these radicals are suppressed, protecting the polymer from continued damage. Hoke, *et al.* examine this phenomenon in more detail in their article in *Advanced Energy Materials*,⁷⁷ in which they find a correlation between the electron affinity of the fullerene derivative used as an acceptor and the photostability of the BHJ blend. They conclude that the use of acceptors with higher electron affinities results in a BHJ that is more stable to photooxidation.⁷⁷

2.3.3. Degradative effects on exciton separation

Upon absorption of a photon, an exciton is formed in the active layer (typically in the donor). Excitons are quasiparticles consisting of a single bound hole-electron pair, with similar behaviour to positronium – a positron-electron quasiparticle that forms in the pair production reaction.^{78,79} Depending on the medium in which they form, excitons can either be highly delocalised (Mott-Wannier excitons), as in the case of some inorganic crystals,⁷⁸ or highly localised – even to a single lattice point (Frenkel excitons).⁸⁰ In the case of organic semiconductors, their low dielectric constants result in excitons that are localised to a single conjugation unit.⁸¹ As quasiparticles, excitons have multiple energy levels and can therefore be excited into higher energy states,⁸⁰ or even fully dissociated. This latter process is equivalent to ionisation of an atom, and has a characteristic energy called the exciton binding energy. As discussed in section 2.3.1, this energy is relatively high in organic semiconductors (higher than thermal energy at 300 K), necessitating the presence of a donor-acceptor interface for exciton quenching to occur via charge transfer.

Charge transfer at the donor-acceptor interface occurs via a short-range interaction,^{81,82} and since excitons in organic semiconductors are highly localised, they must migrate to an interface for charge transfer to occur. Excitons are electrically neutral, meaning that if the temperature is sufficiently high,⁸¹ they migrate via diffusion, roughly obeying random walk statistics.⁸⁰ While diffusing through the donor, the exciton has a certain probability of recombining, either through photoluminescence or non-radiatively via exciton-exciton annihilation (and other mechanisms). This is known as geminate recombination. The RMS displacement of the exciton between formation and recombination is known as the exciton diffusion length.^{81,82} Various methods exist for the measurement and calculation of exciton diffusion length in organic semiconductors,^{81,83} but values found are typically in the range of 5 – 25 nm.⁸¹ For a more rigorous discussion of these subjects, the author encourages interested readers to consult Mikhnenko, Blom, and Nguyen's review in *Energy and Environmental Science*.⁸¹

Given that exciton dissociation only occurs at a donor-acceptor interface and that excitons diffuse (on average) 5 – 25 nm before recombining, it follows that only excitons formed within the exciton diffusion length of an interface will be effectively dissociated. For this reason, BHJ morphologies are designed to have domain sizes on the order of 10 nm.⁸¹ This has the benefit of ensuring that excitons formed anywhere in the active layer are likely to diffuse to a donor-acceptor interface and dramatically increases the surface area of the interface, maximising the active volume of the device. However, this increased surface area has a disadvantage. The donor and acceptor species are (ideally) immiscible to ensure separate domains are formed, although recent studies suggest that some interfacial mixing does occur.⁸⁴ It follows that due to the high interfacial surface area between immiscible (or semi-miscible) phases, like any colloidal system, BHJs are thermodynamically unstable and therefore are kinetically stabilised. This means that a BHJ would be expected to further phase segregate at elevated temperatures, growing donor and acceptor domains beyond the ideal morphology and therefore beyond the exciton diffusion length. As shown in Figure 2.3.7, this is what is observed when a BHJ film is heated.

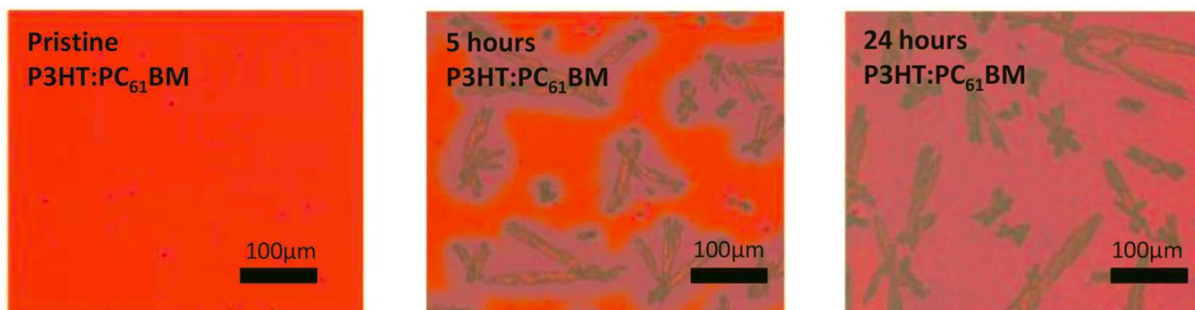


Figure 2.3.7: Optical micrographs of a BHJ film after being annealed at 150°C for the times indicated. Figure adapted from Derue, L. *et al.*, *Adv. Mater.* 26, 5831–5838 (2014).⁸⁵

The growth of crystalline domains with thermal ageing of a BHJ has been noted in the literature for some time.⁸⁶ This can be a beneficial effect when growing acceptor and donor domains to reach an optimal morphology for the active layer.³² However, if the domains grow beyond an optimal size, the recombination rate increases and therefore the extracted photocurrent decreases.⁸⁵ Verploegen, *et al.* carried out an in-depth study of this phenomenon using grazing-incidence x-ray scattering (GIXS) on pure films of P3HT and PCBM, and BHJ blended mixtures.⁴¹ They observe crystallisation of both phases at elevated temperatures (Figure 2.3.8), with P3HT crystallite size being limited by the presence of PCBM, and the size and order of PCBM crystallites being highly correlated to the nucleation density.⁴¹ They also note that the glass transition temperature (T_g) of the PCBM and the melting temperature (T_m) of the P3HT are decreased when in a BHJ blend,⁴¹ which would be expected to raise the (mass) diffusion mobility in the film.

The emergence of large crystalline domains of donor and acceptor compounds is frequently observed in the bulk of the active layer,^{41,85,86} but it can also occur at the interface with the interlayers. This phenomenon is referred to as vertical phase segregation,^{41,87} and is discussed further in section 2.3.4.

In order to have domain growth it is necessary to have effective mass transport through the active layer. The degree to which the matter within a BHJ can reorganise at elevated temperatures is largely determined by the properties of the donor and acceptor compounds. In the case of polymer donors, this is very closely related to T_g of the polymer.³⁰ This temperature does not represent a transition to

a liquid state, like a melting point, but rather the amorphous portions of the polymer transitioning from more solid-like behaviour to viscoelastic behaviour.⁸⁸ Although not strictly a phase transition, it does result in changes in the physical properties of the polymer, in particular its thermal expansion coefficient and free volume.⁸⁸ Above the glass transition temperature, mass transport through polymer-rich regions of the BHJ is made easier because of this (Figure 2.3.8).

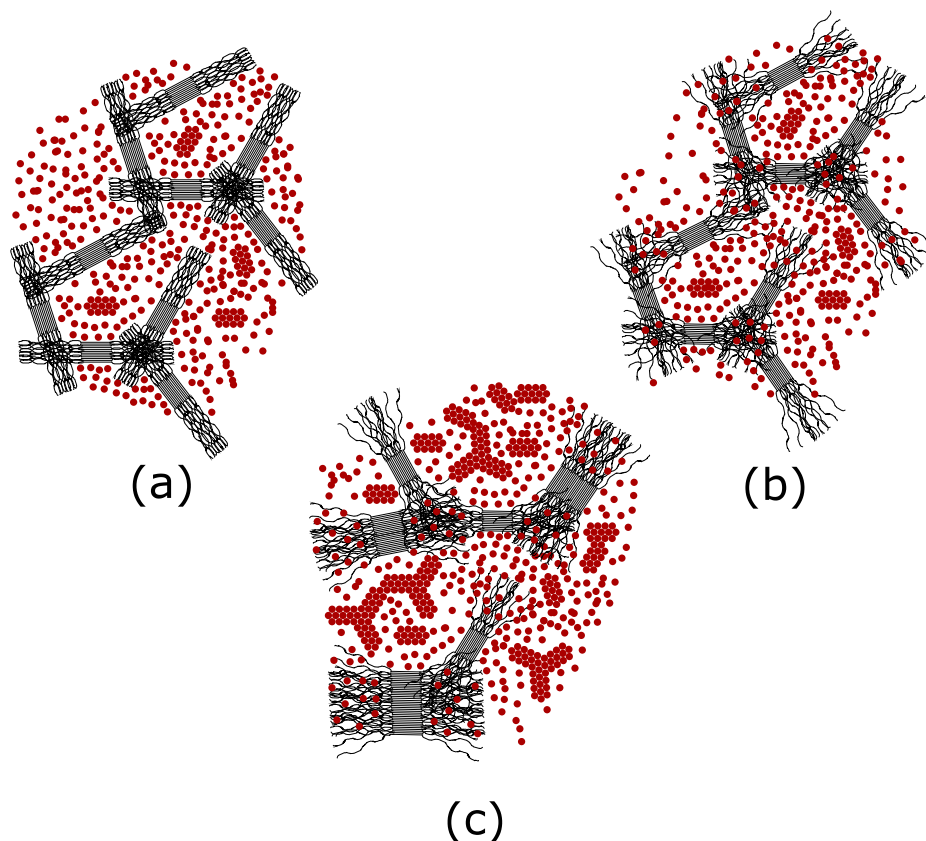


Figure 2.3.8: A schematic of phase separation of a BHJ with thermal degradation, with the semi-crystalline donor shown in black and the fullerene acceptor in red. In (a), the BHJ is has an ideal morphology and is below the T_g of the polymer. In (b), the polymer is above the T_g , which facilitates mass transport through the amorphous regions of the polymer. In (c), the BHJ has been above the T_g of the polymer for an extended period of time, allowing domain growth and crystallisation.

This was first noted with PPV derivative donors, which have particularly low T_g values and were observed to be very unstable under thermal degradation.⁸⁶ In order to find methods of improving thermal stability, Bertho, *et al.* carried out a study which compared the thermal resilience of devices containing PCBM as an acceptor and either: a modified, “high T_g ”, PPV derivative ($T_g \approx 150^\circ\text{C}$), or poly[2-methoxy- 5-(30,70-dimethyloctyloxy)-1,4-phenylene vinylene] (MDMO-PPV) ($T_g \approx 45^\circ\text{C}$).⁸⁹ They reported that, when heated at 110°C , the MDMO-PPV devices exhibited a 40% reduction in fill factor and J_{SC} after 16 hours, while the devices using the high- T_g polymer lost only between 5% and 10%.⁸⁹ Subsequent TEM analysis showed no significant domain growth after thermal ageing in the high T_g PPV devices but significant growth of crystalline domains in the MDMO-PPV devices.⁸⁹

As noted by Bertho, *et al.*, P3HT has a higher glass transition temperature (although this is disputed⁹⁰), and would be expected to have superior resilience to thermal ageing than PPV derivatives.⁸⁹ While it is true that it is superior to PPV derivatives in this sense,⁸⁵ P3HT-based BHJs are by no means thermally stable long term, having a tendency to phase-separate at elevated

temperatures.^{27,91} More recently developed high efficiency polymers do show greater promise in this regard. Of particular note is the polymer PCDTBT. Unlike P3HT, which is semi-crystalline under normal processing conditions,⁹² PCDTBT is completely amorphous when cast, only exhibiting very weak π - π stacking interactions between chains.^{92,93} The polymer remains amorphous when annealed at elevated temperatures and shows little change in absorption properties – even when heated to temperatures as high as 400°C.⁹⁴ When PCDTBT is used in a BHJ active layer of an OPV device with PC₇₁BM, the device shows greatly improved resilience to thermal degradation as compared to P3HT; thermally-induced efficiency loss is reduced by as much as a factor of two.⁹⁵ This dramatic improvement is, as with the PPV-derivatives (*vide supra*), a consequence of PCDTBT having an exceptionally high T_g of around 130°C (depending on the processing conditions).^{92,93} This results in a highly stable morphology in the BHJ, which is largely insensitive to temperature under normal thermal ageing conditions.^{22,93}

While it is desirable to have as high a T_g polymer as possible in a BHJ to ensure a stable morphology, it is not always possible. For this reason, other strategies for stabilising BHJ morphology have been explored. One such strategy involves chemical modification via crosslinking of the BHJ post-deposition to render the structure more rigid, thereby impeding mass transport through the layer and inhibiting the growth of donor and acceptor domains.²⁷ Much of this work involves the chemical modification of either the donor polymer, the acceptor molecule, or both, in order to add chemical moieties that crosslink once the film is exposed to UV radiation or elevated temperatures.²⁷ After crosslinking, the morphology is fixed, preventing phase separation. It has the added benefit of increasing solvent resistance, enabling further solution processing of the device.²⁷ There are three different possibilities for crosslinking in a BHJ film: donor-donor (D-D), donor-acceptor (D-A), and acceptor-acceptor (A-A) (Figure 2.3.9). Each has advantages and disadvantages with regard to the degree to which the crosslinking can be controlled, ease of synthesis, and efficacy in preventing phase separation;²⁷ however, of the three possibilities, A-A has been shown to best inhibit fullerene crystallisation.²⁷

Synthesis of semiconducting polymers and/or fullerene derivatives that have been functionalised for crosslinking can be technically challenging, and it may not be very cost-effective for any commercial application of this technique.²⁷ An alternative approach is to include crosslinking additives in the BHJ that react with the donor and acceptor, crosslinking them. One such additive is the bisazide crosslinker 4,4'-bis(azidomethyl)-1,1'-biphenyl (BABP).⁹⁶ The azide groups react with C=C double bonds in either the donor or acceptor, but only after irradiation with UV light or thermal treatment, meaning that no crosslinking takes place until after the active layer has been deposited.⁹⁶ Devices incorporating BABP-stabilised P3HT:PC₆₁BM BHJ active layers show negligible loss in efficiency after 120 hours of heating at 150°C, whereas non-crosslinked, but otherwise identical devices lose approximately 85% of their initial efficiency due to substantial morphological deterioration of the active layer.⁹⁶

There are other sources of morphological disruption that do not involve the thermal ageing of a BHJ active layer. One such source is solvent additives. These are compounds that are added in trace quantities to a BHJ solution prior to deposition in order to help solubilise the two components and to optimise the morphology.⁹⁷ As the use of these additives often results in a substantial improvement in the efficiency of the devices, particularly those using newer, high efficiency polymers, there is a plethora of studies reporting their use;⁹⁷ however, relatively few studies examine their effects on

device lifetime. One study that does, reported by Schaffer, *et al.* in *Advanced Functional Materials*, examines the role that 1,8-octanedithiol (ODT) plays in morphological instability in PCPDTBT:PC₇₁BM devices.⁹¹ Using a combination of *in situ*, micro-focused grazing-incidence small angle X-ray scattering (μ GISAXS) and IV tracking under illumination from a xenon lamp, the authors were able to show that as the residual additive evaporates from the BHJ during operation, it has the effect of “blurring” the morphology of the BHJ.⁹¹ The loss of ideal morphology leads to a substantial decline in fill factor and J_{sc} . Schaffer, *et al.* conclude that processing additives can be harmful to BHJ morphology if they are allowed to evaporate after processing, and they recommend that such additives be designed so as to remain in the device throughout its lifetime.⁹¹ An example of such an additive would be 1,10-diazidodecane, proposed by Derue, *et al.*, which can act as both a solvent and a crosslinking additive.⁹⁸

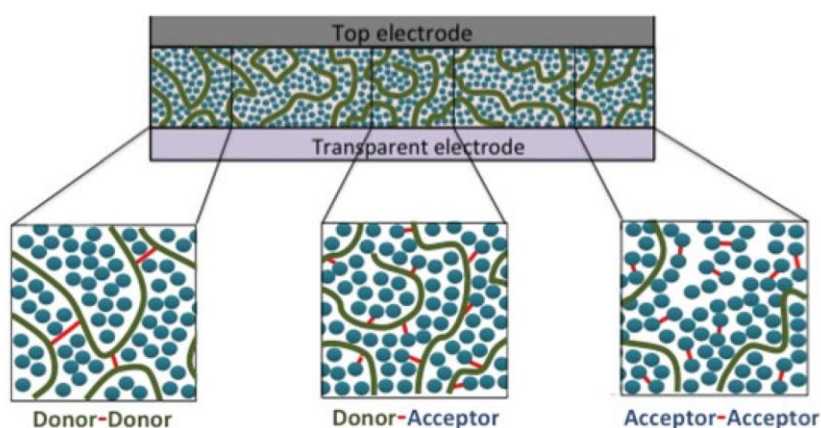


Figure 2.3.9: An illustration of different crosslinking strategies for BHJ morphology stabilisation. Figure taken from Wantz, G. *et al.*, *Polym. Int.* 63, 1346–1361 (2014).

Another cause of morphological change can be photodegradation of the active layer materials. As discussed in section 2.3.2, photooxidation of polymer chains can result in their fragmentation, particularly of any side chains. As well as affecting the absorption properties of the polymer, this can have an impact on the BHJ morphology. In a study of PCDTBT films (neat) that underwent photooxidation, Tournebize, *et al.* observed substantial changes in the morphology of the film, which correlated to the emission of volatile photodegradation products.⁶⁵ These products are shown to originate from cleaved side chains, and it is proposed that, as they out-gas, they disrupt the morphology. Moreover, it is proposed that, without the side chains, the carbazole core of the PCDTBT is more able to π -stack, resulting in a greater degree of self-assembly and crystallinity.⁶⁵ Despite these observations, PCDTBT is relatively photo-stable when employed in BHJ active layers in OPV devices.⁹⁹ A subsequent study from the same group observed that the same cleavage mechanisms take place in a BHJ; however, the fullerene derivative (PC₇₁BM in this case) suppresses any morphological effects. The cleavage occurs via a photo-generated radical mechanism, and, as fullerenes are known as radical scavengers, the polycarbazolyl radical reacts with the fullerene, effectively crosslinking the polymer.⁹⁹ As with the crosslinking reactions noted above, this has a net stabilising effect on the BHJ morphology.⁹⁹

2.3.4. Degradative effects on charge migration

After exciton separation has taken place, the generated free charges must be transported to their respective electrodes for extraction. During this process, as with the un-separated excitons discussed

in section 2.3.3, the charges are vulnerable to recombination. However, this process is different in the case of free charges. With the recombination of excitons, known as geminate recombination,¹⁰⁰ the hole and electron are bound together and are therefore in close proximity to each other. In the case of free charges, however, recombination requires that a free electron and a free hole encounter each other in close enough proximity to experience each other's coulombic attraction. This means that the recombination rate via non-geminate recombination is variable, prone to influence by the materials used in a device, the charge carrier density, and environmental factors. There are two principal mechanisms by which free charges can recombine in the bulk of an OPV device active layer, largely determined by their recombination kinetics: monomolecular (or "trap assisted") recombination, and bimolecular recombination (Figure 2.3.10).¹⁰⁰ In this section, the way in which degradation stimuli can increase the rate of these two types of recombination will be examined.

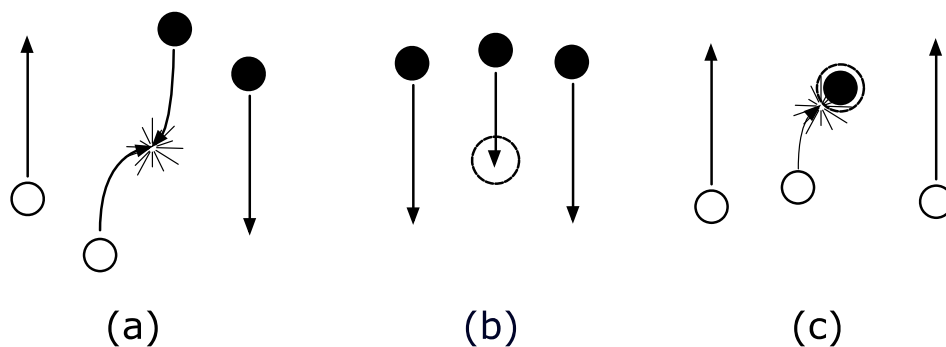


Figure 2.3.10: Schematics of (a) bimolecular recombination of an electron (black) and a hole (white), (b) capture of an electron by a charge trap (dashed circle), and (c) monomolecular recombination of a hole with a trapped electron.

Bimolecular recombination

Of the two mechanisms of recombination examined here, bimolecular recombination is the more ubiquitous in optimised OPV devices.¹⁰¹ As the name suggests, the rate limiting step of the process is the meeting of a mobile hole and mobile electron. This is not a collision in the sense that the two particles must have intersecting paths; rather, the two must pass close enough that they experience a mutual coulombic attraction (Figure 2.3.10).¹⁰⁰ It follows that the bimolecular recombination rate should depend on both the hole and electron charge densities and their mobility. This relationship was first formalised by the French physicist Dr Paul Langevin in his expression:¹⁰²

$$R_L = \frac{q}{\varepsilon} (\mu_n + \mu_p) (np - n_i^2) \quad 2.3.1$$

in which R_L is the Langevin recombination rate, q is the elementary charge, ε is the permittivity, μ_n and μ_p are the electron and hole mobilities respectively, n and p are the electron and hole charge densities respectively and n_i is the intrinsic carrier concentration.¹⁰⁰ This model implies that the recombination rate increases with mobility, which is the case in a gas phase when higher mobilities mean that opposite charge carriers are more likely to meet. In practice, however, the opposite is observed in OPV, as higher mobility means that the charge is more likely to be extracted quickly, lowering the charge carrier density,¹⁰⁰ although simulations show that this can vary at high mobilities depending on if the device is in the open-circuit, short circuit or maximum power state.¹⁰³ This is also why efficient charge extraction is exhibited by thinner active layers in OPV.¹⁰⁰

Charge transport in organic semiconductors mostly takes place via a hopping mechanism;¹⁰⁴ that is, rather than moving through a band structure as in single crystal inorganic semiconductors, they move from state to state through small energy barriers (Figure 2.3.11).¹⁰⁴ Because of this, organic semiconductors exhibit greater charge carrier mobility at elevated temperatures. In molecular solids, the rate limiting step for charge transport is the intermolecular charge transfer. This is also true of polymers, for which charge transport along the polymer backbone can be relatively efficient, but is still limited by inter-chain charge transfer.¹⁰⁴ For this reason, carrier mobility tends to be higher in more ordered molecular solids and is highest in crystalline solids.¹⁰⁴ With respect to semiconducting polymers used in OPV devices, more crystalline polymers like P3HT have considerably higher values for hole mobility than more amorphous polymers like PCDTBT when used in a BHJ.¹⁰⁵

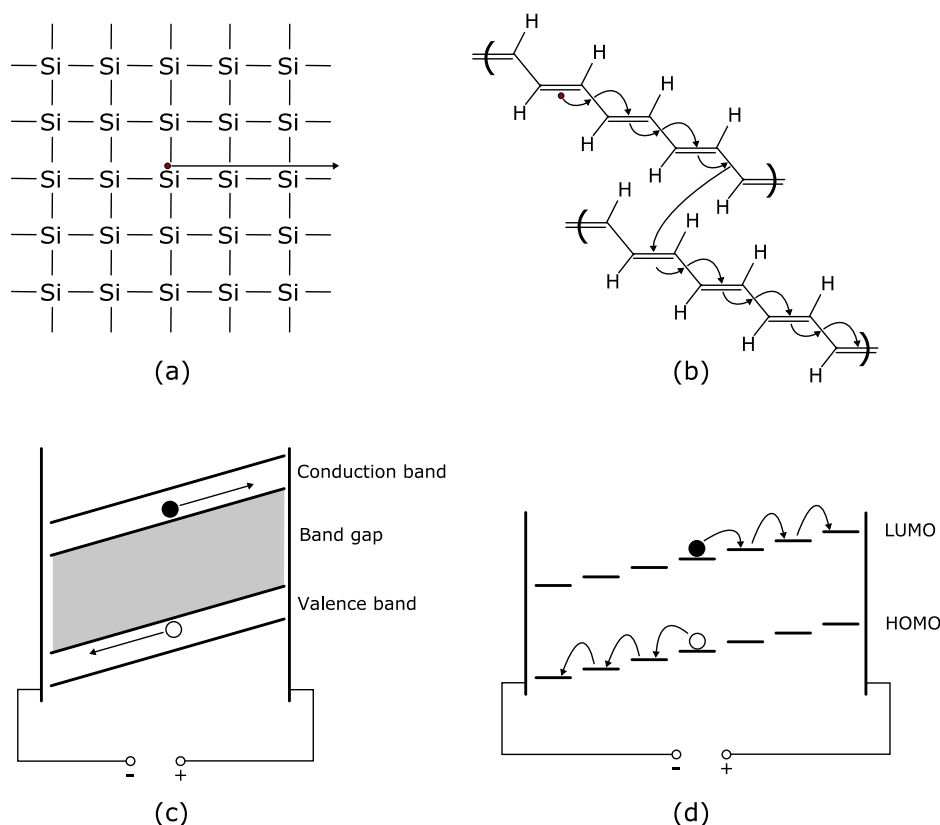


Figure 2.3.11: An illustration of charge transport in an inorganic and an organic semiconductor, illustrating the different mechanisms used. In (a) charge carriers move freely through a crystal of silicon, due to its contiguous band structure, shown in (c). In (b) charge carriers cannot move as freely through an organic semiconductor, having to hop from state to state, as shown in (d).

Determining the exact effects of degradation stimuli on mobility is challenging, as it is very difficult to decouple changes in mobility from other degradation effects. This is further complicated in a device, where donor and acceptor materials are not present in a pure form but rather in a bulk heterojunction. As such, few studies report on this topic. What is clear is that higher carrier mobility comes with more structural order, and higher carrier mobility means a lower bimolecular recombination rate.¹⁰⁰ As discussed in section 2.3.3, BHJ active layers are not thermally stable, the tendency with thermal ageing being towards domain growth and crystallisation (Figure 2.3.8). As this would lead to a more ordered layer, it should follow that charge carrier mobility would increase with thermal ageing, although any effects on the extracted photocurrent would likely be counteracted by

increases in geminate recombination as ageing continues. These effects have been observed in a study of charge transport in P3HT by Mihailetchi, *et al.*¹⁰⁶ With respect to the effects of light and oxygen, photooxidation has been shown in section 2.3.2 to result in the breakup of polymer chains, giving rise to photo-bleaching, which reduces absorption, and ultimately results in a cessation of photocurrent generation. Any breakup of the polymer chain would be expected to have a negative impact on carrier mobility as charge carriers would have to make more jumps between polymer chains. This is suggested by a study by Cho, *et al.* showing that thermal annealing of P3HT and PCDTBT films leads to increases in their mobility at lower temperatures but mobility decline (rapidly in the case of P3HT) above 150°C.⁹⁴ This is most likely due to thermal decomposition of the polymer chains at elevated temperatures. There is also a beneficial effect that oxygen can have on carrier mobility in polymer semiconductors, whereby oxygen doping can raise the conductivity of the polymer chain via the formation of a charge transfer complex with a thiophene unit.¹⁰⁷ However, this effect would be expected to be relatively minor, as mobility is really limited by inter-chain charge transfer, and photooxidative effects on polymer chain length and absorption would have a much greater effect on device performance. Furthermore, there are studies that show the reverse effect with oxygen exposure.¹⁰⁸

Another important factor to consider when discussing mobility changes with ageing in a BHJ active layer is vertical phase segregation. As mentioned in section 2.3.3, this is the tendency for a BHJ to phase separate in such a way that one phase preferentially migrates to the top of the device, and the other to the bottom (Figure 2.3.12). This effect is driven by surface energy and so varies depending on the exact combination of donor and acceptor species and interfaces.⁸⁷ The P3HT:PCBM system has been studied relatively extensively with regards to this phenomenon. It has been observed that when the BHJ is annealed without the top layers of the device, there is a tendency for PCBM to migrate to the bottom interface and P3HT to the top.¹⁰⁹ Conversely, if the device is annealed after deposition of the top layers, the reverse is observed.¹¹⁰

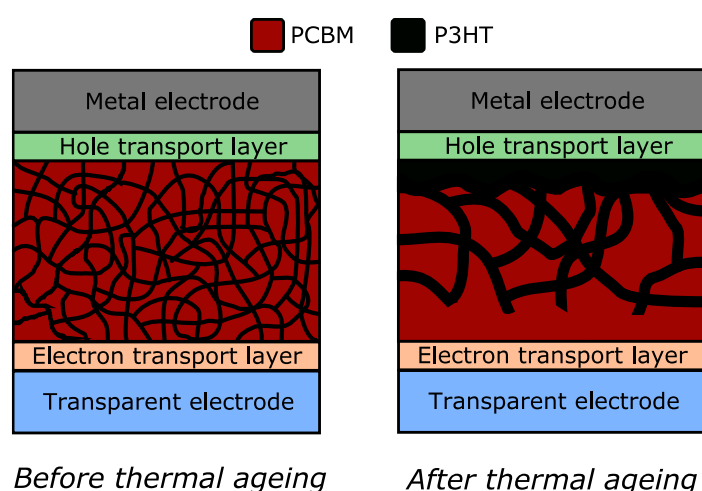


Figure 2.3.12: A schematic showing phase separation in the P3HT:PCBM BHJ active layer of an inverted OPV device. Note that during ageing, enriched domains of P3HT and PCBM have formed near the interfaces with the HTL and ETL respectively. This schematic is not to scale.

Whether this effect is beneficial to device performance or not depends greatly on the geometry of the device. P3HT accumulation at the top interface is beneficial for the operation of inverted devices as it increases the number of pathways for hole extraction via the HTL and metal electrode. This

increases the overall hole mobility of the BHJ, ensuring efficient charge extraction and therefore reducing bimolecular recombination.¹⁰⁰ In a direct device, however, the reverse is true, and so the bimolecular recombination rate increases.

Trap-assisted recombination

In addition to bimolecular recombination, there is also monomolecular, or trap assisted recombination (also known as Shockley-Read-Hall recombination). This is similar to bimolecular recombination, in that it occurs by the mutual coulombic attraction and capture of a pair of charge carriers; however, unlike the bimolecular case, here only one of the charge carriers is moving.⁴⁷ The other is fixed in space in a “charge trap” – an impurity or defect in the active layer that results in the formation of electronic states in the band gap that can take charge carriers from their respective bands.⁴⁷ Once in a charge trap, a charge carrier is unable to migrate but still has the capability to attract nearby opposite charge carriers and recombine. As shown in Figure 2.3.10, recombination via trap states is a two-step process. In the first step, a free charge carrier is captured by a charge trap. In the second step, that charge carrier attracts a free, opposite charge carrier and recombines. From the perspective of kinetics, there are three possible scenarios for such a two-step process: either step one occurs much faster than step two ($R_1 \gg R_2$), step two occurs much faster than step one ($R_2 \gg R_1$), or step two and step one occur at similar rates. In the case of organic semiconductors, it has been shown that the capture of charges by trap states occurs on a much faster timescale than the recombination of trapped charges with free charges, meaning that the rate of recombination effectively depends on the speed at which free charge carriers can “find” the trapped charge.¹¹¹ This is similar to the Langevin model (equation 2.3.1) where one of the charge carriers has a mobility of 0, represented (for electron traps) by the expression:¹¹¹

$$R_{SRH} = \frac{q}{\epsilon} \mu_p N_t p \quad 2.3.2$$

where R_{SRH} is the trap-assisted recombination rate and N_t is the trap density. The equivalent expression for hole traps replaces the hole mobility and charge density terms with the equivalent terms for electrons.

As discussed earlier in this section, in BHJ active layers, trap-mediated recombination typically plays a lesser role in non-geminate recombination than bimolecular recombination.⁴⁷ This may be a result of low trap densities, and it has been shown in PPV derivatives that raising the trap density by adding impurities to the BHJ blend can change the recombination kinetics of the device to being predominantly monomolecular.^{112,113} Another possibility is that the lower contribution of charge traps to recombination is a consequence of phase segregation and the segregation of charge transport in the BHJ. In an ideal BHJ with optimal phase segregation, electrons and holes are transported to their respective electrodes in different phases of the BHJ (the acceptor and donor phases, respectively). It follows that only trapped charge carriers near a donor-acceptor interface are likely to be able to attract an opposite charge carrier and recombine.¹¹⁴ As with bimolecular recombination, it would be expected that increased phase segregation would decrease the trap-assisted recombination, thereby improving fill factor, V_{OC} and J_{SC} . However, such effects would be difficult to observe over the detrimental effects of phase segregation arising from increased geminate recombination (section 2.3.3).

There are a number of sources of charge traps. A major cause of their formation is the introduction of impurities during synthesis of the donor or acceptor, or during device fabrication.¹¹⁵ This relationship has been shown in several studies in which trace impurities are deliberately added to polymer-fullerene blends, such as 7,7,8,8-tetracyanoquinodimethane (TCNQ) being added to a MDMO-PPV:PC₆₁BM BHJ blend,¹¹² and PC₈₄BM being added to a PCDTBT:PC₆₁BM BHJ blend.¹¹⁵ In both cases, the impurities resulted in a dramatic loss of performance of the devices due to an increase in trap-assisted non-geminate recombination. Indeed, these issues are not limited to polymer solar cells. A study by Leong, *et al.* tested the degree to which trace amounts of a synthetic by-product of the small molecule donor 5,5'-bis{(4-(7-(5-hexylthiophen-2-yl))thiophen-2-yl)[1,2,5]thiadiazolo[3,4-c]pyridine}-3,3'-di-2-ethylhexylsilylene-2,2'-bithiophene (p-DTS(PTTh₂)₂) can affect device performance.¹¹³ As the by-product is difficult to separate from the product, it is likely that it is present to some extent in all devices that use p-DTS(PTTh₂)₂ as a donor.¹¹³ The study concluded that this impurity plays a significant role in the formation of charge traps and can, even in small quantities, severely diminish device performance.¹¹³ However, charge traps do not always form solely because of contamination. Regioregularity has been shown to play a role in the formation of trap states, with non-regioregular P3HT showing higher degrees of mono-molecular recombination than more regioregular samples.¹¹⁶ Polydispersity can also be an issue. A study that deliberately included a small quantity of a long-chain PPV derivative in a shorter chain sample found that OLED devices fabricated from the mixture exhibited greatly diminished performance due to charge trapping (as trap-assisted recombination is generally non-radiative).¹¹⁷ Even chain length can be an issue, as longer chains are more prone to twisting and tangling, resulting in the formation of trap states.¹¹⁸ This disorder in certain polymers used in OPV devices can also give rise to a broadening of density of states when photo-aged, which has the effect of lowering the V_{OC} (although this effect is not typically observed in more crystalline polymers like P3HT).¹¹⁹ Despite these effects, the presence of solvent additives (which were discussed in section 2.3.3) does not appear to significantly contribute to the degree of trap-assisted recombination.¹²⁰

One possible origin of charge traps which has received little discussion in the literature is diffusion of interlayer and electrode materials into the active layer. It has been shown by Chambon, *et al.*¹²¹ and Dupont, *et al.*¹²² that inverted devices, when thermally aged, show evidence of interdiffusion between the BHJ, HTL and metal electrode. This inevitably leads to significant concentration of contaminants from the top layers in the BHJ, which could act as charge traps, given the sensitivity of organic semiconductors to contaminants in this regard.^{115,123} This phenomenon also has consequences for charge extraction, which will be discussed in section 2.3.5 and is examined in greater detail in Chapter 4.

In addition to their intrinsic origins, charge traps can also form as a result of exposure to degradation stimuli. Oxygen and water can either diffuse through the top electrode and interlayer or enter the device from the sides.¹² It has already been mentioned that oxygen can dope thiophene-based polymers like P3HT, but it has also been demonstrated that it can give rise to the formation of deep traps (traps with an energy difference to the HOMO/LUMO of several multiples of kT) in the active layer.¹⁰⁸ Few studies appear to have been done on the ability of photooxidation to give rise to charge trap formation in higher efficiency polymers like PCDTBT; however, as discussed in section 2.3.2, it is known that these polymers are vulnerable to photooxidation, the oxygen acting to fragment the polymer backbone via cleavage of the side chains.^{65,99} Given the aforementioned sensitivity of semiconducting polymers to polydispersity and regioregularity with respect to charge trap formation,

it would seem logical that these degradation products could act as charge traps. However, these observations may be somewhat academic, as these reactions also reduce the absorption of the polymers, so any effects from trapping may be difficult to observe and distinguish from the effects of photobleaching. That said, it is possible that the two mechanisms operate on different timescales, so small concentrations of degradation products could have an effect on the recombination rate before the effects of photobleaching become significant. This has been hinted at in previous studies,^{124,125} but has not been fully investigated.

Oxygen is not the only contaminant that may diffuse into a device. In most operational applications of OPV, the device will also have to contend with humidity. Although not yet shown in OPV active layers, evidence of water-induced trapping has been observed in organic thin-film transistors (OTFTs).^{126,127} In these cases, the devices are based on pentacene, and although the exact chemical mechanism is unclear, exposure to water vapour over time did give rise to the formation of electron traps, resulting in operational hysteresis.¹²⁷

2.3.5. Degradative effects on charge extraction

The final step in photocurrent generation is charge extraction. This involves charge transfer between the active layer of the device and either the transparent electrode(s) (in the case of semi-transparent devices, both electrodes are transparent) or the metal electrode. This charge transfer usually takes place via interlayers – materials that preferentially transport one charge carrier or another. The presence of multiple interfaces and chemical interactions at this point in the photocurrent generation process gives rise to a number of degradation pathways that will be discussed in this section.

Most OPV devices incorporate layers between the active layer and the electrodes: a hole transport layer at the hole-extraction interface and an electron transport layer at the electron-extraction interface. The materials used in these roles serve two purposes: to ensure charge selectivity at charge extraction (enhancing FF and V_{oc}) and to act as a buffer between a chemically reactive electrode and the active layer.¹²⁸ To perform the former role, materials must be chosen so as to closely match energy levels with either the HOMO of the donor (for hole extraction) or the LUMO of the acceptor (for electron extraction). The better matched they are, the better device performance.¹²⁹ For electron extraction direct devices, this frequently involved the use of low work-function metals like calcium in combination with an aluminium electrode (although calcium is vulnerable to corrosion, so LiF is a better choice¹²⁹). For hole extraction, the conducting polymer blend PEDOT:PSS is frequently used in direct devices, which is well matched to the HOMO of P3HT.¹²⁹

The use of low work-function metals as ETLs or electrodes does present some major challenges with respect to device lifetime. Due to their low work function, metals like calcium and aluminium are highly reactive in the presence of oxygen and water, forming insulating oxides. The ingress of these gasses has been studied in isotopic labelling experiments, which have demonstrated that in the case of aluminium electrodes, oxygen ingress occurs via pinholes and the sides of the device, while water is capable of diffusing through the aluminium electrode.¹³⁰ Once in the device, water and/or oxygen react with any low work-function electrode or ETL materials to form insulating oxide barriers that prevent electron extraction in the regions where the oxide forms (Figure 2.3.13).

As shown in Figure 2.3.13, growth of an oxide layer can either be one-dimensional, forming a homogenous oxide film between the active layer and the ETL,^{131,132} or two-dimensional whereby the oxide grows laterally from the edges of the ETL/electrode.^{133,134} In the one-dimensional case, the IV curve develops a distinctive inflection point at the V_{OC} , sometimes called an “s-curve”. In the photovoltaic parameters, this manifests as a rapid loss of FF and, as the s-curve becomes more exaggerated, a decline in J_{SC} until device death ($PCE = 0$).^{131,135} This behaviour is best explained as the oxide layer acting as a homogeneous charge extraction barrier, which leads to a build-up of space charge adjacent to the interface in the active layer.^{131,132,134} This space charge acts to screen the internal electric field in the device, which gives rise to the distinctive s-curve and loss of FF . As the oxide layer grows, the potential required to overcome the charge extraction barrier increases, so that the device must be held at increasingly high negative bias to recover the photocurrent.¹³⁴

The IV behaviour of a device undergoing two-dimensional oxide growth is somewhat different to one-dimensional case (Figure 2.3.13). The degradation is manifested as a steady loss of J_{SC} , with little or no variation in FF or V_{OC} .^{133,134} However, what distinguishes this behaviour from other mechanisms that cause J_{SC} loss is that the photocurrent can be recovered if the cell is held at extreme negative bias, at which point an inflection in the IV curve can be observed which resembles the one observed with a homogeneous oxide layer.^{133,134} This recovery of the photocurrent would not be expected in the cases of photobleaching, changes in morphology or other mechanisms for J_{SC} loss. A rigorous model for this behaviour was reported by Züfle, *et al.* in *Advanced Energy Materials*, in which a degraded cell is modelled both as a pristine cell and as a cell with an homogenous insulating oxide layer at the electron extraction interface in a parallel circuit.¹³⁴ As the overall device continues to degrade, Züfle, *et al.* model the area of the pristine cell shrinking and the area of the degraded cell increasing.¹³⁴ This model accurately predicts both the J_{SC} loss, which arises from the decline in the effective area of the device, and the recovery of the photocurrent at negative bias by overcoming the charge extraction barrier in the insulated portions of the device.¹³⁴ These conclusions are supported by results obtained by Voroshazi, *et al.*, which demonstrate that removal of the top layers of an aged device that exhibits signs of lateral oxide growth (using scotch tape) and application of fresh electrodes leads to a complete recovery of device performance.¹³³

At the hole extraction interface, the most widely used material for the hole transport layer is PEDOT:PSS, which is frequently used in a high conductivity form as an ITO substitute in all-polymer OPV devices.^{136,137} Despite performing extremely well as a hole conductor, it has some significant drawbacks, namely its extreme acidity and hygroscopicity.¹³⁶ When devices containing PEDOT:PSS are aged in a humid atmosphere, water diffuses into the device and is absorbed by the PEDOT:PSS layer,¹³⁰ which causes it to increase in sheet resistance over time.¹³⁸ This increase in resistance is attributed to the formation of non-conducting regions (similar to insulating oxide formation with aluminium) that may be due to the separation of the PEDOT and PSS components and the formation of PSS-rich particles.^{138,139} Moreover, the acidity of the hydrated PSS component is such that it chemically etches ITO, resulting in the diffusion of ITO throughout the device and, potentially, a decline in the sheet resistance of the ITO (although it is unclear to what extent this has an effect on device performance).^{30,140} There are a number of alternatives to using PEDOT:PSS as an HTL or electrode, including substituting the PSS component for a less acidic substitute,¹⁴¹ using doped graphene,⁵⁷ or moving away from carbon-based HTLs towards metal oxides like MoO_3 and WO_3 .⁵¹

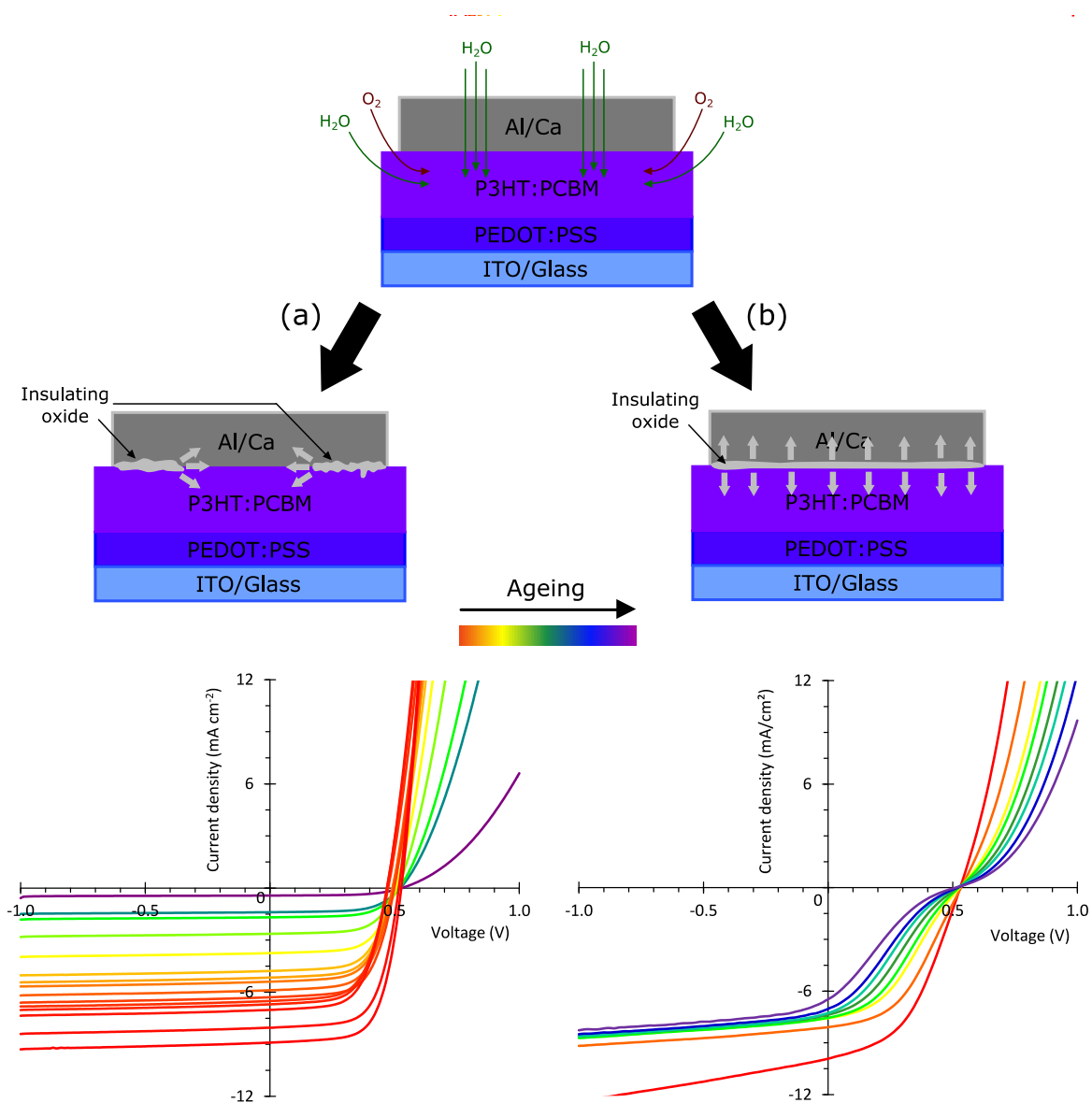


Figure 2.3.13: Oxygen and water ingress into a direct OPV device and subsequent insulating oxide formation by either (a) lateral (2D) growth of the oxide layer from the edges of the ETL/electrode or (b) vertical (1D) growth of a homogeneous oxide layer. The evolution of the IV curve in each scenario is also shown (IV data on left provided by Dr Sylvain Chambon).

Another approach to improving the interfacial stability of OPV devices is to use the inverted geometry, in which holes are collected at the top (typically metal) electrode and electrons are collected at the bottom transparent electrode (Figure 2.3.1).^{142–144} This means that the metal used for the top electrode can be a higher work function material like silver or gold and that the electron selective layer can be made of more stable, solution-processed materials like ZnO, TiO_x, or organic options like PEI or PEIE (replacing calcium or LiF). These developments lead to a dramatic increase in device lifetime,^{145,146} with shelf lifetimes in ambient conditions (no encapsulation) exceeding a year.¹⁴⁷ There is even speculation that the lifetime of such devices, when properly encapsulated and shielded from UV radiation, might exceed 25 years of operational lifetime,¹⁴⁸ although methods for estimating lifetimes on this scale make many assumptions, not least of which that encapsulation can be perfect and economical (see section 2.5). Furthermore, inverted devices that incorporate PEDOT:PSS as an HTL show greater resilience to humid atmospheres than the equivalent direct

architecture devices, potentially as a result of the hygroscopic PEDOT:PSS layer preventing water from diffusing through the rest of the device by absorbing it.¹⁴⁹

In addition to reactions caused by the entry of water and oxygen, there are other photochemical reactions that can take place at charge extraction interfaces in OPV devices. These reactions are particularly prevalent in devices that have direct contact between a metal electrode, or the ITO, and the organic active layer.^{150,151} These degradation pathways, unlike those involving oxygen or water, are largely a feature of device design and therefore cannot be eliminated through the use of good encapsulation (although they may be reduced in severity by UV filtration). The mechanisms of these reactions can be studied by the successive removal of the layers of an aged device and utilisation of surface characterisation techniques like XPS in the manner shown in Figure 2.3.14.³⁰

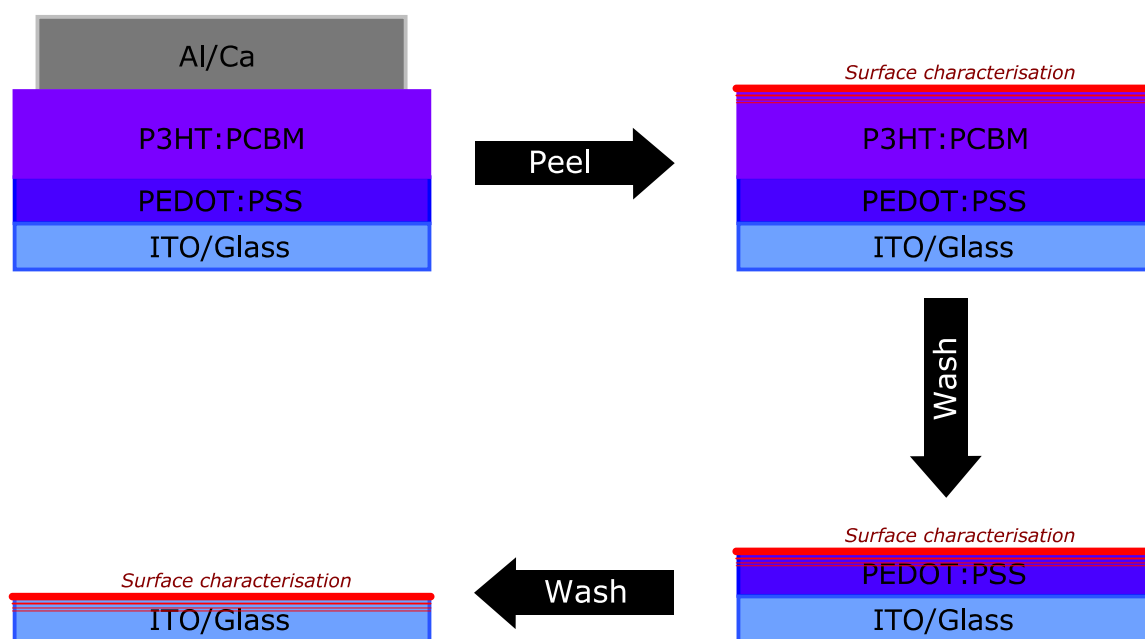


Figure 2.3.14: An example of how device layers might be removed for XPS analysis of interfacial regions. The metal electrode is removed with adhesive tape, the active layer is removed by washing with halogenated solvents and the ETL is removed by washing with water or alcohol. This figure is a reproduction of one shown in Jørgensen, M., et al., *Sol. Energy Mater. Sol. Cells* 92, 686–714 (2008).³⁰

A number of such studies have been reported by the Organic Optoelectronic Materials & Devices Laboratory at the University of Waterloo in Canada.^{150–152} Through XPS analysis, they found that at the electron extraction interface in direct devices without an ETL there was a decline in the number of metal-organic bonds with photo-ageing.¹⁵¹ This correlated to a decline in the adhesion of the electrode to the active layer, which would be consistent with a reduction in metal-organic bond density.¹⁵¹ Such loss of adhesion would be expected to behave like an injection barrier, causing a decline in all device parameters, and this is indeed what was observed.¹⁵³ Similar behaviour was observed at the active layer/ITO interface with respect to a decline in the density of organic-ITO bonds.¹⁵⁰ These observations emphasise the importance of interlayers, not only for improving device performance, but also for extending device lifetime. That said, the same effect (albeit to a lesser extent) was observed when MoO₃ was used as an HTL.¹⁵⁰

When considering interfacial OPV degradation, it is also important to take into account physical degradation mechanisms. This is particularly important if the devices are being considered for application in flexible modules as this will involve putting the device under a physical stress. An example of physical degradation is the delamination of the electrode from the active layer. This can occur because the adhesion between electrodes and active layers is typically very weak¹²² and thus, as discussed earlier in this section, the slightest physical stress can result in its removal.³⁰ In some instances, delamination can occur without physical stress, as demonstrated by Lloyd, *et al.* in their observation of void formation at the metal electrode interface in direct BHJ P3HT:PCBM devices with a calcium/aluminium electrode.¹⁴⁷ Unsurprisingly, this led to a loss of PCE that was driven by a steep decline in J_{sc} .¹⁴⁷

Another physical degradation mechanism is inter-diffusion between layers in devices. When a device is fabricated, the different layers of the device will ideally be well segregated while still maintaining good contact for charge transfer. The thermodynamics of this situation go beyond the scope of this section; however, it follows that such a segregated state is entropically unfavourable. Depending on the surface energies of the different layers and their respective diffusion mobilities (cf. BHJ phase separation in section 2.3.3), this can lead to a mixed state being more favourable than the ideal layer segregation. This has been observed in some studies of OPV devices. Chambon, *et al.* reported in *Materials* that thermal annealing of inverted ITO/TiO_x/P3HT:PCBM/MoO₃/Ag devices at high temperatures (ca. 170°C) resulted in the apparent mixing of the layers at the hole extraction interface.¹²¹ This mixing was visible in Auger electron spectroscopy (AES) depth profiles, which showed clear changes in elemental profile (Figure 2.3.15).¹²¹ Furthermore, these changes in the elemental profile of the samples were not seen when the samples were annealed prior to silver deposition (Figure 2.3.15), indicating that the presence of the silver electrode during annealing is key to the apparent inter-diffusion.¹²¹ However, any intermixing was less clear in Rutherford backscattering spectrometry (RBS) analysis and the authors note that the changes that were observed may be a result of increased sample roughness.¹²¹

Interdiffusion and its effects on interlayer adhesion and efficiency have been examined more closely in a series of studies by Dupont, *et al.* at Stanford University.^{122,154,155} The authors note that thermally induced inter-mixing of the layers at the hole extraction interface has beneficial effects on the mechanical durability of the devices, in particular improving their resilience to mechanical delamination.^{122,155} The devices studied are inverted P3HT:PCBM devices with PEDOT:PSS HTLs and silver electrodes, which are deposited after the annealing step.¹²² PEDOT:PSS HTL layers in inverted devices are typically deposited from aqueous or alcoholic suspensions onto the hydrophobic active layer, often resulting in weak adhesion. Thermally intermixing the HTL and active layers thus improves this adhesion.¹²² This process also has a beneficial effect on device efficiency,¹²² most likely due to an increase in the effective area of the device that results in improved charge extraction. However, the authors note that excessive thermal annealing is destructive to device performance due to phase separation and domain growth in the active layer.¹²²

Dupont, *et al.*'s work also examined the mechanical stability of PEDOT:PSS under different ageing stimuli.¹⁵⁴ Although the mechanical strength of the PEDOT:PSS showed little variation with temperature, it did show a strong dependence on atmospheric humidity.¹⁵⁴ The PEDOT:PSS layers were found to be vulnerable to moisture-induced decohesion at fracture energies lower than those found for a BHJ active layer.¹⁵⁴ The authors attribute this behaviour to water molecules disrupting

the hydrogen bonding between grains in the PEDOT:PSS layer, leading to an overall decline in layer cohesion.¹⁵⁴ Although consequential for mechanical stability of devices, this may also have relevance for device performance. The observation could help partially explain the observed increase in sheet resistance when PEDOT:PSS-containing OPV devices are aged in a humid atmosphere (the authors do not discuss this possibility).

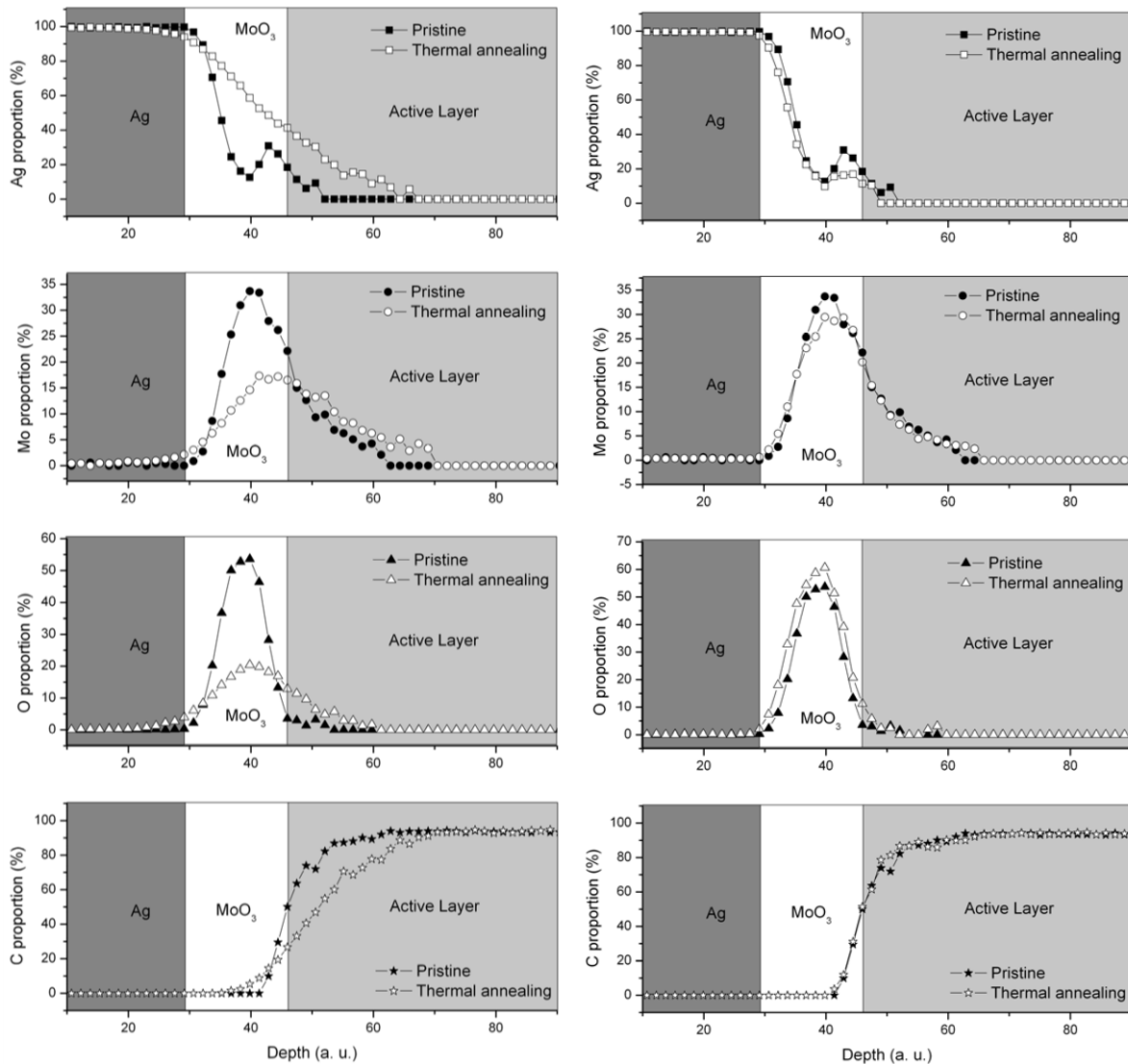


Figure 2.3.15: AES depth profiles of thermally annealed inverted OPV devices. The profiles on the left are of a sample that was annealed after electrode deposition, while the ones on the right are of a sample that was annealed prior to electrode deposition. The approximate ideal position of the layers is illustrated by shading. These data and figures are taken from Chambon, S., et al., *Materials (Basel)*. 5, 2521–2536 (2012).¹²¹

2.4. Studying OPV Device Degradation

2.4.1. The ISOS protocols

The study of OPV degradation is a highly collaborative field, with many research groups scattered around the world carrying out everything from lab-scale ageing under simulated sunlight to outdoor testing under operational conditions.^{21,156} In order to ensure that comparison between results obtained in different laboratories was possible, by 2008 it had become apparent to the leading

researchers in the community that a series of standard testing protocols were needed to progress the field further.²² During the inaugural meeting of the International Summit on OPV Stability (ISOS) in 2008 and the subsequent two meetings in 2009 and 2010, researchers from the National Renewable Energy Laboratory in the United States, the Technical University of Denmark, the *Katholieke Universiteit Leuven* in Belgium, and numerous other private and public sector research organisations around the world agreed on a series of standards for OPV ageing experiments.²² Published in *Solar Energy Materials and Solar Cells* in 2010, these became known as the ISOS protocols and they form the basis for the majority of OPV ageing experiments carried out in the world today,¹⁵⁶ these protocols were followed closely in the experiments carried out in this work.

The protocols cover four types of testing, designed to encompass the different stresses that an OPV would be subjected to under operational conditions and the different stages of commercialisation.²² Dark testing (type D) is carried out to test the shelf life of devices and their resilience to elevated temperatures and humidity. Outdoor testing (type O) tests the devices in direct sunlight under true working conditions (either at maximum power or open circuit). Laboratory weathering testing (type L) is designed to mimic or accelerate the environmental ageing of a device using a well-calibrated solar simulator and a controlled atmosphere. Finally, thermal cycling testing (type T) tests a device's lifetime when subjected to an accelerated version of the daily temperature variation expected in a working device. Each test type can be rated between 1 and 3 in ascending order of rigour. For instance, an L1 test requires only a constant light source and limited monitoring of cell parameters (only V_{OC} and J_{SC} are obligatory), while an L3 test requires a calibrated and filtered AM 1.5 solar simulator, an environmental chamber, and the careful monitoring of all key cell parameters (V_{OC} , J_{SC} , FF and PCE).²² For each possible combination, different test parameters must be recorded for reproducibility; for instance, recording the latitude and time of year would not be critically important for an L3 test, but would be necessary for an O3 test. The requirements for all of these tests are outlined exhaustively by Reese *et al.*²²

2.4.2. OPV degradation behaviour under working conditions

OPV devices have many different architectures and employ a wide variety of materials in their design. As such, there is significant variation in the lifetime of devices with different designs. However, the lifetime of an OPV can be broadly segmented into three stages: burn-in, linear decay and device failure. As shown in (Figure 2.4.1), burn-in is characterised by a rapid, typically exponential, decay in efficiency in the early stages of the device's lifetime.¹³¹ Following this period, the device efficiency decays linearly at a variable rate.¹³¹ The majority of the operational lifetime of the device typically takes place in this stage.¹⁵⁷ Finally, in some devices, a catastrophic failure of the device occurs, characterised by a very rapid decline in efficiency.¹³¹ Depending on the definition one uses, this failure can be said to occur either at this period¹³¹ or the point at which the device decays to 80% of the post-burn-in efficiency, known as the T_{S80} .^{22,148} Regardless of the definition used, each stage of the degradation of the device can impact its lifetime and therefore each stage will be examined in turn.

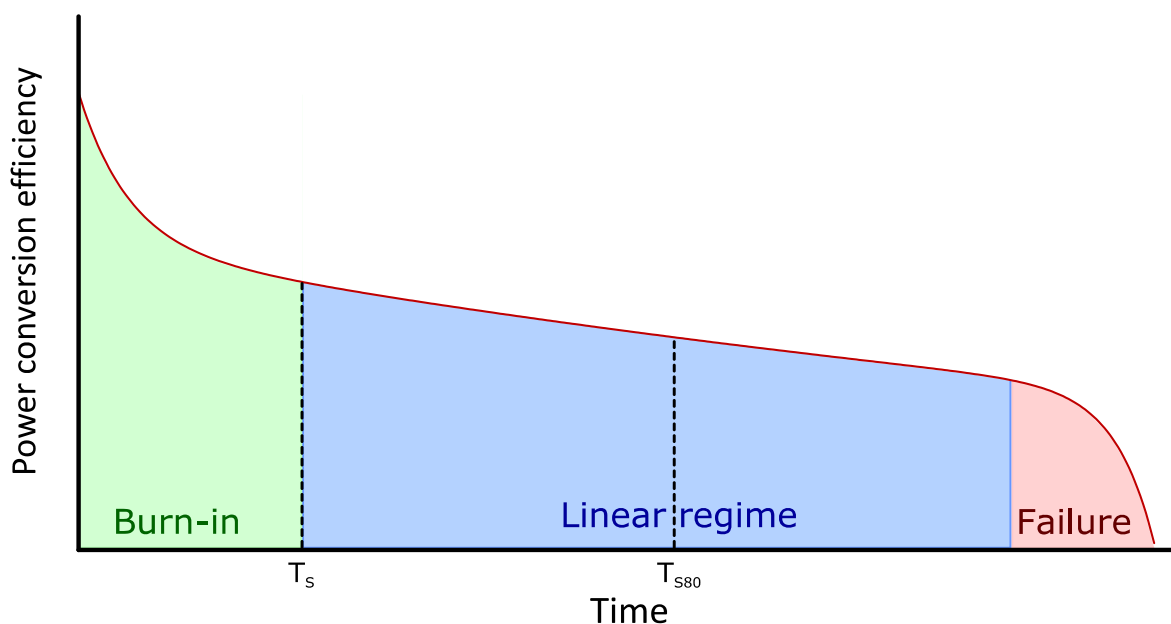


Figure 2.4.1: An idealised photodegradation curve of an OPV device annotated with the key stages of degradation, the burn-in time (T_s), and the time to 80% of the post burn-in efficiency (T_{S80}).

Burn-in

The initial stages of the degradation of an OPV are dominated by an exponential decay of efficiency, known as the burn-in. For a long time, this part of the degradation has been widely accepted as an inevitable component of device degradation, with many definitions of device lifetime actually excluding this portion of ageing and instead defining lifetime from the post burn-in efficiency.^{22,148,157} However, as the magnitude of the burn-in is frequently as high as 40% of the initial efficiency,^{131,158} it merits further investigation and efforts towards its reduction.

The timescale of burn-in is variable but typically takes place in the first 100 – 150 hours of device ageing.^{158–160} Despite some debate about the exact origin of burn-in, there is some consensus that the phenomenon is intrinsic and material-dependant.^{158,159,161} The decline in efficiency results from declines in V_{OC} , FF , and sometimes J_{SC} (depending on the donor species), indicating that there are at least two mechanisms that result in the burn-in.^{131,159} Another clue comes from the conditions in which this degradation occurs: namely, that it only occurs in the presence of light,¹⁶² is not affected by the presence of other degradation stimuli,¹⁴⁸ and strongly depends on the intensity of the light used.¹⁶² It follows that the two or more mechanisms responsible for device burn-in must be forms of photo-degradation somewhere in the device. The fact that they cease, or at least significantly reduce in rate over time, must also be accounted for in any proposed mechanisms.

The V_{OC} component of burn-in is thought to be interfacial in origin because of its dependence on the materials used in the interlayers¹⁵⁸ and the degree to which its magnitude can be affected by the addition of extra layers.¹⁶³ An additional feature of this degradation mechanism is that it is reversible, as demonstrated by Kawano and Adachi.¹⁶⁴ In their study, they discover the formation of two charge-carrier trap levels upon short-term photo-ageing of OPV devices, one at the cathodic interface and one at the anodic interface. This gives rise to space-charge accumulation at the interfaces, ultimately affecting charge extraction and thereby causing a decline in fill factor. The increase in monomolecular recombination near the interfaces would also explain the decline in V_{OC} . However,

they found that, with a simple thermal annealing step, these trap states can be emptied and the degradation recovered.¹⁶⁴ In a later study, Kawano and Adachi also demonstrated that the addition of a thin layer of C₆₀ at the BHJ/ETL in direct devices could prevent the formation of these trap states and effectively suppress V_{OC} degradation during the burn-in.¹⁶³ More recently, Voroshazi *et al.* further reinforced the conclusion that interfacial charge trapping is the origin of burn-in V_{OC} degradation through their studies of inverted devices containing either P3HT/PC₆₁BM or PCDTBT:PC₇₁BM BHJ blends.¹⁵⁸ They showed that the addition of [6,6]-phenyl-C(61)-butyric styryl dendron ester (PCBSD) as a second ETL layer between the zinc oxide and the BHJ acts to almost completely remove V_{OC} degradation from the burn-in, though frequently at the expense of the devices' fill factors (indicating that the additional layer acts as a charge extraction barrier – see section 2.3.5). The authors propose that this additional ETL layer acts as a passivation layer, preventing the formation of the trap states at structural defects in the ZnO layer. They also showed that devices aged without their top layers did not show the same degree of V_{OC} loss during the burn-in, supporting the proposed interfacial origins of the mechanism.¹⁵⁸ The trap states at the top electrode may also originate from intermixed regions that were found to form at interfaces upon thermal cycling of OPV devices.¹⁶⁵ The link between efficiency loss and the formation of sub-bandgap trap states is further explored in a 2012 study by Peters *et al.*, in which the authors propose that there are three possible mechanisms at work, any or all of which may be in effect in a device.¹⁵⁹ These are: trap-mediated charge carrier recombination, reduced carrier mobility, and screening of the externally-applied electric field by space charge accumulation.¹⁵⁹

An additional mechanism for burn-in V_{OC} loss was proposed by Heumueller, *et al.* in their 2015 study reported in *Advanced Energy Materials*.¹¹⁹ Heumueller, *et al.* demonstrated that in certain polymer-based active layers, a broadening of the density of states occurs during the burn-in and, if the charge carrier density is unchanged, that this gives rise to a drop in the Fermi level, and therefore a loss of V_{OC} .¹¹⁹ This mechanism is particularly pronounced in more amorphous polymers like PCDTBT with lower charge carrier densities. However it is almost entirely absent in more crystalline polymers like P3HT, as these have sufficiently high charge carrier densities that a small broadening of the density of states has little effect on the Fermi level.¹¹⁹ Heumueller, *et al.* propose that this is the reason that significant V_{OC} loss is more commonly observed in devices containing amorphous polymers than in those containing more crystalline ones.¹¹⁹

In addition to the reversible V_{OC} -driven degradation, a reduction in J_{SC} can occur during the burn-in.¹³¹ The mechanistic origins for the J_{SC} loss are less clear than those of V_{OC} loss. Voroshazi *et al.* demonstrate that in P3HT:PCBM-based devices, the degradation responsible occurs in the bulk of the polymer; they speculate that it arises from photochemical reactions in the BHJ that crosslink and/or fracture the P3HT and PCBM.¹⁵⁸ Voroshazi *et al.* also examine devices utilising PCDTBT:PCBM and find that the degradation is predominantly fill factor-driven, with only minimal J_{SC} loss observed.¹⁵⁸ The FF -driven degradation is also shown to be interfacial, as devices that had their top electrodes and interlayers added after ageing showed no measureable reduction in fill factor as compared to unaged devices.¹⁵⁸

A recent study by Heumueller, *et al.* published in *Energy and Environmental Science* sheds some light on the origins of burn-in J_{SC} degradation and why it is only observed when certain materials are used in the active layer.¹⁶⁶ The authors attribute the J_{SC} loss to photo-induced fullerene dimerisation, which is proposed to inhibit exciton separation and reduce exciton diffusion length, thereby

decreasing J_{SC} with increasing dimer content.¹⁶⁶ The material dependency is considered to be largely a consequence of the morphology of the active layer, in particular if it is fully amorphous or has some crystalline donor domains. If crystalline domains are present, the rate of dimerisation depends on how fullerene packing occurs within the polymer matrix. Totally amorphous BHJ active layers, such as PCDTBT:PCBM blends, show very little J_{SC} loss as most of the PCBM molecules are spatially separated and, therefore cannot dimerize (Figure 2.4.2). BHJ blends that have well separated donor-acceptor domains but with large amorphous domains of fullerene acceptor were shown to exhibit high degrees of dimerisation (Figure 2.4.2), while those with more crystalline acceptor domains (Figure 2.4.2) did not (and also showed greatly reduced J_{SC} loss).¹⁶⁶ This trend was highlighted with the often-studied P3HT:PC₆₁BM BHJ blend which, when deposited from *ortho*-dichlorobenzene, formed highly crystalline domains of PC₆₁BM and exhibited almost no J_{SC} loss with photo-ageing; however, depositing the same BHJ from chloroform resulted in highly amorphous PC₆₁BM domains and significant J_{SC} loss.¹⁶⁶ Annealing the films to induce fullerene crystallisation was sufficient to suppress the J_{SC} loss.¹⁶⁶ It is also worth noting that the degree of J_{SC} loss depends on the bias applied to the device as it ages, with devices aged in open circuit condition showing greater J_{SC} loss than those aged in short circuit conditions; this suggests that bias voltage plays a role in the dimerisation mechanism.¹⁶⁶

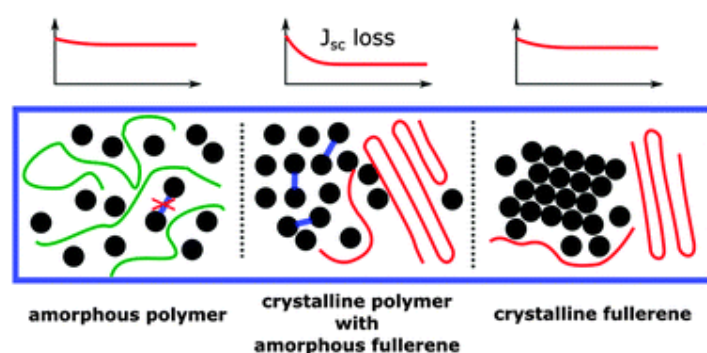


Figure 2.4.2: An illustration of the different structural motifs that may be present in a BHJ active layer, the effect they have on the fullerene acceptors' ability to dimerise under illumination, and the corresponding effect this has on the degree of J_{SC} loss during the burn in. Figure reproduced from Heumueller, T. et al., *Energy Environ. Sci.* 9, 247–256 (2016).¹⁶⁶

Linear degradation regime

The second regime of OPV device degradation under working conditions is the linear regime, which is characterised by a linear decline in efficiency with time (Figure 2.4.1). The linear regime generally accounts for the majority of a device's lifetime. In fact, degradation rate in the linear regime is often used to define lifetime via the T_{S80} (*vide supra*).²² The exact beginning of the linear regime is difficult to define, as the burn-in is exponential and thus does not have a strict end. In many cases, researchers determine the end of the burn-in manually, by semi-arbitrarily choosing the point at which the degradation curve appears to have gained linear character.²² While evidently not an ideal way to define a key device lifetime parameter, it can be shown that manually determining the end of burn-in can be reliable in the calculation of T_{80} lifetime estimates.¹⁴⁸

More systematic strategies for estimating the end of the burn-in exist. An option is to use a multi-exponential fit of the degradation curve rather than a single exponential curve and subsequent linear trend.²³ One such method, proposed by Roesch, *et al.*, is to use the following biexponential model:¹⁵⁶

$$\eta(t) = Ae^{-t/\tau_1} + Be^{-t/\tau_2} \quad 2.4.1$$

in which η is the PCE, A and B are scaling constants and the two τ terms are the time constants for the respective exponential terms.¹⁵⁶ The first exponential term can be thought of as representing the burn-in and the second term as representing the “linear” regime. As such, the end of the burn-in ($t = T_S$) can be defined as the point when the first term reaches 1% of its initial value, i.e.:¹⁵⁶

$$T_S = -\tau_1 \ln 0.01 \quad 2.4.2$$

It follows that an estimate of the T_{S80} lifetime can be given by:¹⁵⁶

$$T_{S80} = T_S - \tau_2 \ln 0.80 \quad 2.4.3$$

Although not widely used in the OPV degradation research community, it is clear that this model does allow the easy calculation of a number of key degradation and lifetime statistics.¹⁵⁶

As the linear regime spans the majority of a device’s lifetime, the post burn-in degradation rate can be due to any or all of the mechanisms discussed in section 2.3. This means that degradation rate is determined by a mixture of intrinsic mechanisms that are a consequence of the normal operation of the device and extrinsic mechanisms that are a consequence of the device’s environment and exposure to ageing stimuli and thus can (to some extent) be removed. Although no encapsulation or UV filtration is perfect, extrinsic degradation mechanisms can be greatly minimised. This means that device lifetime is predominantly limited by intrinsic degradation mechanisms, and so device design and the choice of materials are the key factors in extending lifetime.¹⁴⁸

To illustrate this point there are two studies worth highlighting. The first is one reported by Voroshazi, *et al.* in *Solar Energy Materials and Solar Cells* in 2011.¹³¹ In it, the authors carried out the ageing of direct P3HT:PC₆₁BM BHJ devices under full AM1.5 illumination (there is no mention of any UV filtration) in a dry nitrogen atmosphere. The first set of devices they examined were ITO/PEDOT:PSS/P3HT:PCBM/Yb/Al devices, which showed rapid post burn-in degradation and eventual catastrophic failure (*vide infra*).¹³¹ Device lifetimes (limited in some cases by catastrophic failure) were no more than 300 to 400 hours. However, by changing the materials used as interfacial layers, particularly swapping the corrosive and hygroscopic PEDOT:PSS for a metal oxide equivalent (MoO₃), device lifetime was able to be extended well beyond 1000 hours.¹³¹

The second study was reported by Mateker, *et al.* in *Chemistry of Materials* in 2015.¹⁴⁸ In it the authors were able to demonstrate lifetimes of direct and inverted OPV devices exceeding 8000 hours (the length of the test) and extrapolated lifetimes (*vide infra*) of more than two decades. In particular, the studied devices showed almost no detectable degradation after the burn-in.¹⁴⁸ It is worth considering what factors distinguish this study from the one above. With respect to extrinsic sources of degradation, the ageing takes place in the same atmospheric conditions but uses a different radiation source that has no UV component, removing the possibility of a number of photodegradation mechanisms (see section 2.3). There are also some differences in device design. The active layer in the second study is a PCDTBT:PC₇₁BM BHJ, which, as discussed by Tournebize, *et al.*, is inherently more morphologically stable than P3HT:PC₆₁BM due to the high T_g of PCDTBT and is capable of further stabilisation under illumination via crosslinking.⁹⁹ An interesting observation is that either the removal of UV light or the change of materials for the active layer results in the direct

architecture incorporating the acidic PEDOT:PSS becoming much more stable, although differences in processing conditions of the PEDOT:PSS cannot be discounted.

A final point to note from the Mateker, *et al.* study is the method used by the authors for estimating the lifetime of their devices. When a device lifetime becomes very long, it can be impractical to study the device for its entire lifetime, especially when that lifetime can be as long as decades. One could consider OPV solar cells a victim of their own success in this regard. As researchers seek to extend lifetime even further, estimating the eventual lifetime of the device will become increasingly difficult. In the study by Mateker, *et al.*, the authors use a linear extrapolation of the efficiency degradation curve to estimate the T_{S80} .¹⁴⁸ Whilst sometimes useful to estimate the device lifetime, there are some serious drawbacks to this method, most revolving around the assumption that that degradation is linear with time and would continue to be linear beyond the end of the study. Depending on the materials used, some devices show an abrupt catastrophic failure after a certain amount of time in the linear regime (Figure 2.4.1)¹³¹ that would not be accounted for in the model. It assumes that any extrinsic sources of degradation are either minimal or will remain at a constant level for the device lifetime – i.e. assuming perfect encapsulation across device lifetime. Finally, there seems little basis for assumption that the degradation in the linear regime is linear at all. As discussed earlier in this section, it can be accurately modelled with a biexponential model.¹⁵⁶ In the case of the Mateker, *et al.* study, data presented in the supplementary information reveal that estimates of T_{S80} lifetime from linear extrapolation vary wildly, in some cases they model lifetimes as long as centuries or even show no degradation at all.¹⁴⁸ There are not only apparent extreme overestimations of lifetime to be found, but it is possible that in assuming linearity in the case of degradation data from inverted devices, they underestimate lifetime, as the degradation curve appears weakly exponential at the end of the study.¹⁴⁸ Linear extrapolation is, therefore, an imperfect method for lifetime estimation; still, other methods like accelerated ageing studies have their own drawbacks.¹⁵⁶

Catastrophic failure

When considering device failure, it is important to examine the manner of that failure. On the one hand, it is possible to choose a point on a degradation curve and define that as the end of a device's life¹⁵⁶ (the T_{S80} is frequently used for this purpose²²). However, a consideration of the T_{S80} does not reveal how the device has failed. It may be that the device is degrading linearly, and device death is not due to any change in the degradation behaviour. It is also possible, though, that device death comes as a result of a different degradation mechanism causing a sudden loss of efficiency – this is known as catastrophic failure.¹⁵⁶ As this failure is caused by different mechanisms to degradation within the linear regime, if catastrophic failure is limiting lifetime, addressing these mechanisms can extend lifetime.

An example of catastrophic failure is examined in the study by Voroshazi, *et al.* that was profiled in the linear degradation section above.¹³¹ In that study, direct devices with the structure ITO/PEDOT:PSS/P3HT:PCBM/Yb/Al were shown to exhibit significant loss of FF after 300 hours of ageing under AM1.5 illumination, characterised by the appearance of an s-shape in the IV curve.¹³¹ This s-shape eventually leads to the complete loss of photocurrent and thus effective device death. As discussed in section 2.3.5, this behaviour is due to the growth of a charge extraction barrier across the whole working area of the device leading to the build-up of a space charge that screens the electric field in the device.¹³⁴ Voroshazi, *et al.* were able to demonstrate that by changing the

materials used as charge extraction layers, they were able significantly postpone catastrophic failure or even prevent it entirely.¹³¹ In fact, longer duration ageing studies on more stable architectures frequently do not observe catastrophic failure as a result of intrinsic degradation, even when measurement is carried out for up to 10 000 hours.¹⁶⁷

While catastrophic failure due to intrinsic mechanisms can be significantly postponed and potentially prevented entirely through intelligent device design, there are also extrinsic origins of catastrophic failure to consider. Most of these originate from the environment in which the device is used and the effects of environmental conditions on encapsulation materials. Repeated diurnal or seasonal temperature variations, seasonal freeze-thaw cycles, high levels of humidity, or large amounts of precipitation can degrade encapsulation materials, exposing the device to the elements.¹⁵⁶ These conditions can also corrode electrical contacts, rendering the device unusable.¹⁵⁶ Mechanical stress should also be considered here. One of the stated advantages of OPV solar cells is the ability to fabricate flexible devices;¹⁵ however, it has also been shown that the adhesion of metallic electrodes to organic active layers is comparatively weak.¹⁵⁵ Repeated mechanical stress can lead to electrode delamination, destroying the device.^{155,156}

2.5. Strategies to minimise device degradation

As already discussed in this chapter, degradation of OPV devices has its origin in both intrinsic and extrinsic mechanisms. Any attempt to increase the lifetime of a device must incorporate strategies that address both aspects of degradation. In this section some of these strategies will be briefly examined.

The minimisation of intrinsic OPV degradation requires careful device design and materials selection. Many such considerations have already been discussed in section 2.3, and so specific information regarding their function will not be repeated in detail. A few strategies to improve intrinsic device stability include:

- synthesising more photo-stable and morphologically stable donor species;⁶⁵
- pairing donor and acceptor species such that photodegradation is further minimised and the BHJ morphology is stabilised;⁹⁹
- using crosslinking of the donor and acceptor species (either through specifically designed donor and acceptor species or through crosslinking additives) to stabilise the BHJ morphology;²⁷
- using more chemically inert interlayers and electrodes;¹³¹
- and using the more stable inverted device architecture.¹⁴³

The improvement of a device's resilience to extrinsic degradation stimuli must incorporate many of the strategies outlined above, but ultimately some form of encapsulation is required to ensure device stability on commercially relevant timescales. To a degree, a device's inherent stability to oxygen and water will also determine the type of encapsulation required – the less stable the device, the higher the quality of encapsulation that will be required (both with respect to its permeability and its longevity).¹⁶⁸ Typically higher quality encapsulation comes at higher cost and higher fabrication energy requirements.¹⁶⁹ As encapsulation represents a significant portion of final device cost, this has implications for the financial viability and energy payback time of the device.¹⁶⁹ In

other words, the familiar trade-off must always be made between device lifetime, device cost, and device efficiency.

There are many different encapsulation strategies that may be employed with OPV devices and modules. A common example is the glass-on-glass method. In this method the device is fabricated on a glass substrate and an additional piece of glass is secured on top of the sample with an adhesive.¹⁷⁰ This is a very effective form of encapsulation as the only effective route of water and oxygen ingress is around the edges of the encapsulated device. It does, however, have some disadvantages, in particular its inapplicability for roll-to-roll processing and flexible devices.¹⁶⁹ Another method involves the use of thin-film polymer materials.¹⁷¹ An individual thin polymer film does not offer a barrier to oxygen and water nearly as effective as glass. This is due to imperfections, defects, and pinholes in the films.¹⁷¹ If, however, a multilayer laminate film is used, the path-length of diffused gasses through the barrier is greatly increased, decreasing diffusion rates to levels that are acceptable for OPV device encapsulation.^{168,171} Such laminate films can be used as both substrates and encapsulation barriers using a variety of sealing strategies to effectively encapsulate devices.^{169,171,172} They can also be paired with roll-to-roll processing, allowing the production of 30 cm wide sheets of encapsulated OPV modules at up to 20 m min⁻¹.¹⁶⁹

There are many more strategies for the design and fabrication of encapsulation materials for high throughput production of OPV devices and modules; however, a detailed review of all of them goes beyond the scope of this work. Interested readers should consult reviews by Ahmad, *et al.*,¹⁷³ Krebs, *et al.*,¹⁷⁴ and Park, *et al.*¹⁷¹

The suppliers and other information about the materials used in this section are given in Table 3.4.2.

3.1. Thermal degradation study of inverted OPV devices

3.1.1. Fabrication of OPV devices

The structure of the OPV devices used in this study is shown in Figure 3.1.1.

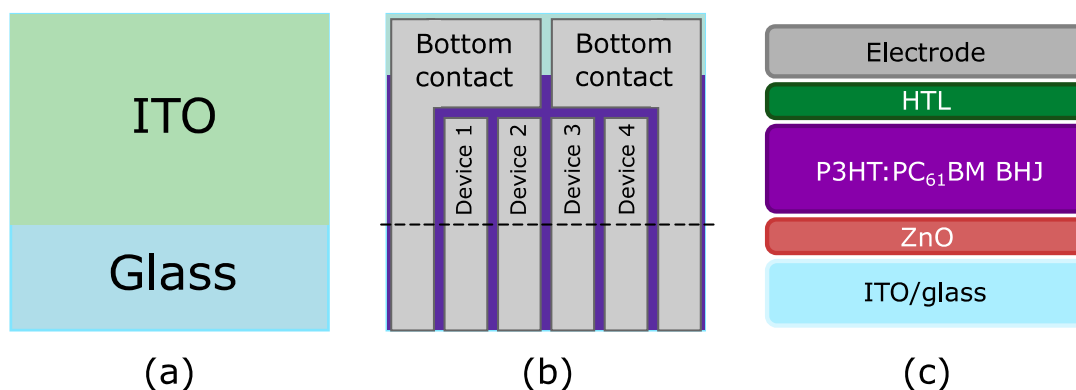


Figure 3.1.1: Schematics of (a) an uncoated ITO/glass substrate; (b) the electrode layout of a completed sample with four devices; and (c) the vertical structure of the OPV devices used in this study. Note that in (b) the dashed line represents the extent of the ITO layer on the substrate and therefore defines the bottom edge of the devices. The substrates measured 15 mm × 15 mm and the area of each device was 10 mm².

Substrate preparation

The ITO/glass substrates were unpackaged and degreased via one of two methods. The first method was immersion of the substrates in an ultrasonic bath of acetone, then technical ethanol, then isopropanol for 10 minutes each at 25°C. The other method was immersion in an ultrasonic bath of a surfactant/de-ionised water mixture at 60°C for 15 minutes, followed by immersion three times in an ultrasonic bath of deionised water at 60°C for five minutes to remove any residual surfactant, and then submersion in an ultrasonic bath of isopropanol at 25°C for 10 minutes. Both techniques produced devices with identical reliability and performance.

Following degreasing, the substrates were blow-dried with compressed air and placed in a UV/ozone cleaner (Jelight 42-220) for 15 minutes.

ZnO deposition

The ZnO layer was deposited via a sol-gel method, based on the method used by Vongsaysy, *et al.* in their 2014 study published in *Advanced Energy Materials*.⁴⁰ The precursor solution was prepared as follows:

- 165 mg of zinc(II) acetate dihydrate powder was weighed out into a 6 mL glass vial
- 45 μ L of ethanolamine was added to the vial, followed by 5 mL of absolute ethanol
- The mixture was stirred at 50°C for exactly 30 minutes
- The vial was then transferred to a stirrer-plate for storage at room temperature for at least two hours before use.

The coating of the substrates was done in a laboratory fume cupboard immediately after the UV/ozone step described above, and was done by spin coating at 2000 rpm for 60 seconds. The sol-gel layer was then removed from the top of the sample with a cotton bud soaked in absolute ethanol so that electrical contact could be made with the bottom electrode in the completed device. Finally, the coated samples were annealed at 180°C for at least 30 minutes. The resulting layer thickness was 24 ± 4 nm, measured with a mechanical profilometer (KLA-Tencor, Alpha-Step IQ).

P3HT:PC₆₁BM active layer deposition

Into a 4 mL brown glass vial, a sufficient mass of P3HT and PC₆₁BM were weighed out so as to make the concentration of the final solution 20 mg mL⁻¹ in each substance (a 1:1 ratio). The vial was then transferred to a glovebox which was under a nitrogen atmosphere (<0.1 ppm O₂, H₂O). All subsequent fabrication steps were carried out in the glovebox (with one exception, *vide infra*). The P3HT and PC₆₁BM were dissolved in 1,2-dichlorobenzene and stirred for 20 minutes at 80°C, before being stored stirring at 50°C. Immediately prior to use, the solution was filtered with a syringe filter (1.0 μ m, PTFE, Thermo Scientific), and the filtered solution was heated at 80°C for five minutes before being returned to the storage hot plate.

Immediately prior to coating with the active layer solution, the samples were rinsed with chloroform and dried by spinning on the spin-coater. Coating of the samples was carried out by spin coating at 1000 rpm for 10 seconds less than the amount of time required to dry the sample (this was typically 40 seconds, but varied significantly from batch to batch). Before drying, the sample was transferred to an enclosed petri dish and left for one hour to fully dry, annealing in the residual solvent vapour.¹⁷⁵ Where necessary, a cotton bud was used to remove excess solution from the corners of the sample prior to solvent annealing. The resulting active layers were 170 nm thick.

PCDTBT:PC₇₁BM active layer deposition

10.5 mg of PCDTBT and 29.4 mg of PC₇₁BM were weighed out into a 4 mL brown glass vial. The vial was then transferred to a glovebox which was under a nitrogen atmosphere (<0.1 ppm O₂, H₂O). All subsequent fabrication steps were carried out in the glovebox (with one exception, *vide infra*). 2 mL of 1,2-dichlorobenzene were added to the vial, and the mixture was left to stir at 85°C for two days, before being transferred to a storage hotplate where it was kept stirring at 50°C.

Prior to deposition, a number of test samples were prepared to determine the optimal spin-coating speed to produce a 90 nm thick active layer. This varied between sample batches, but was typically between 700 rpm and 1300 rpm. The thickness was determined with a mechanical profilometer. Once the optimal speed was determined, all the samples were coated at that speed for 90 seconds following a chloroform cleaning step (*vide supra*).

No further annealing steps were needed.

Deposition of metal-oxide HTLs

Deposition of the MoO₃ or WO₃ HTL was carried out by electron-beam evaporation (Playssys MEB 550). The oxides were deposited at rate of ca. 0.1 nm s⁻¹ onto the whole surface of the sample to a thickness of 10 nm. The thickness was monitored with a resonating quartz balance inside the chamber.

Deposition of the PEDOT:PSS HTL

The samples were spin coated with a PEDOT:PSS solution, spinning at 1500 rpm for 60 seconds then 2500 rpm for 15 seconds. It was necessary to carry out this spin coating step in air as the PEDOT:PSS solution is aqueous and would contaminate the glovebox, however the samples were kept in the dark as much as possible. Following spin coating, the samples were immediately returned to the glovebox where they were annealed for 10 minutes at 120°C. The resulting layer thickness was measured with a mechanical profilometer to be 20 nm.

Deposition of metal electrodes

Deposition of the aluminium or silver electrodes was carried out by thermal evaporation (MBraun). The silver was deposited at rate of ca. 0.6 nm s⁻¹, while the aluminium was deposited at ca. 2.0 nm s⁻¹. The electrodes were defined as shown in Figure 3.1.1 by a shadow mask and were deposited to a thickness of 80 nm unless otherwise stipulated. The thickness was monitored with a resonating quartz balance inside the chamber.

3.1.2. IV characterisation of OPV devices

Device activation

The devices all exhibited a light activation phenomenon whereby they would have a high threshold voltage (measured in the dark) until exposed to UV light. After 30 seconds of exposure to simulated sunlight, the threshold voltage decreased permanently to near the V_{OC}. This activation could also be partially achieved by exposing the ZnO-coated substrates to UV radiation (365 nm) prior to the application of the active layer.

This effect has been observed previously in inverted OPV devices that use ZnO ETLs and has been attributed to the presence of adsorbed oxygen at the ETL/active layer interface that is released upon UV exposure.¹⁷⁶ Previous studies suggest that a short reverse bias pulse would also activate the devices,¹⁷⁶ but this was not tested.

Testing apparatus

The devices were characterised in a glovebox under a nitrogen atmosphere (<0.1 ppm O₂, H₂O) using an HMI lamp fitted with an AM1.5G filter. The lamp was calibrated to an intensity of 1000 W m⁻² with a photometer (International Light Technologies IL1400BL).

IV curves were obtained using a Keithley 2400 source measurement unit (SMU) that was controlled by a customised LabVIEW measurement program. The four devices on a sample were connected to the SMU via a Keithley 2700 multimeter fitted with a Keithley 7700 20 channel multiplexing card, and were measured in sequence – once in darkness, and once under illumination.

Data acquisition and processing

The program used to measure the IV curves and automatically determine PV device statistics was developed by the author specifically for the experiments in this work using the LabVIEW programming environment. The program is designed to rapidly and easily measure an entire batch of 20 samples (80 individual OPV devices), save the current density/voltage data in a single file, and save the device statistics for all the devices in a single, separate file. It functions by constructing a virtual sample list, then working down the list looping through measurement and analysis protocols for each sample, prompting the user when human intervention is required to either place the sample over the lamp, or change the sample, until the entire batch of samples is measured. Users can customise the number of samples to be measured, the number of devices to measure on each sample, and the names of the samples.

The program determines seven statistics: the shunt resistance, the series resistance, the resistance at V_{OC} , the J_{SC} , the V_{OC} , the FF, and the PCE automatically from the dark and illuminated IV curves. The shunt and series resistances are determined from the inverse of the slopes dark IV curve at -0.5 V and at a user-selected high forward bias voltage ($+0.9$ V in these experiments) respectively. The remaining five statistics are determined by linear extrapolation and peak fitting of the light IV and power curves in the manner shown in Figure 3.1.2.

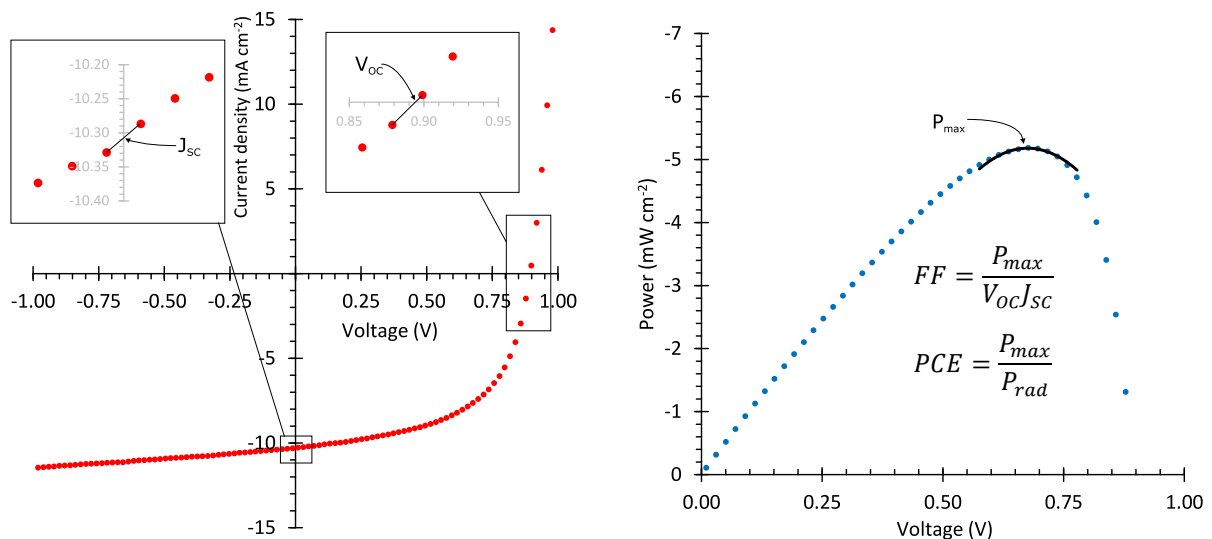


Figure 3.1.2: (left) an annotated IV (scaled to current density) showing how the V_{OC} and J_{SC} are determined by linear extrapolation between data points; and (right) a power curve in the forward bias region showing how P_{max} is found by peak fitting, and then how P_{max} is used to find the FF and PCE. In this figure, P_{rad} represents the intensity of the incident radiation.

3.1.3. Thermal ageing of the OPV devices

Experiment design

The samples were grouped by the combination of materials used for the HTL and top electrode. Each group consisted of four samples that were aged (16 devices), and one control sample (four devices). The control samples were stored in the dark in the same glovebox that the other samples were aged in, and measured at every time point with the other samples. This was done in order to distinguish genuine effects of thermal ageing from the effects of measurement and repeated handling.

Sample ageing

The samples were aged on a covered hotplate (Unitemp GmbH) at 85°C in a glovebox with a nitrogen atmosphere (<0.1 ppm O₂, H₂O), consistent with the ISOS-D-2 protocol.²² Ageing would be stopped periodically to characterise the samples, which was also done under an inert atmosphere in a glovebox. The time interval between measurements increased throughout the experiment at an arbitrary rate, starting at two minutes and reaching 72 hours by the end of the experiment. This was done to ensure that fast acting degradation mechanisms were observed while minimising any potential damage to the samples from repeated measurement.

3.2. Rutherford backscatter spectrometry and atomic force microscopy (AFM) experiments

3.2.1. Preparation of samples for RBS

The samples were prepared on glassy carbon substrates, with the structure shown in Figure 4.3.1. The substrates were degreased using the multi-solvent system discussed in section 3.1.1 and blow-dried. They were then coated across their entire surface with either MoO₃ or WO₃ using an e-beam evaporator, then either aluminium or silver using a thermal evaporator. The thicknesses of the layers were chosen to optimise peak separation in the RBS data (as determined by simulation – SIMNRA), and are given in Table 3.2.1.

Table 3.2.1: The oxide and metal layer thicknesses in the samples used in the RBS experiments

Metal/oxide	Oxide thickness (nm)	Metal thickness (nm)
Al/MoO ₃	100	100
Al/WO ₃	80	80
Ag/MoO ₃	100	70
Ag/WO ₃	50	25

The samples were aged in the same conditions as the OPV devices (see section 3.1.3) except that ageing was not paused before completion. Two groups of aged samples and one control group were measured in the RBS experiment. One group of aged samples were aged at 85°C, like the OPV samples, for 570 hours. The other group of aged samples underwent accelerated ageing at 150°C for 90 hours. The samples were exposed to air when transferred to the particle accelerator for measurement, but were kept in the dark whenever possible.

3.2.2. Instrument settings and parameters

The RBS measurements were carried out on an He⁺ beamline of the 2 MeV particle accelerator in the Aquitaine Regional Multidisciplinary Ion Beam Facility (*Applications Interdisciplinaires de Faisceaux d'Ions en Région Aquitaine* - AIFIRA) at the Bordeaux-Gradignan Centre for Nuclear Research (*Centre Etudes Nucléaires de Bordeaux Gradignan* - CENBG) with a current of approximately 1 nA, beam diameter of 3 mm, and a scattering angle of 160° (see Figure 4.3.2).

The majority of the AFM measurements were carried out on the RBS samples and OPV samples (aged samples and control samples) with a Bruker Innova large area scanner atomic force microscope in tapping mode. The AFM measurements done for the silver thickness experiment were carried out by Dr Gilles Pecastaings with a Dimension FastScan AFM (Bruker) in tapping mode. Silicon cantilevers (Fastscan-A) with a typical tip radius of ≈ 5 nm, a spring constant of 18 N m^{-1} and a cantilever resonance frequency of about 1.4 MHz were used.

3.3. Fracture analysis experiment

3.3.1. Sample fabrication

The samples used for fracture analysis were deposited on large glass substrates, measuring $76 \text{ mm} \times 52 \text{ mm} \times 1 \text{ mm}$. The substrates were prepared by degreasing using the surfactant method detailed in section 3.1.1, and then blow-dried.

The ZnO layer was formed from a sol-gel which was deposited by doctor blade, using a procedure and solution developed by Dr Elodie Destouesse. The solution was prepared by dissolving zinc(II) acetate dihydrate in butanol at a concentration of 0.18 mol L^{-1} , to which ethanolamine was added to give a molar ratio (ethanolamine/ $\text{Zn}(\text{OAc})_2$) of 0.45. The solution was stirred in three stages: at 60°C for one hour, at 80°C for one hour, and then at room temperature for 48 hours. Finally, the solution was diluted by a factor of two before use. Deposition was carried out at a speed of 10 mm s^{-1} , with a blade height of $12 \mu\text{m}$, a solution volume of $20 \mu\text{L}$ and a temperature of 50°C . The coated samples were subsequently annealed at 140°C for one minute. The resulting layers of ZnO were measured by mechanical profilometry, and were found to be between 30 nm and 40 nm thick.

The deposition of the P3HT:PC₆₁BM active layer using the doctor blade was done using a procedure developed during this study. The development and optimisation of this procedure are detailed in section 4.4.2. Following deposition and solvent vapour annealing of the active layer, the HTL and metal electrode were deposited in the same way as those in the OPV samples with the same thicknesses (section 3.1.1).

3.3.2. Sample transportation

Details concerning the logistics of sample transportation are given in Appendix A.

3.3.3. Sample preparation for fracture analysis and measurement

The preparation of the samples for fracture analysis was done by a procedure adapted from the common practises of the Dauskardt group at Stanford University. The procedure used is as follows:

- A $72 \text{ mm} \times 56 \text{ mm}$ sample is taken from the glovebox for cutting. The two uncoated ends of the sample are cut away with a diamond scribe
- The sample is cut into five or six $11 \text{ mm} \times 56 \text{ mm}$ strips
- Each strip is bonded to an identically-sized glass strip with an epoxy adhesive. This glass strip acts as the second “beam” in the DCB geometry (see Chapter 4). The epoxy is allowed to dry in a glovebox
- Once dry, excess epoxy is removed from the edges of the sample with a razor blade

- At one of the 11 mm ends of the strip, a crack is initiated with a razor blade. This “pre-crack” is ideally ca. 1 cm long
- At the pre-cracked end, two metal tabs are bonded to the strip (one on each beam) for the instrument to pull

Once ready, the strips were mounted in the testing apparatus (Delaminator DTS, Menlo Park, CA). The specimens were loaded under displacement control from which a load (P) versus displacement (Δ) curve was recorded, in the manner described in Chapter 4.

3.3.4. Fracture analysis data processing

Values for the fracture energy were determined from the load-displacement curves using a macro in Origin, developed by the Dauskardt group. Subsequent data collation and averaging was carried out with a LabVIEW program developed for this study.

3.3.5. X-ray photoelectron spectroscopy (XPS) and Kelvin probe analysis

Both the determination of the fracture paths in the samples and the elemental depth profiling was carried out using XPS (PHI 5000 Versaprobe). The fracture path was determined by a survey scan (0 – 1100 eV) of each fractured half of a sample with monochromatic Al K_{α} X-radiation at 1487 eV. The depth profiling was carried out by etching the sample with an Ar⁺ ion beam (0.5 μ A, 1.0 kV), rastered over a 2 mm \times 2 mm square and scanning every 30 seconds with a 200 μ m \times 200 μ m X-ray beam spot at a detection angle of 35°. Supplementary AFM analysis of these samples was carried out with a XE-70, Park Systems atomic force microscope in non-contact mode.

Kelvin probe analysis was carried out on some of the fractured samples using a scanning Kelvin probe (KP Technology Model 5050). All measurements were calibrated to a specimen of highly oriented pyrolytic graphite (HOPG) with a work function of 4.65 eV.¹⁷⁷

3.4. Photodegradation experiments

3.4.1. Sample fabrication and experiment design

The samples used for the photodegradation experiments were fabricated in the same way as those in the thermal degradation experiments (see section 3.1.1). The samples that incorporated WO₃ HTLs were heated for two hours at 85°C after fabrication, prior to the start of the experiment, to ensure they started the experiment at the maximum efficiencies identified in the thermal ageing experiments (see Chapter 4).

As with the previously-discussed studies, samples in the photodegradation experiments were grouped by the combination of materials used for their HTLs and metal electrodes. In the experiments that only examined metal-oxide HTLs, there were four different combinations of materials (Al/MoO₃, Al/WO₃, Ag/MoO₃, and Ag/WO₃) and each group had four samples (16 devices) aged, and one control sample (four devices) that was stored in the dark in an inert atmosphere for the duration of the experiment. The purpose of the control sample was to ensure that the brief exposure to oxygen and humidity during the loading of the samples did not cause any of the ageing

effects observed in the samples. In the experiments that incorporated samples with PEDOT:PSS HTLs, there were five groups (Al/MoO₃, Al/WO₃, Ag/MoO₃, Ag/WO₃, and Ag/PEDOT:PSS), each with three aged samples (12 devices) and one control sample (four devices). The reason for the difference is that the sample holder in the ageing chamber can only hold a maximum of 16 samples.

3.4.2. External quantum efficiency measurements

The samples' EQE was measured using a custom-built apparatus in the IMS laboratory. The apparatus incorporates a 500 W Xe lamp and TRIAX 180 spectrometer (Horiba, Jobin Yvon), and a fibre-optic cable, which were calibrated using an integrating sphere (Labsphere) immediately prior to measurement with a picoammeter Keithley 6487. The apparatus was controlled by a LabVIEW program developed by Marcin Kielar.

3.4.3. Construction and use of the ageing chamber

The requirements of the ageing chamber were that it be able measure the performance of up to 64 OPV devices under illumination by simulated sunlight in a range of different atmospheric conditions, all while continuously monitoring the temperature, radiation intensity and humidity. This section examines the design of the chamber that was constructed to carry out the photodegradation experiments in accordance with the ISOS-L-1 protocol,²² with particular focus on the electrical and atmospheric systems.

The exterior of the ageing chamber is depicted in Figure 3.4.1, and a diagram of the interior of the chamber is shown in Figure 3.4.2.

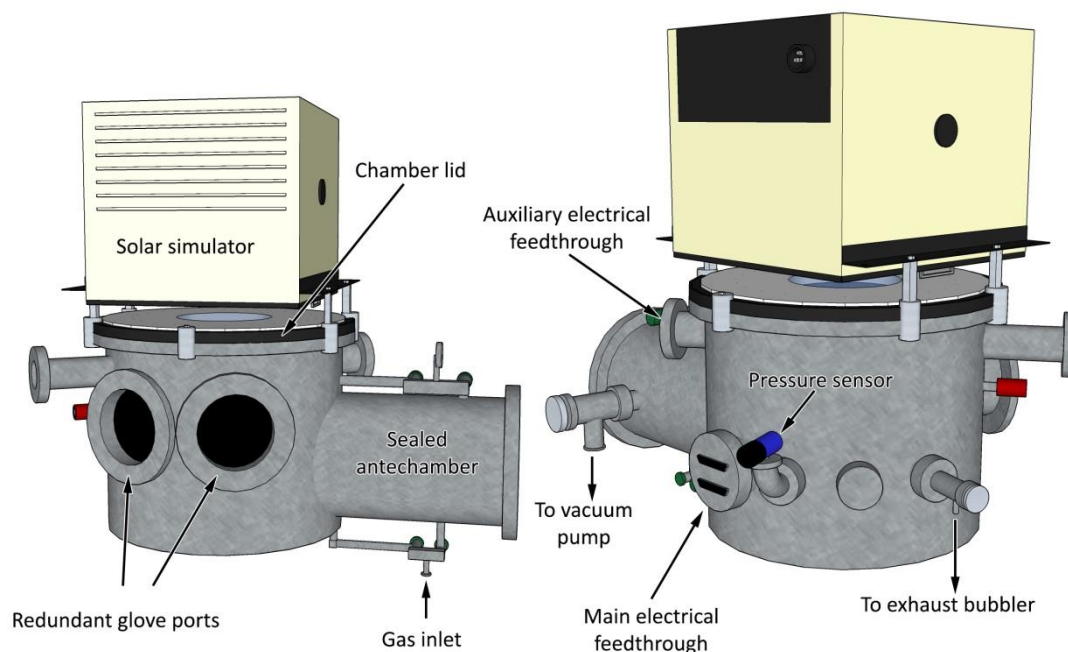


Figure 3.4.1: An illustration of the exterior of the ageing chamber with the important components annotated

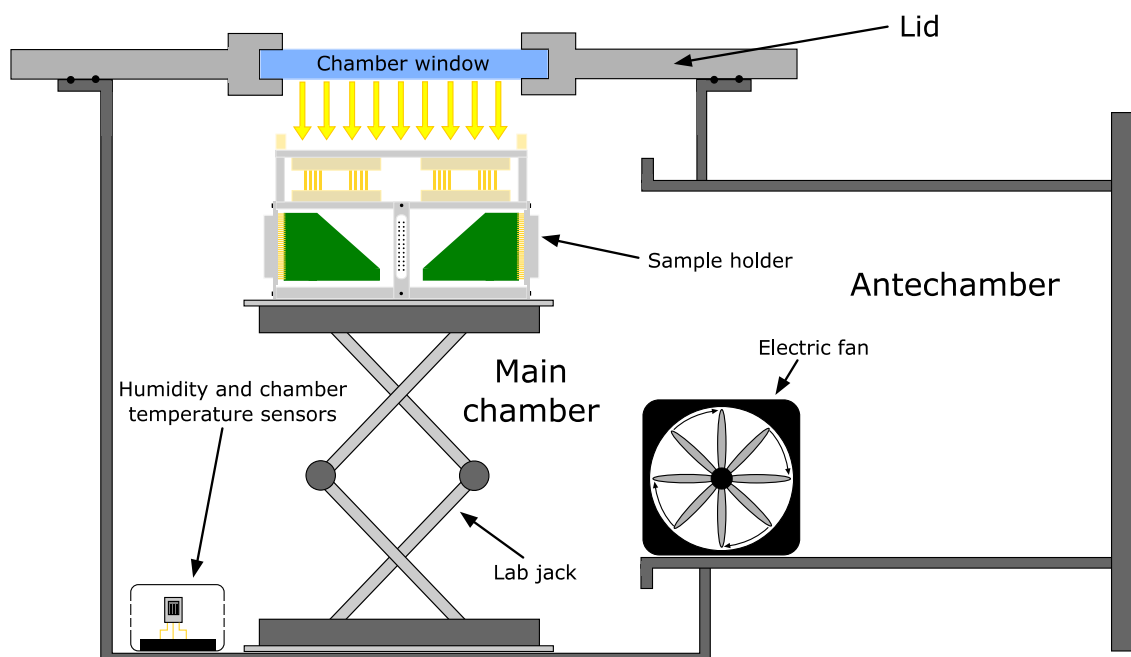


Figure 3.4.2: An illustration of the interior of the chamber with the principal components annotated. Note that wires, cables, feedthroughs, electrical adaptors, and atmosphere inlets/outlets are not depicted for clarity.

The chamber was constructed from an old MECA2000 UHV chamber, which was heavily modified to fit the requirements of the experiment. Additional electrical feedthroughs and valves were fitted around the chamber (supplied by Kurt J. Lesker), and a new lid was fabricated for the chamber (fabricated by the workshop at *le Centre Etudes Nucléaires de Bordeaux Gradignan*). A new window was incorporated into the lid – constructed from borosilicate glass, which has good transparency across the AM1.5G spectrum (Fabricated by V.E.R.A.L.).^{178,179} The window is circular, with a diameter of 20 cm and thickness of 8 mm. The solar simulator, which was mounted above the chamber (struts fabricated by the IMS laboratory workshop), is an unfiltered, 1.2 kW HMI lamp fitted with a diffusion plate that can deliver up to one sun intensity across a 35 cm × 35 cm area with less than 5% spatial variation in intensity (SolarConstant 1200 supplied by ATLAS). The HMI bulbs were replaced before each experiment.

The chamber was originally fitted with gloves in the hope that, by using the antechamber, it could be used like a glovebox. However, due to space requirements in the chamber, this was not eventually possible. The glove ports were covered inside the chamber with permeable covers which prevented the gloves from ingressing when the chamber was under vacuum.

Atmosphere control system

An atmospheric control system was developed for the ageing chamber which would allow the chamber to be operated in a range of atmospheric conditions. A schematic of this system is shown in Figure 3.4.3 and the different operating settings in Table 3.4.1. The parts for this system were supplied by Kurt J. Lesker, Sigma-Aldrich, Fisher Scientific, and Radiospares France. The vacuum pump is a rotary pump, supplied by Edwards. After the samples were loaded, the chamber would be purged twice by evacuating the chamber to 0.1 mbar and then re-pressurising with the dry gas to be used in the experiment, prior to turning on the lamp and starting the experiment.

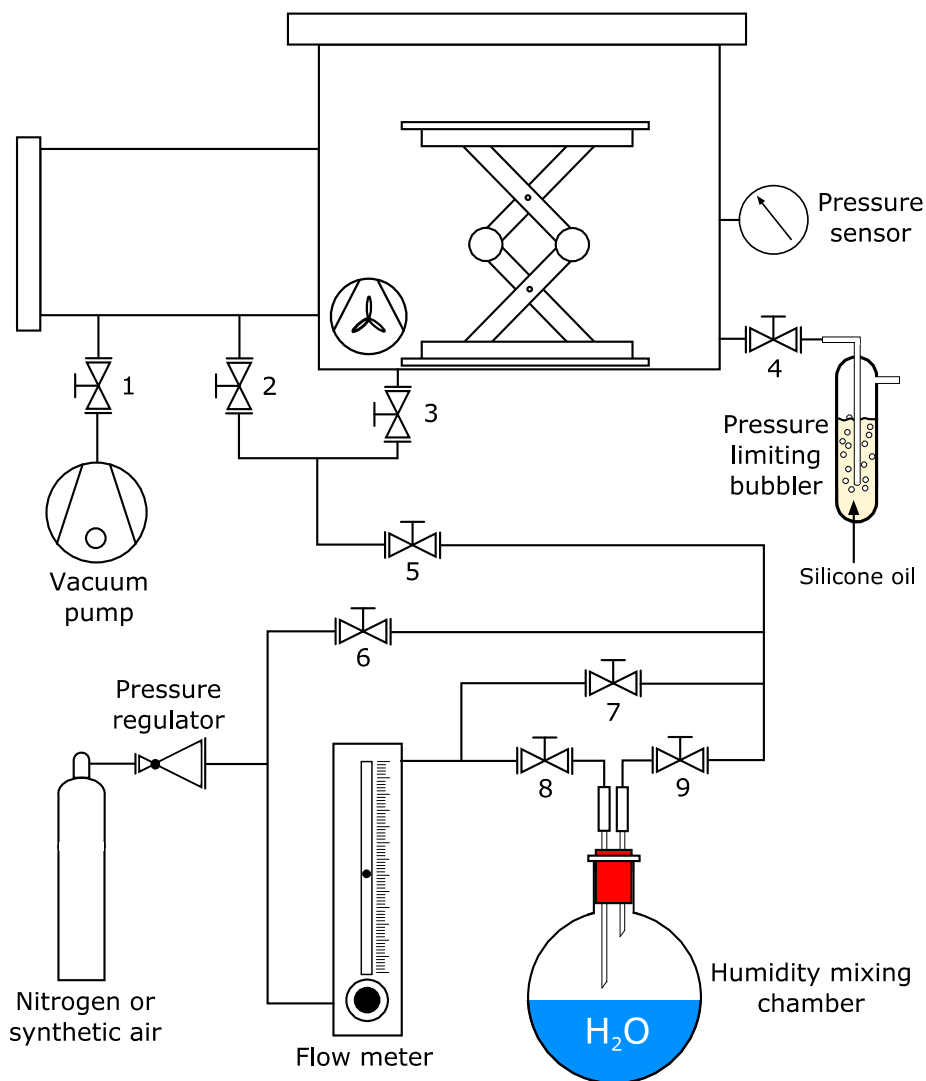


Figure 3.4.3: A schematic of the atmospheric control system used with the ageing chamber. Note that the numbered items are manual valves.

Table 3.4.1: Settings for carrying out the different processes used in the operation of the ageing chamber. The valve numbers correspond to the labels in Figure 3.4.3

Process	Valves closed	Valves opened	Gas cylinder
Evacuate (purge)	4, 5	1, 2, 3	N ₂ or 20% O ₂ /N ₂
Pressurise (purge)	1, 4, 7, 8, 9	2, 3, 5, 6	N ₂ or 20% O ₂ /N ₂
Dry nitrogen experiment	1, 6, 8, 9	2, 3, 4, 5, 7	N ₂
Dry air experiment	1, 6, 8, 9	2, 3, 4, 5, 7	20% O ₂ /N ₂
Humid nitrogen experiment	1, 6, 7	2, 3, 4, 5, 8, 9	N ₂
Humid air experiment	1, 6, 7	2, 3, 4, 5, 8, 9	20% O ₂ /N ₂

In humidity experiments, the water in the humidity mixing chamber was de-gassed by bubbling nitrogen through it for 30 minutes before starting the experiment. Note that the pressure regulator was set to between 1.0 bar and 1.5 bar, and the flow meter to 15 mL min⁻¹ while an experiment was

running. The flow meter was fully closed while purging. The chamber had 90 ppm of O₂ contaminants when operating under nitrogen and the humidity levels in dry experiments were below the detection limit of the sensor.

Electrical system

A layout of the electrical connections within the ageing chamber is shown in Figure 3.4.4.

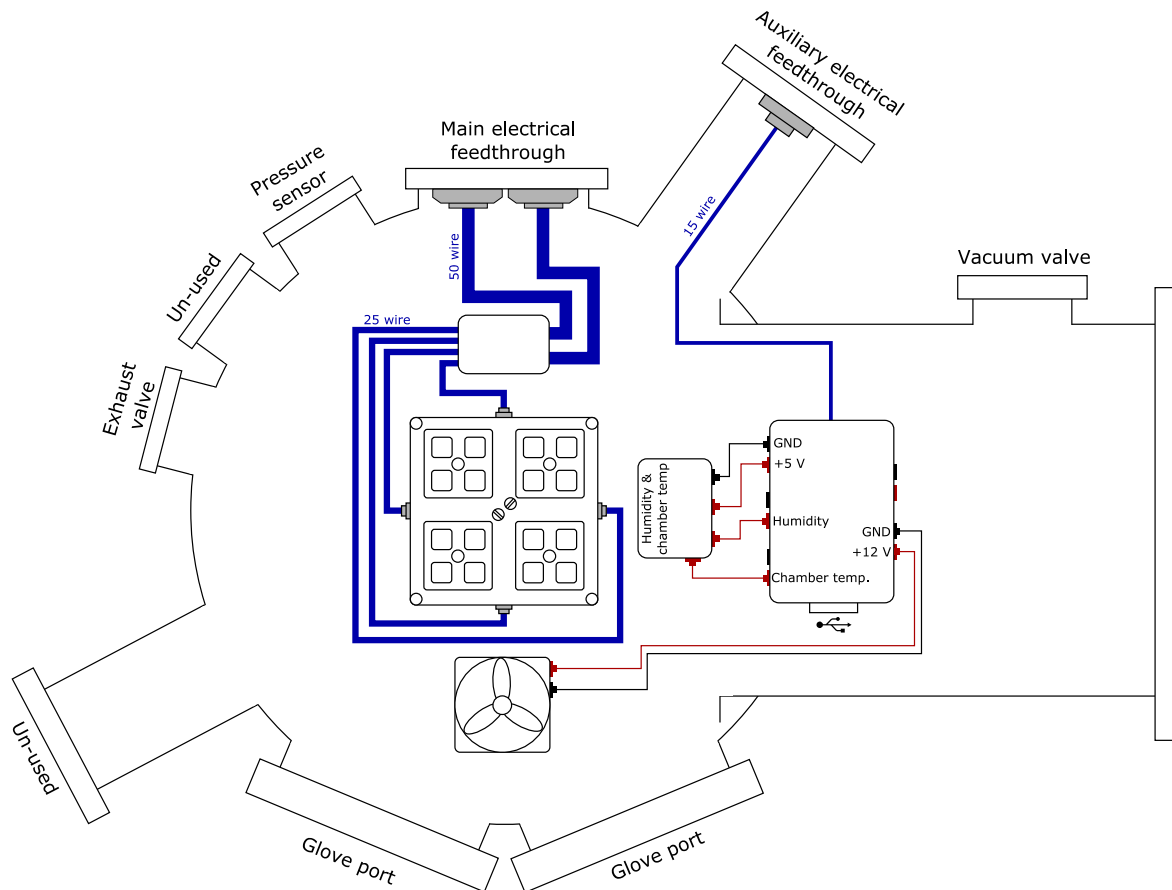


Figure 3.4.4: A diagram of the electrical connections inside the ageing chamber. The thick blue lines represent multi-wire cables

The majority of the electrical connections in the chamber are to the sample holder, which has a maximum of 100 channels, and is connected to the exterior of the chamber via a 100 pin feedthrough. Additional sensors to those in the sample holder (a Honeywell HIH-4000 humidity sensor and a PT100 temperature sensor), as well as power for the fan, auxiliary connections and a USB port are routed via an additional 15 pin feedthrough. Outside the chamber, the sensor and device channels are connected to a Keithley 3706s multimeter fitted with two 120 channel Keithley 3723 multiplexing cards in single-pole mode, the output of which is connected to a Keithley 2400 SMU by a five metre coaxial cable. All of these connections and cables were measured for their resistance, which is compensated for programmatically where needed. Both the multiplexer and SMU are connected to a computer which controls them via a LabVIEW program (*vide infra*), the former via USB, and the latter via GPIB. The +12 V and +5 V DC channels are connected to an ELC AL991s three channel DC power supply. All of the sensors, devices, and the fan are on a common

earth connection, which is connected to both the SMU and the power supply earths. All of the electronic components in the chamber and the cables were supplied by Radiospares France.

The frame of the sample holder was fabricated by the workshop of *le Centre de Recherche Paul Pascal* from aluminium and polyether ether ketone (PEEK). The PEEK was chosen for its high T_g , as other, low T_g polymers were found to be unsuitable for this application in earlier tests. The structure and use of the sample holder are depicted in Figure 3.4.5.

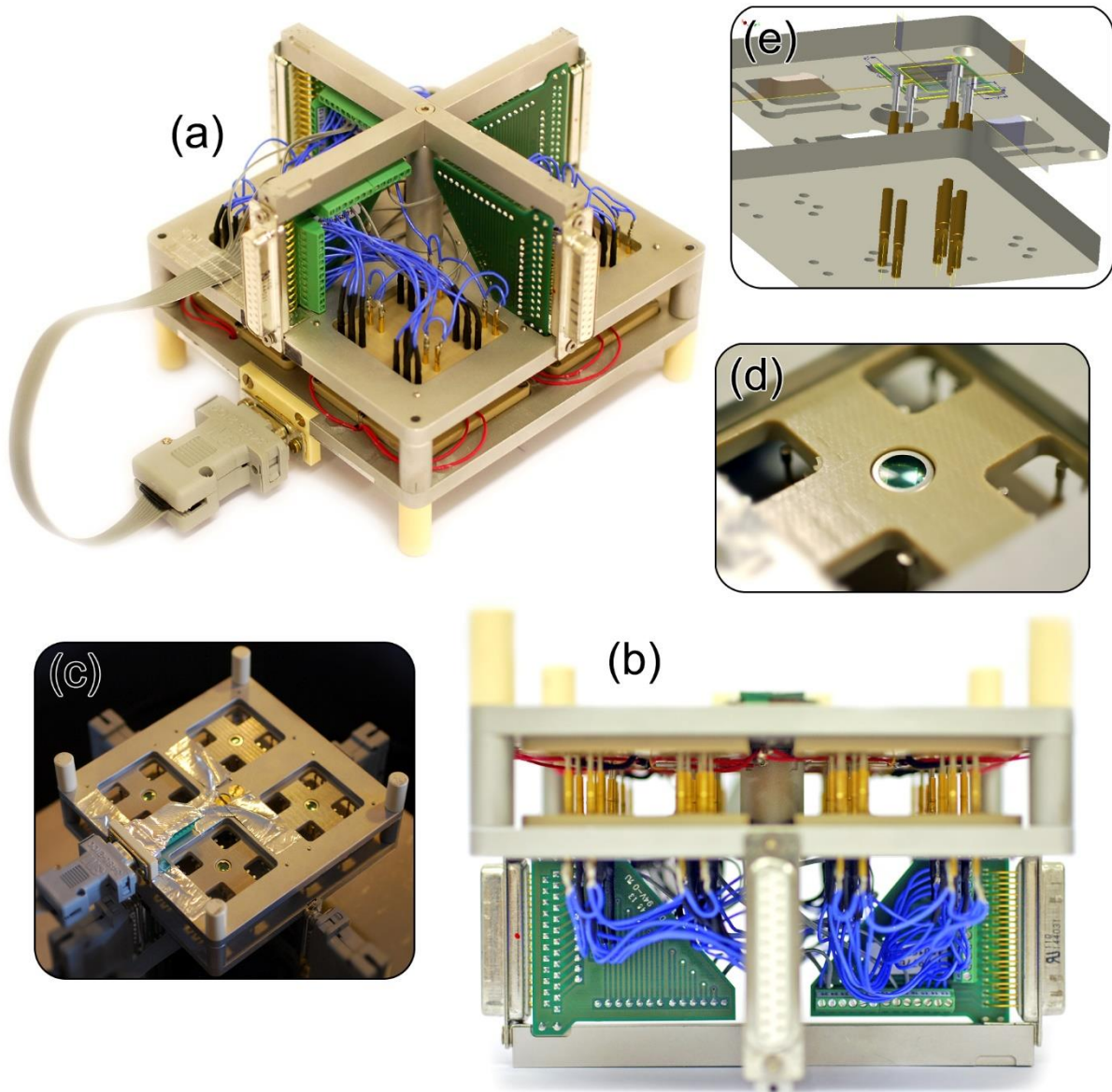


Figure 3.4.5: Depictions of the sample holder. In (a) the sample holder is shown inverted to illustrate the wiring between the power pins and the cable connectors. In (b) the sample holder is shown side-on to show the positions of the power pins and the two halves of the sample holder. In (c) the sample holder is shown mounted in the ageing chamber with all cables connected (but no samples mounted). In (d) the position of one of the four photodetectors is shown. Finally, in (e) a 3D model illustrating the way the power pins make contact with a sample is shown. All photographs were taken by Marcin Kielar.

As shown in Figure 3.4.5(b), the sample holder has two halves. The samples and the sensors are located in the top half, while the wiring and cable connectors are in the bottom half. Loading or unloading samples is done by inverting the holder, and separating the halves. When loaded, the 96

spring-loaded power pins in the holder make electrical contact with all the electrodes on the samples, and act to hold the samples in place during the experiment (Figure 3.4.5(e)). The sensors are connected to the bottom half by a nine wire ribbon cable that can be disconnected to separate the halves. Each of the power pins were individually soldered to wires that are connected to one of four screw connector 25 pin D-sub adaptor cards to interface with the cables (Figure 3.4.5(a + c)). All these components were supplied by Radiospares France.

In addition to the characterisation of up to 64 OPV devices, the sample holder contains four temperature sensors (PT100 RTDs, Radiospares France) which are embedded in the PEEK blocks that hold the samples so as to provide temperature readings that are as close as possible to the true sample temperatures. As shown in Figure 3.4.5(c + d) the sample holder also has four silicon photodetectors to monitor the radiation intensity. The photodetectors are Centronic BPW21 photodiodes (supplied by Radiospares France) which are responsive in the range of 460 nm – 750 nm and have peak responsivity at 560 nm. Due to the limited spectral range of the sensors, their output was calibrated using a Newport 91150V calibrated reference solar cell. The reason for the number of sensors was both for redundancy in the case of malfunction, and also to check for spatial variation in the radiation or temperature (no such variation was observed). The sensors channels were distributed amongst the four 25 wire cables in order to connect to the multiplexer.

3.4.4. Ageing chamber control and data processing applications

It was necessary to develop two separate programs for using the ageing chamber. One is a control program, which carries out the measurements, collects the IV data and calculates the PV parameters. The other is a data analysis program, designed to process the large quantity of data generated by the ageing chamber and display the trends of the PV parameters over the course of the experiment, or the evolution of the IV curves of the devices. Both of these programs were developed using LabVIEW.

Ageing chamber control application

The ageing chamber control application functions as shown in Figure 3.4.6.

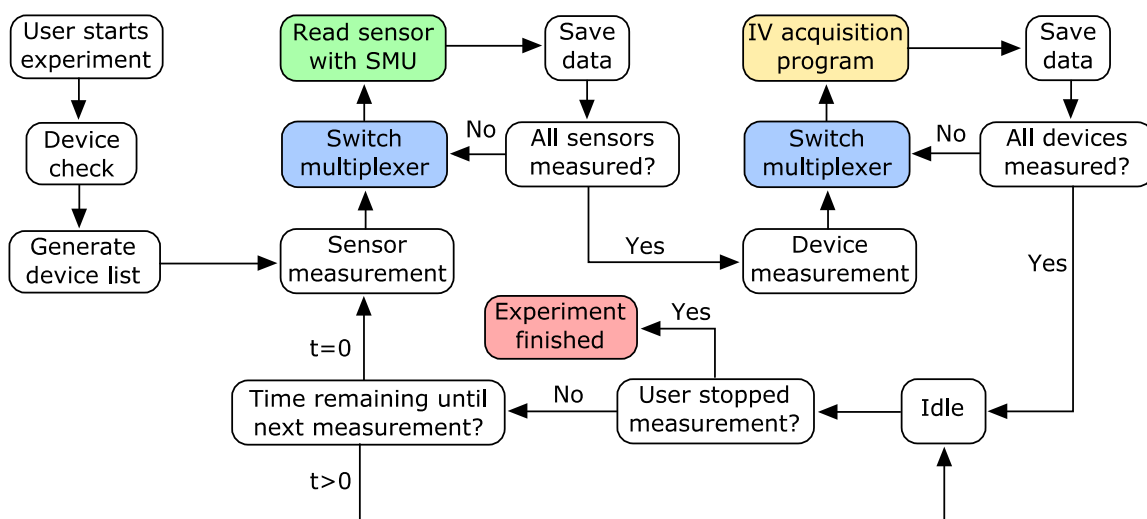


Figure 3.4.6: The procedure followed by the chamber control application to carry out a photodegradation experiment with the ageing chamber.

At the core of the application are the measurement and analysis components of the program that was developed for the thermal ageing experiments in section 3.1.2. These components are run as a subroutine to measure every device, with the results being saved to the hard disk in-between each measurement. The sensors are measured in a similar way, but with a modified command to the SMU as appropriate to the type of sensor. The chamber control application also incorporates a quick device check at the start of the experiment to see how many samples have been loaded into the holder, and to avoid the measurement of defective devices during the experiment. With the maximum number of devices, and measuring 50 data points per IV curve, a measurement cycle takes approximately 10 minutes. When a measurement cycle is complete, the program sits in an idle state until it determines that it is time to start the measurement cycle again for the next time point, or the user stops the experiment. The IV curve and PV parameter data are saved in a customised file format (a “.expt” file) so that they can be analysed by the data processing application.

The user interface for the measurement program (while it is running) displays the chamber status, including average temperature, light intensity, and humidity levels, as well as the operation being performed by the program (idle, measuring, etc.). It also displays both the time elapsed in the experiment, and the time remaining until the next measurement. In addition, the user interface contains a visual representation of the sample holder, displaying the status of every sensor and device in the sample holder. This visual representation uses colour to indicate the degree of degradation a device has experienced, or if it is inactive.

This program was purpose-written for this study, with the assistance of Thibaud Marazano.

Ageing data processing application

A typical photodegradation experiment generates between 10 and 15 million data points (if the measurement period is 20 minutes, as it was in this study), generating data files which are over 100 MB in size. As most commercial data analysis programs are not well equipped to easily handle or manipulate this volume of data, a customised data processing application was written to do this.

At the heart of the data processing application is the .expt file, which stores data in three-dimensional arrays, referred to “data cubes”. Each .expt file has two data cubes, one for the PV parameters and one for the IV curves. In the parameter data cube, the data are indexed by: the type of parameter – FF, J_{sc} , etc. (columns); the device (rows); and the time point (layers). In the IV curve data cube, it is by: dark or light measurement (columns); the device (rows); and the time point (layers). The IV data cube could be considered as a five-dimensional array, as each indexed cell in the data cube contains a sub-array with the voltage and current density data, but as these are plotted as whole units, the additional two dimensions are largely irrelevant to the program function. It should be noted that in photodegradation experiments, no dark measurements were carried out, so this column is always empty. These data files are typically generated automatically by the chamber control application, but they can also be created manually within the data analysis application by loading measurement data from individual time points (such as those in the thermal ageing experiments).

The plotting of the evolution of the PV parameters for an arbitrary group of devices with ageing is easily achieved when starting from a data cube. The program first selects the column that corresponds to the selected parameter, producing a two-dimensional array (time and device). The

program then extracts a subset of the two-dimensional array that only contains the rows corresponding to the selected devices. Finally, the program averages along the rows, finding the average value and standard deviation for the selected PV parameter at each time point. These can then be displayed on a PV parameter vs time plot as data points and error bars. It is also possible to produce normalised parameter plots in this way by normalising the values in the two-dimensional array to the $t=0$ values prior to averaging. Plotting the IV curves from an experiment for a particular device can also easily be achieved by indexing the appropriate row and column, and plotting the IV data for each time point (layer) as an individual series. In these ways, the program is not simultaneously accessing all of the data, which substantially decreases the required computational resources.

Once generated, a plot of (for example) PCE against time for several groups of devices in a photodegradation experiment might only contain a few thousand data points, and so these data can then be exported and used in other graphing applications. This “data sorting” capability was one of the principal ways that the application was used. The other was data visualisation, as the application can display the output of any combination of the devices or the sensors over the entire experiment, both after the experiment has finished, and in real time. Users can save up to 10 customised plots that look at different groupings of samples, or sensors, and each plot can easily be changed to look at a different PV parameter or sensor output using a drop-down menu. This allows for rapid comparison between very large datasets and the finding of correlations which would otherwise be very difficult to find. The application also contains a curve-fitting and degradation analysis tool, which is discussed in more detail in Chapter 5.

Table 3.4.2: The suppliers and details for the different materials used in this study.

Material	Supplier	Details
ITO-coated glass substrates	Visiontek	10 Ω/\square
Acetone	VWR - France	>99%
Technical ethanol	VWR - France	>96%
Isopropanol	Fisher Scientific	>99.9%
Deionised water	-	18 M Ω cm
Degreasing surfactant	Hellma Analytics	Hellmanex III
Zinc(II) acetate dihydrate	Sigma-Aldrich	>99.0%
Ethanolamine	Sigma-Aldrich	>99%
Absolute ethanol	VWR - France	>99.95%
P3HT	Plextronics	Plexcore OS2100, 53 kDa
PC ₆₁ BM	Solaris Chem.	>99%
Nitrogen (gas)	Air Liquide	α -gas
1,2-dichlorobenzene	Sigma-Aldrich	>99%
Chloroform	Sigma-Aldrich	>99%
PC ₇₁ BM	Solaris Chem.	>99%
PCDTBT	St-Jean Photochemicals	M _w =125 kDa, PDI=5.2
MoO ₃ (evaporated)	Neyco	>99.95%
WO ₃ (evaporated)	Neyco	>99.95%
PEDOT:PSS (solution)	Heraeus	Heraeus Clevios
Aluminium	Neyco	>99.95%
Silver	Neyco	>99.95%
Glassy carbon substrates	Oxford	
Large glass substrates	Marienfeld GmbH	
1-Butanol	Sigma-Aldrich	>98%
Chlorobenzene	Merck	>99.0%
Epoxy adhesive	Loctite	E-20NS Loctite epoxy
Synthetic air	Air Liquide	α -gas, 20% O ₂ 80% N ₂

IV

Chapter 4

Thermal ageing mechanisms in OPV solar cells

4.1. Introduction

All ageing mechanisms in OPV can be broadly classed into two categories: intrinsic and extrinsic. Extrinsic degradation arises from stimuli that can be removed without impeding the functioning of the device, such as any mechanisms arising from oxygen or water exposure. While it is important to design devices in such a way as to minimise their impact, other mitigation strategies beyond device design (like encapsulation) can be employed to decrease their impact.

Intrinsic mechanisms, on the other hand, arise from the normal use of the device and can only be mitigated through device design and materials selection. Thermal degradation is one such class of degradation. A highly efficient OPV solar cell might have a power conversion efficiency of 10%,¹¹ meaning that 90% of the incident power on the cell is not converted to electrical power. Once reflection and photoluminescence are taken into account, a significant portion of that power is converted to heat. A polymer film exposed to sunlight can experience temperatures as high as 20°C higher than the ambient air temperature – meaning that in hot climates, OPV device temperatures could be over 60°C.¹⁸⁰

The effects of elevated temperatures on OPV devices have been well studied with respect to the BHJ active layer. As documented in Chapter 2, elevated temperatures can have both beneficial and detrimental effects on cell performance. In order to maximise efficiency, a BHJ must have a morphology with acceptor and donor domain sizes smaller than or near the exciton diffusion length. This design minimises the geminate recombination rate and maximises the chance that diffusing excitons will find a donor/acceptor interface and separate *via* charge transfer.⁸¹ Conversely, domains must be large enough so that the charge carrier mobility in the film is not too low, resulting in increased rates in non-geminate recombination.⁴⁷ Mobility can also be affected by vertical phase separation, which also can be beneficial or detrimental depending on the device geometry and on the interface to which the donor and acceptor species migrate.⁴⁷ Given these considerations, many device fabrication procedures incorporate a short thermal annealing step in order to optimise the BHJ morphology. Longer term exposure to elevated temperatures is, however, detrimental to BHJ morphology, resulting in losses of J_{sc} .⁸⁹

The degree to and the rate at which elevated temperatures cause the BHJ morphology to deteriorate is largely determined by the materials used in the BHJ. With polymer donors, the closer the temperature is to the T_g of the polymer, the easier it is for matter to diffuse through it, resulting in the growth of donor and acceptor domains.³⁰ Consequently, BHJs that incorporate high T_g polymers are much more stable to thermal degradation.^{94,95} Where BHJs incorporate low T_g polymers, it is also possible to stabilise them via cross-linking.²⁷

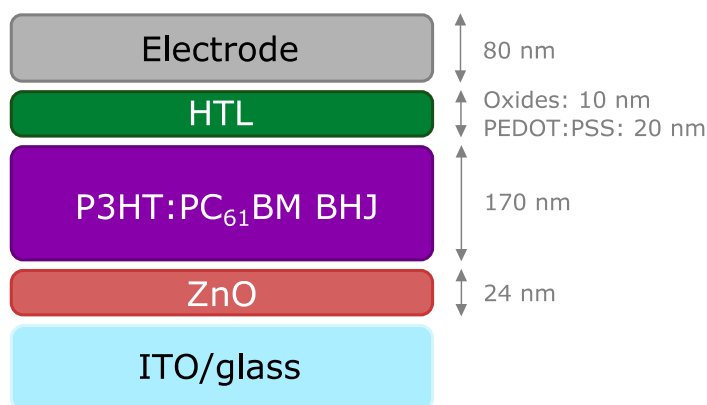
The active layer is not the only part of the device to be affected by thermal degradation. As discussed in section 2.3.5, it has been demonstrated that in inverted devices with silver top electrodes, the silver may be capable of diffusing through the HTL and into the active layer at elevated temperatures.¹²¹ However, this silver diffusion has not been linked to any specific declines in device performance statistics. Another interfacial effect of long term exposure to elevated temperatures occurs when a PEDOT:PSS HTL forms an intermixed layer with the active layer.¹²² This is a broadly beneficial effect as it improves contact between the two layers and raises the adhesion of the HTL and electrode to the active layer.¹²²

The purpose of this series of studies is to examine the interfacial effects in inverted OPV devices of long term exposure to elevated temperatures. In particular, the aim is to understand the role that the use of different materials at the hole extraction interface plays in any observed degradation mechanisms. In order to achieve this, a series of device studies were carried out, initially to gain information on the impact different HTL and electrode materials have on the evolution of cell statistics with thermal ageing, followed by a number a physical characterisation studies to investigate the physical origins of any decline in device performance.

4.2. OPV Device Studies

4.2.1. P3HT Study Outline

The inverted OPV devices were fabricated with the architecture shown in Figure 4.2.1.



Electrode: Aluminium or Silver
 HTL: MoO₃, WO₃, or PEDOT:PSS

Figure 4.2.1: Sample architecture used for thermal degradation device studies.

16 devices for each of the six HTL/electrode combinations were aged at 85°C in the dark under an inert atmosphere (ISOS-D-2)²² for up to 500 hours (see section 3.1.3). A further four devices per HTL/electrode combination were stored at room temperature in the same atmosphere, and measured with the same frequency to act as a control group. For details concerning the device fabrication and the measurement/processing of the IV curves, please see Chapter 3.

4.2.2. Results Overview

The evolution of the devices' PCE with thermal ageing time is shown in Figure 4.2.2, and their initial device parameters are shown in Table 4.2.1.

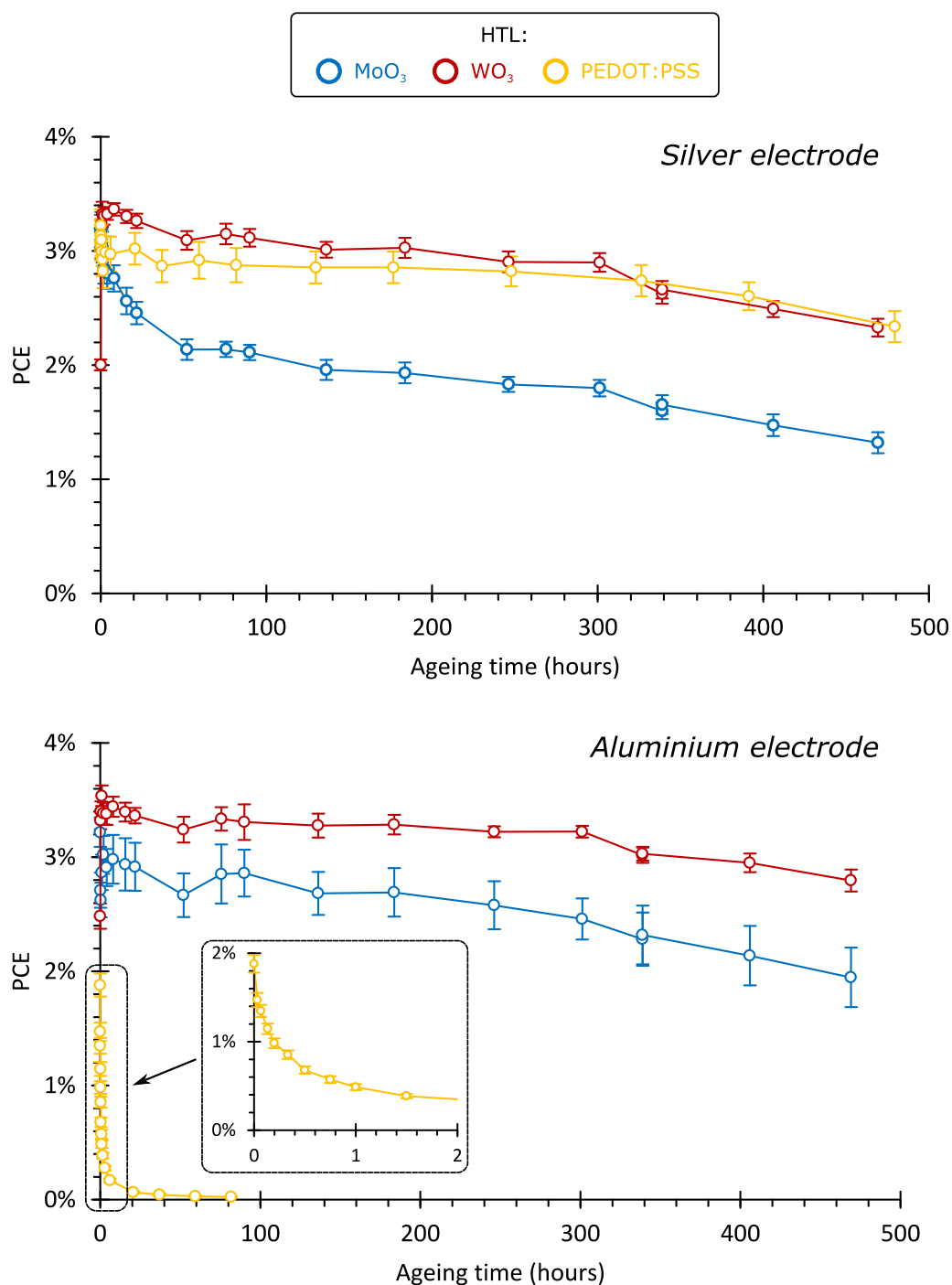


Figure 4.2.2: The evolution of the PCE of inverted OPV devices with thermal ageing in an inert atmosphere in the dark with different HTL and electrode materials. The inset shows the first two hours of ageing of the Al/PEDOT:PSS sample. The error bars represent one standard deviation across 16 devices.

Table 4.2.1: The device parameter values (PCE, J_{sc} , V_{oc} , and FF) for OPV devices fabricated in this study. Both the initial values, and the values after one hour of thermal ageing at 85°C (in the dark, under an inert atmosphere) are shown, with the higher value emphasised. Uncertainties represent one standard deviation across 16 devices.

HTL/Metal		PCE	J_{sc} (mA cm ⁻²)	V_{oc} (mV)	Fill factor
MoO ₃ /Al	Initial	3.21±0.13%	11.77±0.45	0.504±0.006	0.542±0.010
	1 hour	2.87±0.15%	9.79±0.41	0.516±0.008	0.568±0.004
WO ₃ /Al	Initial	2.48±0.11%	10.00±0.37	0.477±0.005	0.521±0.015
	1 hour	3.54±0.09%	10.43±0.33	0.530±0.005	0.641±0.007
PEDOT:PSS/Al	Initial	1.88±0.10%	7.95±0.56	0.538±0.006	0.440±0.009
	1 hour	0.49±0.03%	5.51±0.33	0.527±0.009	0.167±0.004
MoO ₃ /Ag	Initial	3.18±0.14%	11.62±0.41	0.509±0.004	0.536±0.009
	1 hour	3.03±0.14%	9.44±0.38	0.536±0.006	0.599±0.010
WO ₃ /Ag	Initial	2.00±0.05%	9.58±0.14	0.477±0.005	0.438±0.009
	1 hour	3.32±0.11%	10.40±0.37	0.534±0.005	0.598±0.006
PEDOT:PSS/Ag	Initial	3.22±0.14%	9.41±0.50	0.551±0.004	0.622±0.019
	1 hour	3.01±0.07%	8.62±0.52	0.548±0.002	0.621±0.016

Al/PEDOT:PSS Samples

The devices with aluminium electrodes and PEDOT:PSS HTLs exhibited extremely rapid degradation in the first few hours of thermal ageing. The decline in the cell statistics and the changes in the IV curve are shown in Figure 4.2.3.

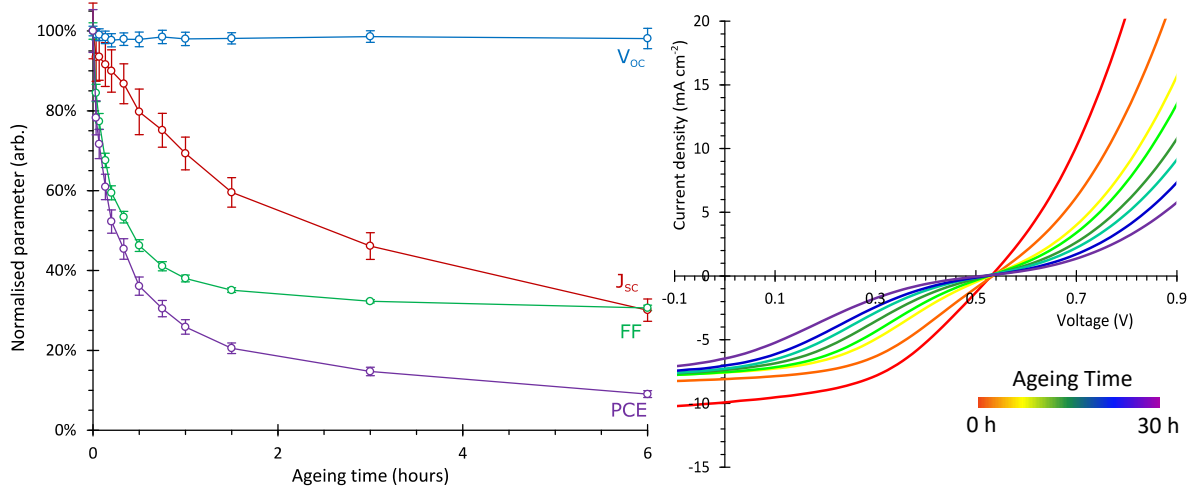


Figure 4.2.3: (left) evolution of the device parameters of Al/PEDOT:PSS inverted devices with thermal ageing and (right) the change in the IV curves of the Al/PEDOT:PSS samples as a function of thermal ageing. The error bars represent one standard deviation across 16 devices, the parameters are normalised to their initial values.

The steep decline in the devices' PCE is initially driven by a substantial loss in FF followed by a decline in J_{sc} . In contrast, the V_{oc} is relatively unaffected. On the IV curve, it is clear that this comes from the formation of an s-shape in the curve at the V_{oc} . This behaviour is consistent with the formation of a homogeneous barrier oxide at one of the interfaces. This behaviour is different from that seen in the catastrophic failure of Ca/Al direct devices, in which failure is caused by two-dimensional growth of an insulating oxide layer at the electron extraction interface.^{131,134} In this case the oxide is formed homogeneously all over the active area. This oxide layer, formed at the hole selective electrode, acts

as a charge extraction barrier. This effect is comparable to including a electron transport material at the hole selecting electrode.^{181,182} At low effective voltage (close to the V_{OC}), the charges cannot be extracted and the space charge that accumulates at the top electrode shields the internal field of the device, lowering fill factor.¹³⁴

As degradation continued in this study, the oxide layer became thicker and thicker giving rise to a stronger potential barrier. The s-shape became more and more pronounced leading, finally, to a complete suppression of photocurrent, which could only be recovered when the device was held at extreme negative bias (~ 3 V) – further evidence of the presence of a charge extraction barrier.¹³⁴ Many examples of this behaviour in the literature deal with direct devices with low work function electrodes,¹³¹ however these devices are almost certainly experiencing barrier formation at the hole extraction interface due to the formation of Al_2O_3 from the aluminium electrode. This can be surmised from the fact that this behaviour was not observed with any other material combination and all devices have the same materials (sol-gel processed ZnO and ITO) at the electron extraction interface.

The origin of this behaviour is most probably a reaction between the acidic PSS in the PEDOT:PSS HTL and the aluminium electrode, potentially aided by residual water in the PEDOT:PSS (which was deposited from an aqueous/alcoholic solution). It is worth noting that the control samples also degraded in a similar fashion, although at a slower rate, so this degradation is not a strictly thermal mechanism. Additionally it is important to note that the degradation mechanism in this case (inverted architecture, thermal ageing, inert atmosphere) originates from the one-dimensional growth of an oxide film across the entire electrode/HTL interface. Conversely, in the degradation studies performed by Züfle *et al.*¹³⁴ and Voroshazi *et al.*¹³³ (direct architecture, shelf lifetime, humid atmosphere) the mechanism is the two-dimensional lateral and vertical growth of an oxide layer from the edges of the device between the electrode and HTL. Simulations suggest that this leads to the formation of two photovoltaic devices in parallel: one with a fresh aluminium electrode and one with an Al_2O_3/Al electrode.¹³⁴ In the two-dimensional case, the effect on the IV curves is a continuous decrease of the J_{SC} with unchanged FF and V_{OC} , which is not observed with the samples in this study. This effect is similar to a reduction of the effective active area of the solar cell. This degradation was not examined in more detail, as it is likely that the only amelioration strategy envisagable is to never use aluminium in direct contact with PEDOT:PSS, although it may be possible to decrease the corrosiveness of the PEDOT:PSS by altering its processing conditions or replacing the PSS component with a less acidic alternative.¹⁴¹ In contrast, silver electrodes show no such issues when used with PEDOT:PSS in the inverted devices in this study, suggesting that either the silver does not react with PEDOT:PSS or (more likely) that the reaction products do not form a charge extraction barrier.^{183,184}

Short-term annealing effects

In addition to exhibiting long-term degradation due to thermal effects (Figure 4.2.2), some samples show a modest improvement in efficiency after being heated for a short time (Figure 4.2.4). The precise values for the device parameters are shown in Table 4.2.1.

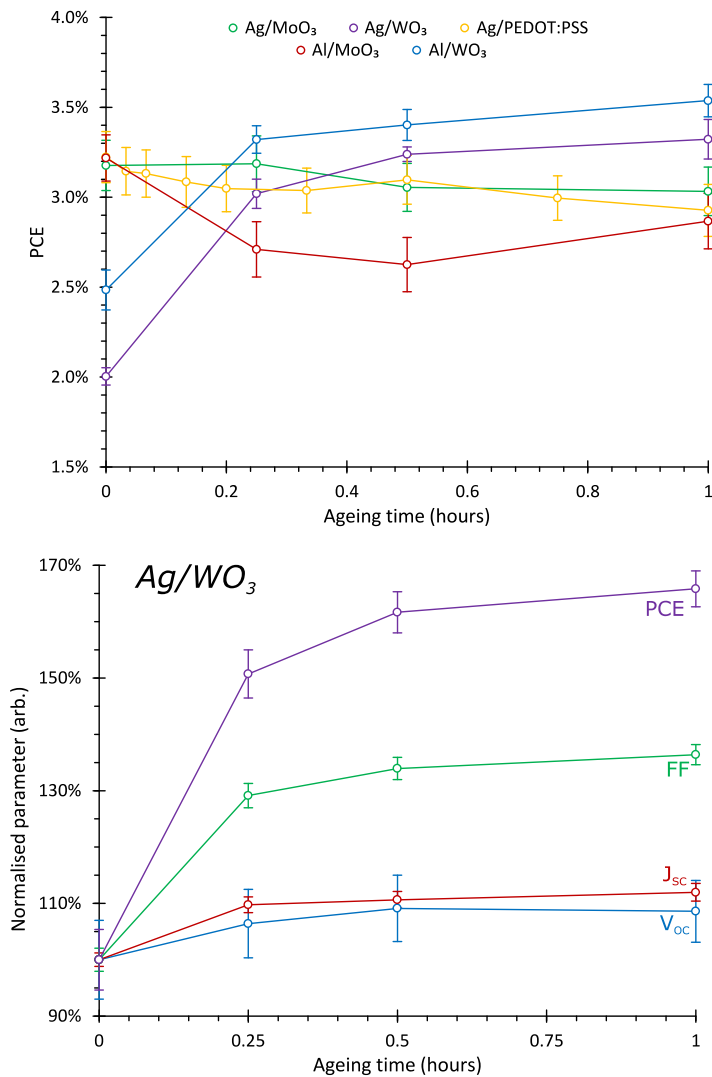


Figure 4.2.4: (top) evolution of the PCE of the samples in the first hour of heating (the Al/PEDOT:PSS sample is omitted) and (bottom) the normalised device parameters of the Ag/WO₃ samples over the same period. Note that the error bars represent one standard deviation across 16 devices.

It is not uncommon to see an improvement in device performance with thermal annealing. This is typically a consequence of morphology optimisation.³² As discussed in Chapter 2, thermal annealing can grow donor/acceptor domains in the BHJ to enhance mobility, and as long as the domains do not grow larger than the exciton diffusion length, a significant improvement in J_{SC} can be observed. This is not the case in this study, however, which is evident for three reasons:

- the samples have already undergone a morphology optimisation step (solvent annealing);
- if this were an morphology effect, we would expect to see it in all samples, but we only see it in the samples with WO₃ HTLs (Figure 4.2.4(top)); and
- the improvement in efficiency is FF-driven, while J_{SC} is only slightly affected (Figure 4.2.4(bottom)).

The initial IV curves of the WO₃ samples do not show an obvious s-shape, suggesting that there is not a significant barrier to charge extraction prior to annealing. The fact that it only occurs with WO₃ samples and that it occurs with both electrode materials suggests that it is either related to the structure of the WO₃ layer, or the BHJ/WO₃ interface. It is possible that it results from improved

electrical contact between the two layers, interfacial doping, or improved charge transport through the HTL; however, this phenomenon was not investigated further.

Behaviour of the control samples

Most of the control samples (which underwent no thermal treatment) exhibited little or no evidence of degradation throughout the study, as desired. However, the samples containing MoO₃ active layers did exhibit some degradation when measured repeatedly (Figure 4.2.5).

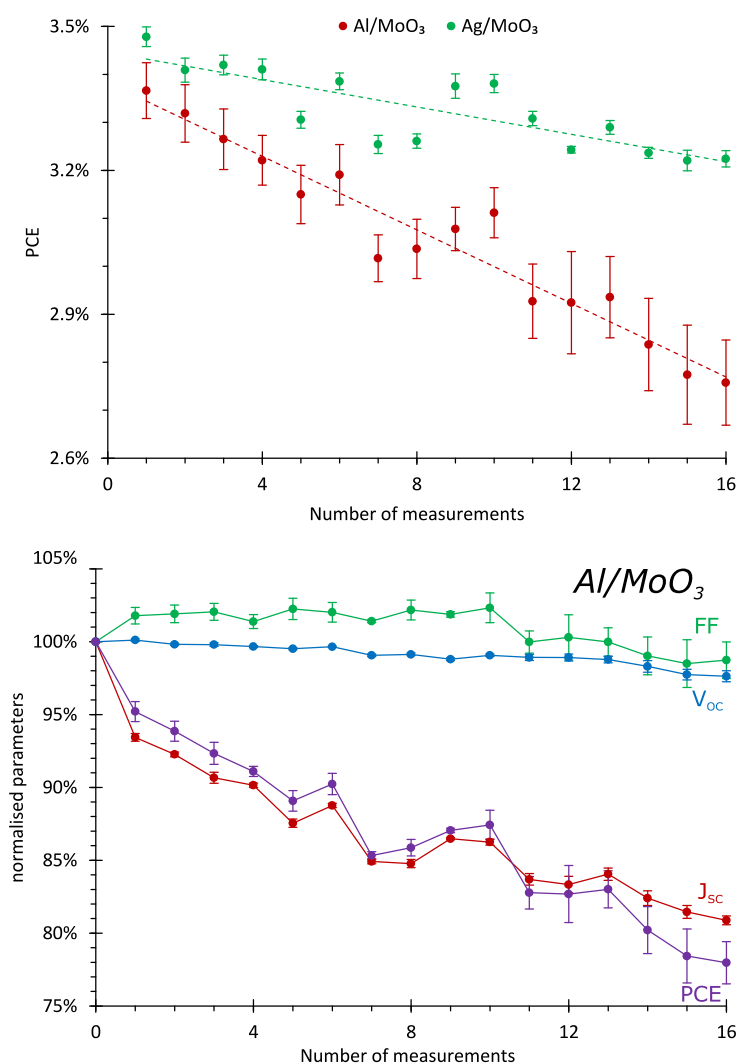


Figure 4.2.5: (top) The PCE of the control samples containing MoO₃ HTLs as a function of the number of times the devices are measured; and (bottom) the normalised device parameters of the Al/MoO₃ control devices as a function of the number of times the devices were measured. The error bars represent one standard deviation across four devices (if not visible it is because they are obscured by the data point) and the normalised parameters are normalised to their initial values. The trend lines shown in the PCE plot are indicative only.

As the control samples were not exposed to any other degradation stimuli and were very stable when stored for months under an inert atmosphere in the dark, the observed degradation must be a result of accumulated light exposure from IV measurements. Despite being J_{sc} -driven, this is not simple photo-degradation of the BHJ active layer (as was discussed in Chapter 2) since it is only observed in devices containing MoO₃ HTLs and is more severe when paired with an aluminium electrode. The exact origin of this degradation is unclear. Although it does mimic some aspects of

photodegradation detailed in Chapter 5, it is far more rapid considering that the Al/MoO₃ devices lose 20% of their efficiency in only approximately 20 minutes total exposure to an AM1.5G spectrum.

While the exact origins of this degradation are unclear, it should be taken into account in the consideration of the degradation of the thermally aged samples as, through measurement, they too would have been exposed to the same photo-degradation stimuli as these control samples.

Long-term thermal degradation trends

With the exception of the Al/PEDOT:PSS samples (*vide supra*), all the devices exhibit a gradual loss of efficiency with thermal ageing. Most devices degrade relatively slowly over the course of the 500 hours. This longer-term degradation is largely J_{SC} driven and will be discussed more fully in section 4.2.3.

The devices with silver electrodes and MoO₃ HTLs show the same long-term behaviour as the other samples, but in the short term they degrade much faster than the other samples (Figure 4.2.2). This degradation, unlike the gradual degradation observed over the full 500 hours of the experiment, is largely driven by V_{OC} and FF . This degradation will be discussed in section 4.2.4.

It should be noted that the discontinuity after 340 hours is due to a pause in the experiment during which the samples were stored for a month in the dark under an inert atmosphere. No significant changes in the devices were observed during this time.

4.2.3. J_{SC} -driven thermal degradation

All the samples showed gradual degradation over time with thermal ageing. This was mostly driven by declines in the devices' J_{SC} , as shown in Figure 4.2.6.

The example given in Figure 4.2.6 is that of the Al/MoO₃ devices. As is evident from the evolution of the IV curve, the devices exhibit a drop in J_{SC} . It should be noted that the observed drop in J_{SC} and PCE exceed that of the control devices discussed in section 4.2.2, indicating that this degradation goes beyond the effects of measurement and is a genuine result of thermal degradation. When compared to the other device parameters, it becomes evident that this is driving long term degradation post-300 hours of thermal ageing. Although the results from Al/MoO₃ have been highlighted here, this behaviour was seen with all material combinations (Figure 4.2.7) with the exception of Al/PEDOT:PSS, as these samples did not survive long enough (see section 4.2.2). The universal presence of this J_{SC} decline post-300 hours suggests that it must come from a common structural element to all the different device designs – either the active layer or the electron extraction interface. If this were caused by the development of a charge extraction barrier at the bottom interface, then a steep decline in FF would be expected,¹³⁴ as was observed during the degradation of the Al/PEDOT:PSS samples. It is therefore more likely that the J_{SC} loss is caused by a change in the BHJ. This was proven when the experiment was repeated with a different active layer and the J_{SC} loss was no longer observed (see section 4.2.5).

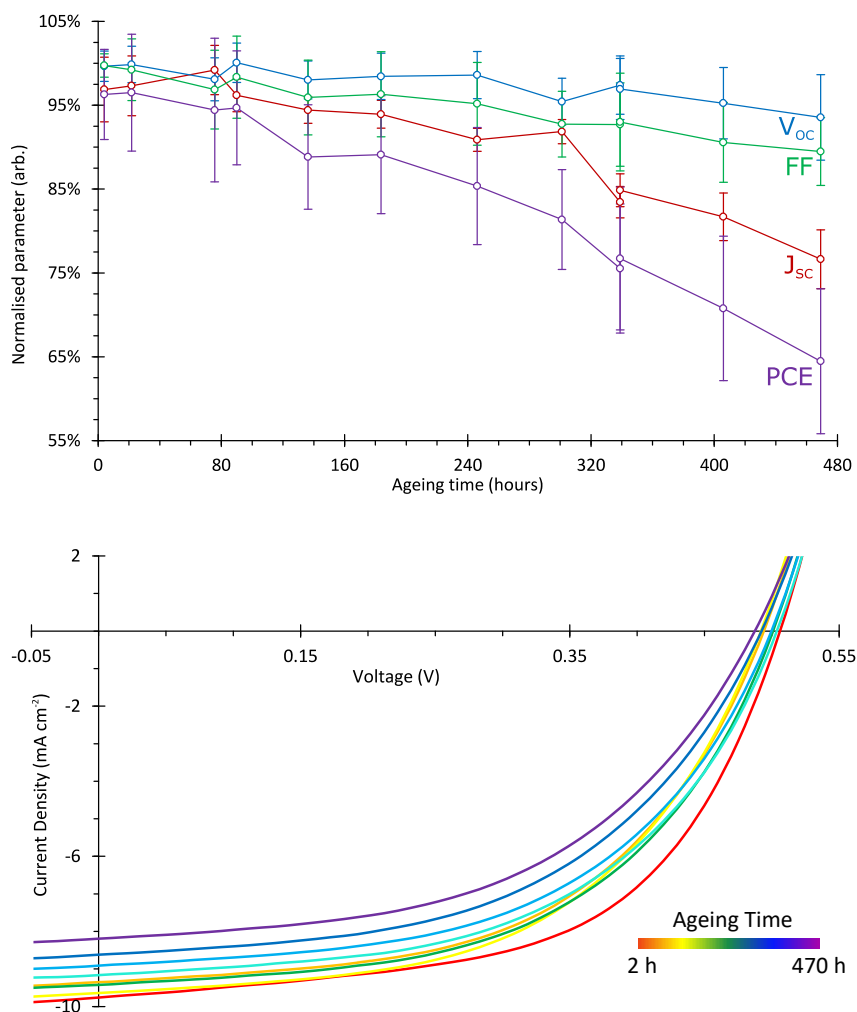


Figure 4.2.6: (top) the normalised device parameters of inverted Al/MoO₃ OPV devices as they are thermally aged; and (bottom) changes in the IV curve of an Al/MoO₃ inverted OPV device with thermal ageing. The uncertainties represent one standard deviation across 16 devices and the parameters are normalised to their values after two hours of thermal ageing.

The likely origin of the J_{SC} loss is thermally-induced changes in the BHJ morphology. As was discussed in Chapter 2, BHJ solar cells can be prone to thermally-induced phase separation. This can result in both the growth of donor and acceptor domains,⁴¹ and vertical phase separation, leading to the accumulation of donor and acceptor species at opposite interfaces.⁸⁷ Both these phenomena have been observed in P3HT BHJ active layers.^{85,87} The growth of donor and acceptor domains can lead to expansion beyond the exciton diffusion length; this decreases the probability that photo-generated excitons will be able to migrate to a donor/acceptor interface and separate and thereby increases the geminate recombination rate and lowers J_{SC} .⁸⁹ If vertical phase separation is unfavourable to the device geometry (section 2.3.4), this would lower the charge carrier mobility in the BHJ, which increases the rate of bimolecular recombination as charges are cleared out of the device more slowly (and also lowers J_{SC}).¹⁸² If vertical phase segregation were the main driving force in the decline of J_{SC} , it is likely that such an effect would be asymmetric with respect to electrons and holes (i.e. mobility for one would decline more than the other). This would result in a build-up of space charge from the more mobile charge carrier, shielding the internal field of the device and significantly decreasing the

fill factor.^{47,101} As a significant decrease in fill factor is not observed, it is more probable that the observed J_{SC} loss is due to domain growth and the resulting increased recombination.

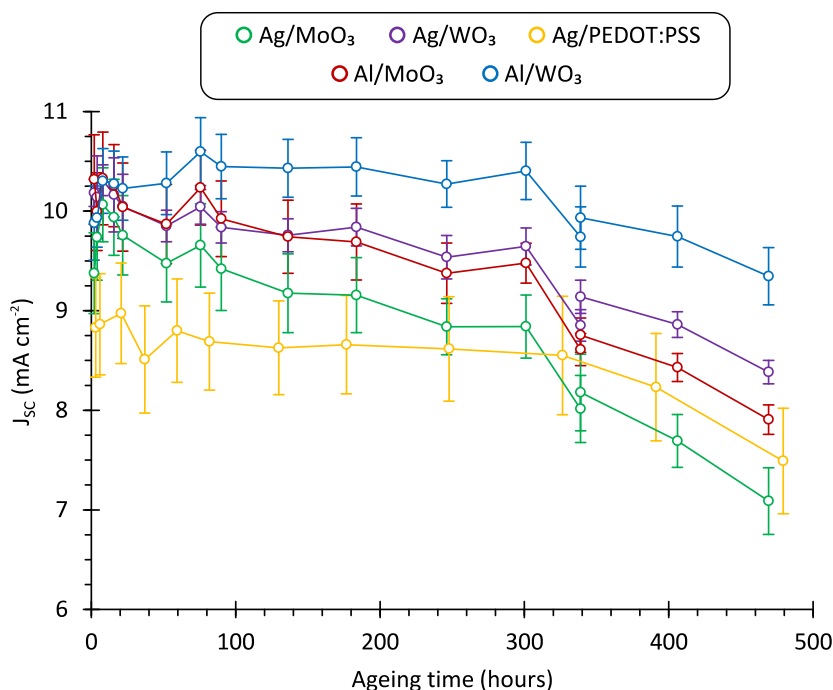


Figure 4.2.7: Evolution of the J_{sc} values for inverted OPV devices using different material combinations for the HTL and hole extraction electrode. The uncertainties represent one standard deviation across 16 devices.

BHJ phase separation is a common problem in low- T_g polymer-based OPV devices.⁸⁹ As operating temperatures often can be near or even above the T_g of the polymer, domain growth can easily occur. As discussed in Chapter 2, this problem can be solved via two strategies:

- replacing low T_g polymers like P3HT in the BHJ with higher T_g alternatives; and
- crosslinking the BHJ to freeze the structure in place and prevent mass transport.

Depending on the system in use, the former strategy may require the use of a less efficient polymer and thus may not be suitable. The latter strategy can be challenging if crosslinking moieties are to be incorporated into the structure of the donor or acceptor; however, the use of crosslinking additives renders this unnecessary.²⁷ The use of crosslinking additives to thermally stabilise an active layer has been successfully demonstrated in various donor:acceptor BHJ active layers.⁸⁵

4.2.4. V_{OC} and FF -driven degradation

While all of the samples showed J_{SC} -driven degradation after 300 hours of ageing and were generally fairly similar in their thermal degradation behaviour, the devices containing MoO₃ HTLs and silver-top electrodes exhibited very different behaviour in the first 100 hours of ageing (Figure 4.2.2). As shown in Figure 4.2.8, this arises from a loss of V_{OC} and FF .

Unlike the J_{SC} -driven degradation discussed in section 4.2.3, this V_{OC}/FF -driven degradation is highly material selective, occurring only with the combination of silver and MoO₃. If either the electrode or HTL are changed, it is not observed (Figure 4.2.9). This is clear evidence that, unlike the J_{SC} -driven degradation, the V_{OC}/FF -driven degradation is an interfacial phenomenon.

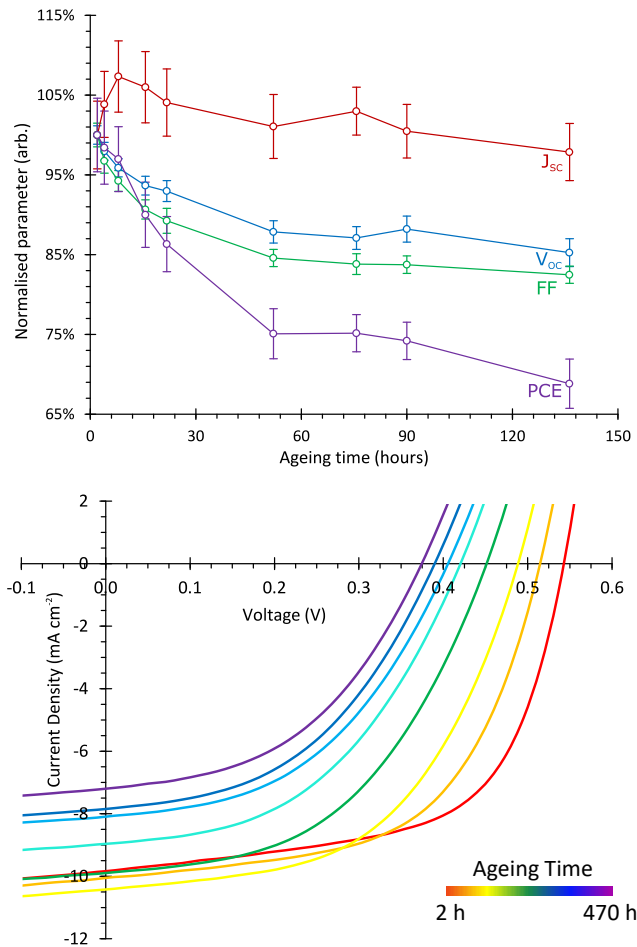


Figure 4.2.8: (top) the normalised device parameters of inverted Ag/MoO₃ OPV devices as they are thermally aged; and (bottom) changes in the IV curve of an Ag/MoO₃ inverted OPV device with thermal ageing. The uncertainties represent one standard deviation across 16 devices and the parameters are normalised to their values after two hours of thermal ageing.

The high degree of material selectivity and the interfacial nature of this degradation greatly limits the number of possible mechanistic origins that could explain it. Moreover, any proposed mechanism must account for the dependence on both the HTL material and the electrode material. For instance, if it were proposed that the origin of the V_{oc} decay was doping of the active layer by the HTL material, this model would only explain the selectivity for the HTL material and not the electrode; the same is true if one proposes degradation of the electrode as the basis for the phenomenon.

There are several possible physical origins of this behaviour:

- the diffusion of silver through the HTL into the active layer. This has been demonstrated to take place during the thermal ageing of OPV devices previously.¹²¹ Any such diffusion would vary greatly between electrodes and HTL materials as the HTL could act as a barrier to diffusion;
- the doping of the HTL by the silver electrode, which would cause changes in the V_{oc} by modifying the MoO₃ Fermi level. This too has been demonstrated to occur in the ageing of OPV devices previously;¹⁶⁰
- dewetting/delamination of the electrode. This would explain the material selectivity as the interfacial adhesion between the different HTL and electrode materials would vary significantly between material combinations; and delamination has been observed previously in OPV

ageing.¹⁴⁷ However, this would be unlikely to result in a loss of V_{OC} , and would be more likely to result in a decline in J_{SC} as the effective area of the device decreased.

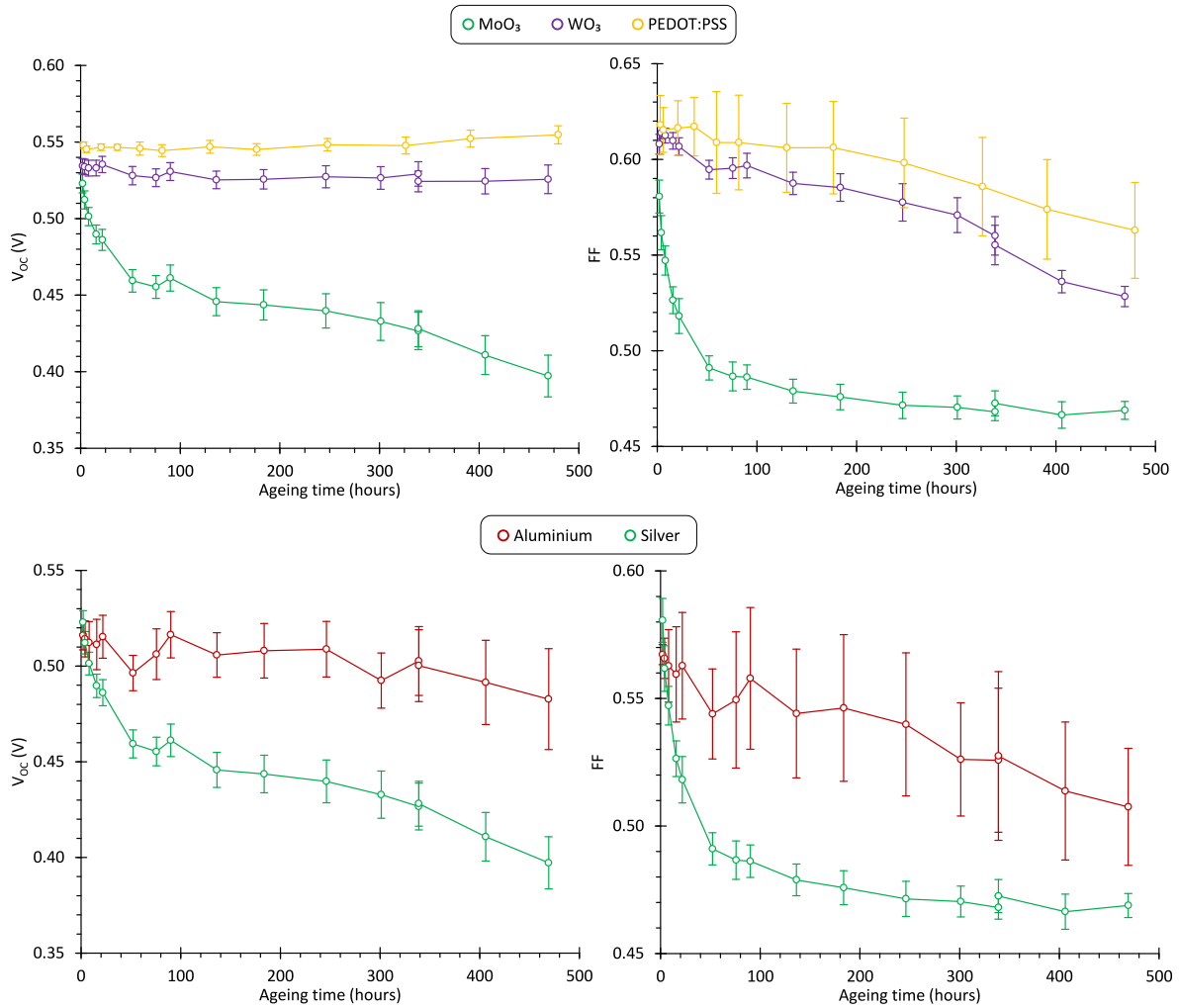


Figure 4.2.9: The evolution of the V_{OC} and FF of inverted OPV devices when thermally aged with (top) a silver electrode and various HTL materials and (bottom) a MoO₃ HTL and various electrode materials. The uncertainties represent one standard deviation across 16 devices.

Of these three, silver diffusion explains the observed degradation trends the best. V_{OC} loss in OPV can be related either to a decrease of the charge carrier density (with unchanged density of states) due to an increased trap-mediated recombination rate or to a broadening of the density of states (with unchanged carrier density).^{119,158,185} Both phenomena would result in a decrease of the quasi-Fermi levels splitting and subsequently in a loss of V_{OC} . FF loss, on the other hand, is frequently observed as a result of screening effect, whereby the build-up of space charge screens the internal field of the device.¹³⁴

The presence of contaminants in the BHJ near either electrode can give rise to the formation of trap levels in the band gap.^{47,123} These charge traps would have the effect of increasing the recombination rate via trap-assisted recombination, in which one charge carrier is held in the trap level until it recombines by collision with the opposite charge carrier, decreasing the V_{OC} , and furthermore giving rise to space charge formation, decreasing FF .^{115,159,186} It is therefore possible

that the diffusion of metallic elements into the BHJ could lead to V_{oc} and FF loss via charge trap formation.

While studies of OPV device degradation through IV characterisation can reveal much, physical characterisation was required to truly understand the origins of this mechanism; this is detailed later in this chapter.

4.2.5. Thermal degradation of PCDTBT:PC₇₁BM devices

A further thermal ageing study was carried out using PCDTBT:PC₇₁BM active layers in the geometry shown in Figure 4.2.10.

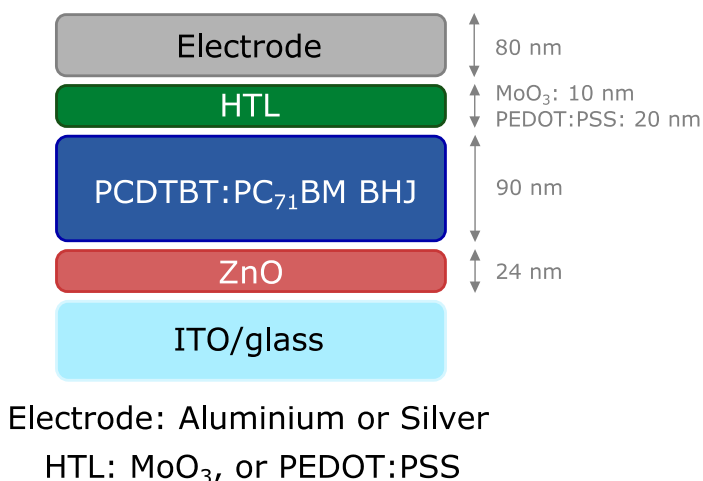


Figure 4.2.10: Sample architecture used for the PCDTBT:PC₇₁BM thermal degradation device study.

In this study, silver or aluminium were used as electrode materials and MoO₃ or PEDOT:PSS were used as HTL materials. WO₃ was not used, as device studies carried out by colleagues in the Organic Electronics Group indicated that it was incompatible with PCDTBT and produced very low efficiency devices. The combination of aluminium and PEDOT:PSS was also not investigated, following the results of the P3HT study detailed in section 4.2.2. The initial device statistics are shown in Table 4.2.2 and the evolution of the device efficiency over time is shown in Figure 4.2.11.

Table 4.2.2: Initial device statistics for the PCDTBT:PC₇₁BM devices. Uncertainties represent one standard deviation across 12 devices.

HTL/Metal	PCE	J_{sc} (mA cm ⁻²)	V_{oc} (mV)	Fill factor
MoO ₃ /Al	5.16±0.13%	10.34±0.14	0.889±0.005	0.562±0.009
MoO ₃ /Ag	5.02±0.09%	9.70±0.17	0.890±0.004	0.582±0.005
PEDOT:PSS/Ag	2.99±0.17%	7.95±0.53	0.803±0.007	0.469±0.008

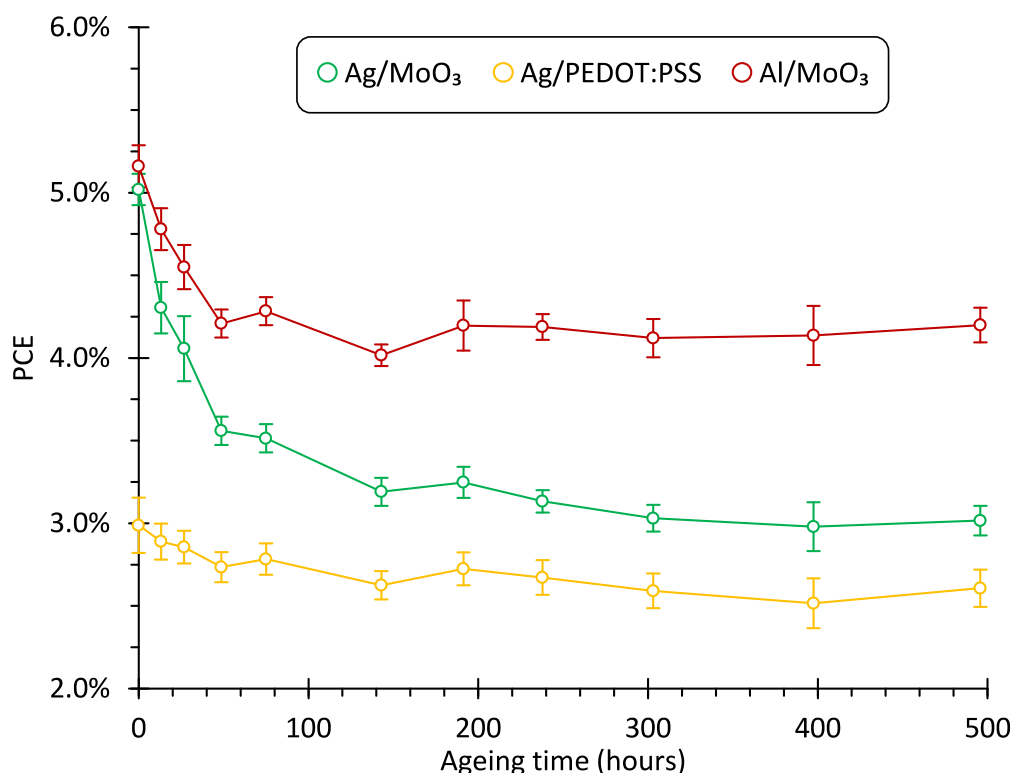


Figure 4.2.11: Evolution of the PCE of the PCDTBT:PC₇₁BM devices with thermal ageing in the dark under an inert atmosphere. The uncertainties represent one standard deviation across 12 devices.

The devices with MoO₃ HTLs show an initial rapid decline in efficiency (Figure 4.2.11) that stabilises quickly and is followed by little to no degradation. The devices with PEDOT:PSS HTLs show no signs of degradation when compared to control samples. This long-term stability is in stark contrast to the P3HT:PC₆₁BM devices, which all showed significant J_{SC} loss after 300 hours of ageing. As shown in Figure 4.2.12, the J_{SC} of the PCDTBT:PC₇₁BM devices is stable long-term, following an initial, rapid decline in the MoO₃-containing samples. This initial J_{SC} decline is of a similar magnitude to the one observed during the very early stages of the P3HT experiment (although over a much longer timescale), in which MoO₃-containing OPV with P3HT:PC₆₁BM active layers exhibited a 30% drop in J_{SC} in the first 15 minutes of ageing (which subsequently experienced a partial recovery). As this is specific to MoO₃-containing samples, and appears in samples with different active layers but with altered timescales, it is reasonable to conclude that this arises due to a thermally-activated interaction between the MoO₃ and the active layer.

The principal difference between the two polymers in terms of their thermal properties is the T_g . PCDTBT has an exceptionally high T_g of 130°C,⁹⁴ meaning that mass transport is much more difficult through BHJs that incorporate PCDTBT than through those that incorporate P3HT.⁹³ This in turn means that the morphology is relatively fixed at 85°C so that there is little possibility for the donor and acceptor domains to grow beyond the exciton diffusion length, which has the effect of increasing geminate recombination and decreasing J_{SC} . This may also explain the difference in the initial J_{SC} loss with MoO₃ HTLs between the two active layer materials, as if the mechanism responsible involves any mass transport into the active layer, this would occur much more slowly in a high- T_g polymer.

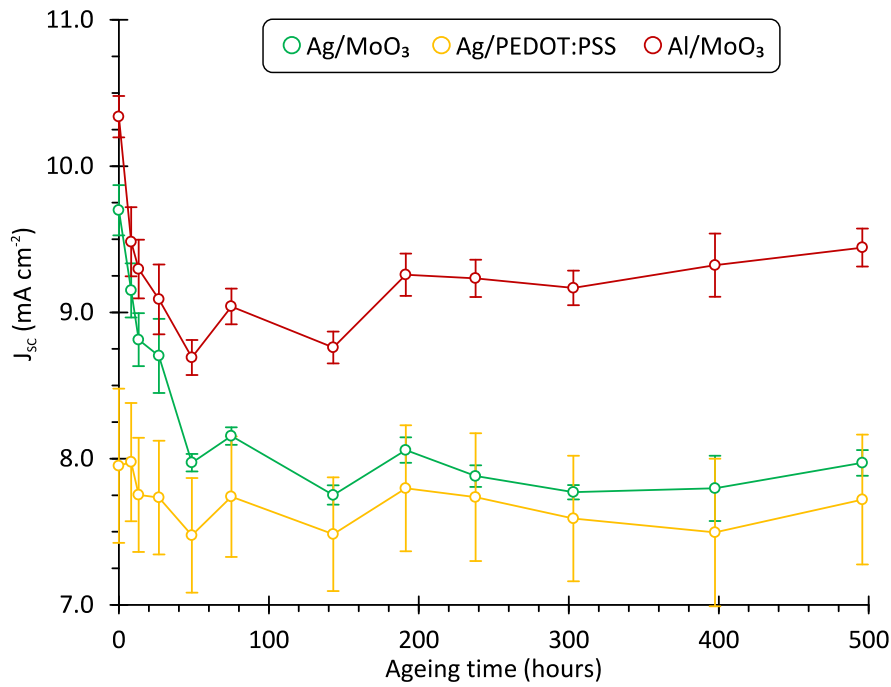


Figure 4.2.12: Evolution of the J_{sc} of the PCDTBT:PC₇₁BM devices with thermal ageing in the dark under an inert atmosphere. The uncertainties represent one standard deviation across 12 devices.

Whether the V_{oc} / FF degradation mechanism observed in MoO₃/Ag devices in the P3HT experiment is still present in the PCDTBT samples is less clear. The evolution of the V_{oc} and FF of the Ag/MoO₃ and Al/MoO₃ PCDTBT samples is shown in Figure 4.2.13.

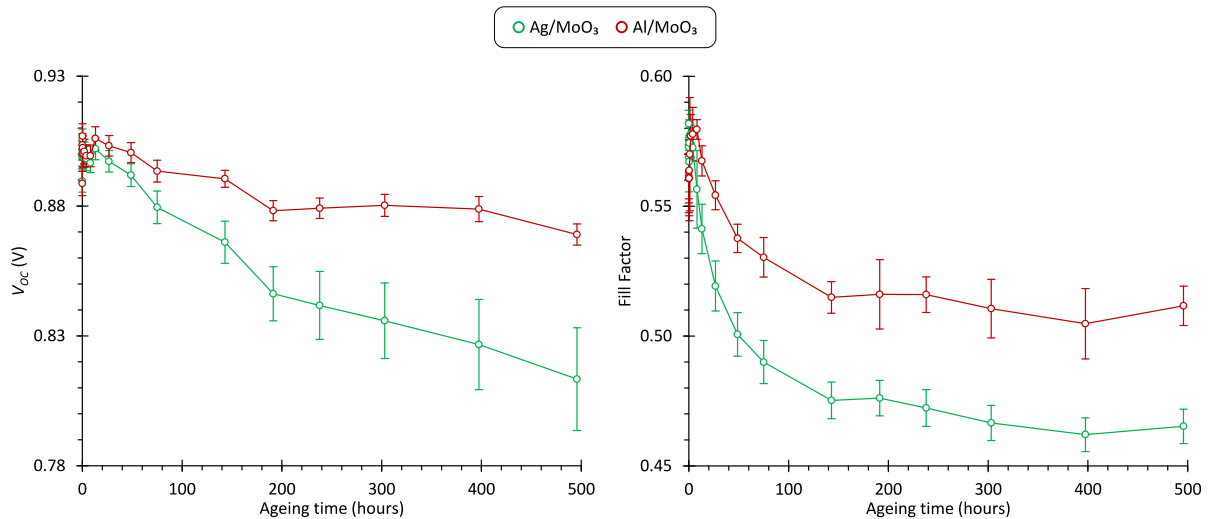


Figure 4.2.13: Evolution of the V_{oc} (left), and FF (right) of the Ag/MoO₃ and Al/MoO₃ PCDTBT:PC₇₁BM devices with thermal ageing in the dark under an inert atmosphere. The uncertainties represent one standard deviation across 12 devices.

The FF loss in the Ag/MoO₃ samples with the PCDTBT:PC₇₁BM BHJ is very similar to the trend observed with their P3HT counterparts (c.f. Figure 4.2.8), in which a 15% to 20% reduction in the FF is observed in the first 150 hours of thermal ageing. On the other hand, the V_{oc} loss in the PCDTBT samples occurs over a much longer timescale, only declining by 10% after 500 hours of ageing, compared with an approximately 20% V_{oc} loss with the ageing of the P3HT samples. This difference in timescale is more pronounced when one considers that the majority of that V_{oc} loss in the P3HT

samples occurs in the first 200 hours of ageing with an exponential-like trend. It is possible that the same trend is exhibited in the Ag/MoO₃ samples with the PCDTBT:PC₇₁BM active layer, and would be evident if the experiment had been allowed to continue and the V_{oc} to decline further.

This difference in the kinetics of V_{oc} loss between the two experiments can be best explained by the difference in T_g values for the two polymers, much like the observed difference in J_{sc} behaviour (*vide supra*). If the origin of this degradation mechanism were reliant on mass transport in the active layer, for instance the diffusion of metallic species into the active layer, then some differences in timescale would be expected due to the higher T_g of PCDTBT. As in the case of P3HT:PC₆₁BM active layer, by changing the top electrode from Ag to Al, the V_{oc} loss can almost be entirely suppressed, only 3-4% drop was observed after 500h of ageing in the Al/MoO₃ samples. This suggests that the mechanism behind the V_{oc} loss is the same whatever the active layer material is and that it can be removed by modification of the top electrode.

Conversely, the trends in FF in the Ag/MoO₃ samples are very similar between the two experiments, suggesting that the mechanism governing it is not reliant on mass transport in the active layer. However, there is an indication of similar FF behaviour in the Al/MoO₃ samples, so it is possible that some of the FF loss originates from a different mechanism than the one identified in the P3HT:PC₆₀BM samples as no significant FF loss was observed in the Al/MoO₃ samples in the early stages of the P3HT experiment.

4.3. RBS and AFM Studies

4.3.1. Overview of the studies

Following the results of the device studies detailed in section 4.2, further research was needed to understand the physical origins of the observed thermal degradation. In particular, the V_{oc}/FF -driven degradation observed in inverted OPV devices with MoO₃ HTLs and silver electrodes was shown to be an interfacial mechanism; however, on the basis of the IV studies, it was only possible to speculate as to why this degradation was observed.

The physical characterisation of the devices was structured in a similar fashion to the IV characterisation. The samples were fabricated using either WO₃ or MoO₃ HTLs, and either silver or aluminium electrodes. Where the studies differed was in the structures of the devices used. In addition to the inverted OPV structure (only used for AFM, *vide infra*), a simplified structure was used as a way of examining an isolated interface (Figure 4.3.1). The simplified structure has no active layer, ETL, or bottom electrode, which means any degradation not associated with the hole extraction interface is not examined and is better suited to RBS (*vide infra*).

Some alteration to the ageing conditions was also carried out. In addition to the samples that were aged at 85°C in the dark, under an inert atmosphere, for 570 hours, a series of samples was aged under accelerated conditions at 150°C for 90 hours, in the dark, under an inert atmosphere, to ensure that any degradation processes happening on a longer timescale than 500 hours would be observed.

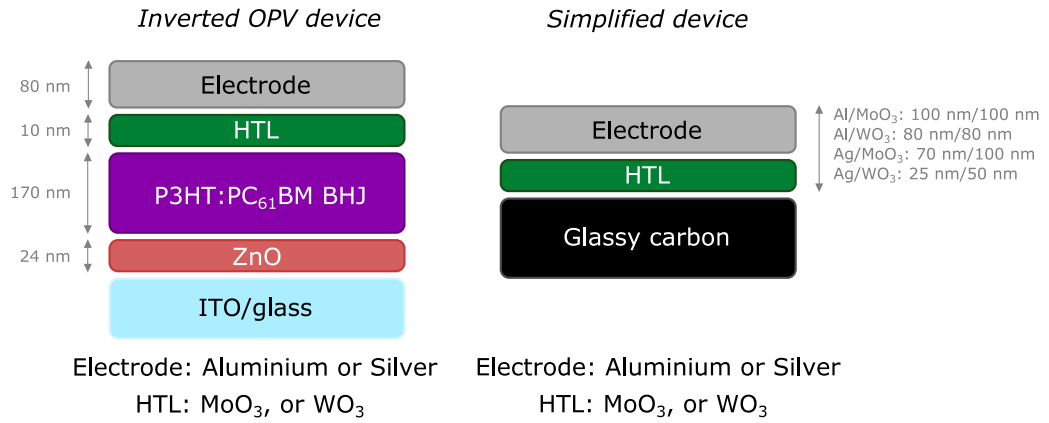


Figure 4.3.1: The sample structures used for the physical characterisation studies.

4.3.2. Rutherford backscattering spectrometry analysis

Background to RBS

RBS is a nuclear characterisation technique which can give information about the elemental profile of thin film samples. The technique evolved from the experiments of the New Zealand physicist Lord Ernest Rutherford and his students, Sir Ernest Marsden and Dr Hans Geiger. In their experiments they examined the scattering of alpha particles by thin metal foils, which led to the discovery of the atomic nucleus.^{187,188} They found that the scattering of the beam strongly depended upon the thickness of the sample and the atomic mass of the material in the sample,¹⁸⁸ leading to the development of the modern analytical technique.

The measurement of a sample is carried out in a vacuum chamber with a configuration similar to the one shown in Figure 4.3.2. The majority of the incident beam passes through the sample with little or no interaction.^{187,189} A small percentage of the particles scatter off nuclei in the sample being tested due to the strong coulombic interaction between the positively charged beam particles and the nuclei of the test sample.¹⁸⁷ The differential cross-section (the likelihood of an elastic “collision” between a beam particle and sample nucleus) can be derived from Coulomb’s law as:^{187,189}

$$\frac{d\sigma}{d\Omega} = \left[\frac{Z_1 Z_2 e^2}{4E \sin^2 \frac{\theta}{2}} \right]^2 \quad 4.3.1$$

in which $\frac{d\sigma}{d\Omega}$ is the differential scattering cross-section, Z_1 and Z_2 are the beam particle and sample nucleus atomic numbers, respectively, e is the elementary charge, E is the beam particle energy before scattering, and θ is the scattering angle (Figure 4.3.2).¹⁸⁹ It should be noted that this formula is only valid in the limiting case that the mass of the beam particle is much less than the mass of the sample nucleus; however, the trends it implies also hold true in more general treatments.¹⁸⁹ In particular, the scattering cross-section is higher for larger atomic numbers. For a more detailed discussion of the theoretical framework behind RBS, the reader is referred to Chu, Mayer, and Nicolet’s book *Backscattering Spectrometry* (Academic Press, 1978).¹⁸⁹

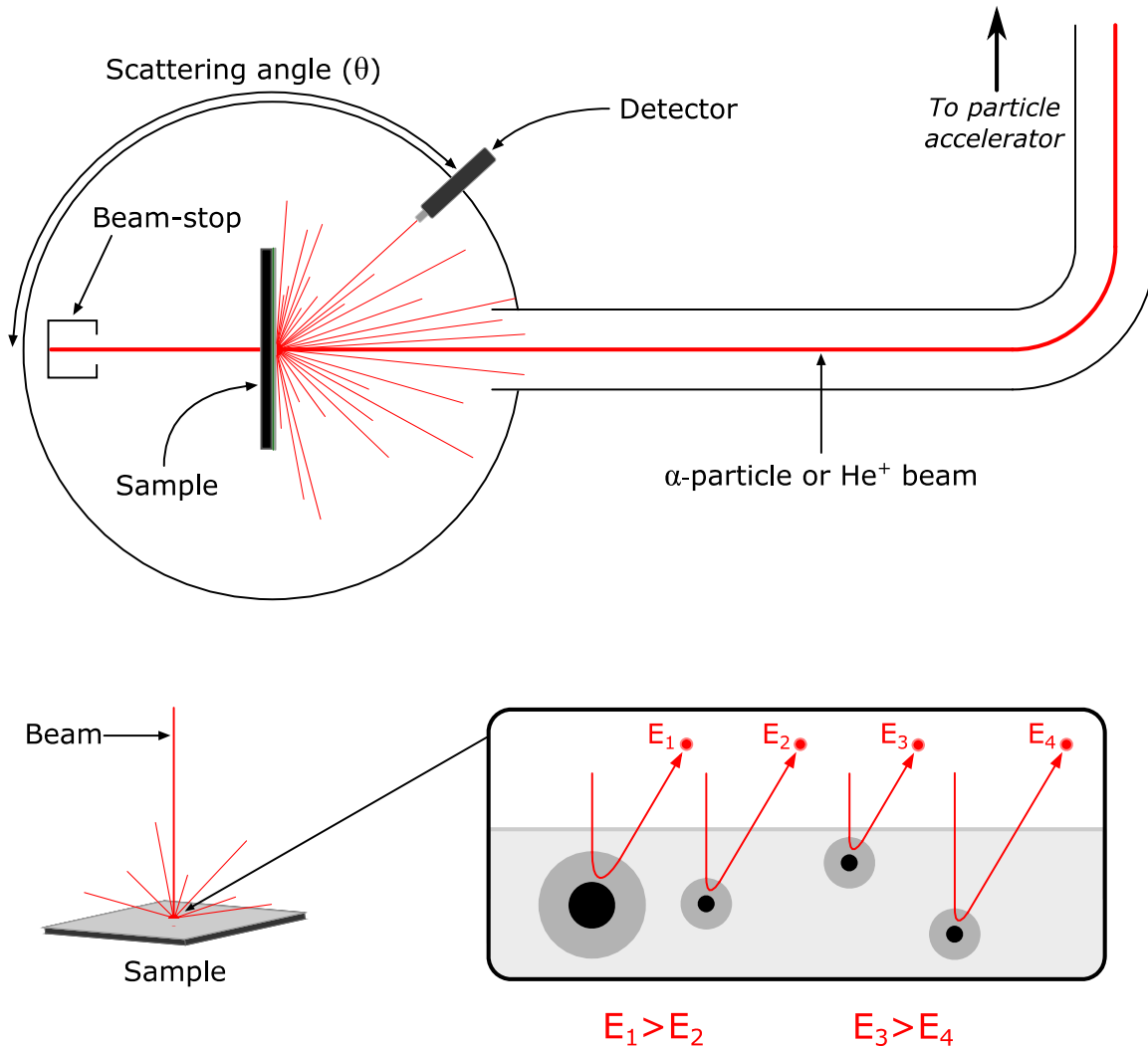


Figure 4.3.2: (top) a schematic of an RBS experiment apparatus, which would be connected to a beamline of a particle accelerator, and (bottom) an illustration of how the energy of a scattered beam particle can vary by the atomic mass of the sample nucleus and depth in the sample

The scattering of a beam particle by a sample nucleus can be considered as a two-body elastic collision between a stationary particle b of mass M_b and a less massive moving particle a of mass M_a . The ratio between the final and initial energies $\frac{E_{af}}{E_{ai}}$ of the beam particle when scattered through an angle θ can be expressed as:¹⁸⁹

$$\frac{E_{af}}{E_{ai}} = \left(\frac{\sqrt{M_b^2 - M_a^2 \sin^2 \theta} + M_a \cos \theta}{M_a + M_b} \right)^2 = \left[\frac{\sqrt{1 - \left(\frac{M_a}{M_b}\right)^2 \sin^2 \theta} + \frac{M_a}{M_b} \cos \theta}{1 + \frac{M_a}{M_b}} \right]^2 \quad 4.3.2$$

From this expression it follows that at a fixed scattering angle, the greater the mass-imbalance between the beam particle and the sample nucleus, the less energy the beam particle loses in the collision. The practical consequence of this for RBS measurements is, as shown in Figure 4.3.2, that

particles scattered from higher mass elements will have a higher energy (or strictly speaking, lose less energy) than those that scatter from lower mass elements.

The final effect to consider is the depth of the scattering. If the beam particle scatters off a nucleus deep in the sample, then the scattered particle loses energy as it travels through the thickness of the film due to electrostatic interactions with the nuclei it passes.¹⁸⁹ Combining these three effects, data like those shown in Figure 4.3.3 are obtained when scattering is measured at a fixed angle. Consider a homogeneous, anisotropic film of composition AB, where A and B are elements for which $Z_A < Z_B$ and $M_A < M_B$. As shown in Figure 4.3.3, each element has a separate scattering peak (a consequence of equation 4.3.2) with a characteristic scattering energy $E_{A/B}$. The width of the peak is a function of the depth of the film while its height is a function of atomic number (a consequence of equation 4.3.1). These effects allow RBS to give information about both the elemental composition of a sample and its elemental depth profile.

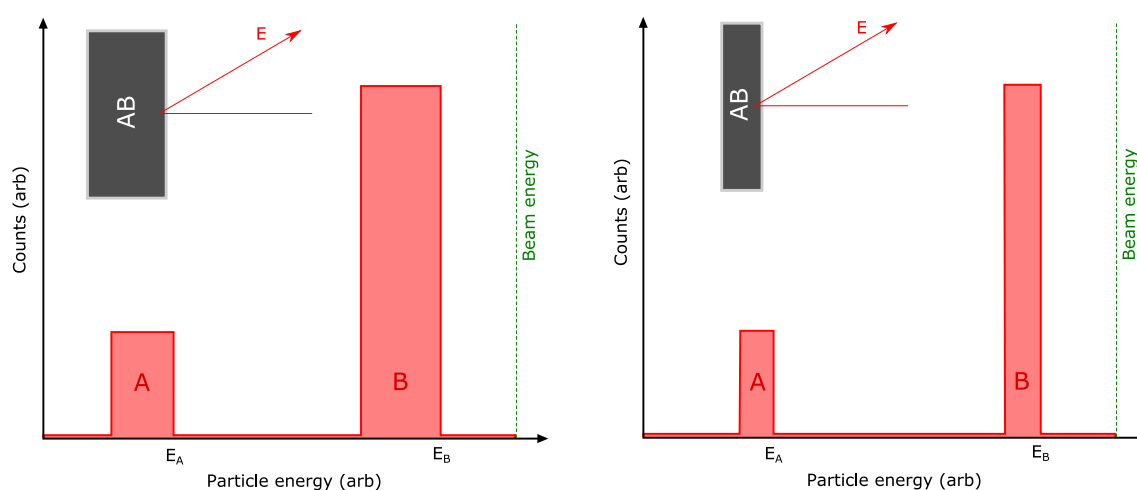


Figure 4.3.3: An example of the results of a fixed-angle RBS experiment conducted on a sample AB, in which A and B are elements with $M_A < M_B$ and $Z_A < Z_B$. Two thicknesses are shown to illustrate the peak-broadening effect of thickness and also that the leading edges of the peaks (E_A/E_B) are the same energy in each case. Note that beam energy is annotated here to aide the reader and is not usually evident in back-scatter data.

RBS has advantages and disadvantages when compared to other techniques that study the elemental depth profile of samples. By far its biggest advantage is that the technique is mostly non-destructive. Other techniques that can give depth profile information about a sample, like TOF-SIMS and XPS, require that the sample is etched during the measurement. Ion etching damages the sample and in some cases can alter the elemental distribution, invalidating the results.¹⁸⁹ RBS requires no sputtering as the beam penetrates and scatters off the entire sample. The technique is also highly sensitive to high molecular mass elements while also being insensitive to low mass contaminants containing carbon, nitrogen or oxygen.¹⁸⁹ In some applications, it can even give crystallographic information.¹⁸⁹

While equation 4.3.1 dictates that the technique is highly sensitive to high mass elements (like those used in metal oxide HTLs and metal electrodes), it also means that it is largely insensitive to lower mass elements and is therefore not well suited to characterising organic layers.¹⁸⁹ This can be further complicated by the tendency of high energy beams to damage organic layers, requiring lower energy beams be used; this improves the scattering cross-section (equation 4.3.1), but also increases the measurement time.¹⁸⁹ This was one of the reasons why the simplified architecture shown in Figure

4.3.1 was chosen for the RBS experiments. A further disadvantage is that, because the technique utilises nuclear interactions, it is blind to the chemical environment and thus gives no information about bonding, oxidation state, etc. – although, depending on the sample, this may be an advantage.¹⁸⁹ Finally, despite being relatively easy to set-up and having simple data processing, the technique does require a particle accelerator or similar α -particle/other-beam-particle source.

RBS experiment results

The RBS data obtained from the silver samples are shown in Figure 4.3.4, and the aluminium ones in Figure 4.3.5. The thicknesses for the different layers are shown in Figure 4.3.1, and were chosen on the basis of simulations that showed that they would minimise peak overlap (see section 3.2.1).

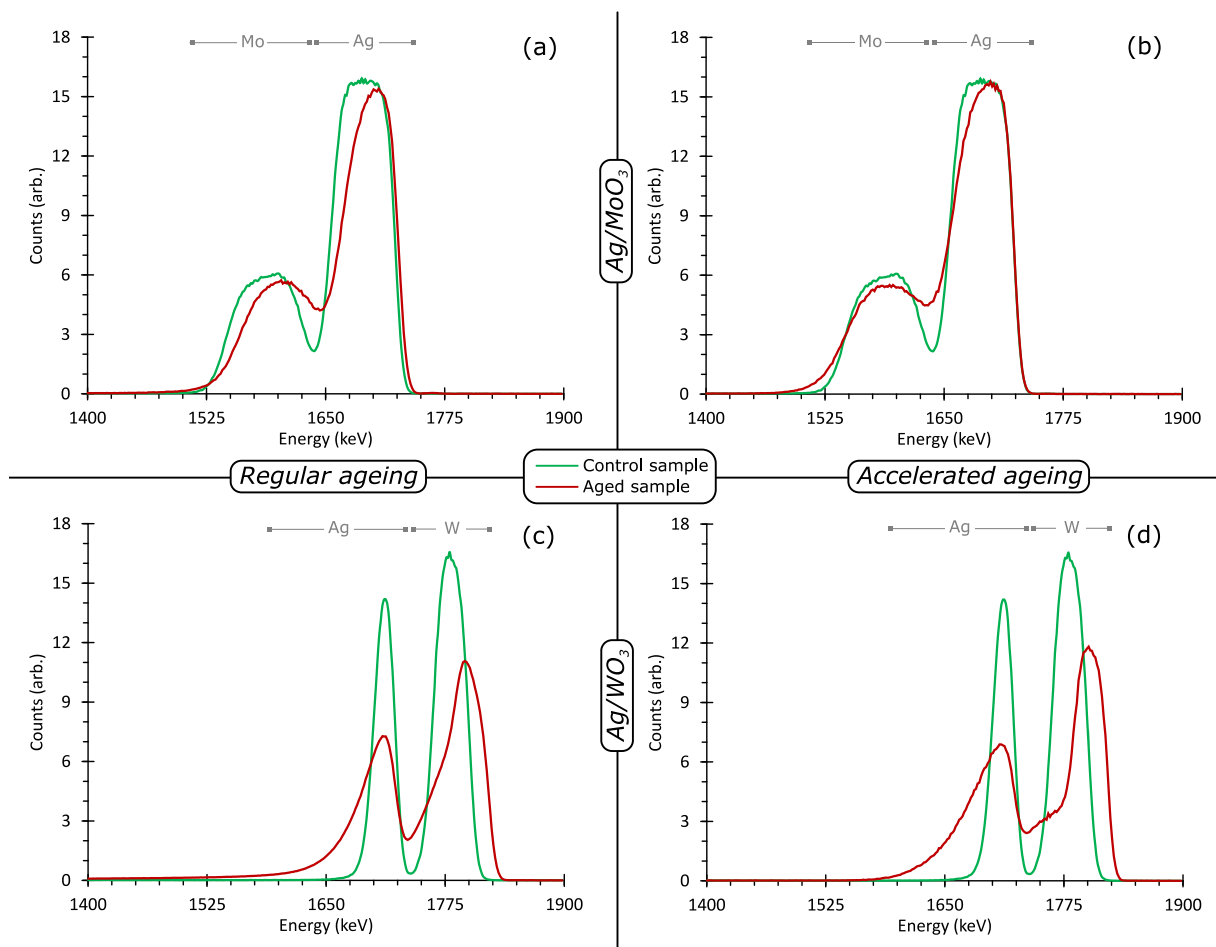


Figure 4.3.4: RBS data obtained from aged and unaged control samples with silver electrodes. The samples in (a) and (b) have MoO_3 HTLs, while (c) and (d) have WO_3 HTLs. The aged samples in (a) and (c) were aged under regular conditions, while those in (b) and (d) were aged under accelerated conditions. Counts are normalised to the same point on the carbon substrate shoulder (not shown). These measurements were made at the Aquitaine Regional Multidisciplinary Ion Beam Facility (AIFIRA) at the CENBG.

It is evident that the elemental depth profile of the silver samples changes with thermal ageing. While the high energy side of the silver peak remains at the same energy (this is the surface of the sample), the lower energy side develops a tail, indicating that silver is present deeper in the sample. The tungsten or molybdenum peaks shift to higher energies and broaden, consistent with intermixing with the silver.

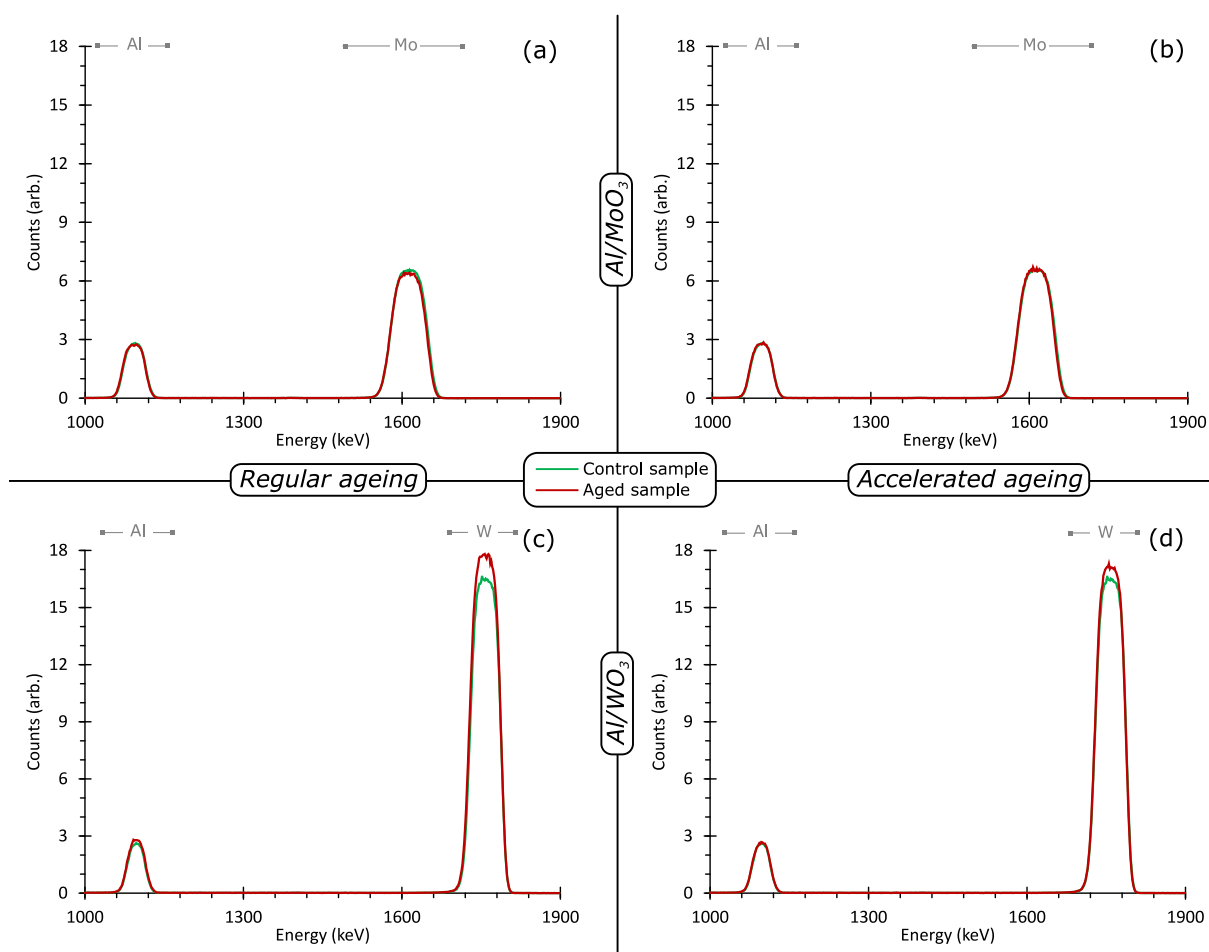


Figure 4.3.5: RBS data obtained from aged and unaged control samples with aluminium electrodes. The samples in (a) and (b) have MoO_3 HTLs, while (c) and (d) have WO_3 HTLs. The aged samples in (a) and (c) were aged under regular conditions, while those in (b) and (d) were aged under accelerated conditions. Counts are normalised to the same point on the carbon substrate shoulder (not shown). These measurements were made at the Aquitaine Regional Multidisciplinary Ion Beam Facility (AIFIRA) at the CENBG

When comparing the two HTL materials, it is difficult on first inspection to see whether the silver migrates more in one material than the other. While the silver peak shows a more pronounced tail in the Ag/WO_3 sample, it is possible that the same tail is present in the data from the Ag/MoO_3 sample but concealed beneath the Mo peak. However, the drop in peak height is much more pronounced with the Ag/WO_3 data, indicating that there is likely more peak broadening, and thus more apparent silver migration, in the Ag/WO_3 sample. In addition, the high-energy edge of the W peak exhibits a substantially greater shift than the Mo peak, which would suggest a greater change in the Ag/WO_3 samples. Furthermore, using equation 4.3.2, and the value for the beam energy of 2 MeV, it is possible to calculate the energy that the W peak would have if there were WO_3 present at the surface of the sample, which is 1838 keV. From Figure 4.3.4(c) and (d) it is clear that the high-energy edge of the W peak attains this scattering energy, indicating the presence of WO_3 at the surface of the sample. On the other hand, the calculated energy for Mo at the surface is 1700 keV, which is much higher than the Mo peak in Figure 4.3.4(a) and (b), so it is unlikely that any MoO_3 is present at the surface of the sample. These results indicate that more intermixing occurs with the Ag/WO_3 samples than the Ag/MoO_3 and that this mixing is so severe that WO_3 is present at the surface of the sample – consistent with either extreme interdiffusion or dewetting of the silver to expose the WO_3 . Furthermore, the steepness of the high-energy edge of the tungsten peaks in the aged samples

suggests that the WO_3 is present at the surface in significant quantities – suggesting that de-wetting is more probable than interdiffusion.

There are some slight differences in peak broadening between the regularly aged samples and the accelerated aged samples, but overall there is little difference between them. This indicates that the process that gives rise to the changes in the samples when they are aged at 85°C for 570 hours has completed in 90 hours of ageing at 150°C .

When the silver electrode is replaced with an aluminium one, the ageing behaviour of the samples changes significantly (Figure 4.3.5). Unlike their silver counterparts, the accelerated aged or regularly aged samples exhibit few, if any, changes. The Al/MoO_3 aged curves are identical to those of the control sample. The Al/WO_3 samples show a slight increase in the intensity of the tungsten peak but no change in peak breadth, so this is not likely to be significant.

Potential origins of changes in the RBS data

It is clear the samples with silver electrodes undergo a change in their elemental depth profile with thermal ageing, while the aluminium ones do not. While it is tempting assign these observations to inter-diffusion between the HTL and electrode layers, this is not the only possible explanation for the results detailed above, as an increase in the surface roughness would give similar results (Figure 4.3.6).

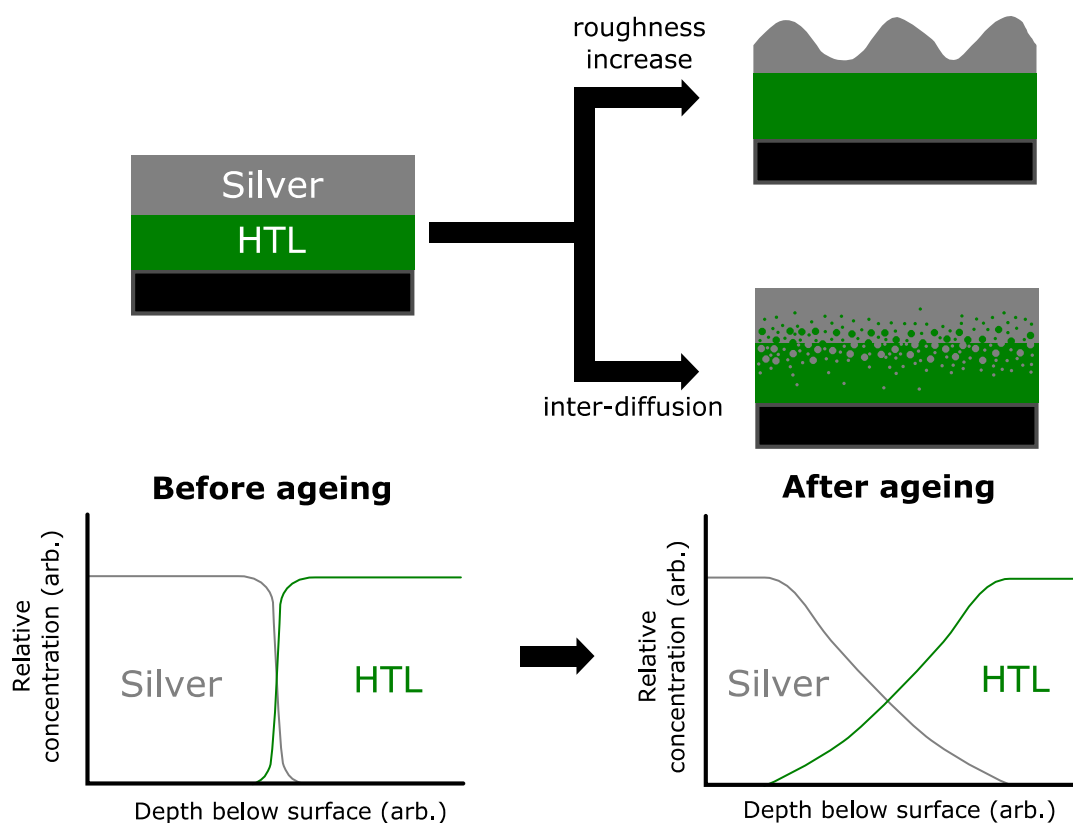


Figure 4.3.6: (top) Two possible changes in the sample that could explain the observed changes in the RBS data with thermal ageing: an increase in surface roughness or inter-diffusion between layers; and (bottom) the change in elemental depth profile which would be observed by RBS (note that the post-ageing profile is the same for inter-diffusion and increased roughness).

The reason for this is that RBS is blind to changes in the surface morphology in the sample and can only detect depth below the surface of the sample (i.e. the path length of the beam through the sample), although, as shown above, changes in the elemental composition of the surface can be detected.¹⁸⁹ This means that if the roughness of the electrode increases, it decreases the depth below the surface of the HTL in places (Figure 4.3.6), which would cause the peak associated with the HTL to broaden and give the appearance of inter-diffusion. In particularly severe instances of electrode dewetting, this might expose the underlying HTL, meaning that HTL material would be detected at the surface of the sample, although this too could be observed as a result of extreme interdiffusion of the layers.

However, the RBS data would not be completely identical in either case. In the event of inter-diffusion only, the carbon shoulder would be expected to remain the same after ageing as the substrate would not be expected to be altered by temperatures in this range. However, if the roughness increases this would cause a broadening of the shoulder, as the depth of the substrate below the surface of the film would vary across the sample. As shown in Figure 4.3.7, the carbon shoulder does broaden in both silver samples, showing that the roughness is increasing. Moreover, this is more pronounced with the WO_3 -containing samples than with the MoO_3 -containing samples, indicating that the increase in roughness is more severe with WO_3 HTLs (consistent with observations of the W peak).

These two scenarios are not mutually exclusive. It is possible that both inter-diffusion between the HTL and electrode as well as changes in the surface morphology of the electrode are occurring. If that is the case, this RBS experiment cannot conclusively prove the presence of inter-diffusion; however, it can rule it out in the case of the aluminium samples, as no peak broadening was observed.

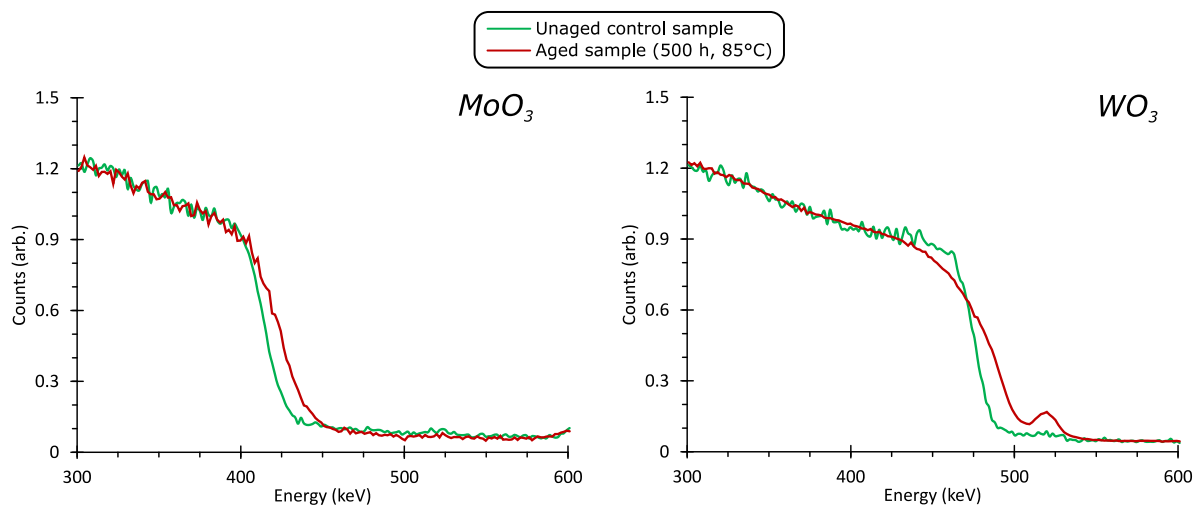


Figure 4.3.7: The RBS carbon shoulder for the MoO_3/Ag and WO_3/Ag samples before and after thermal ageing. Note that in both cases the shoulder broadens. The small peak on the aged Ag/WO_3 curve is most likely due to a carbon-containing surface contaminant on the sample.

4.3.3. AFM experiments

In order to see how the surface morphology of the samples changed with thermal ageing, a series of AFM experiments were carried out, commencing with the RBS samples (Figure 4.3.8, Table 4.3.1).

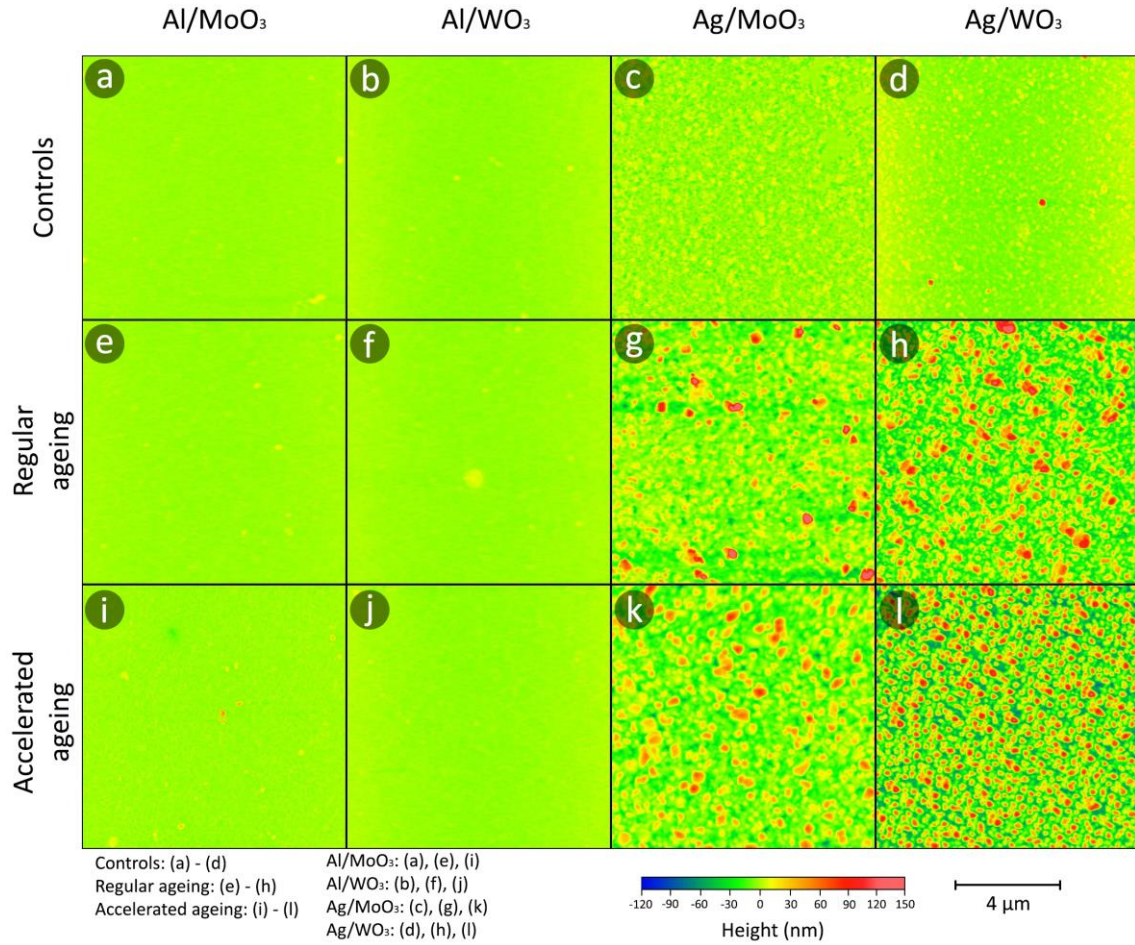


Figure 4.3.8: AFM data (topography) obtained from the samples prepared for RBS with the simplified architecture (Figure 4.3.1).

Table 4.3.1: RMS roughness values for the RBS samples measured by AFM on a $10\ \mu\text{m} \times 10\ \mu\text{m}$ square. The values are given in nanometres.

	Al/MoO ₃	Al/WO ₃	Ag/MoO ₃	Ag/WO ₃
Control	1.13	1.08	5.69	5.53
Regular ageing	1.28	1.02	17.3	26.5
Accelerated ageing	2.01	1.07	17.9	34.3

As shown in Table 4.3.1 and Figure 4.3.8, the changes in the samples observed by RBS correlate well to changes in the samples' surface morphology. The samples with aluminium electrodes show little variation in morphology with either regular or accelerated thermal ageing and are generally very smooth. The samples with silver electrodes are slightly rougher than the aluminium ones initially and then show significant increases in roughness with thermal ageing. This roughening phenomenon is accentuated with the use of WO₃, which correlates well to the RBS measurements of the aged Ag/WO₃ samples. However, while these samples do exhibit an increase in roughness and possible dewetting, the Ag/WO₃ OPV devices do not exhibit V_{OC} loss like the Ag/MoO₃ OPV devices, which suggests that another mechanism is responsible for the V_{OC}/FF loss in the Ag/MoO₃ devices. There is little difference between the regular ageing and accelerated ageing except in the case of the Ag/WO₃

samples, which appear slightly rougher with accelerated ageing. The fact that there is no significant further roughening of the samples with accelerated aging, and the appearance of the AFM height data are suggestive of island formation, whereby de-wetting silver forms isolated patches that cannot grow any further. This is supported by the RBS observations of WO_3 at the surface of the Ag/WO_3 aged samples. However, if this were the case, it would be expected that the “islands” would contrast with the underlying layer on AFM tapping phase images as they would have different chemical compositions. No such contrast is observed (Figure 4.3.9) which contradicts the island formation hypothesis. Rather, these results indicate that even after this roughening phenomenon, the silver electrode is still continuous all over the active area. This is difficult to reconcile with the RBS observations of WO_3 at the surface of the Ag/WO_3 aged samples, although it may be that the WO_3 is intermixed with silver so as to not provide a significant AFM phase contrast, or that size of the exposed WO_3 domains is below the detection limit of this AFM instrument.

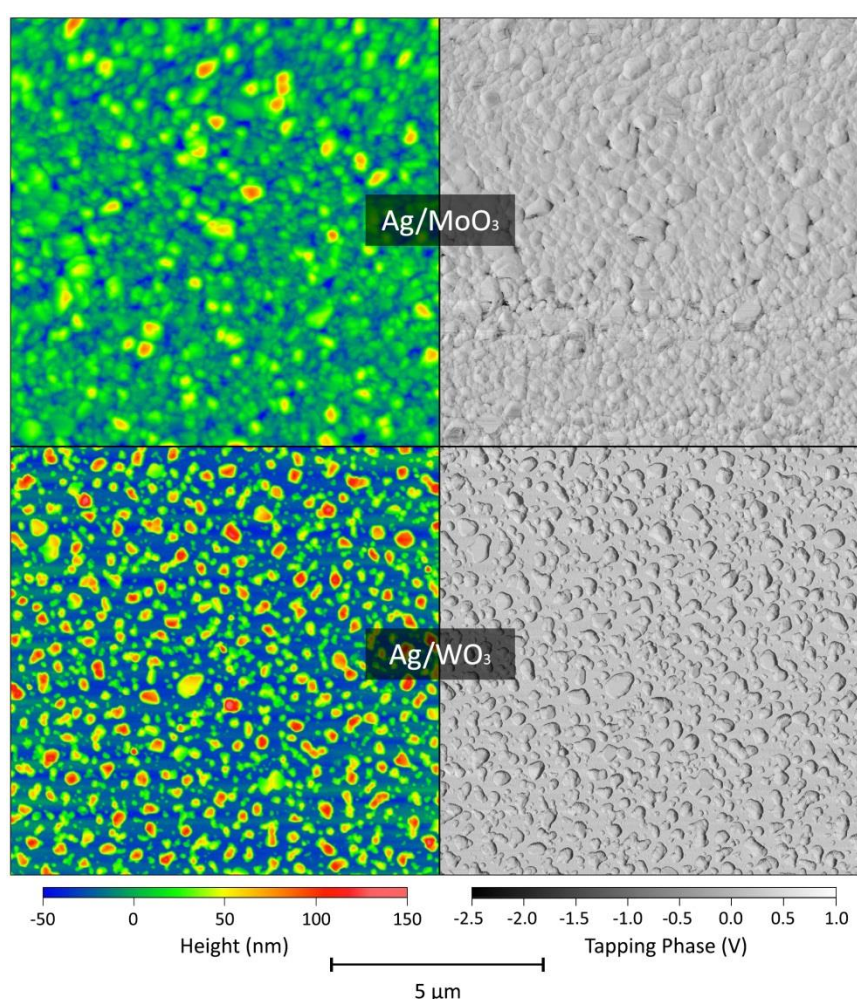


Figure 4.3.9: AFM height and tapping phase data from the accelerated aged RBS samples with silver electrodes.

At this point it is worth considering whether or not these morphology changes are present in full devices or only in the simplified architecture. To answer this question, full inverted devices (Figure 4.3.1) were prepared with the same oxide HTL and metal combinations. The devices were aged 500 hours at 85°C, under an inert atmosphere, in the dark, and then analysed by AFM. Unaged control samples were also measured for comparison purposes. The results of this analysis are shown in Figure 4.3.10 and Table 4.3.2.

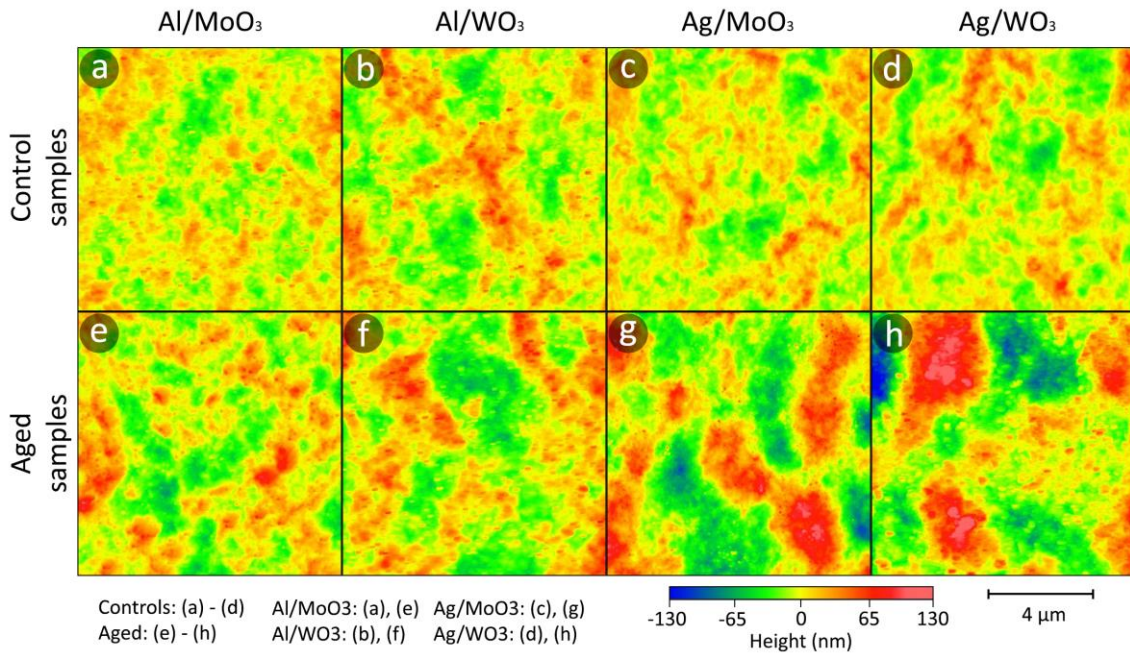


Figure 4.3.10: AFM data obtained from the OPV device samples prepared with the full inverted architecture (Figure 4.3.1).

Table 4.3.2: RMS roughness values for the full inverted device samples measured by AFM on a 10 μm × 10 μm square. The values are given in nanometres.

	Al/MoO ₃	Al/WO ₃	Ag/MoO ₃	Ag/WO ₃
Control sample	16.2	20.9	18	19.5
Aged sample	23.9	26.3	37.8	42.2

The full inverted architecture control samples are much rougher than the unaged simplified architecture samples. This is most likely a result of the effects of solvent annealing upon a BHJ active layer, as it has been previously demonstrated that solvent annealing can significantly increase the roughness of the active layer.¹⁰⁹ There is also a slight increase in roughness with thermal ageing in the full inverted aluminium devices that was not seen in their simplified counterparts that is likely a consequence of changes in the bulk morphology of the active layer arising from thermal ageing and are linked to J_{sc} loss (see Chapter 2).

There is also a noticeable increase in the roughness of the silver-containing samples that is of a similar magnitude to that observed with the simplified architectures and much greater than the increase in roughness in the aluminium-containing samples. This shows that the effect is a consequence of the materials and not whether the simplified structure or full inverted OPV structure are used. Interestingly, the trend observed in the simplified structure, i.e. that the Ag/WO₃ samples exhibit a greater increase in roughness than the Ag/MoO₃ ones with thermal ageing, is also observed with the full inverted OPV architecture. This result indicates that it is not just the silver that plays a role in this roughening phenomenon, but also the WO₃.

However, this increase in surface roughness does not appear to fully correlate to any of the trends observed in cell parameters with thermal ageing. One of the possible explanations for the material-selective degradation observed in the PV parameters of the inverted devices with MoO₃ HTLs and silver top electrodes was delamination/de-wetting of the electrodes (section 4.2.4). If this was occurring, then an increase in surface roughness would be expected. However, the increase in roughness is observed with both HTL oxides, not just MoO₃, but also WO₃. Furthermore, the Ag/WO₃ samples exhibit a greater increase in roughness than the Ag/MoO₃ samples with thermal ageing. Besides, the degradation observed in the Ag/MoO₃ samples was primarily driven by a loss of V_{oc} and FF , which would not be easily explained by dewetting or delamination, as noted in section 4.2.4. It therefore seems unlikely that the roughness increases observed in the silver samples and the V_{oc}/FF loss observed in the Ag/MoO₃ samples are related, or if they are, there must be another mechanism by which the V_{oc} and FF loss occur that can also explain the HTL selectivity. It should also be reiterated that none of the above observations have ruled out the presence of interlayer diffusion with the silver electrodes; rather, they do not conclusively prove it.

4.3.4. Variations in thermal ageing with electrode thickness

The possibility of island formation in silver electrodes with thermal ageing seems not to be an issue when relatively thick electrodes are used. While the increase in observed with the Ag/WO₃ full inverted architecture sample (Table 4.3.2), is significant compared to the thickness of the sample, it is still much less than the thickness of the deposited electrode of 80 nm. It is worth considering what the consequences of using a thinner electrode might be in this regard, and to this end a study was carried out to investigate the resilience of inverted OPV devices with silver top electrodes of various thicknesses to thermal ageing. The experiment was carried out with the samples shown in Figure 4.3.11, which were aged at 85°C, in the dark, under an inert atmosphere.

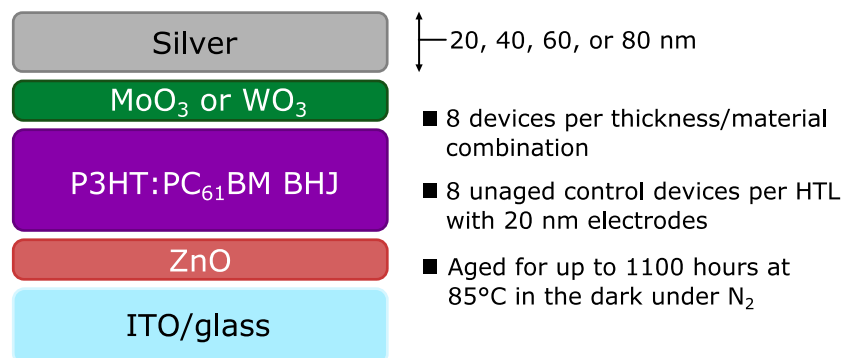


Figure 4.3.11: Experiment design for the silver electrode thickness experiment. Note that the layer thicknesses are the same as those detailed in Figure 4.2.1, unless otherwise specified

The initial device parameters of the samples are shown in Table 4.3.3 and the evolution of their efficiencies with time are shown in Figure 4.3.12. The samples with 20 nm electrodes exhibit slightly lower initial values for J_{sc} and PCE as the electrodes are partially transparent at this thickness. As was observed in section 4.2, the WO₃ samples show an initial improvement in performance due to an improvement in the FF that occurs in the first hour of thermal treatment. The MoO₃ samples also show a decline in the performance of the unaged control sample (20 nm electrode), which is consistent with the effects of photo-ageing that were observed in section 4.2.2 when samples were repeatedly measured on a solar simulator.

Long-term, the samples exhibit the same J_{SC} -driven degradation observed in the other P3HT:PC₆₁BM samples (section 4.2.3) after 300 hours of thermal ageing. As this experiment has been carried out over a longer period of time than the previous ones, it can be observed that this long-term degradation has a limiting behaviour, with the degradation rate having greatly decreased by the end of the experiment. This would be consistent with domain growth, as, after the donor and acceptor domains have reached a certain size, the region around them would become depleted of material to fuel the growth. The Ag/MoO₃ samples exhibit the same V_{OC} and FF loss throughout the experiment as was observed in section 4.2.4 with the 80 nm electrodes, however, beyond 500 hours of ageing both sets of samples also exhibit a slight decline of V_{OC} . As this occurs in all aged samples, and is not correlated to a decline in the FF , it is unlikely that this is related to the large decline in V_{OC} and FF observed in the Ag/MoO₃ samples in the first 100 hours of ageing, and is most likely a bulk phenomenon.

Table 4.3.3: Device statistics for the silver electrode thickness experiment. The MoO₃-containing samples' statistics are their initial values, while the ones from the WO₃-containing samples are taken after one hour of thermal ageing in order to incorporate previously observed improvements in efficiency with thermal annealing. Uncertainties represent one standard deviation across eight devices.

HTL	Ag thickness (nm)	PCE	J_{SC} (mA cm ⁻²)	V_{OC} (mV)	Fill factor
MoO ₃	20	3.34±0.09%	11.06±0.1	0.520±0.002	0.581±0.010
	40	3.72±0.05%	11.75±0.17	0.527±0.005	0.600±0.005
	60	3.48±0.20%	11.22±0.71	0.521±0.007	0.596±0.019
	80	3.62±0.09%	11.71±0.19	0.516±0.006	0.599±0.015
WO ₃	20	3.10±0.03%	9.10±0.01	0.533±0.005	0.639±0.002
	40	3.27±0.08%	9.22±0.25	0.537±0.005	0.662±0.005
	60	3.39±0.12%	10.08±0.18	0.528±0.009	0.637±0.021
	80	3.63±0.04%	10.34±0.08	0.537±0.003	0.653±0.004

As shown in Figure 4.3.12, both of the 20 nm electrode samples exhibit a catastrophic failure, whereas the others do not. This is particularly pronounced in the 20 nm Ag/WO₃ devices, most of which have failed by 50 hours of ageing. In comparison, the catastrophic failure of the 20 nm Ag/MoO₃ devices occurs significantly later, around 750 hours of ageing. As noted in Table 4.3.1 and Table 4.3.2 and discussed in section 4.3.3, the Ag/WO₃ samples (both simplified and full devices) exhibit the greatest increase in roughness with ageing compared to Ag/MoO₃. The device failure, in both cases is driven initially by a decline in FF which is followed by a decline in J_{SC} . The V_{OC} shows some declines immediately before device death, but this is thought to be due to inaccuracies in determining the V_{OC} at low photocurrent. In the case of the 20 nm Ag/MoO₃ devices, V_{OC} and FF decline were also observed in the early stages of the experiment, in agreement with previous observations of this material combination (section 4.2.4). The slight dip shown in the efficiency of the 20 nm Ag/MoO₃ devices between 150 hours and 250 hours of ageing was a consequence of poor contact with some of the devices, which was repaired for subsequent measurements.

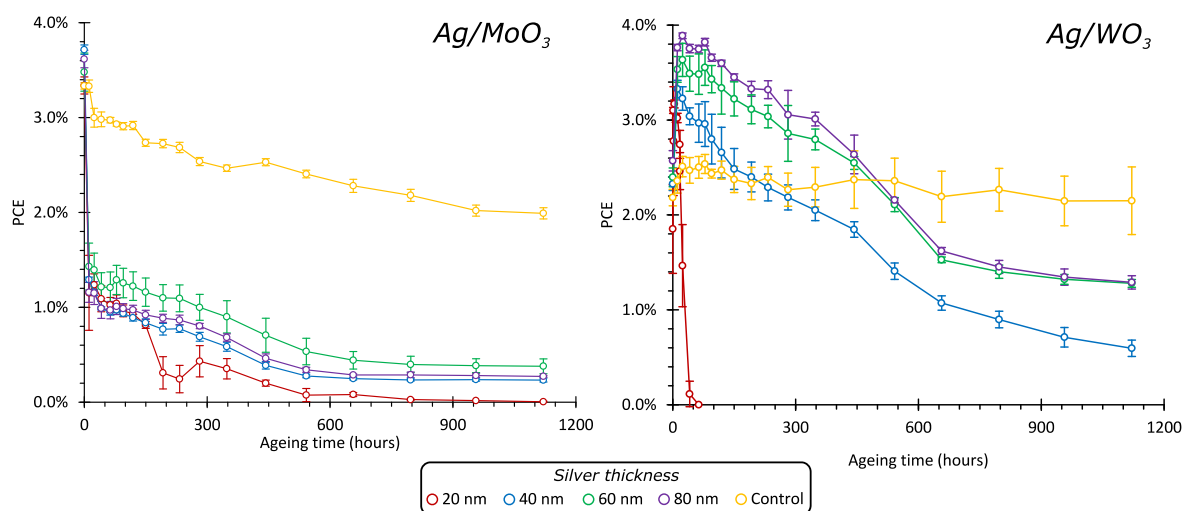


Figure 4.3.12: Evolution of the PCE of the aged samples and the unaged controls in the silver electrode thickness experiment. It should be noted that the control devices were measured at the same time as the aged devices, but were not subjected to thermal ageing and are only shown for comparison purposes. The uncertainties represent one standard deviation across eight devices.

The increase of roughness appears to be the cause of the catastrophic failure of the 20 nm devices. Focusing on Ag/WO₃ devices, the change of the IV curve during the device failure is shown in Figure 4.3.13. It is evident from these results that there is a significant increase in the series resistance in this device, decreasing the fill factor and, as it becomes more severe, eventually suppressing all photocurrent. As shown in Figure 4.3.13, across all the 20 nm Ag/WO₃ devices there is a very sharp rise in the series resistance that begins around 20 hours of thermal ageing. This would be entirely consistent with an electrode ceasing to be conductive due to island formation.

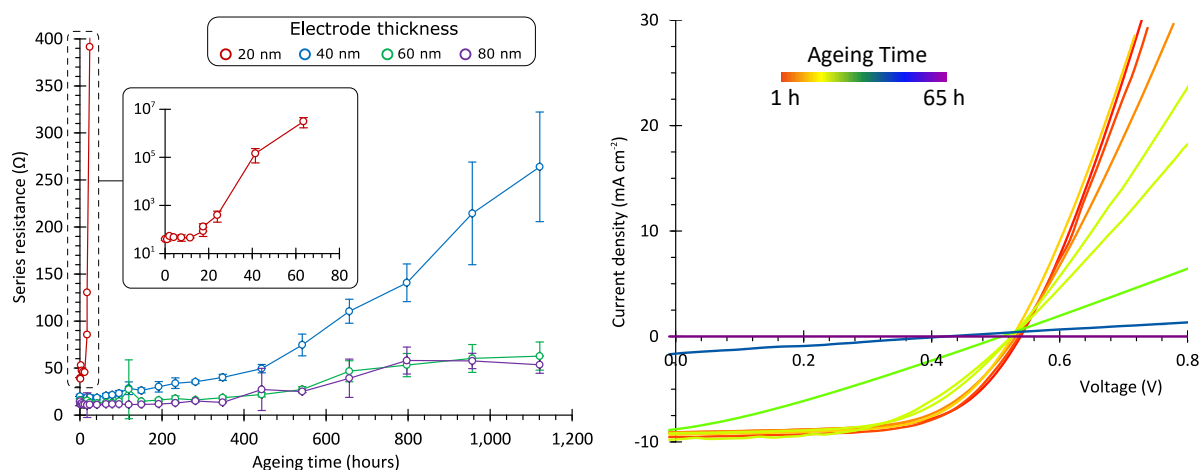


Figure 4.3.13: (left) The series resistance of the Ag/WO₃ devices with different electrode thicknesses as a function of thermal ageing time (the 20 nm electrode sample is shown in the inset on a log scale); and (right) the evolution of an Ag/WO₃ device with a 20 nm-thick electrode with thermal ageing. Uncertainties represent one standard deviation across eight devices.

What is also interesting is that differences in the series resistance can explain the observed stability trends with electrode thickness, i.e. that the devices with thicker electrodes in this experiment were more stable (Figure 4.3.12). Although not as dramatic an increase as the 20 nm Ag/WO₃ samples, the 40 nm samples also exhibit an increase in series resistance, while the 60 nm and 80 nm samples show

only a slight increase (consistent with the behaviour of the control samples). This behaviour could be explained by partial dewetting of the 40 nm electrode, which is not enough to completely inhibit the function of the device, but sufficient to increase the resistance of the electrode and reduce the effective area of the device. A steeper decline in J_{SC} is observed in the ageing of these samples (Figure 4.3.14), which supports this conclusion, and suggests that if this experiment had continued, the 40 nm Ag/WO₃ samples would have exhibited the same catastrophic failure as the 20 nm ones. It also suggests that there is an electrode thickness threshold, beyond which this increase in electrode roughness has no impact on the ageing of the device, and that the results of this experiment indicate that this thickness is between 40 nm and 60 nm.

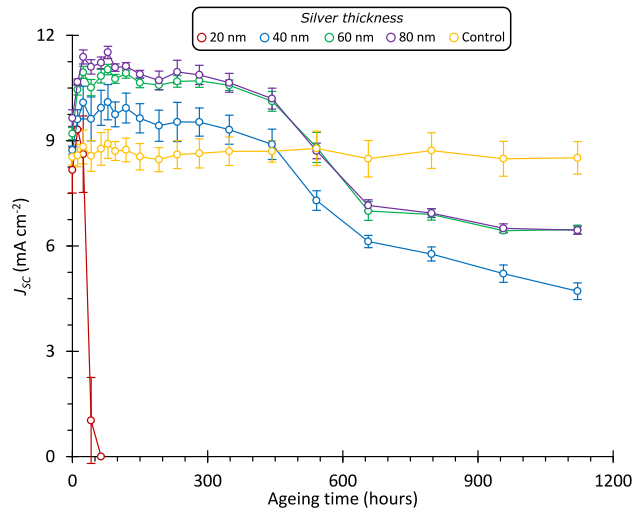


Figure 4.3.14: Evolution of the J_{SC} of the Ag/WO₃ samples in the silver electrode thickness experiment as the samples are thermally aged under an inert atmosphere in the dark. Note that the uncertainties represent one standard deviation when averaged across eight devices

In order to show the presence (or otherwise) of island formation of the electrode in the 20 nm Ag/WO₃ samples, the samples were examined by AFM. The data from these measurements are shown in Figure 4.3.15. As with the thicker electrode samples (Figure 4.3.10), there is a clear difference in the height images between the control and aged specimens (although there is only a slight difference in RMS roughness between the control and aged samples, most likely due to the roughness of the underlying active layer). Unlike the phase data in Figure 4.3.9, in which no contrast was observable between the peaks and valleys in the phase image of the aged samples, in these measurements such a contrast is visible (Figure 4.3.15). In the zoomed area in Figure 4.3.15 the peak regions are shown as having a smooth texture, while the valleys have a speckled texture. This would be consistent with dewetting of the silver from the underlying WO₃, which is visible in the valley regions.

This was also observed in the RBS measurements, in which WO₃ was shown to be present at the surface of the aged Ag/WO₃ samples. It is strange, therefore, that the island formation was not fully visible in the AFM measurements of the RBS samples (Figure 4.3.9), in which no contrast was observed in the phase image between the peak and valley regions, whereas it is when full devices are aged (Figure 4.3.15) This is despite both the RBS samples and these samples having similar electrode thicknesses. This may be because different instruments were used for the two measurements and the one used for the full devices has better resolution. It is also possible that this was exacerbated by

the intermixing of silver and WO_3 in the valley regions which would make the phase contrast less pronounced.

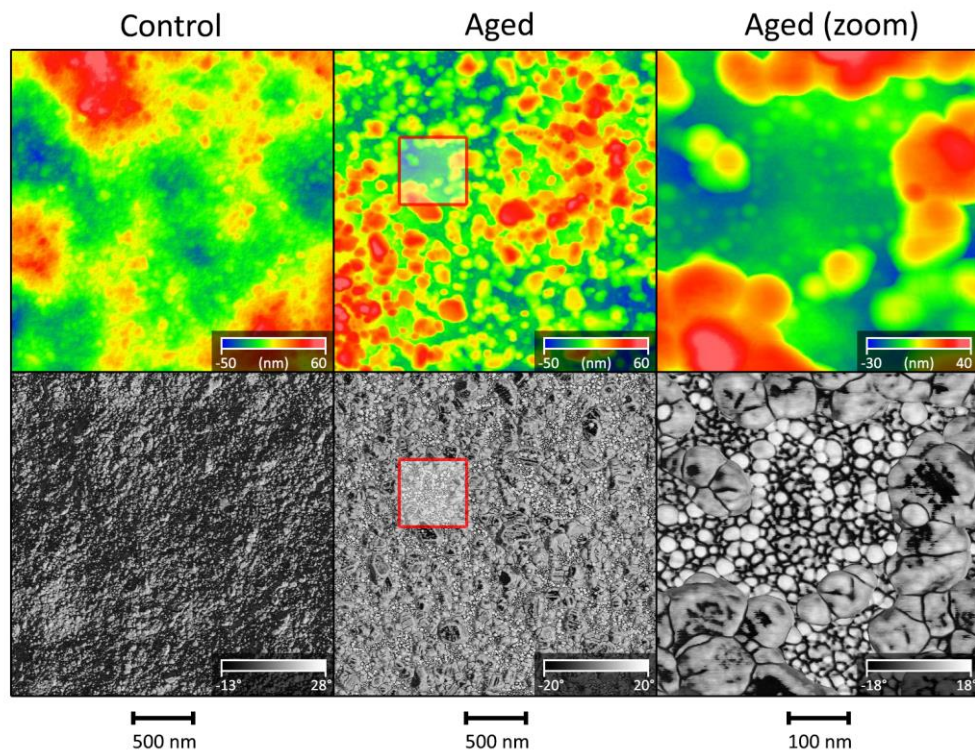


Figure 4.3.15: AFM height (top) and phase (bottom) data measured from both control and thermally aged Ag/WO_3 samples with 20 nm electrodes. The zoomed images represent the regions in the red squares in the images of the aged sample. These data were measured by Dr Gilles Pecastaings on a Dimension FastScan AFM (Bruker) in tapping mode

4.4. Fracture analysis

4.4.1. Introduction to fracture analysis

As has been demonstrated in the previous sections of this chapter, inverted OPV exhibit a number of thermal degradation mechanisms at interfaces in their structures, in particular at the hole-extraction interface. In addition to having consequences for the photovoltaic properties of the device, this can also affect the mechanical properties of the device. One of the stated applications of OPV devices is in flexible solar modules that can withstand moderate mechanical deformation. It follows that it is important to consider any of the consequences of thermal ageing with respect to the mechanical stability of devices. Fracture analysis is a useful tool to examine this. Mechanical failure of a device can occur either by a loss of inter-layer adhesion or by decohesion within a layer. By fracturing a sample in a controlled and measurable fashion, it is possible to identify the device's point of failure and quantitatively analyse the strength of the device.

The propagation of a crack in a solid can be considered in terms of energy balance. Prior to the cracking of the solid, chemical bonds near the crack site are under stress due to externally-applied stress and the presence of defects.¹⁹⁰ Following the formation of the crack, the surface area of the solid has increased, meaning that the surface energy is greater. It follows from the first law of thermodynamics that, in order for a crack to propagate, the energy liberated from the broken bonds

must be equal to or exceed the gain in surface energy.¹⁹⁰ The ease with which a crack can propagate can vary greatly depending on the type of bonding in the solid and its structure. A solid might be difficult to fracture because it has few defects and the yield stress of the bonds is too high, or because the surface energy cost is too high, or both. The energy required to form a crack is referred to as the *fracture energy*.¹⁹⁰ Usually this is measured as the energy required to grow a crack per unit area of crack, and represented by the symbol G_c .¹⁹⁰ This is also sometimes referred to as the *fracture toughness* of a material.¹⁹⁰

The path a fracture takes through a solid is a function of a number of different factors. It is, however, universally true that at minimum applied stress, a crack will (if able) propagate through the weakest point in a solid.¹⁹⁰ This is a simple matter of probability and energy, as bonds at a weak point in the device will break under less stress, either due to the bonds themselves being weaker (such as at an interface between two materials) or due to additional stress arising from defects.¹⁹⁰ It should be noted that only the propagation of a fracture, and not the initiation of a fracture, is under discussion here. Typically a fracture takes much more external stress to initiate than to propagate.¹⁹⁰ This extra stress, if it is still applied after initiation, can lead to very rapid propagation throughout the entire solid, and not necessarily along the ideal fracture path. It is for this reason that, in this study, all of the samples were pre-cracked (initiated) and stress was applied gradually to the samples to ensure that the fracture only propagated at the weakest point in the sample.

In this study the double cantilever beam (DCB) geometry was used to carry out fracture analysis of the samples. This method consists of pulling apart two “beams” of equal thickness (h) and width (B) with equal and opposite load (P) on each of the beams at the start of the fracture (Figure 4.4.1). In this geometry the fracture length is represented by the symbol a . This geometry is the most commonly used for fracture analysis testing as it is relatively simple and therefore allows for easy data analysis.¹⁹⁰ In practical terms, the measurement of thin film samples via this method is achieved by adhering a piece of glass to the top of the sample with an epoxy adhesive (Chapter 3); this piece acts as one “beam”, the other being the substrate.

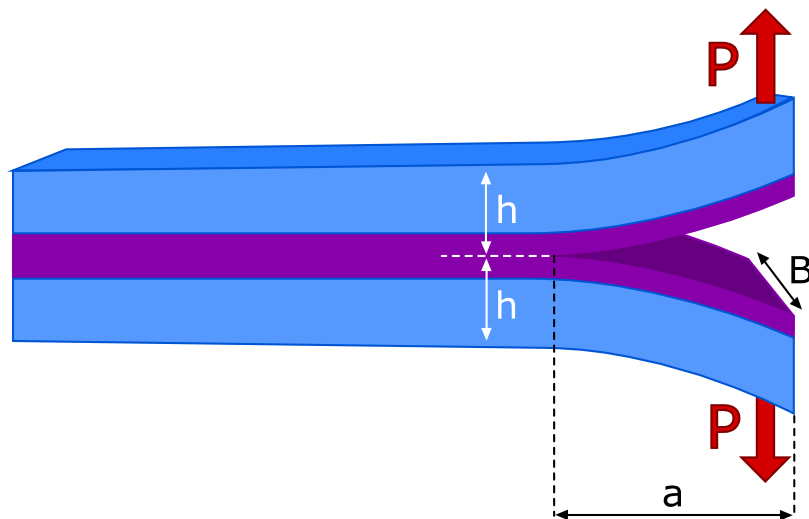


Figure 4.4.1: A schematic of the DCB fracture analysis testing geometry. Here h is the beam thickness, B is the width of the sample, a is the crack length and P is the applied load.

It can be shown that the fracture energy (in J m^{-2}) of a sample in an ideal DCB configuration is represented by:

$$G_c = \frac{12P_c^2 a^2}{B^2 h^3 E'} \quad 4.4.1$$

in which P_c is the critical load at which the sample fractures, E' is the plane strain Young's modulus and the other symbols are the same as those stated in Figure 4.4.1. However, equation 4.4.1 assumes that the beams have a very large width. In this experiment, a slight modification to formula 4.4.1 was used to account for smaller beam widths:¹⁹¹

$$G_c = \frac{12P_c^2 a^2}{B^2 h^3 E'} \left(1 + 0.64 \frac{h}{a}\right)^2 \quad 4.4.2$$

The data obtained from a typical fracture experiment are shown in Figure 4.4.2.

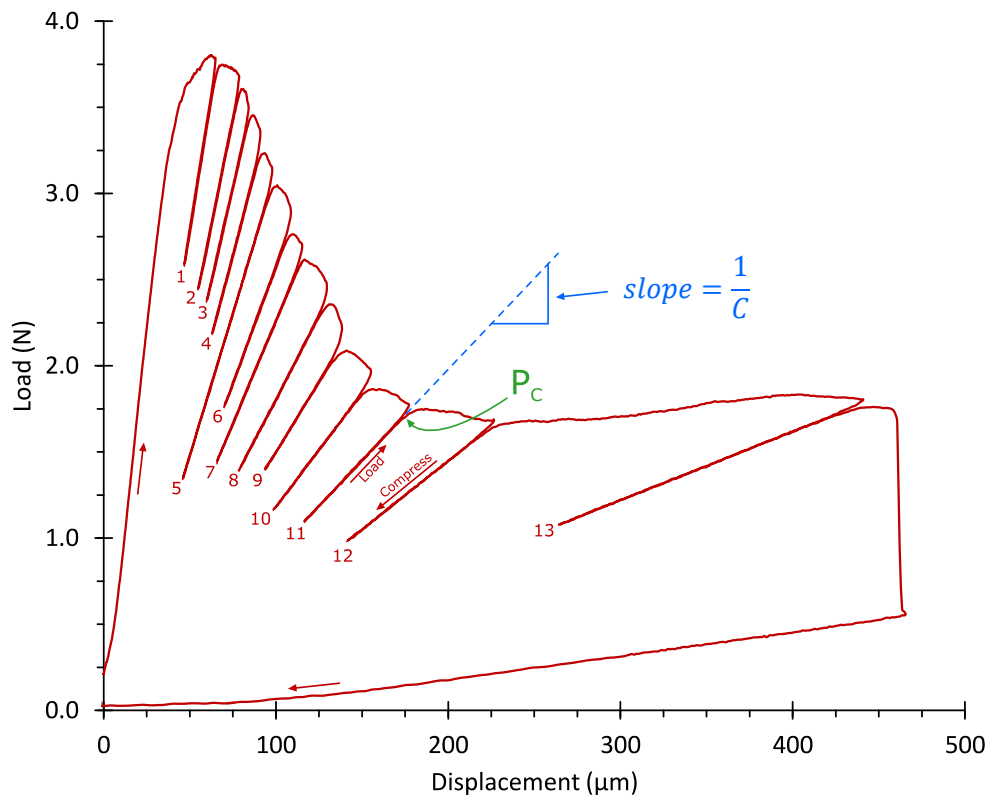


Figure 4.4.2: Load curve data obtained from a typical fracture analysis experiment in this study. This experiment has 13 load-compress cycles (numbered 1-13), giving 13 values for G_c . The critical load (P_c) can be found from the point in the load portion of a cycle where the curve deviates from a linear slope and the compliance can be found from the slope of the linear portion.

In each experiment the sample is fractured in multiple steps, allowing determination of the fracture energy for many different fractures lengths (although in practice, values obtained near either end of the sample are discounted due to invalidation of the underlying model) and thus providing an uncertainty in the value quoted for the sample. In practical terms, this means applying an increasing load until the crack grows (signified by a deviation from linear), compressing until the crack stops propagating, and then repeating. From equation 4.4.2, it is clear that the two critical terms to determine are the critical load and the fracture length for each load-compress cycle. As shown in

Figure 4.4.2, the critical load is easily determined by finding the point at which the crack starts propagating while load is being applied, i.e. the deviation from linear on the load curve. The crack length can be determined from the compliance (C), which is the inverse of the slope of the linear part of the load curve. It can be shown that the compliance in an ideal DCB experiment is related to the crack length as follows:¹⁹⁰

$$C = \frac{8a^3}{BE'h^3} \quad 4.4.3$$

Taking into account the small width of the beams, this formula is slightly modified in this experiment to give:^{190,191}

$$C = \frac{8}{BE'} \left(\frac{a}{h} + 0.64 \right)^3 \quad 4.4.4$$

meaning that the crack length can be found from the compliance via:

$$a = \frac{h}{2} \left(\sqrt[3]{BCE'} - 1.28 \right) \quad 4.4.5$$

For a more complete discussion of fracture analysis by the DCB method and fracture theory, the reader is referred to *Fracture mechanics: fundamentals and applications* by T. L. Anderson (CRC press, 3rd ed., 2005).¹⁹⁰

4.4.2. Experiment design and optimisation

This experiment was designed in a similar way to the RBS and AFM experiments, in that devices with each combination of MoO₃ or WO₃ as HTLs and silver or aluminium as electrodes were fabricated. The initial sample structure is shown in Figure 4.4.3.

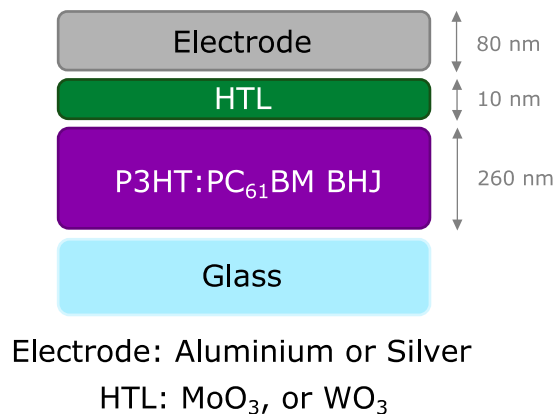


Figure 4.4.3: The initial structure of the samples prepared for the fracture analysis experiments. This diagram does not include the glass beam adhered to the top of the sample with epoxy adhesive for measurement.

The aim was to examine the effects that different materials would have on the mechanical stability of the samples after undergoing thermal ageing and to correlate any observed material dependence to the trends observed in the cell statistics and in the RBS and AFM experiments. However, unlike in the previous experiments, the practical requirements of fracture analysis are such that larger samples are needed. This meant that the fabrication of the samples had to be reconsidered – in particular, the active layer had to be deposited via doctor blade instead of spin coating. As this technique has not

before been used to deposit an active layer in the Organic Electronics group at the University of Bordeaux, an optimisation study was required.

Optimisation of active layer deposition by doctor blade

There are five main variables to consider in doctor blade coating:

- blade height
- coating speed
- sample temperature
- ink solvent
- ink concentration

The aim was to produce an active layer with similar characteristics to one produced via spin coating – specifically, an even active layer with a thickness between 200 nm and 300 nm. The substrates used for the final samples were pieces of glass measuring 70 mm x 52 mm x 1 mm, but for the optimisation, samples with a smaller width (26 mm instead of 52 mm) were used. As these samples were not destined to be used as OPV devices no bottom electrode was needed, and so the layers were deposited on glass alone, with no ITO. The outcome of a first round of tests is shown in Table 4.4.1.

Table 4.4.1: Characteristics of the first active layer films deposited by doctor blade coating. It should be noted that the concentration refers to the concentration of each active layer component (1:1 ratio) in the ink solution (i.e. a 30 mg mL⁻¹ solution has 30 mg mL⁻¹ of P3HT and 30 mg mL⁻¹ of PCBM). These tests were carried out with a fixed blade height of 250 μm

<i>Solvent</i>	<i>Concentration (mg mL⁻¹)</i>	<i>Temperature (°C)</i>	<i>Blade speed (mm s⁻¹)</i>	<i>Film texture</i>	<i>Thickness (nm)</i>
Chlorobenzene	30	70	15	Even	327 ± 13
Chlorobenzene	30	80	20	Even	245 ± 40
Chlorobenzene	30	60	20	Uneven	355 ± 34
Chlorobenzene	30	70	20	Even	311 ± 26
Chlorobenzene	20	70	40	Uneven	186 ± 2
Chlorobenzene	30	70	10	Even	183 ± 44
Chlorobenzene	20	70	20	Even	151 ± 16
Chlorobenzene	20	70	10	Even	88 ± 9
1,2-dichlorobenzene	20	80	2.5	Even	28 ± 2
1,2-dichlorobenzene	20	80	7.5	Uneven	150 ± 16
1,2-dichlorobenzene	20	80	15	Uneven	149 ± 17

From the preliminary tests, a few conclusions can be reached about this system:

- inks using chlorobenzene as a solvent produce more even and thicker films than those using 1,2-dichlorobenzene;
- more concentrated inks produce thicker films;
- lower sample temperatures produce thicker and less even films; and
- faster blade speeds produce thicker and less even films.

Following these tests, films were deposited with a 250 μm blade height, 30 mm s^{-1} blade speed, 70°C sample temperature and a 30 mg mL^{-1} (in each component) ink in chlorobenzene. The resulting average film thickness was 262 ± 52 nm, and the films were very even in texture. The only issue with the films was that they showed a longitudinal variation in thickness in the blade sweep direction, with the film becoming thinner in the direction the blade moved. The end-to-end variation was approximately 150 nm. While this is a significant variation across the whole sample, because of the way the samples were to be cut for fracture testing (see Chapter 3), an individual slice being tested would show much less variation. Furthermore, preliminary fracture analysis tests conducted by Nicholas Rolston at Stanford University found no significant variation in fracture energy from one end of the sample to the other, so this was not deemed an issue.

In order to mimic the preparation of the spin-coated samples, the large samples also underwent solvent annealing under similar conditions. To do this, an apparatus was developed to expose the coated samples to 1,2-dichloromethane vapour. A schematic of the apparatus is shown in Figure 4.4.4 along with images of the effect on a sample, which are similar to the spin-coated samples.

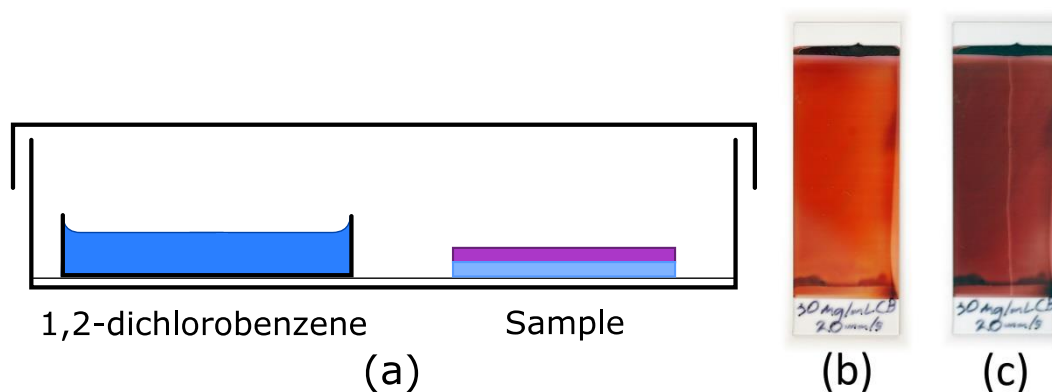


Figure 4.4.4: (a) the apparatus used to subject the samples to solvent annealing; (b) a sample prior to solvent annealing; and (c) a sample after solvent annealing.

It should be noted that the doctor blade coating and solvent annealing were carried out in air, but all subsequent fabrication and ageing steps were carried out under an inert atmosphere.

Preliminary fracture testing

Samples with the structure shown in Figure 4.4.3 were prepared with silver electrodes and MoO_3 HTLs. These samples were then packaged under inert atmosphere and transported to Stanford University for preliminary fracture measurements (carried out by Nicholas Rolston). The tests showed evidence that instead of fracturing at either the hole extraction interface or in the P3HT:PC₆₁BM BHJ active layer, the samples were delaminating at the active layer/glass interface in places (Figure 4.4.5). This meant that any fracture energy values obtained for these samples would only reflect the adhesion of the active layer to glass, which does not reflect the structure of an OPV device that would have a bottom electrode and an ETL. To remedy this, further samples were prepared with a ZnO layer (Figure 4.4.5), using a procedure and formulation developed by Dr Elodie Destouesse (see Chapter 3). Subsequent testing showed that doing so completely eliminated the problem of delamination of the active layer.

samples in this study (all except the Ag/WO₃) are higher; however, Dupont, *et al.* postulate that there would be an unfavourable interaction between the hydrophilic PEDOT:PSS layer and the hydrophobic P3HT:PC₆₁BM BHJ active layer in their samples that would decrease adhesion between the top layers and the active layer and result in the especially low fracture energies.¹²² It is therefore unsurprising that in the absence of such an interaction, most of the samples in this study would have higher fracture energies, and perhaps indicates that the results for the Ag/WO₃ sample are anomalous.

In addition to studying the fracture energy, the fracture paths through the samples were also analysed, first by visual inspection and then by XPS if the sample appeared to be fracturing at the active layer/HTL interface (Appendix B). An example of the difference in texture between a sample that fractures in the active layer and one that fractures at the HTL/active layer interface is shown in Figure 4.4.7.

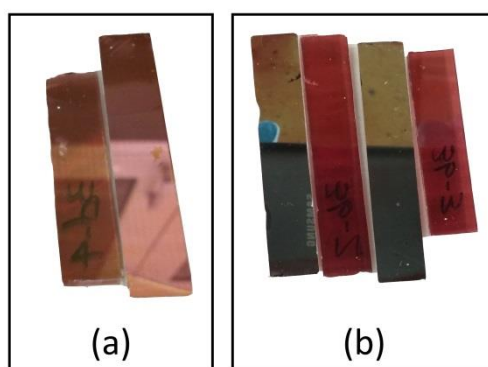


Figure 4.4.7: Photographs of fracture analysis samples that (a) fractured in the active layer and (b) at the HTL/active layer interface. Note that in (a) the top half of the device is shown on the right, and the bottom half on the left. In (b) the order is: top, bottom, top, bottom for the two fractured samples shown.

As the difference in texture between a sample that fractures within the active layer and one that fractures at the BHJ/HTL interface is substantial, visual inspection is usually sufficient to correctly identify the fracture path (although in this study interfacial fracturing was confirmed by XPS). When the unaged samples were fractured, all of the top halves of the fractured samples appeared metallic, consistent with delamination at the active layer/HTL interface. This was confirmed in all but one case. As shown in Figure 4.4.6, the Al/WO₃ samples had a very thin layer of active layer on their top halves that was not visible to the naked eye. This layer was, however, extremely thin, as all trace of carbon peaks in the XPS data were removed after only 30 seconds of argon sputtering (1 kV, 0.5 μ A); as only two spots (on separate slices) were tested, it is difficult to know whether this layer covered the entire surface of the fractured sample or just the areas tested. Given the proximity of the fracture path to the interface, these samples were considered as having fractured, like the rest, at the active layer/HTL interface.

4.4.4. Fracture analysis trends with thermal ageing

The evolution of the samples' fracture energy and fracture path are shown in Figure 4.4.8. The data obtained from the XPS survey scans used to determine the fracture paths in the samples that fractured at the active layer/HTL interface can be found in Appendix B.

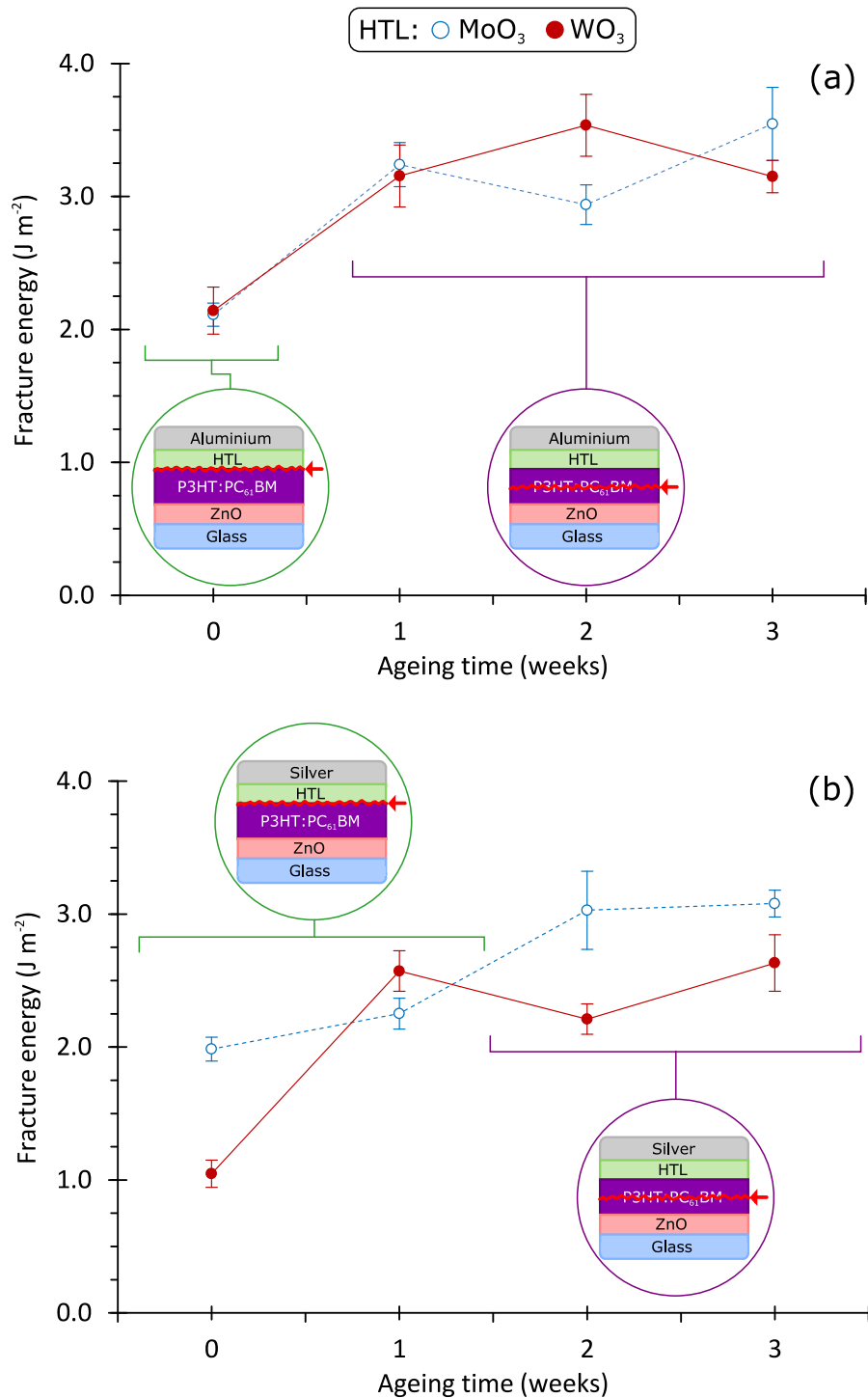


Figure 4.4.8: Evolution of the fracture energy of the samples with (a) aluminium electrodes and (b) silver electrodes. The insets show the fracture paths in the samples as determined by visual analysis or XPS. Uncertainties represent a standard error when averaged across 20-60 measurements. For reference to earlier experiments, three weeks is 504 hours.

In the first week of ageing, all the samples display an increase in fracture energy. The increase is on the order of 1.0 J m^{-2} in all but the Ag/MoO₃ samples – these show a much smaller increase after one week, though they are measured to have a similar fracture energy to the Ag/WO₃ samples and show a more significant increase in the second week of thermal ageing. This increase in the fracture energy is an evidence of interface strengthening for all the material combinations, whether the samples are

fracturing in the BHJ (Al samples) or at the interface (Ag samples). This is the only way an increase of the fracture energy can be observed compared to the unaged control samples.

However, there is no certainty that these increases have the same origin – different materials are present at the interfaces in each case. Evidence for the increases having different origins comes from the migration of the fracture path during the same time. In the aluminium devices, the fracture energy increases to 3.0 J m^{-2} and the fracture path migrates immediately to within the active layer, i.e. the fracture no longer propagates via delamination of the top layers from the active layer but rather by decohesion of the active layer. This indicates that the adhesion at the HTL/BHJ interface increased beyond the cohesion of the active layer, but it does not reveal whether this was entirely due to the increase in adhesion, or if it was also due to a decline in cohesion of the active layer. In the case of the silver samples the fracture energy increases to $2.2 - 2.6 \text{ J m}^{-2}$ but the fracture path remains at the HTL/active layer interface. This indicates that there has been an increase in adhesion of the top layers to the active layer in the silver-containing samples, and that if a decline in cohesion of the active layer has occurred, it was not by enough to cause a shift in the fracture path. Based on the fracture energies and paths of the two sets of samples, it is reasonable to conclude that the cohesion energy of the BHJ is somewhere between 2.6 J m^{-2} and 3.0 J m^{-2} after one week of thermal ageing.

In the long term (after two or more weeks of ageing), all of the samples fracture in the active layer, without exhibiting significant changes in the fracture energy. This movement of the fracture path could be a sign of a weakening of the active layer. Evidence for weakening comes from the behaviour of the Ag/WO₃ samples between the end of week one and the end of week two of ageing. In that time the fracture path shifts from the HTL/active layer interface to within the active layer but, crucially, there is negligible change in the fracture energy. The only way that this behaviour can occur is if the active layer cohesion strength decreases at the same time as the adhesion between the HTL and active layer increases, as this is the only way for the active layer to become the weakest point in the device without a change in the fracture energy.

It is evident from the fracture data obtained from the silver samples that there are two phenomena occurring in parallel: an initial increase in the adhesion of the top layers to the active layer and a longer-term weakening of the active layer. It is worth considering the timescales on which these occur and comparing them to the changes in the photovoltaic parameters observed at the same time. The increase in the adhesion of the top layers takes place over the same timescale as the loss in V_{oc} and FF observed in the Ag/MoO₃ samples with thermal ageing (Figure 4.2.8 and Figure 4.2.9), while the decline in the strength of the active layer correlates to the long-term J_{sc} -driven degradation observed in all of the samples (Figure 4.2.6 and Figure 4.2.7). The latter degradation mechanism was assigned to changes in the morphology of the BHJ active layer – in particular, the growth of donor and acceptor domains beyond the exciton diffusion length giving rise to an increase in geminate recombination (see section 4.2.3). If this indicates a significant phase segregation of the donor and acceptor species, it would likely mechanically weaken the active layer as the two phases become less intermixed. It has been demonstrated previously that increased phase separation in a BHJ active layer facilitates crack propagation in the boundaries between P3HT-rich and PC₆₁BM-rich domains.^{122,165} Moreover, it has been shown that if a fullerene-rich layer forms (as might occur with vertical phase segregation), the fullerene layer is weaker.¹⁹² Fullerenes can also act as defects in polymer matrices, so fullerene domain growth could place the polymer matrix under stress, reducing

the external stress required to propagate a fracture in the active layer.¹⁹² For these reasons, it is likely that the phase segregation is simultaneously responsible for both the J_{SC} loss and the reduction in the mechanical strength of the active layer with thermal ageing.

Relating the V_{OC}/FF -driven degradation mechanism identified in section 4.2.4 to the strengthening of the active layer/HTL interface in the early stages of thermal ageing is not as clear-cut. It is true that the timescales of each phenomenon are matched; however, much like the increase in roughness of the devices observed in section 4.3, the correlation is incomplete. While the improvement in adhesion is observed with the silver electrode and both HTL materials, the V_{OC}/FF loss is only observed with the combination of silver and MoO_3 . If the increase in adhesion is related to the V_{OC}/FF loss, it follows that there must be an additional reason why the latter is only observed with MoO_3 HTLs. However, an increase in adhesion does shed light on some of the proposed reasons for the material selectivity of this degradation that were discussed in section 4.2.4 – namely the possibility of electrode delamination. This can be explicitly ruled out based on the fracture analysis results – any delamination would easily be identified by fracture analysis as a decline in adhesion at the HTL/active layer interface, and the opposite is observed.

On the other hand, an increase in the adhesion of the top layers to the active layer would be consistent with inter-diffusion. Any intermixing of the layers in the device would effectively increase the surface area of a delaminating fracture, thereby raising the requisite fracture energy (see section 4.4.1). This phenomenon has been observed by Dupont, *et al.* in inverted OPV devices that used PEDOT:PSS HTLs.¹²² Initially (as noted in section 4.4.3), samples with PEDOT:PSS interlayers were found by the authors to have low fracture energies and to delaminate at the HTL/active layer interface due to unfavourable interactions between the hydrophobic active layer and hydrophilic PEDOT:PSS.¹²² However, as the devices were thermally annealed, the two layers inter-diffused, forming a mixed layer at the HTL/active layer boundary that in turn significantly increased the fracture energy of the devices.¹²² If inter-diffusion is occurring in the early stages of thermal ageing in this study, then an improvement in adhesion of the top layers to the active layer would be expected. The presence of diffused species in the active layer could, as discussed in section 4.2.4, give rise to an increase in charge trapping near the interface that would increase the monomolecular recombination rate, lowering V_{OC} ,^{119,158} and lead to space charge formation, lowering the FF by screening the internal electric field.¹³⁴

The presence of diffusion would also agree with the observations made during the AFM and RBS study (section 4.3). While these techniques show that there is a significant increase in the roughness of silver electrodes with thermal ageing in inverted OPV devices and simplified devices, they cannot prove or disprove that diffusion is occurring, as changes in the elemental profile of silver with thermal aged observed in RBS experiments can be explained by roughness changes, diffusion, or both. However, the RBS data do explicitly demonstrate that the elemental profile of aluminium does not change, and therefore that aluminium does not diffuse, with thermal ageing. Although there is an increase in the fracture energy of the aluminium samples, this cannot be attributed to diffusion and therefore must occur via another mechanism, such as improved contact between the layers due to an annealing effect (section 4.2.2), or changes in the bonding environment at the interface.

4.5. XPS depth profiling and Kelvin probe analysis

4.5.1. Overview

In order to understand the changes in the silver-containing samples during the fracture analysis experiments that gave rise to the increase in adhesion of the top layers to the active layer with thermal ageing (section 4.4), the fractured samples underwent physical characterisation via two techniques: X-ray photoelectron spectroscopy (XPS) elemental depth profiling and Kelvin probe analysis.

XPS is a non-destructive surface analysis technique which can give information about the elemental composition of a surface as well as the oxidation state of the elements present in the sample. It functions by irradiating a sample with X-rays that excite core electrons in surface atoms via the photoelectric effect. The ejected electrons are captured and measured. The electron binding energy (the difference in energy between the orbital they occupied and vacuum energy) can be found by subtracting the kinetic energy of the captured electron from the X-ray energy. This binding energy is characteristic of the element from which the electron was emitted as well as the oxidation state of the atom.¹⁹³ However, it is a surface analysis technique that is only capable of analysing elemental composition up to a few nanometres deep in a sample (depending on its X-ray and electron cross-sections).¹⁹³ In order to obtain an elemental depth profile it is necessary to use ion bombardment sputtering to etch the sample. In this study, this was done using an argon ion beam. Unlike RBS, this technique is destructive to the sample and is limited in how deep it can analyse, as sputtering for too long can distort the results due to both the preferential etching of some elements over others and to the intense heat the beam generates.¹⁹³ The use of a higher-current etching beam can etch deeper and faster, but this may also lower the depth resolution.¹⁹³ This trade-off means that, in this study, only samples that fracture at, or near, the HTL/active layer interface could be analysed using this technique (Figure 4.5.1); those samples that fractured in the active layer would require etching through ca. 100 nm of P3HT:PC₆₁BM BHJ before the profile of the top layers could be examined. For more information on XPS and its use in elemental depth profiling, the reader is encouraged to read Professor Siegfried Hofmann's book, *Auger- and X-Ray Photoelectron Spectroscopy in Materials Science* (Springer Berlin Heidelberg, 2013).

Kelvin probe analysis is an analytical method of determining the work function (or more accurately, surface potential) of a sample by measuring the contact potential difference (CPD) between it and another sample with a known work function.¹⁹⁴ The technique is based on a series of experiments carried out by Lord Kelvin in the 1890s in which he identified and measured the CPD of a number of different metallic samples.¹⁹⁵ The CPD arises when two different conducting samples with different work functions in close proximity to each other are placed in electrical contact with one another.¹⁹⁴ In order to equilibrate the Fermi levels of the two samples, charge flows from one to the other, establishing a charge imbalance, and thus a potential difference, between the two samples (the CPD).¹⁹⁴ Kelvin probe analysis measures the CPD by applying a bias voltage to the samples in order to reach the zero charge point (i.e. no transferred charge between the two samples), which is exactly equal and opposite to the CPD.¹⁹⁴ In a standard Kelvin probe experiment, the work function of the probe is determined by measuring its CPD with a sample of known work function (in this experiment highly oriented pyrolysed graphite, or HOPG), and then the work function of the sample is determined from the work function of the probe. In some cases, this technique can be paired with

AFM to carry out *Kelvin probe force microscopy*,¹⁹⁴ but that was not done in this experiment. As this technique requires that a sample be electrically conductive, only samples that fracture at the active layer/HTL interface can be analysed using this technique (Figure 4.5.1).

4.5.2. Sample structure

The sample structure, preparation, and measurement in the XPS depth profile and Kelvin probe experiments are depicted in Figure 4.5.1.

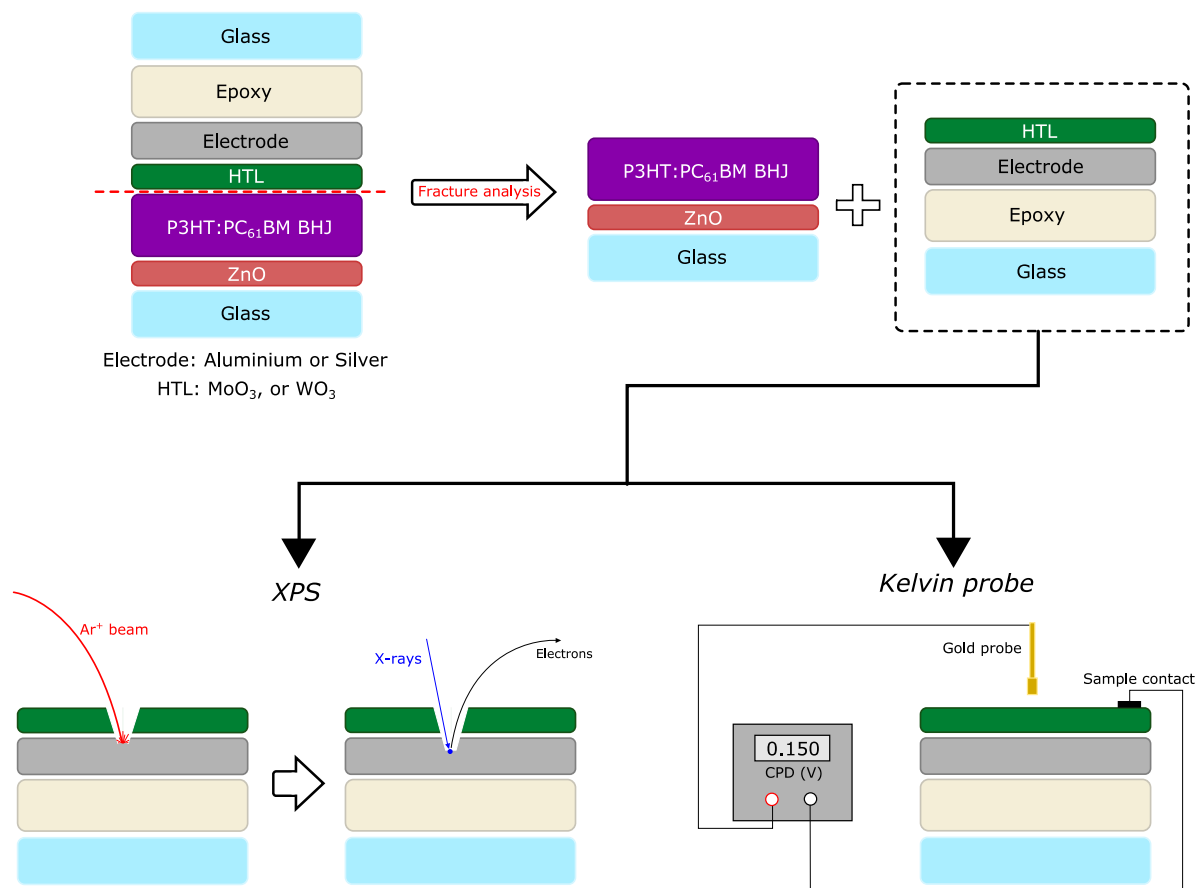


Figure 4.5.1: An illustration of the sample preparation and measurement in the XPS depth profile and Kelvin probe experiments.

4.5.3. XPS elemental depth profile measurements

The results of the XPS elemental depth profile experiments with the aluminium-containing unaged control samples are shown in Figure 4.5.2. While no data were able to be obtained from aged aluminium samples (because they fractured in the active layer), the unaged samples do differ substantially from their silver counterparts. Unlike the silver-containing samples, which show clear demarcation between the different layers in the device (Figure 4.5.3), there appears to be some intermixing between the metal electrode and the HTL in the aluminium samples. As the sample is sputtered for increasingly longer times, some of this intermixing is possibly a result of etching artefacts,¹⁹³ though this is unlikely to explain it entirely. It may be that some intermixing occurred during the deposition of the aluminium electrode, as it was deposited at higher temperatures than the silver electrode. Certainly its presence in control samples means that it cannot be a result of any thermal ageing effects.

Another interesting observation is the oxygen concentration trend in the intermixed region, which increases rather than declining with the molybdenum or tungsten (as would be expected). This could be a sign of stoichiometric variation in the HTL oxide or, equally, an etching artefact. A further possibility is that this is a sign of a redox interaction between the aluminium and HTL, forming small regions of Al_2O_3 . This could raise the local oxygen density to cause the oxygen concentration trend in Figure 4.5.2. However, it is likely that if this were occurring, it would also impact the J_{SC} of the device as it would lower the effective area of the electrode¹³⁴ and, as shown in Table 4.2.1, the J_{SC} values of the aluminium-containing OPV devices are similar to the silver-containing ones (except in the case of the Al/PEDOT:PSS device due to corrosion of the electrode – see section 4.2.2).

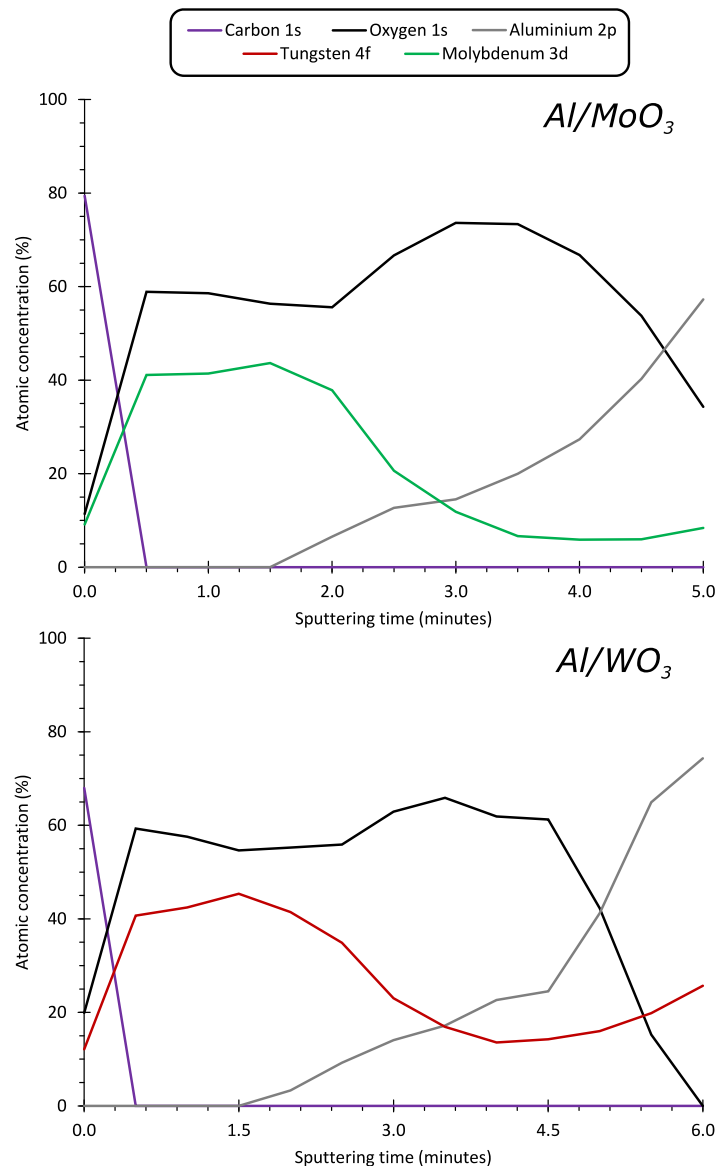


Figure 4.5.2: XPS elemental depth profile data obtained from fractured control samples with aluminium electrodes. The XPS measurements were carried out by Nicholas Rolston.

The XPS elemental depth profile data from the fractured samples with silver electrodes are shown in Figure 4.5.3. Unlike the aluminium samples shown above, the fracture path in the silver samples remained at the active layer/HTL interface during the first week of thermal ageing; because of this, samples that have been aged one week can be depth profiled in addition to the control samples. It is

evident from the data shown in Figure 4.5.3 that a substantial change in the structure of the samples occurs in the first week of thermal ageing. The previously well-segregated electrode, HTL and active layer exhibit a high degree of inter-mixing. At the interface between the HTL and the BHJ in the control samples, there is very clear delineation between the carbon of the active layer, and the tungsten/molybdenum and oxygen of the HTL. The transition between the two takes place in the first 30 seconds of etching. At the silver/HTL interface the transition is more gradual; however this may be due to an etching artefact. In the aged samples, the HTL elements are smeared over all of the sample depth that was analysed, and can still be detected after five or six minutes of sputtering. There doesn't appear to be any clear difference between the two HTLs in this respect. This is coupled with the concentration of carbon from the active declining much slower with depth, so much so that it intermixes with silver from the electrode. The silver concentration increases much more slowly with depth in the aged samples than was observed in the control samples.

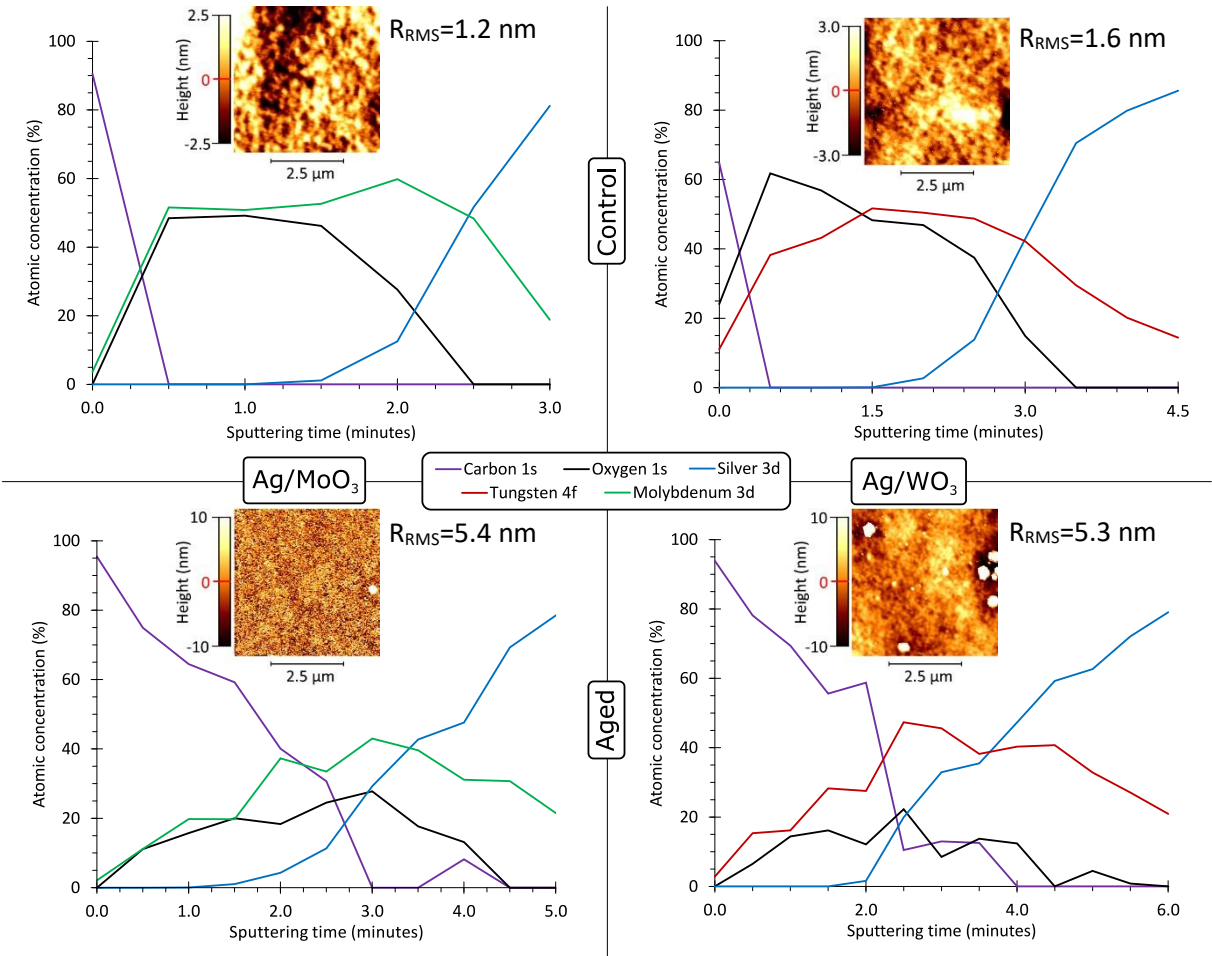


Figure 4.5.3: XPS elemental depth profile data obtained from the fractured samples with silver electrodes. The control samples were unaged, while the aged samples were thermally aged at 85°C for one week. The insets show AFM height data obtained from the same samples along with their RMS roughness values. The XPS and AFM measurements were carried out by Nicholas Rolston.

It is also important to note the differences in sputtering times between the control and aged samples, which are significantly longer in the case of the latter. It is difficult to correlate the position within an un-fractured sample of the two experiments to each other as, while it is clear that both sets of samples are fracturing at the active layer-HTL interface, the position of that interface is poorly defined in the case of the aged samples. It could be assumed that mid-point of the HTL is at the same

depth in an un-fractured sample in both the aged and control samples, which would allow direct comparison of the elemental profiles in Figure 4.5.3 by matching the mid-point of the HTL. However, there seems little basis on which to make this assumption, especially when one considers the high degree of intermixing exhibited by the aged samples.

While this is *a priori* evidence for inter-diffusion between the layers, other possibilities should first be considered:

- these results are due to roughness increases; or
- they are an artefact of the argon etching.

As seen in the RBS measurements in section 4.3, an increase in the roughness of a sample can result in changes in the elemental profile of a sample similar to those resulting from inter-diffusion. This is equally true of XPS depth profiling. An added complication arising from rough samples is that they can experience uneven etching by the argon beam, which would further exacerbate the above effect (although this problem is mostly solved by rotating the sample during etching).¹⁹³ However, the observed inter-mixing cannot be due to increases in sample roughness, as AFM measurements of the same samples showed only minimal increases in roughness with thermal ageing (Figure 4.5.3). The likely reason for the difference between this experiment and the RBS/AFM experiments in section 4.3 is that the surface roughness of the samples being analysed in the XPS depth profile experiment is determined by the fracture path, rather than by changes during ageing.

The other possibility is that the observed inter-mixing is a result of etching artefacts. While this is almost certainly a factor with longer etching times,¹⁹³ the intermixing is apparent even after only a very short amount of sputtering time. Moreover, both the control samples and the aged samples were subjected to the same sputtering conditions, and yet inter-mixing is only seen in the aged samples. If inter-mixing were due to the sputtering alone, then the same effects would be expected in the control samples, which is not observed (Figure 4.5.3).

It follows that the observed changes in the elemental profile of the silver-containing samples are due to inter-diffusion between the silver electrode, HTL and active layer. This is entirely consistent with the results observed in the fracture analysis experiment, as inter-diffusion would increase the surface area, and thus the surface energy requirement, of any interfacial fracture.¹⁹⁰ It is also consistent with the results of the RBS experiment, as the changes in the elemental profile observed in that experiment could be caused by both inter-diffusion and an increase in roughness.

4.5.4. Kelvin probe measurements

The results of the Kelvin probe analysis of the samples that fractured at the active layer/HTL interface are shown in Figure 4.5.4.

There is significant variation in surface potential between the control samples, both in the HTL material and the electrode material. This indicates that the surface potential being measured actually reflects an ensemble average of the work functions of the materials used, rather than just the material at the measured surface (the HTL). The samples using WO_3 as an HTL have an increased surface potential compared to their MoO_3 counterparts, but this is much more pronounced with the sample with an aluminium electrode than the one with a silver electrode.

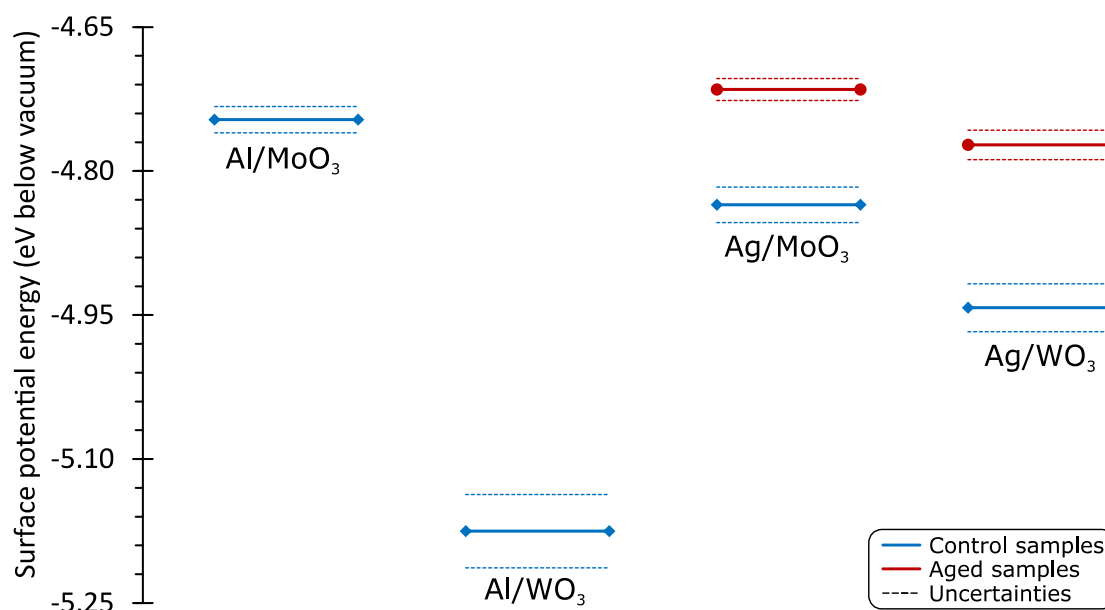


Figure 4.5.4: Kelvin probe analysis of the fractured samples. The levels in blue (diamonds) correspond to the unaged samples, while those in red (circles) correspond to samples with silver electrodes that had been aged one week. Uncertainties (dashed lines) represent a standard error when averaged across 50 measurements.

The effect of thermal ageing is to lower the surface potential energy of the silver samples, by 140 meV in the case of the Ag/MoO₃ samples and by 160 meV in the case of the Ag/WO₃ samples. This is consistent with the previous observations of inter-diffusion in this study, as a change in the composition of the measured (fractured) surface would result in a change in the surface potential.

It was noted earlier in this chapter that in the first 100 hours of thermal ageing, inverted OPV devices with MoO₃ HTLs and silver electrodes exhibit a substantial decline in FF and V_{oc} that is only observed in this combination of materials. It was stated in section 4.2.4 that one of the possible causes of this behaviour is diffusion of silver into the active layer of the device. This was later shown to occur and to take place on the same timescale as the V_{oc} loss, but without the same material selectivity. One possibility is that the diffusing silver acts to dope the MoO₃ HTL and not the WO₃ HTL, which could have an impact on the V_{oc} . If that were the case it is likely that it would be apparent in the Kelvin probe data; however, as Figure 4.5.4 shows, the diffusing silver has approximately the same effect on the surface potential of the WO₃ sample as on the MoO₃ sample. This leaves the formation of charge traps due to the diffusion of species from the top layers into the active layer as the most likely explanation for the FF and V_{oc} loss. It is unclear why charge traps are only formed with a MoO₃ HTL. This could be explained by a chemical interaction between the MoO₃ and the diffused silver; it is also possible that the diffused MoO₃ is actually responsible for the charge trapping, and that this does not occur in the aluminium-containing samples because these samples do not exhibit inter-diffusion between the layers at the hole-extraction interface.

4.6. Summary

In this chapter, the thermal degradation of inverted OPV devices using different HTL and electrode materials has been studied with the aim of relating any observed losses in OPV device performance to physical changes in the devices. It was shown that all devices with P3HT:PC₆₁BM BHJ active layers exhibited J_{sc} loss with long-term thermal ageing, which is most likely due to morphology changes in

the BHJ. This degradation was insensitive to the HTL and electrode materials and was only eliminated when a higher T_g polymer, PCDTBT, was used in the place of P3HT in the BHJ. An additional degradation mechanism driven by a loss of V_{oc} and FF was also identified in the thermally-aged inverted OPV devices. This mechanism was only observed in devices that had both a MoO_3 HTL and a silver electrode, and not in any other material combination, suggesting that the presence of both is critical for this degradation pathway and, therefore, that this mechanism is interfacial in origin.

An RBS study was carried out on samples with a simplified architecture that mimics the hole extraction interface in inverted OPV devices. It was observed that samples with silver electrodes exhibited a change in their elemental profile with both accelerated thermal ageing and thermal ageing under operating conditions that was not seen in aluminium samples. This behaviour was observed with both MoO_3 and WO_3 HTLs. It was initially supposed that this was a sign of diffusion of the silver into the samples; however, further analysis of the RBS data indicated that at least one component of the changes in elemental profile arises from an increase in the surface roughness of the sample. This was confirmed in subsequent AFM analysis, which showed substantial increases in the surface roughness of both simplified and full devices with silver electrodes. This roughness increase was not enough to perturb the functioning of the top electrode providing that the electrode was sufficiently thick; however, it was demonstrated that, in thin electrode devices, thermal ageing resulted in island formation in the electrode that removed its ability to carry a current.

A fracture analysis study was carried out on large samples, for which a procedure for depositing a P3HT:PC₆₁BM BHJ active layer by Doctor blade coating was developed. The fracture analysis data showed that the samples initially fractured at the active layer/HTL interface, but that this fracture path moved to the active layer with thermal ageing as the adhesion of the top layers of the samples to the active layer improved and the cohesion of the active layer declined. The long-term decrease in the cohesion of the active layer was attributed to changes in the BHJ morphology and is therefore linked to the long-term decline in the J_{sc} that occurs after 300 hours of thermal ageing at 85°C.

The increase in the adhesion of the top layers to the active layer occurred on different timescales for the silver and aluminium-containing samples. In the silver samples, the fracture path remained at the interface after one week of ageing, enabling these samples to be studied by XPS elemental depth profiling and Kelvin probe analysis. It was shown that in the first week of ageing at 85°C, the silver-containing samples exhibit inter-diffusion between the electrode, HTL and active layer, which is most likely the origin of the increase in adhesion. The aluminium samples were not able to be analysed in this way; however, it is unlikely that they behave in the same way when subjected to thermal ageing, as that would be expected to be visible in the RBS data.

The inter-diffusion of the layers at the hole extraction interface with thermal ageing occurred on the same timescale as the V_{oc}/FF degradation observed in the OPV device study, indicating that the two phenomenon are likely related. The presence of diffused species in the active layer would explain a loss of V_{oc} and FF via charge trapping as this would increase the monomolecular recombination rate, and the accumulation of space charge, screening the internal field of the device. The problem with this explanation is that inter-diffusion is seen with both WO_3 and MoO_3 HTLs, but the V_{oc}/FF mechanism is only seen with MoO_3 ; there must be an additional interaction between the silver and MoO_3 that explains it.

To conclude, the degree and nature of thermal degradation in inverted OPV is, to a large extent, determined by the choice of materials used for the device. Many of the degradation mechanisms studied here can be avoided by choosing to use different materials in the active layer, HTL and electrode. For instance, a device with a relatively thick aluminium electrode, MoO₃ HTL, and PCDTBT:PC₇₁BM active layer would not exhibit any of the degradation mechanisms studied here due to both the high morphological stability of PCDTBT and the thermal stability of the aluminium-MoO₃ electrode/HTL combination. Furthermore, such improvements in performance stability need not require any sacrifices in efficiency. It should also be mentioned that not all of the trends with thermal ageing listed here are detrimental to the longevity of the device. The improvement in adhesion of the top layers of the samples to the active layer (noted in the fracture analysis experiment) is beneficial for mechanical stability, which would be important in any application of flexible devices. In some materials combinations, this can represent a trade-off between mechanical stability and performance (Ag/MoO₃), but this can be avoided through careful materials selection.



Chapter 5

Degradation of OPV solar cells under simulated working conditions

5.1. Introduction

When an OPV device is used in any commercial setting, it will be exposed to a number of degradation stimuli which interact together and separately with the materials in the device to lower the device's performance. Some of these stimuli can be reduced, or mostly removed, from the device without impeding its function. As discussed in Chapter 2, these are known as *extrinsic degradation stimuli*. Examples of these include oxygen and humidity. While both of these can be controlled through encapsulation, no encapsulation is perfect, so it is still important to understand how these stimuli can act to shorten the lifetime of a device.

There are also intrinsic stimuli which cannot be reduced, as their presence is fundamental to the operation of the device. An example of this was discussed in Chapter 4, thermal degradation, which is an unavoidable consequence of exposing an absorbing material to solar radiation, and can only be mitigated through designing devices that are less vulnerable to heat. Light also plays a significant role in the degradation of OPV solar cells, and exposure to light is critical to the operation of OPV devices. In this sense light may be considered an intrinsic degradation stimulus, as its removal inhibits the functioning of the device. On the other hand, the most damaging portion of the solar spectrum with respect to the photodegradation of OPV is UV radiation,³⁰ but this comprises a relatively small portion of the sun's power output.¹⁷⁹ Consequently, these effects can be greatly reduced through UV filtration, or even through the addition of photo-conversion layers that down-convert the UV radiation into visible radiation, without adversely affecting device performance.¹⁹⁶ In this sense, light can also be considered an extrinsic degradation stimulus.

When the PCE of a device is monitored under operating conditions, a curve similar to the one in Figure 2.4.1 is observed.^{30,131} The three components of the curve (burn-in, linear, and catastrophic failure) vary from device to device due to the interplay between the degradation stimuli that are present and the materials used in the device. To effectively study degradation, it is necessary to compare the interaction of each degradation stimulus with different combinations of materials and observe how each of the different stages of the degradation curve is affected. For instance, the burn-in, which can represent a significant loss of efficiency, has been shown to be present even when no degradation stimuli other than visible light are present.^{148,159} The origin of the burn-in varies between material combinations and is typically driven by a decline in multiple cell parameters.^{158,159} A reversible decline in V_{OC} is frequently observed in the burn-in but shows great variability between active layer and ETL materials, strongly suggesting that the phenomenon has an interfacial origin.¹⁵⁸ As discussed in Chapter 2, this V_{OC} loss can be eliminated entirely if a buffer layer is placed between the ETL and the active layer,^{158,163} and it is greatly reduced when inverted devices are aged before the application of the top layers, showing that the origin of this V_{OC} loss is at the charge-extraction

interfaces.¹⁵⁸ However, an irreversible V_{OC} decline can also be observed in some specific cases, specifically with amorphous donor polymers, and is due to a broadening of the density of states.¹¹⁹ In some devices, this is accompanied by a decline in J_{SC} ; this effect varies depending on the polymer used in the active layer (typically observed with P3HT) and is associated with photochemical reactions in the active layer¹⁵⁸—specifically, the dimerisation of fullerene acceptors, which is facilitated by how they pack within the polymer matrix.¹⁶⁶ FF -driven degradation is also observed in the burn-in of some devices, particularly those using PCDTBT; unlike the J_{SC} -driven degradation observed in P3HT devices, this is attributed to an interfacial process, as it is not observed in devices that are aged prior to the deposition of their top layers.¹⁵⁸ Interestingly though, the FF loss has been demonstrated in a range of HTL and electrode materials and in both device geometries,^{158,159} indicating that the FF loss concurrent with photo-ageing, despite being interfacial in origin, has no apparent material dependence (excepting the active layer). This shows that while burn-in is frequently accepted as an inevitable, intrinsic phenomenon,^{22,148,156} it can be greatly reduced through careful choice of materials.

As discussed in Chapter 2, the lifetime of a device is frequently defined in the linear regime - the part of the ageing curve that immediately follows the burn-in.^{22,156} This section of the curve is highly dependent on the presence of extrinsic degradation stimuli. Within a highly controlled laboratory setting in which OPV samples are exposed to visible radiation (no UV) in a pure nitrogen atmosphere at temperatures well below the T_g of the polymer, it has been shown that little to no loss of performance occurs across thousands of hours of continuous light exposure.¹⁴⁸ Although promising, these conditions do not represent the commercial realities of how OPV will be used, and it is necessary to understand how to minimise the devices' vulnerability to UV light, oxygen and water.

The various mechanisms by which photooxidation occurs in polymers that are used in BHJ active layers have been extensively researched (and were discussed at length in Chapter 2). The oxygen attacks initially at side-chains in the polymers via a photo-activated radical mechanism.⁶⁷ Cleavage of the sidechains follows. While not catastrophic to the function of the polymer in itself, the radical liberated from the cleavage can further propagate into the polymer backbone, causing further cleavage reactions, disrupting the conjugation of the polymer and inhibiting absorption.⁶⁷ The end result is photobleaching and a complete loss of photocurrent.^{65,67} In a device, this can manifest as a rapid decline in J_{SC} ; however, this is not always the case, as competing crosslinking reactions with fullerene acceptor molecules in the BHJ can suppress radical propagation in some polymers, in particular PCDTBT, partially stabilising the active layer.⁹⁹

In addition to the role oxygen plays in the photobleaching of the active layer, oxygen can attack the active layer via other pathways. As discussed in Chapter 2, oxygen can form charge transfer complexes with polythiophene rings,³⁰ effectively doping the polymer.¹⁰⁸ This doping can cause a decline in the J_{SC} , which is highly detrimental to device efficiency when combined with the effects of photobleaching.¹⁰⁸ Oxygen can also be detrimental to charge transport through the formation of deep charge traps.¹⁰⁸ This increases the monomolecular recombination rate, thereby decreasing V_{OC} , and results in an accumulation of space charge that shields the internal field of the device and decreases the fill factor.¹⁵⁹

The active layer is not the only part of the device that is vulnerable to oxidative attack. Oxygen can also attack the interlayers and electrodes of the device. Depending on the structure of the device and

the materials used in the device, oxygen can ingress through the sides of the device or diffuse through the electrodes and react to form an insulating oxide layer.¹³⁴ This oxide layer acts as a charge extraction barrier, causing significant FF loss or decreasing the effective area of the device.¹³⁴ The first phenomenon is usually reflected in the appearance of an s-shape in the IV curve and the second one results in a loss of J_{SC} without any change on FF and V_{OC} .¹³⁴ The appearance of the s-shape typically represents a catastrophic failure of the device.¹³¹ Water can also attack the interfacial regions in this way and is similarly reactive with low work function metals. This phenomenon is a particular problem in direct devices that utilise aluminium and calcium as electrode and ETL materials. Water has been shown to diffuse through aluminium/calcium electrodes and ingress through the sides of the device along with oxygen.¹³⁰ It was for this reason that the inverted device was developed, as inverted devices do not require the use of low work function metals and are therefore not vulnerable to this mechanism to the same extent.^{142–144}

Water is known to attack direct devices at the hole extraction interface when PEDOT:PSS is used as an HTL material.³⁰ PEDOT:PSS is usually extremely hygroscopic and absorbs water that diffuses into the device, leading to an increase in the sheet resistance and adversely affecting its charge extraction capabilities.³⁰ Furthermore, the PSS component of PEDOT:PSS is acidic and, in the presence of water, can corrode adjacent layers (particularly ITO).³⁰

This chapter examines the degradation of OPV samples under simulated operating conditions. These experiments used a custom-built environmental chamber (see Chapter 3) to monitor the cell statistics of up to 64 devices as they were exposed to simulated solar radiation (with a UV component, see section 5.2.3) in different atmospheric conditions, namely: dry nitrogen, dry synthetic air (20% oxygen in nitrogen), and humid nitrogen (76% relative humidity). The experiments were carried out in accordance with ISOS-L-2 protocols. In each experiment, different combinations of materials at the hole extraction interface were used in order to observe the different interactions the materials have with these degradation stimuli under illumination. By comparing the results for each material combination, it was possible to propose potential degradation mechanisms.

5.2. Photo-degradation studies under an inert atmosphere

5.2.1. Analytical modelling of PCE loss

In order to compare many different OPV efficiency degradation curves, it is useful to fit them to mathematical models that can allow the easy and/or automated determination of the different ageing parameters of the cell, such as burn-in time (T_S), efficiency loss ($\Delta\eta_s$), and the time taken to get to 80% of the post burn-in efficiency (T_{S80}), commonly used as a definition for the device lifetime. As discussed in Chapter 2, the use of these models should be approached with caution, as they are unable to predict catastrophic failure of the device; being strictly empirical in origin, parameters predicted outside of the timeframe of an experiment may not reflect the real behaviour of the device. This is particularly true when the parameter being predicted, such as the T_{S80} , is many times greater than the timeframe of the experiments, as this can lead to unrealistic estimates.¹⁴⁸

A simple model of PCE loss with photo-degradation is the exponential-linear model:¹⁹⁷

$$\eta(t) = Ae^{-t/\tau} - Bt + C \quad 5.2.1$$

in which the exponential portion of the equation models the burn-in and the linear portion models the linear regime. This has the advantage that it is relatively simple to fit to experimental data, particularly after burn-in where the exponential component is negligible and the constants B and C can easily be found by linear regression. If the same definition of the burn-in is applied as was discussed in Chapter 2, in which the burn-in is defined as having ended when the exponential portion of the model has decayed to 1% of its initial value, then the T_S can be found from:

$$T_S = -\tau \ln 0.01 \quad 5.2.2$$

The proportional loss of efficiency in the burn-in can be found from:

$$\frac{\Delta\eta_S}{\eta_0} = \frac{\eta_S - \eta_0}{\eta_0} = \frac{-0.99A - BT_S}{A + C} \quad 5.2.3$$

and the value for T_{S80} is given by:

$$T_{S80} = 0.8T_S + 0.2 \frac{C}{B} \quad 5.2.4$$

Despite its simplicity, this model does have some disadvantages. While using a single exponential term to model the burn-in fits experimental data well,¹⁵⁶ using a linear term to fit the curve post-burn-in is potentially problematic when projecting beyond the timeframe of the experiment for the determination of T_{S80} . While the post-burn-in portion of the curve may be accurately represented by a linear trend within the experiment timeframe, there is little basis for the assumption that it is linear beyond this timeframe. Any time-variant function, when sampled on a sufficiently short timescale, can appear linear within a margin of error. Moreover, it should not be forgotten that the decline in PCE post burn-in is due to numerous chemical reactions that occur throughout the device. In the kinetics of chemical reactions, linear behaviour is only observed when the rate of a reaction is not dependent on the concentration of the reagents – a so-called “zero order” reaction, which is quite unusual.¹⁹⁸ Usually, either of two scenarios occurs: the rate of a reaction is dependent on the concentration of one reactant (a first order reaction), or only the concentration of one reagent, upon which the rate is dependent, is changing significantly (a pseudo-first order reaction).¹⁹⁸ First order and pseudo first order reactions can be modelled by the following integrated rate law:¹⁹⁸

$$\frac{[X]}{[X]_0} = e^{-kt} \quad 5.2.5$$

where $\frac{[X]}{[X]_0}$ is the fraction of the reagent X remaining after the reaction has proceeded for time t and k is the rate constant, which can be found from the Arrhenius equation:¹⁹⁸

$$k = Ae^{-E_a/k_B T} \quad 5.2.6$$

in which E_a is the activation energy, k_B is the Boltzmann constant, T is the absolute temperature and A is an empirical constant.

Explicitly relating the post-burn-in degradation trends of the PCE of a device to the kinetics of individual chemical reactions in the device would go well beyond the scope of this work. Such a

treatment would require the consideration of many complex variables beyond the kinetics of the reactions themselves, including the role that diffusion of oxygen and water into the devices plays in limiting the reaction rate as well competing side reactions. It is, however, more likely that the overall result of these considerations would have some exponential character than be purely linear.

It was for this reason that a purely exponential model was used in this experiment. The biexponential model favoured by Roesch, *et al.*,¹⁵⁶ which was discussed in Chapter 2, is an example of such a model. In this model, the loss of efficiency with photoageing is modelled by:

$$\eta(t) = Ae^{-t/\tau_1} + Be^{-t/\tau_2} \quad 5.2.7$$

in which A and B are scaling constants and the two τ terms are the time constants for the respective exponential terms.¹⁵⁶ Applying this model to real PCE data, and using the same definition of burn-in as the linear-exponential model (*vide supra*), it is possible to find the T_S with:

$$T_S = -\tau_1 \ln 0.01 \quad 5.2.8$$

and the T_{S80} with:

$$T_{S80} = T_S - \tau_2 \ln 0.80 \quad 5.2.9$$

The proportional efficiency loss in the burn-in is given by:

$$\frac{\Delta\eta_S}{\eta_0} = \frac{B(e^{-T_S/\tau_2} - 1) - 0.99A}{A + B} \quad 5.2.10$$

where A , B , and τ_2 are defined as in equation 5.2.7. As shown in Figure 5.2.1, the fit of ageing data by the biexponential model is similar to the linear-exponential, but the models would be expected to diverge long-term (beyond the end of the experiment). This indicates that estimates for the T_S and $\frac{\Delta\eta_S}{\eta_0}$ would be similar for the two models, but estimates for the T_{S80} may differ.

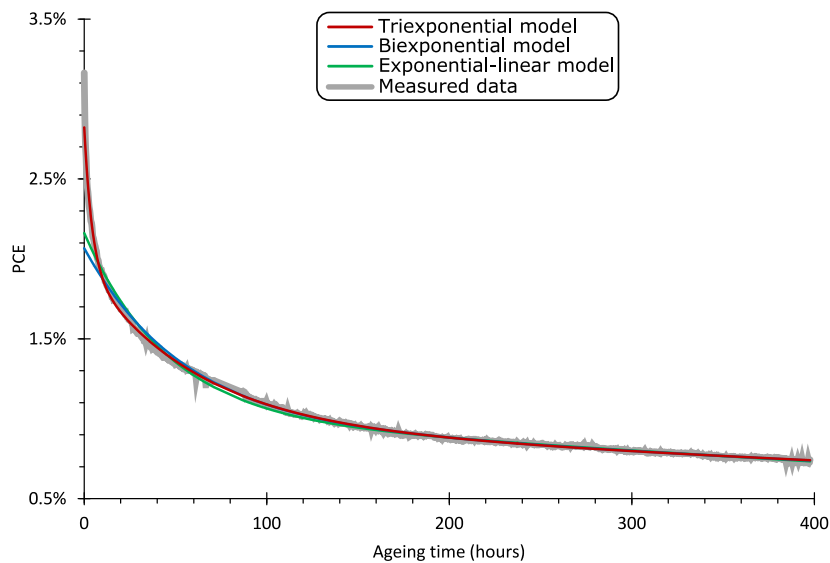


Figure 5.2.1: Ageing data obtained in this study from a photo-aged OPV device (grey) fit with a linear-exponential model (green), biexponential model (blue) and a triexponential model (red). The latter two models were fit using the algorithm developed for this study.

When the biexponential model was applied to the data measured in this study, it fit the long-term degradation behaviour well. However, this model was less accurate in modelling the initial degradation behaviour of some devices, as shown in Figure 5.2.1.

In some cases (although not all), the devices exhibit a very rapid loss of efficiency in the first few hours of ageing, then degrade at a more gradual rate before reaching the end of the burn-in. This two stage burn-in is not accounted for in the biexponential model; consequently, the following triexponential model was developed to accommodate it:

$$\eta(t) = Ae^{-t/\tau_1} + Be^{-t/\tau_2} + Ce^{-t/\tau_3} \quad 5.2.11$$

When applied to the PCE data measured from OPV devices that exhibit this two stage burn-in, the triexponential model fits the data more closely than the biexponential model (Figure 5.2.1). There is some minor divergence in the very early stages of the degradation, but this does not appear to affect any of the calculated values from the model. Using the triexponential model, the various ageing statistics for a device can be calculated using the following expressions:

$$T_{S1} = -\tau_1 \ln 0.01 \quad 5.2.12$$

$$T_{S2} = -\tau_2 \ln 0.01 \quad 5.2.13$$

$$T_{S80} = T_{S2} - \tau_3 \ln 0.80 \quad 5.2.14$$

$$\frac{\Delta\eta_S}{\eta_0} = \frac{\eta_S - \eta_0}{\eta_0} \approx \frac{C(e^{-T_S/\tau_3} - 1) - A - 0.99B}{A + B + C} \quad 5.2.15$$

where T_{S1} is the end of the first stage of the burn-in and T_{S2} is the end of the second stage of the burn-in (and thus the overall burn-in time). It should also be noted that in equations 5.2.13, 5.2.14, and 5.2.15 the contribution from the first exponential term in equation 5.2.11 is assumed to be negligible.

In order to fit the triexponential model to the ageing data, an algorithm was developed to integrate with the existing LabVIEW-based ageing data processing software discussed in Chapter 3. This algorithm is detailed in Figure 5.2.2. The development of this algorithm was required because of the large volume of data generated in a photodegradation experiment (10 to 15 million data points).

The premise of the algorithm is to split the data into three parts, in each of which one exponential term dominates. For instance, in Figure 5.2.1, the first exponential term is dominant in the first 20 hours of ageing, the second between 20 hours and 200 hours, and the third between 200 hours and 400 hours. The boundaries of these zones are initially chosen by the user but are refined by the algorithm, so an approximation is sufficient (the same initial estimates are usually valid for a full batch of devices). The algorithm starts by fitting the third exponential to the third zone (by linear regression of $\ln \eta$ vs. t), then fits the second exponential to the second zone (having subtracted the results from zone three from the data), and finally fits the first exponential to the first zone (having subtracted the results from zones two and three). This process is then repeated by feeding in the results from the first iteration (as shown in Figure 5.2.2) until the algorithm passes an iteration limit and stops, or satisfies the convergence criteria of less than 1% variation between iterations. The use

of this algorithm allowed the automatic determination of degradation statistics for a set of up to 64 devices.

In the cases where the biexponential model (equation 5.2.7) was a better fit, the same algorithm was used with the following modifications: only two zones were needed, the variable B was set to zero, and the steps involving zone B were omitted.

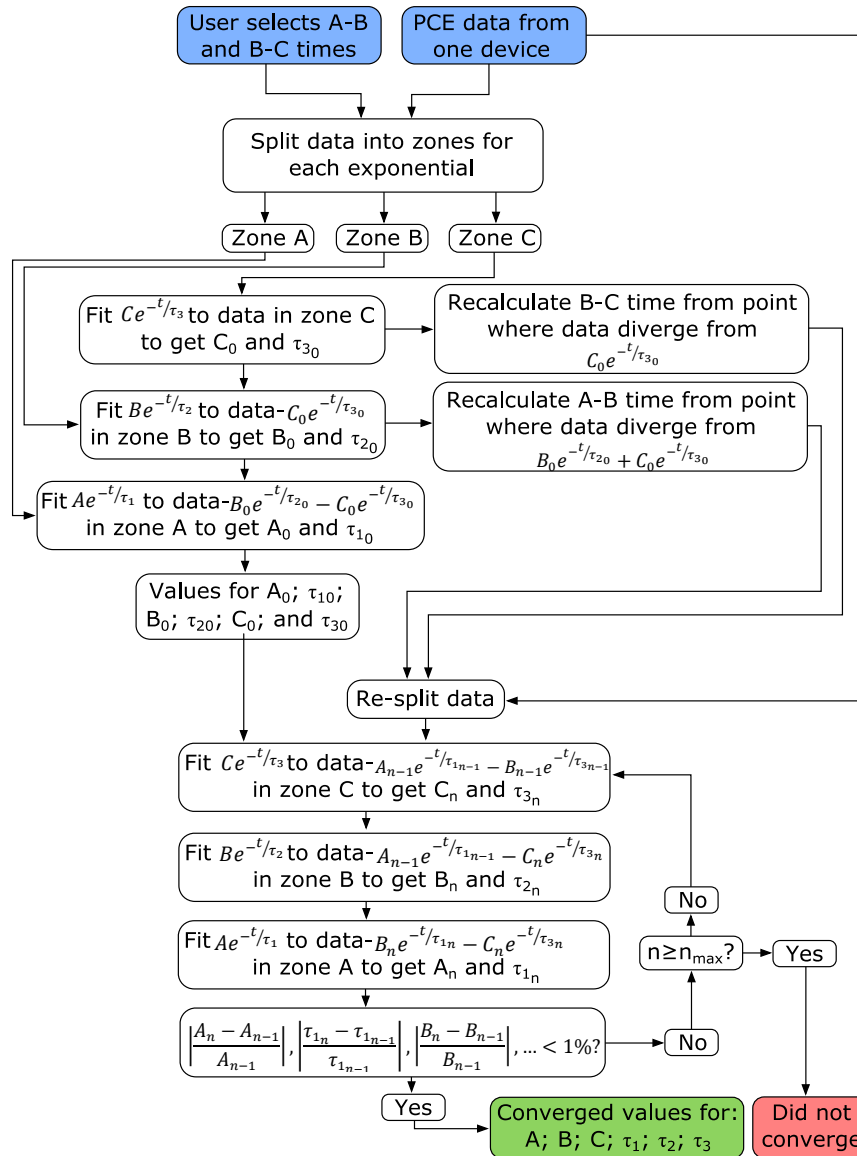


Figure 5.2.2: The algorithm used to fit the triexponential degradation model to the photo-ageing data.

5.2.2. Material-dependence of PCE ageing parameters

A photo-ageing experiment was carried out in an inert atmosphere with inverted OPV devices that used the same structure and materials as the thermal ageing experiments (Figure 4.2.1), omitting the Al/PEDOT:PSS combination due to the extreme intrinsic instability observed in this combination of materials in Chapter 4. The PCE trends observed over the course of this experiment are shown in Figure 5.2.3, and the PCE degradation statistics in Figure 5.2.4.

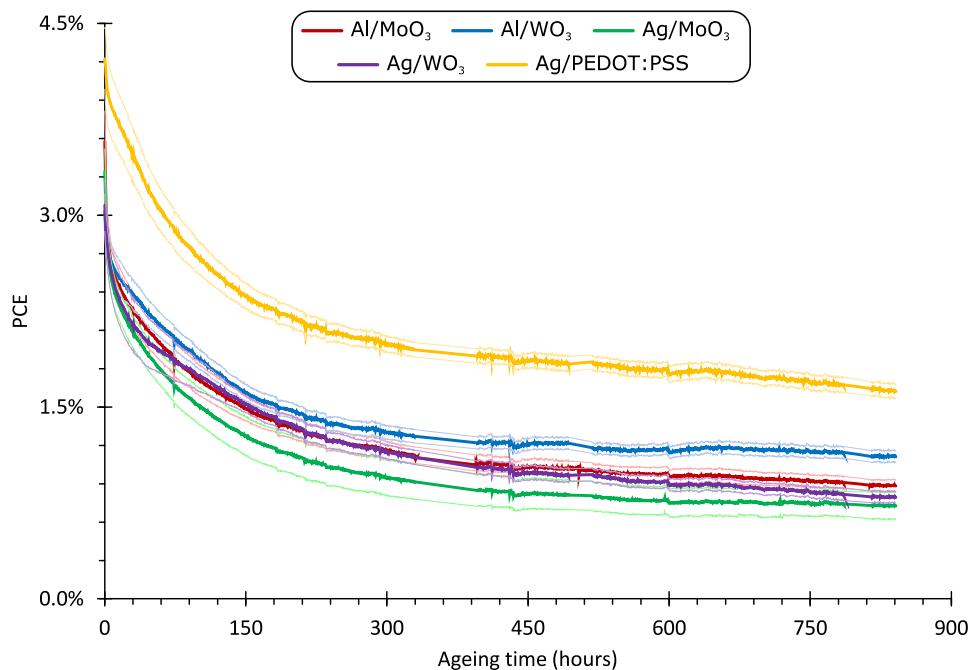


Figure 5.2.3: The evolution of the PCE with photo-ageing of inverted OPV devices in a nitrogen atmosphere with various combinations of materials as HTLs and top electrodes. Uncertainties, indicated by the lighter-shaded and thinner curves, represent one standard deviation across ca. 12 devices.

Most of the devices with metal-oxide HTLs exhibit similar behaviour when ageing under illumination. They are best fit by a triexponential model and have similar values for burn-in time (~ 550 hours), burn-in efficiency loss (~ 70 - 75%), and projected T_{S80} lifetime (~ 50 days). The exception to this is the samples with WO_3 HTLs and aluminium electrodes, which lose significantly less efficiency in the burn-in ($\sim 60\%$), and have an average projected T_{S80} lifetime that is approximately twice as long as the other material combinations. This is mostly due to a more stable V_{OC} , and will be discussed in more detail in section 5.2.4. The Ag/PEDOT:PSS samples also perform well with respect to burn-in, having both a shorter and less severe burn-in than the metal-oxide HTL samples due to a more rapidly declining FF (which shortens the burn-in) and a more stable V_{OC} (which decreases the severity of the burn-in). However, their comparatively rapid post-burn-in degradation means that the Ag/PEDOT:PSS samples have a significantly shorter projected T_{S80} lifetime than the Al/ WO_3 samples – similar in value to the other metal-oxide HTLs.

A further observation is that, unlike most of the samples, the Ag/PEDOT:PSS and Al/ WO_3 samples' degradation is best modelled with a biexponential model. When attempts were made to fit the triexponential model to the data from these samples, either the contribution from the first exponential ("A" in equation 5.2.11) was negligibly small or the algorithm did not converge (Figure 5.2.2). In the cases where it did converge, the values calculated for the statistics in Figure 5.2.4 were identical to those calculated with the biexponential model. The presence, or otherwise, of a two-part burn-in is a consequence of the evolution of the different PV parameters, as shown in Figure 5.2.5.

In samples that are modelled by the triexponential model, the origin of the first part of the burn-in differs depending on the materials used. As shown in Figure 5.2.5, the samples containing MoO_3 HTLs exhibit an initial rapid loss of J_{SC} (similar to some of the behaviour exhibited by MoO_3 -containing, thermally-aged OPV in Chapter 4) which is the primary reason for the initial rapid loss of efficiency that constitutes the first stage of the burn-in (a small drop in the V_{OC} also contributes). On the other

hand, the Ag/WO₃ samples' first stage of burn-in is due to a rapid loss of FF, which is not exhibited by the Al/WO₃ samples. As the Al/WO₃ samples and the Ag/PEDOT:PSS samples do not exhibit either of these behaviours, they do not exhibit a two-stage burn-in.

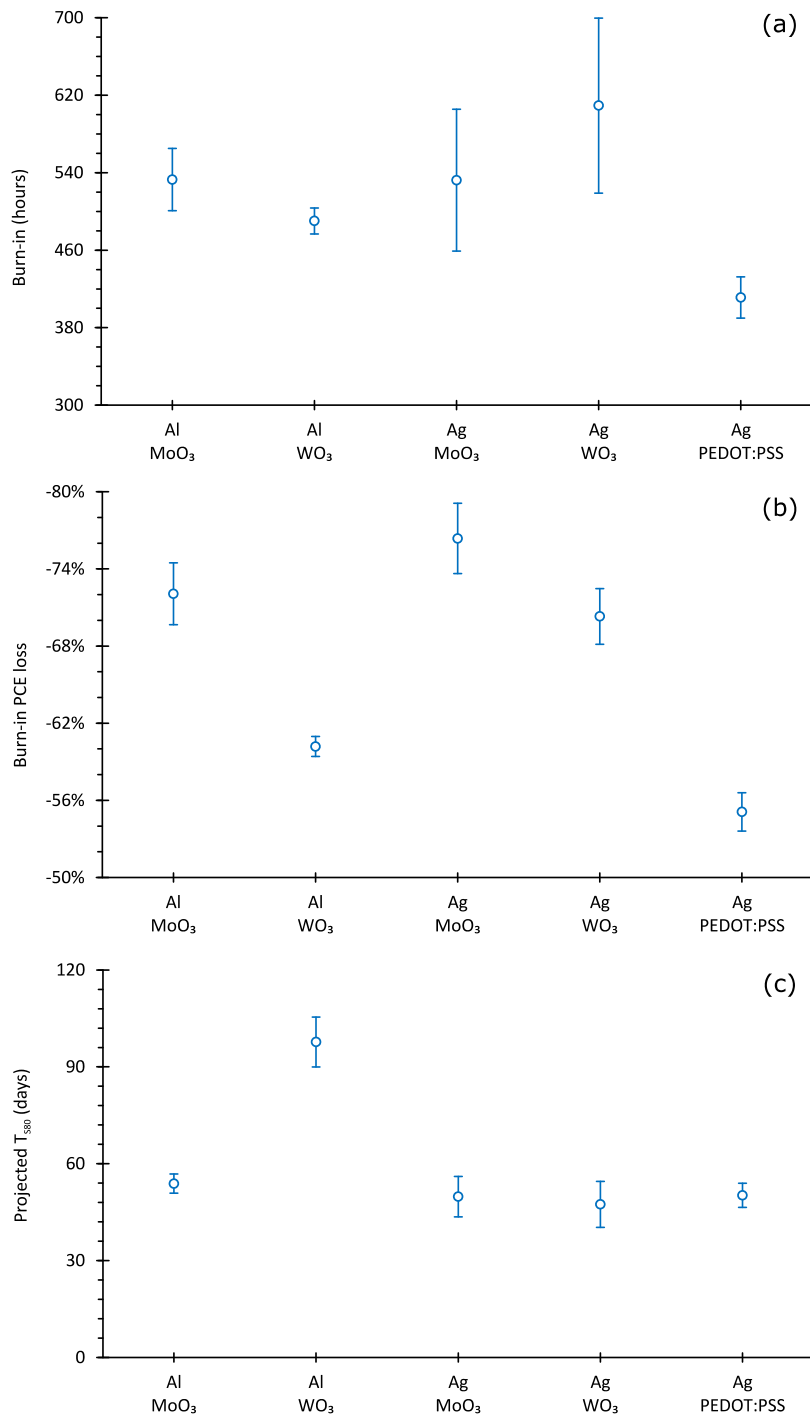


Figure 5.2.4: Variation with HTL/electrode material of: (a) burn-in time; (b) proportion of initial efficiency lost in burn-in; and (c) projected T_{S80} in the photo-ageing of inverted OPV devices in an inert atmosphere. Uncertainties represent one standard deviation across ca. 12 devices. These statistics were found by fitting the PCE data with the triexponential model (equation 5.2.11), except for the PCE data for the Al/WO₃ and Ag/PEDOT:PSS devices, which were fit with the biexponential model (equation 5.2.7). It should be noted that in (b), the burn-in efficiency loss is normalised to the real η_0 and not the η_0 value predicted by the model.

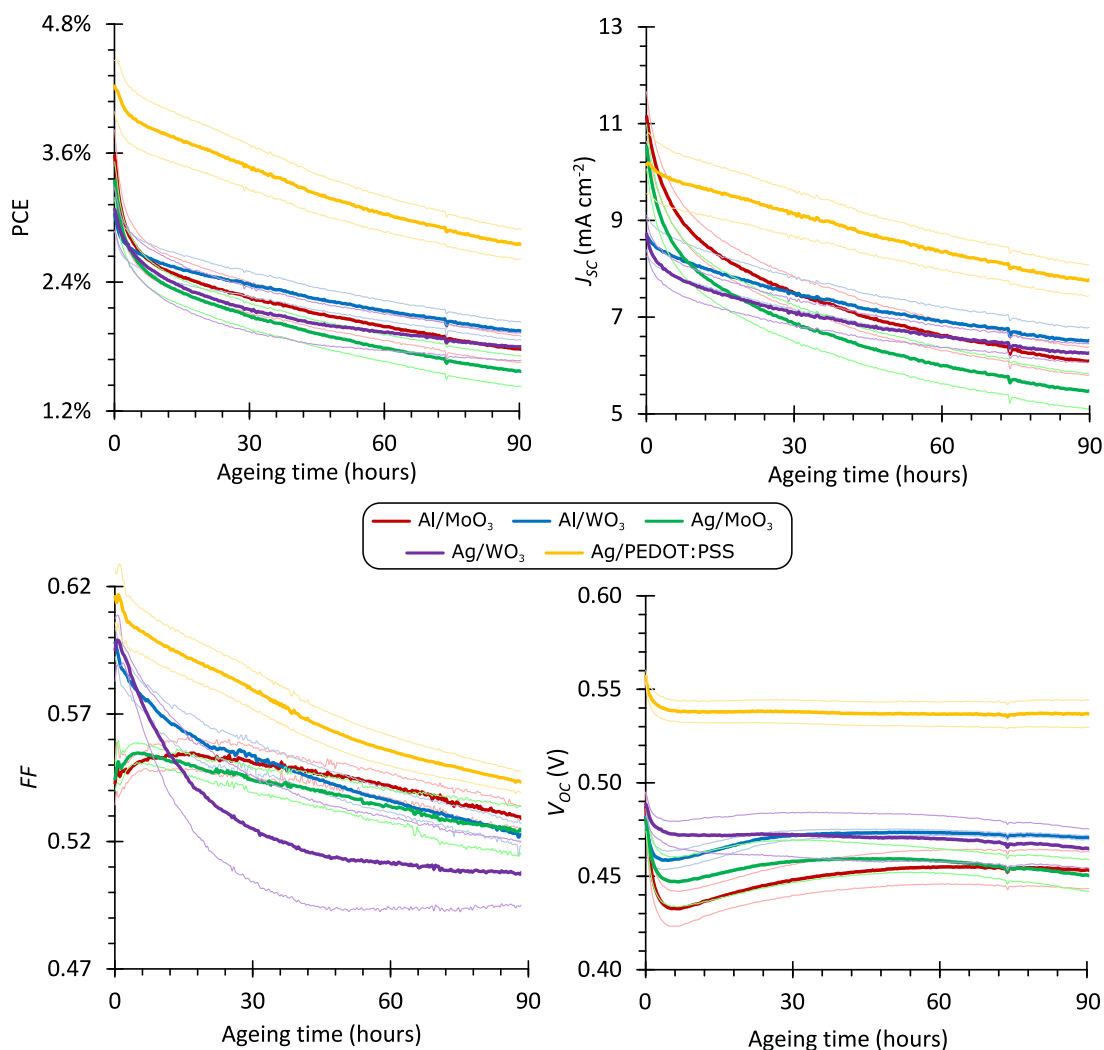


Figure 5.2.5: The evolution of the PV parameters of the OPV samples during the first 90 hours of photoageing under a nitrogen atmosphere. Uncertainties represent one standard deviation when averaged across ca. 12 devices.

It is interesting to note that the presence of the initial rapid loss of efficiency (exponential A in the triexponential model) is correlated with a more severe loss of efficiency in the burn-in, but that variations in the burn-in time and projected T_{S80} lifetime do not correlate to the model used. These results suggest that the second stage of burn-in (exponential B in the triexponential model), which determines the burn-in time in triexponential samples, is most likely driven by the same mechanisms that are behind the burn-in in biexponential samples (exponential A in the biexponential model). The mechanisms that are behind the first stage of the burn-in only act to intensify the burn-in, by accelerating initial PCE loss, but act entirely independently of the degradation mechanisms involved the second part of the burn-in and subsequently in the post burn-in degradation.

The presence (or otherwise) of the initial, rapid efficiency loss has little impact on the device's long term degradation behaviour, or projected T_{S80} lifetime, given the difference between the estimates for the Al/WO₃ and Ag/PEDOT:PSS devices. However, such statistics can be deceptive; while the Ag/PEDOT:PSS devices do have a shorter projected T_{S80} , they benefit from a higher value for η_S . This means that the projected efficiency of the Ag/PEDOT:PSS devices at the T_{S80} (η_{S80}) is higher than that of the Al/WO₃ devices ($1.50 \pm 0.04\%$ and $0.94 \pm 0.04\%$, respectively). Furthermore, if the

model is further extrapolated for the Ag/PEDOT:PSS devices using the same duration of ageing as the T_{S80} value for the Al/WO₃ samples (97.7 ± 7.7 days), the predicted efficiency of the Ag/PEDOT:PSS samples is still slightly higher than the η_{S80} of the Al/WO₃ samples ($1.10 \pm 0.03\%$). So while it is technically true that the Ag/PEDOT:PSS devices have shorter projected lifetimes than their Al/WO₃ counterparts, care should be taken in the use of such values – for the half of the projected life of the Al/WO₃ devices in which the Ag/PEDOT:PSS devices are considered “dead”, the Al/WO₃ devices would still have a lower efficiency than the “dead” Ag/PEDOT:PSS devices.

5.2.3. Analysis of the burn-in

Material-dependent Voc behaviour

In this study, the OPV devices exhibited unusual behaviour with respect to their V_{oc} loss in the burn-in. The V_{oc} behaviour of the OPV devices with photo-ageing in this study are shown in Figure 5.2.6. In the early stages of burn-in, the samples with a metal-oxide HTL exhibit a steep decline in V_{oc} , followed by a partial recovery, then a more gradual decline for the remainder of the burn-in.

What is immediately apparent is that this behaviour is highly material dependent (there is also a dependence on the radiation intensity, *vide infra*). The devices containing PEDOT:PSS HTLs and silver electrodes have a small, rapid loss of V_{oc} in the early stages of ageing, but then exhibit none of the signs of recovery or subsequent slower V_{oc} loss seen in the other material combinations. Of the metal-oxide HTL-containing samples, those devices with MoO₃ HTLs exhibit the greatest V_{oc} loss and recovery, while the WO₃-containing have a much smaller loss and recovery – almost none at all in the case of Ag/WO₃. Following the recovery, the silver-containing devices exhibit a greater V_{oc} decay than the aluminium samples, with the exception of the Ag/PEDOT:PSS samples that show very little decline. There was no variation in the temperature of the samples, the radiation intensity, or in the atmospheric composition that would explain this behaviour.

V_{oc} loss in the burn-in was discussed in Chapter 2, in which several studies were highlighted that attributed the loss of V_{oc} in the burn-in to charge-trapping near either the hole-extraction interface or the electron-extraction interface.^{158,159,163,164} The material dependence observed in this study would certainly be consistent with such a mechanism, and indeed several studies have illustrated that ageing devices without their top layers,¹⁵⁸ or adding an additional interlayer at the interface,^{158,163} can significantly reduce or eliminate such V_{oc} loss. An additional possible mechanism was discussed by Heumueller, *et al.*,¹¹⁹ who propose that V_{oc} loss is caused by a broadening of the density of states. This is unlikely to explain the V_{oc} loss in this study, however, as that mechanism is thought only to be a significant factor in low-mobility amorphous polymers like PCDTBT, and not in higher-mobility crystalline polymers like P3HT;¹¹⁹ it would also not explain the material dependence seen in this study.

The presence of two different periods of V_{oc} loss in the burn-in can most easily be explained by two different sets of charge traps; however, there is no immediately apparent mechanistic explanation for the recovery, aside from the observation that it is only present in samples with metal-oxide HTLs. It is likely that this behaviour can only be observed at reduced radiation intensities (*vide infra*), as employed in this study, as the V_{oc} loss is otherwise too rapid to allow perception of the different behaviour (Figure 5.2.8). This pattern of V_{oc} loss also relates to the two-stage burn-in behaviour discussed in sections 5.2.1 and 5.2.2, though that behaviour is mostly due to the J_{sc} trends, with

some contribution from the FF in some samples (Figure 5.2.5). In the first stage of V_{oc} loss, a steep decline of V_{oc} is observed in all material combinations, but the severity correlates to the HTL material (Figure 5.2.6); it follows that charge trap formation likely occurs due to the interaction of the HTL material and the active layer, as well as radiation from the solar simulator. In particular, samples with MoO_3 HTLs exhibit a greater loss of V_{oc} in this period than samples with WO_3 or PEDOT:PSS HTLs. In the second period of V_{oc} loss, the silver-containing metal-oxide HTL samples exhibit greater V_{oc} loss than their aluminium counterparts. One possible explanation for this is thermally-induced diffusion of silver into the device from the electrode, observed in Chapter 4. This would occur on a longer timescale in this experiment than in the thermal degradation experiments, as the sample temperatures were much lower in this photo-ageing experiment ($39 \pm 3^\circ\text{C}$ vs. 85°C), and it would not be observed in the devices with PEDOT:PSS HTLs, as the PEDOT:PSS layer is thicker (20 nm) than the metal-oxide layers (10 nm) and has a very different structure, meaning that a PEDOT:PSS layer may offer a greater diffusion barrier than a metal oxide layer. However, more study is needed to confirm this hypothesis. Mechanistic explanations aside, these results reveal that of the three HTL materials examined, PEDOT:PSS has the most stable V_{oc} , followed by WO_3 , and MoO_3 has the least stable V_{oc} when photoaged in the absence of oxygen or moisture. With respect to the electrode materials, less V_{oc} loss is observed with aluminium than silver.

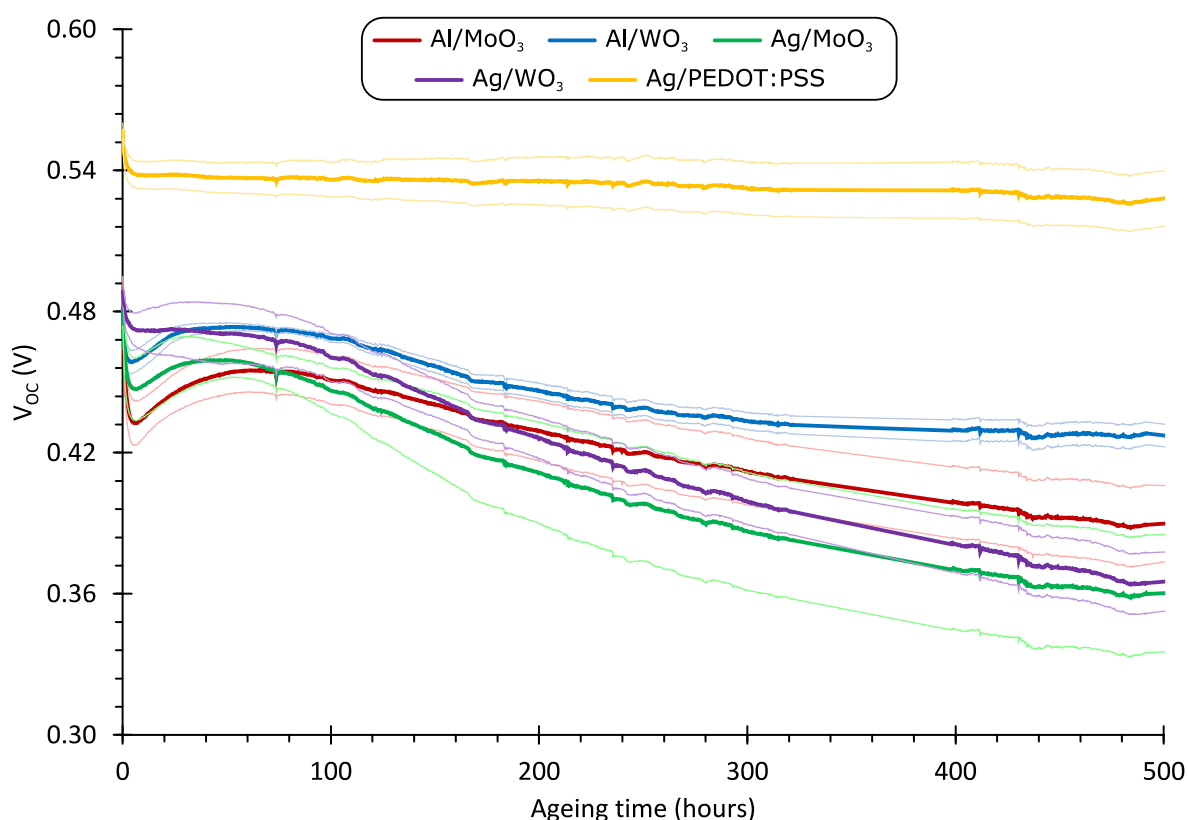


Figure 5.2.6: V_{oc} behaviour of the inverted OPV devices during the burn-in when aged in an inert atmosphere under 800 W m^{-2} simulated solar radiation. Uncertainties, indicated by the lighter-shaded and thinner curves, represent one standard deviation across ca. 12 devices; the parameters are normalised to their initial values.

Differences with other studies

As discussed in (Chapter 2), the burn-in of an OPV device typically lasts between 50 hours and 200 hours of ageing, with an efficiency loss of between 10% and 30% of the unaged device

efficiency.^{30,131,157–159} It is apparent from Figure 5.2.3 and Figure 5.2.4 that the burn-in observed during the ageing of the devices in this experiment is substantially greater, both in terms of efficiency loss and duration. The origins of the greater efficiency loss and the longer burn-in time will be examined in this section.

One of the key differences between this experiment and the ones in the studies cited above is the intensity of the simulated solar radiation used. In most studies, the AM1.5G spectrum¹⁷⁹ is used, which has an integrated intensity of 1000 W m^{-2} , or 1.0 sun.¹⁷⁹ However, in most of the photoageing experiments done in this study, a radiation intensity of 800 W m^{-2} (0.80 sun) was used. This was done for primarily practical reasons; it was necessary to have the ability to tune the power of the lamp up or down during an experiment to compensate for fluctuations in the lamp's output, which was not possible if the lamp was set to maximum power. This remains within the range recommended by the ISOS protocols.²² However, some earlier experiments were carried out at 1000 W m^{-2} for calibration purposes, so a comparison of the trends with photoageing at the two different intensities could be made, and is shown in Figure 5.2.7.

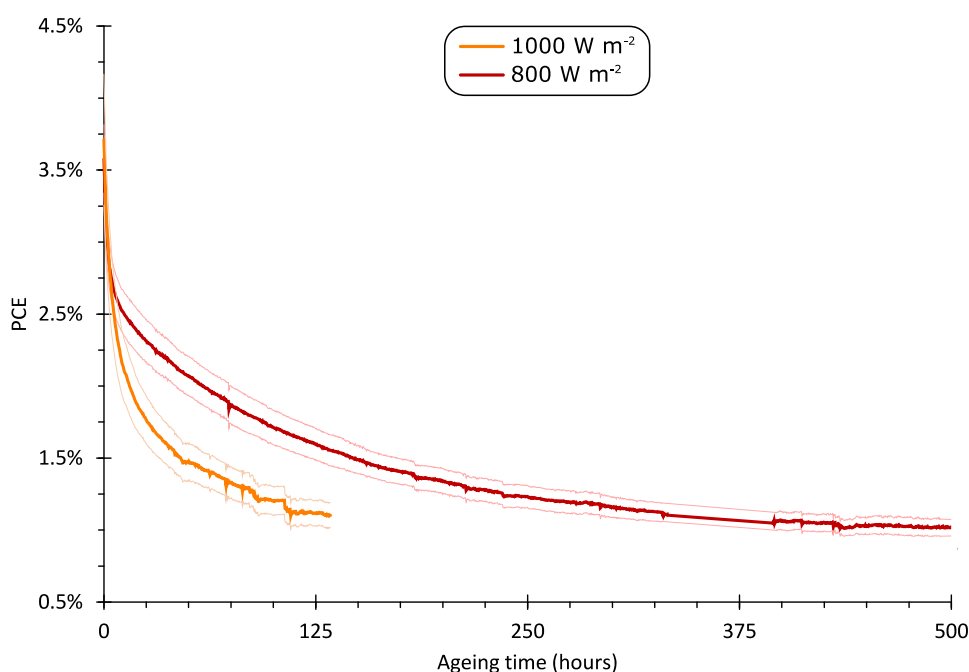


Figure 5.2.7: Comparison of the PCE trends with photo-ageing at 1000 W m^{-1} and 800 W m^{-1} . Both curves were measured from inverted OPV devices with aluminium top electrodes and MoO_3 HTLs under a nitrogen atmosphere. Uncertainties (shown by the thinner, lighter curves) represent one standard deviation when averaged across between 12 and 16 devices.

The PCE data shown in Figure 5.2.7 span the entirety of the calculated burn-in time of the Al/ MoO_3 devices when aged under 800 W m^{-2} radiation in an inert atmosphere. It is apparent from Figure 5.2.7 that when identical devices are aged under 1000 W m^{-2} radiation in identical conditions, the burn-in time is substantially shortened. Although the 1000 W m^{-2} experiment was stopped prior to the end of the burn-in, meaning that the algorithm to determine ageing statistics could not reliably be used, a visual analysis suggests that the eventual post-burn-in efficiency would be approximately the same as the value found in the 800 W m^{-2} experiment. These results suggest that decreasing the radiation intensity prolongs the burn-in but has little impact on the efficiency loss.

In order to ascertain why burn-in time decreased with increasing radiation intensity, the trends of the photovoltaic parameters with photo-ageing are examined in Figure 5.2.8.

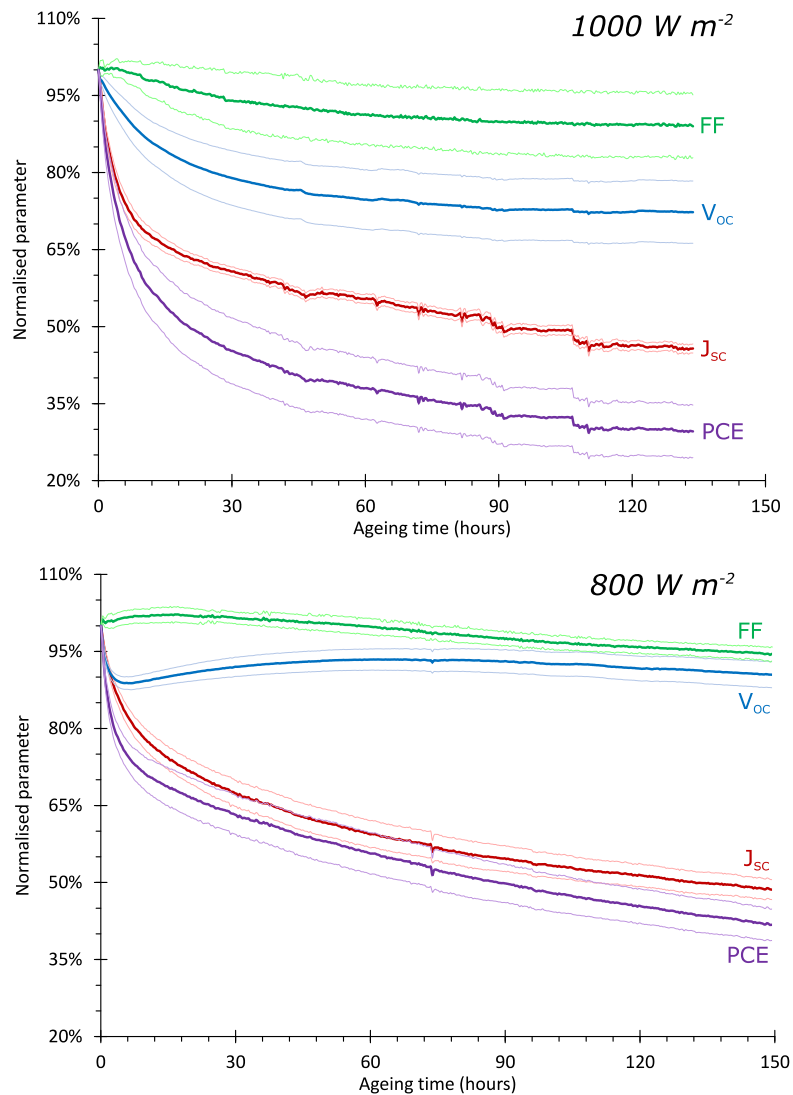


Figure 5.2.8: The evolution of the normalised photovoltaic parameters of inverted OPV devices when aged under 1000 W m^{-2} radiation (top) and 800 W m^{-2} radiation (bottom). In both experiments, the devices have aluminium top electrodes and MoO_3 HTLs. All parameters are normalised to their initial values. The uncertainties (the thinner, lighter curves) represent one standard deviation when averaged across 12 devices in the 1000 W m^{-2} experiment and across 11 devices in the 800 W m^{-2} .

As seen in Figure 5.2.7, the PCE loss is more rapid in the higher intensity radiation experiment than in the lower intensity radiation experiment. For the Al/ MoO_3 samples, in both experiments the burn-in is driven by J_{sc} and V_{oc} loss, while the FF is relatively unchanged. The trends in J_{sc} exhibited by the samples are relatively similar in both the 1000 W m^{-2} and 800 W m^{-2} experiments. Although the J_{sc} loss is initially more rapid in the higher intensity experiment, after 150 hours of photo-ageing the samples in both experiments show relatively similar losses in J_{sc} (around 50%). It follows that the difference in the PCE trends is largely a result of differences in the V_{oc} behaviour. In the 800 W m^{-2} experiment, the V_{oc} initially declines before reaching a minimum, then increases, and finally stabilises (*vide supra*); in contrast, in the 1000 W m^{-2} experiment, the V_{oc} does not stop declining.

Although these data alone cannot reveal the mechanism behind this difference in behaviour, the fact that the V_{OC} is affected by the light intensity more strongly than the J_{SC} gives some clues, based on previous studies of V_{OC} loss in the burn-in. As discussed in Chapter 2, V_{OC} -driven burn-in can be due to an interfacial phenomenon¹⁵⁸ and is frequently associated with the formation of charge traps in the active layer.^{158,159} It has been shown that when a device is aged without its top layers, or with interlayers designed to suppress trap formation, the V_{OC} loss can be suppressed.¹⁵⁸ If the formation of charge traps occurs due to interactions between the interfacial region and the incident radiation, it follows that more intense radiation would cause the more rapid formation of these traps and would therefore expedite V_{OC} loss, as was observed in this study. It appears counter-intuitive that only a 20% reduction in radiation intensity could have such a significant effect on the burn-in time, however there is no immediately apparent reason why such a process should linearly vary in timescale with radiation intensity. Without knowing the chemical process(es) behind the trap formation, it is difficult to speculate further.

The other difference between the burn-in observed in this photo-degradation study shown in Figure 5.2.3 and similar studies published in the scientific literature is the proportion of the initial efficiency that is lost in the burn-in. A 2014 study by Voroshazi, *et al.* published in *Advanced Energy Materials* examined the photo-ageing of devices with near-identical architectures and materials (inverted devices with the structure ITO/ZnO/P3HT:PC₆₁BM/MoO₃/Ag/Al) as the samples in this study under an AM1.5G spectrum in an inert atmosphere.¹⁵⁸ Unlike the samples in this study (Figure 5.2.1, Figure 5.2.7), the efficiencies of these devices only dropped by ca. 40% over the course of the burn-in. This difference is primarily due to J_{SC} loss. Voroshazi, *et al.* observed an approximately 30% loss in J_{SC} over the course of burn in, whereas OPV devices examined in this study lost over 50% J_{SC} during the same period when aged under 1000 W m⁻² radiation (Figure 5.2.8). This can be explained either by a difference in the ageing conditions or the composition of the samples. While the studies are identical in most respects, the radiation used for ageing is different. Voroshazi, *et al.* report that the samples were aged under “a metal halide lamp with AM1.5G spectrum (containing UV light)”,¹⁵⁸ implying that although the incident radiation on the samples had a UV component, it was partially filtered to conform to the AM1.5G spectrum. In contrast, this study used an unfiltered hydrargyrum medium-arc iodide (HMI) metal-halide lamp as the radiation source during photo-ageing. As the lamp in this study is unfiltered, it most likely has a more significant UV component in its output than the one used in the Voroshazi, *et al.* study. As shown in Figure 5.2.9, the spectral output of this lamp has a significantly larger near-UV component than the AM1.5G spectrum, indicating that it is likely that the samples in this study received a higher dosage of UV radiation than those examined by Voroshazi *et al.*

The origin of J_{SC} loss in the burn-in was discussed in Chapter 2. The presence or absence of J_{SC} degradation varies between active layer materials, and correlates with the degree of crystallinity of the fullerene domains in the active layer and, as a consequence, how readily fullerene dimerization can proceed.¹⁶⁶ Heumueller, *et al.* propose that in a more amorphous PC₆₁BM/PC₇₁BM domains, fullerene acceptors are more likely to be oriented in such a way as to facilitate photo-induced dimerization, thereby leading to a greater loss of J_{SC} in the burn-in, and observe such differences in ordered and disordered P3HT:PC₆₁BM active layers.¹⁶⁶ It is possible that some morphological differences exist between the devices fabricated in the study by Voroshazi, *et al.* and this one, particularly since the samples in this study were prepared with a solvent vapour annealing step in order to attain the ideal BHJ morphology, whereas those in the Voroshazi, *et al.* study were prepared

using thermal annealing.¹⁵⁸ However, this is unlikely to fully explain the observed differences in J_{SC} behaviour during the burn-in. Both the samples in this study and those in the study by Vorohazi, *et al.* had optimised BHJ morphologies but as they were optimised via different techniques, they may have different degrees of crystallinity in the fullerene domains in the BHJ, which can cause a difference in J_{SC} loss with photoageing.¹⁶⁶ However, when compared with the results of Heumueller, *et al.*, it seems unlikely that this effect is large enough to be solely responsible for the large J_{SC} loss observed in this study.

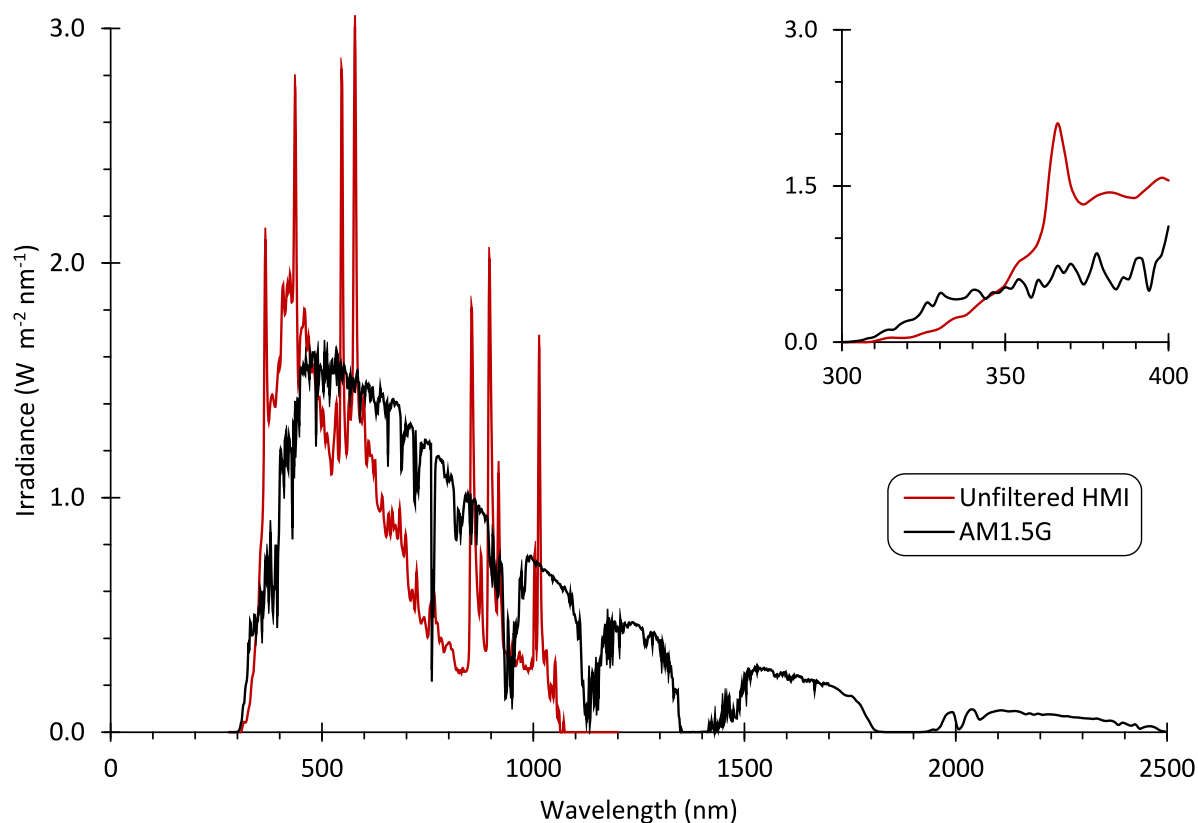


Figure 5.2.9: A comparison of the irradiance spectrum of the HMI lamp used for ageing in this experiment (data measured by Dr Uyxing Vongsaysy) and the AM1.5G spectrum, with the near-UV portion of the spectrum shown in the inset. Data for the AM1.5G spectrum are detailed in the ASTM international industrial standard G173-03(2012),¹⁷⁹ and were downloaded from the United States National Renewable Energy Laboratory (NREL) website.¹⁹⁹

It is likely that the larger component of UV radiation in this study was a contributing factor in the increased J_{SC} loss in the burn-in resulting in greater efficiency loss. If this is the case, then there must be mechanism additional to the fullerene dimerisation discussed above that is acting to cause the J_{SC} loss – if this were the only mechanism present, a difference in the radiation could only accelerate the J_{SC} loss, not intensify it. A possible explanation for the origins of this behaviour comes from a study conducted by Pearson, *et al.*, published in *Organic Electronics* in 2016.²⁰⁰ In it, the authors demonstrate that when the solvent additive 1,8-diiodooctane (DIO) is used in the deposition of the active layers of their OPV devices, and those devices are aged under a radiation source with a strong UV component, the devices exhibit a severe burn-in of up to 80% of the initial PCE in inverted OPV devices.²⁰⁰ As in this study, the severe burn-in is driven by a substantial loss of J_{SC} .²⁰⁰ The authors demonstrate that this J_{SC} loss is effectively suppressed if either the DIO is replaced or UV filters are employed during ageing.²⁰⁰ These results highlight the fact that impurities or solvent traces, in

combination with UV, can result in a severe J_{SC} burn-in. The large UV component of the radiation used to age the samples in this study may be responsible for the severe burn-in that they experience, as the samples in this study were prepared with a batch of P3HT of unknown purity and using solvent vapour annealing. The active layer is likely to contain impurities (from the P3HT batch) and/or solvent traces (ODCB) that could have an effect similar to the DIO in the Pearson *et al.* study.

5.2.4. Post-burn-in degradation

The post-burn-in or “linear” portion of a photo-degradation PCE curve typically makes up the majority of a device’s lifetime.³⁰ It therefore follows that even very subtle differences in degradation rate between devices can result in significant variation in the lifetime of the device. As is shown in Figure 5.2.4, most of the materials have projected lifetimes on the order of 50 days, with the exception of samples containing aluminium electrodes and WO_3 HTLs, which had a projected lifetime of 97.7 ± 7.7 days. Although P3HT has been shown to not be the optimal choice of polymer for long-lived OPV devices, these lifetime estimates must be considered short even taking such caveats into account.^{148,157}

In a 2011 study published in *Advanced Energy Materials*, Peters, *et al.* demonstrate that direct P3HT:PC₆₁BM devices, when aged under inert conditions, can have projected lifetimes of between 2.8 and 3.8 years.¹⁵⁷ There are some differences in methodology with respect to lifetime estimation that may result in difference in the lifetime estimates between the Peters, *et al.* study and this one. In their study, Peters, *et al.* use the linear extrapolation method to estimate lifetime, rather than the multi-exponential approach employed here.¹⁵⁷ However, this would be more likely to underestimate, rather than overestimate, the T_{S80} lifetime, as a linear tangent of a decaying exponential function will always have a lower value than the exponential (except at the point of intercept). The Peters, *et al.* experiment was also conducted over a much longer period of time (>4000 hours), and therefore samples a greater portion of the linear part of the degradation curve than this experiment.¹⁵⁷ This means that it is possible that this study under-estimates lifetime due to sampling an overly small section of the post-burn-in portion of the degradation curve. This also seems unlikely, however, as measurements in this experiment were carried out for 859 hours, which is 72% of the estimated lifetime of most of the devices—this would indicate that the T_{S80} estimates are likely to be accurate.

Another major difference between this study and the one by Peters, *et al.* is the spectrum of radiation used to age the samples.¹⁵⁷ Unlike the unfiltered HMI lamp used in the ageing of the samples in this study, which has a significant near-UV component (Figure 5.2.9), the samples in the Peters, *et al.* study were aged with a sulfur plasma lamp with almost no UV component.¹⁵⁷ As discussed in Chapter 2, a significant number of degradation pathways have been identified in the active layer of polymer-based OPV that involve the joint action of UV light and oxygen,^{67,201} however, aside from some trace quantities (90 ppm), the samples in this experiment were not exposed to significant quantities of oxygen during ageing. In the burn-in, a significant J_{SC} loss was observed, which was attributed to the combined effects of high levels of UV radiation and impurities in the active layer. However, as shown in Figure 5.2.10, the efficiency loss in the metal-oxide HTL-containing devices post-burn-in is primarily driven by losses in the V_{OC} , so a different mechanism must be responsible. Moreover, while some cross-spectrum EQE loss was observed during ageing (Figure 5.2.10), this is most likely caused by the same mechanism responsible for the J_{SC} loss in the burn-in.

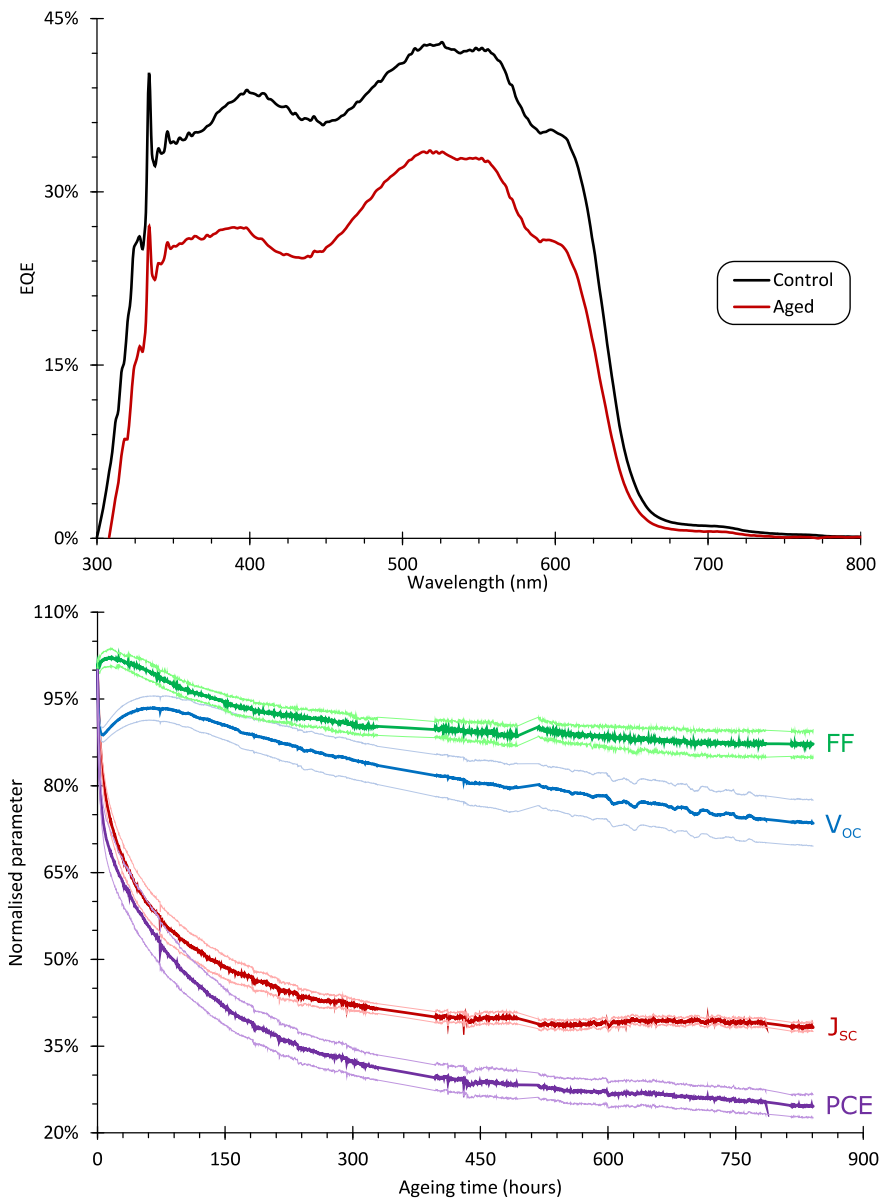


Figure 5.2.10: (top) EQE data obtained from unaged control and photo-aged (859 hours, 800 W m^{-2}) Al/MoO₃ inverted OPV devices; and (bottom) the evolution of the normalised photovoltaic parameters of the Al/MoO₃ inverted OPV devices as they were photo-aged in a nitrogen atmosphere, illustrating that in the post-burn-in period, PCE loss is primarily driven by V_{oc} loss. Uncertainties in the bottom plot represent one standard deviation when averaged across 12 devices, the parameters are normalised to their initial values. The aged and control curves in the top plot are representative of several devices from this experiment that were measured.

The behaviour of the samples with metal-oxide HTLs observed in this experiment resembles the results of an unpublished study by Drs Giorgio Mattana and Sylvain Chambon at the University of Bordeaux. In their study, Mattana and Chambon examine the role that the material used for the ETL can play in photodegradation under an inert atmosphere as well as the interaction with the UV part of the solar spectrum. As shown in Figure 5.2.11 (top), they observed that when a ZnO ETL is used, devices with P3HT:PC₆₁BM active layers, MoO₃ HTLs and silver electrodes exhibited a decline in V_{oc} under illumination with full solar radiation.²⁰² The V_{oc} loss was greatly diminished when identical devices were aged under the same conditions but with the UV component of the simulated solar radiation removed.²⁰² This behaviour was also observed when different materials were used for the active layer, but varied when ZnO was substituted with TiO_x.²⁰² Further experiments suggest that

when ZnO is used as an ETL material in samples that are aged with UV radiation, an increase in the doping of the active layer occurs, and that this is the most likely origin of the V_{OC} loss.²⁰²

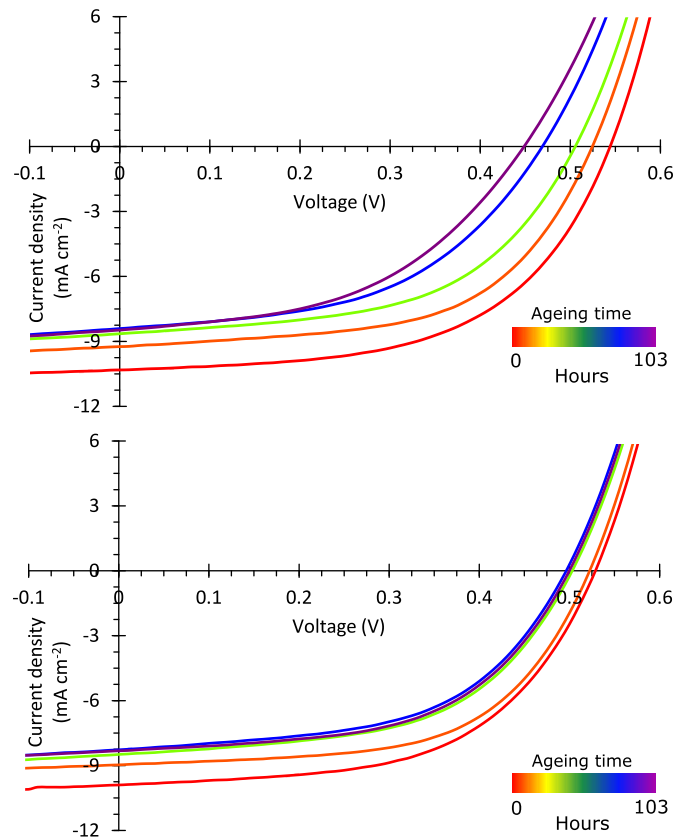


Figure 5.2.11: Changes in the IV curves of inverted OPV devices with ZnO ETLs when photo-degraded under an inert atmosphere with the full spectrum of radiation (top), and the near-UV component filtered out (bottom). Data collected by Drs Giorgio Mattana and Sylvain Chambon and reproduced with permission. It should be noted that these devices were aged at 1000 W m^{-2} , so timescales observed may not correlate exactly to the ageing data discussed earlier in this chapter.

The additional degradation mechanism at the ETL/active layer interface due to the interaction of UV and metal-oxide interlayer (such as ZnO) would be consistent with the observations from this experiment. V_{OC} loss is observed in all samples post burn-in, and although the timescales differ, this could easily be explained by the lower intensity radiation used in this experiment compared to Mattana and Chambon's, which was carried out at 1000 W m^{-2} .²⁰² Unlike most long-term photo-degradation mechanisms,^{30,67} this one:

- does not require the presence of oxygen to proceed;
- would not significantly affect the absorption of the active layer (and thus EQE), being an interfacial effect; and
- would not be expected to be observed in any experiment that either filters near-UV radiation or does not use ZnO as an ETL material.

In fact, the study by Peters, *et al.* that found projected lifetimes of 2.8 to 3.8 years for P3HT:PC₆₁BM devices¹⁵⁷ used a direct architecture, with PEDOT:PSS HTLs and calcium/aluminium as ETL/top electrode pairs – a combination that is highly unstable in the presence of oxygen or water, but seemingly very stable if these extrinsic degradation stimuli are removed.¹⁴⁸

In addition to the V_{OC} loss discussed above, the devices with PEDOT:PSS HTLs also exhibit an increase of series resistance during and after the burn-in (Figure 5.2.12).

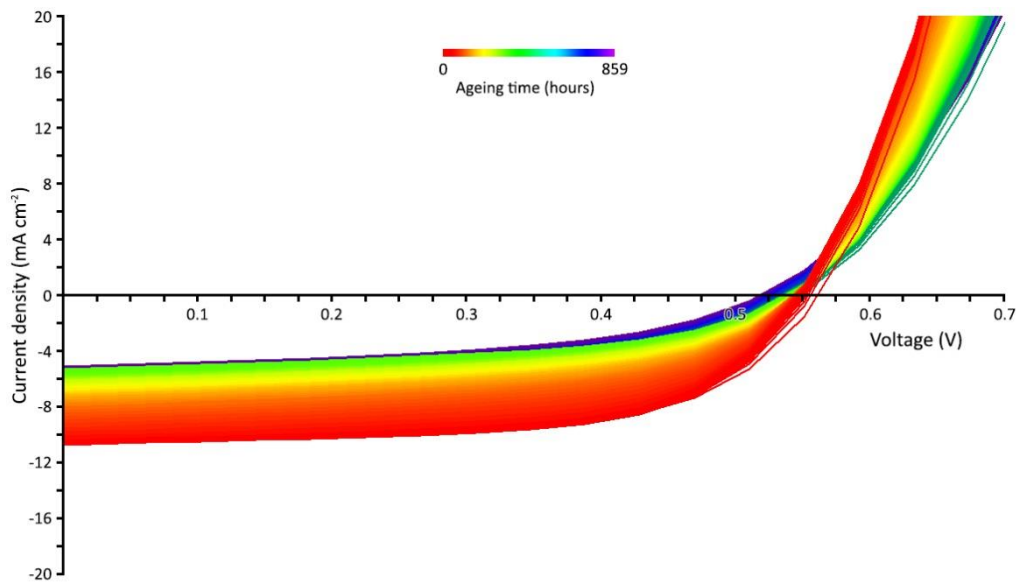


Figure 5.2.12: Evolution of the IV curve of a PEDOT:PSS-containing device as the device is photo-degraded at 800 W m^{-2} , illustrating the increase in series resistance with photo-ageing exhibited by these devices.

This increase in series resistance is only observed in the devices that use PEDOT:PSS as an HTL material and not with either metal-oxide HTL. The increase in series resistance causes a decline in the FF of the devices (Figure 5.2.13) which, when combined with the previously-discussed V_{OC} loss, leads to a faster efficiency loss post burn-in and results in a shortened projected T_{S80} lifetime, despite having a shorter and less intense burn-in than the other material combinations (Figure 5.2.4).

This behaviour is typical of PEDOT:PSS thin layers in the presence of humidity, although its presence in an inert atmosphere is not without precedent.¹³¹ PEDOT:PSS is highly hygroscopic, and absorbed water causes the formation of large non-conducting regions within the film.¹⁵⁴ This film was, however, aged in a dry nitrogen atmosphere with no humidity, and the increase in series resistance is much slower than that observed in a humid atmosphere (*vide infra*). One possibility is that the increase in series resistance occurs because the PEDOT:PSS layer and/or the rest of the device either retained water from fabrication or absorbed water from the air when the devices were transferred to the ageing chamber. The latter explanation is less likely, as the samples were only exposed to air for 5 – 10 minutes, and no changes were observed in the control samples despite being exposed to the air for the same amount of time. In addition, if water were already present in the device when ageing commenced, it would likely result in a high series resistance at the start of the experiment rather than causing changes as the experiment progressed.

The series resistance increase could possibly be the result of degradation in the active layer or corrosion of the silver electrode by the acidic PSS component of the PEDOT:PSS, as was observed in the thermal ageing of Al/PEDOT:PSS samples in Chapter 4. In that experiment, an inflection point, or S-shape, developed during ageing as the aluminium electrode was corroded. That is not observed in this experiment, indicating that if the PEDOT:PSS is corroding the surrounding layers, it is not doing so in a way that forms a charge extraction barrier covering the entire area of the electrode, but an additional resistance instead.¹³⁴ The possibility that the product of the corrosion of the silver

electrode is silver(I) oxide would be consistent with these observations, as while silver(I) oxide is electrically conductive, it is less conductive than silver, so an increase in series resistance would be expected.²⁰³ The PSS could also be degrading the active layer as the sample ages, however as no significant drop in J_{sc} is evident post burn-in, this seems less likely.

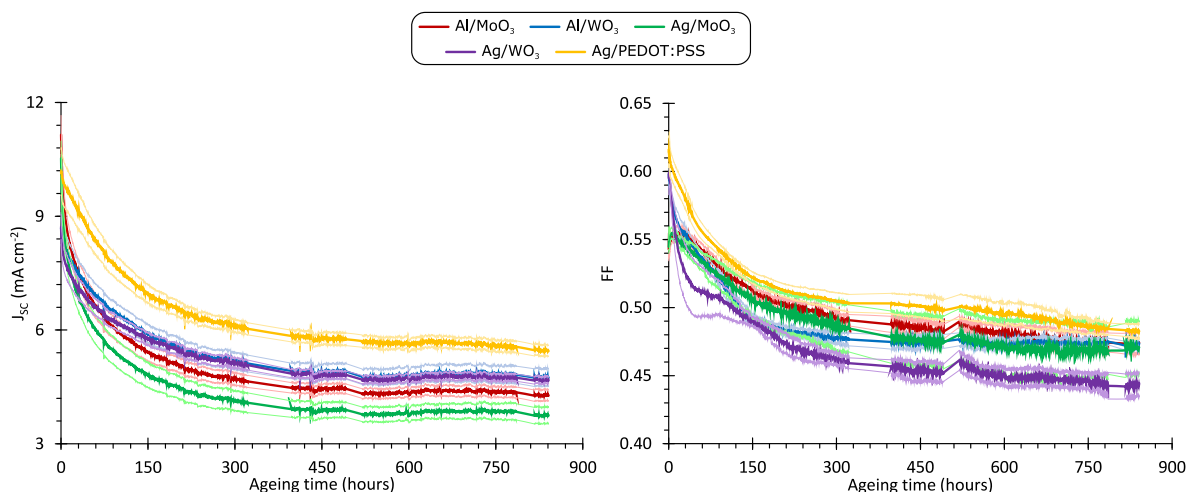


Figure 5.2.13: The evolution of the J_{sc} (left) and FF (right) with photo-ageing of inverted OPV devices in a nitrogen atmosphere with various combinations of materials as HTLs and top electrodes. Uncertainties, indicated by the lighter-shaded and thinner curves, represent one standard deviation across ca. 12 devices.

5.3. Effects of atmospheric composition on photodegradation

5.3.1. Degradation in dry synthetic air

The experiment detailed in section 5.2 was repeated with a dry synthetic air atmosphere (20% v/v oxygen in nitrogen). The PCE trends observed over the course of this experiment are shown in Figure 5.3.1, and the PCE ageing statistics (with a comparison to the values obtained from the dry nitrogen experiment) are shown in Figure 5.3.2. For practical reasons, PEDOT:PSS HTLs were not examined in this experiment.

Exposure to oxygen has a dramatic effect on the degradation of the devices. The primary effect is to accelerate degradation. As shown in Figure 5.3.1 and Figure 5.3.2, the devices experience a much faster burn-in, two to three times faster in the synthetic dry air experiment than in the dry nitrogen experiment. The burn-in is also more intense, with all material combinations exhibiting a greater proportional PCE loss in the burn-in when exposed to oxygen. This is particularly pronounced in the devices with MoO_3 HTLs, which can lose as much as 85% of their initial PCE in the burn-in. Finally, the projected T_{S80} lifetimes of the devices are substantially shorter when aged in the presence of oxygen (although the relevance of the T_{S80} after an 85% loss of PCE in the burn-in is debateable). Any semblance of material dependency of the lifetime is gone, with all material combinations exhibiting lifetime estimates on the order of 25 days, constituting a 50% reduction in lifetime as compared to the nitrogen experiment with most material combinations, and a 75% reduction when considering the devices with WO_3 HTLs and silver electrodes. It is also interesting to note that all material combinations now exhibit a two-stage burn-in and can be modelled with equation 5.2.11 and the algorithm in Figure 5.2.2 (although it is uncertain if this would also be true for PEDOT:PSS devices).

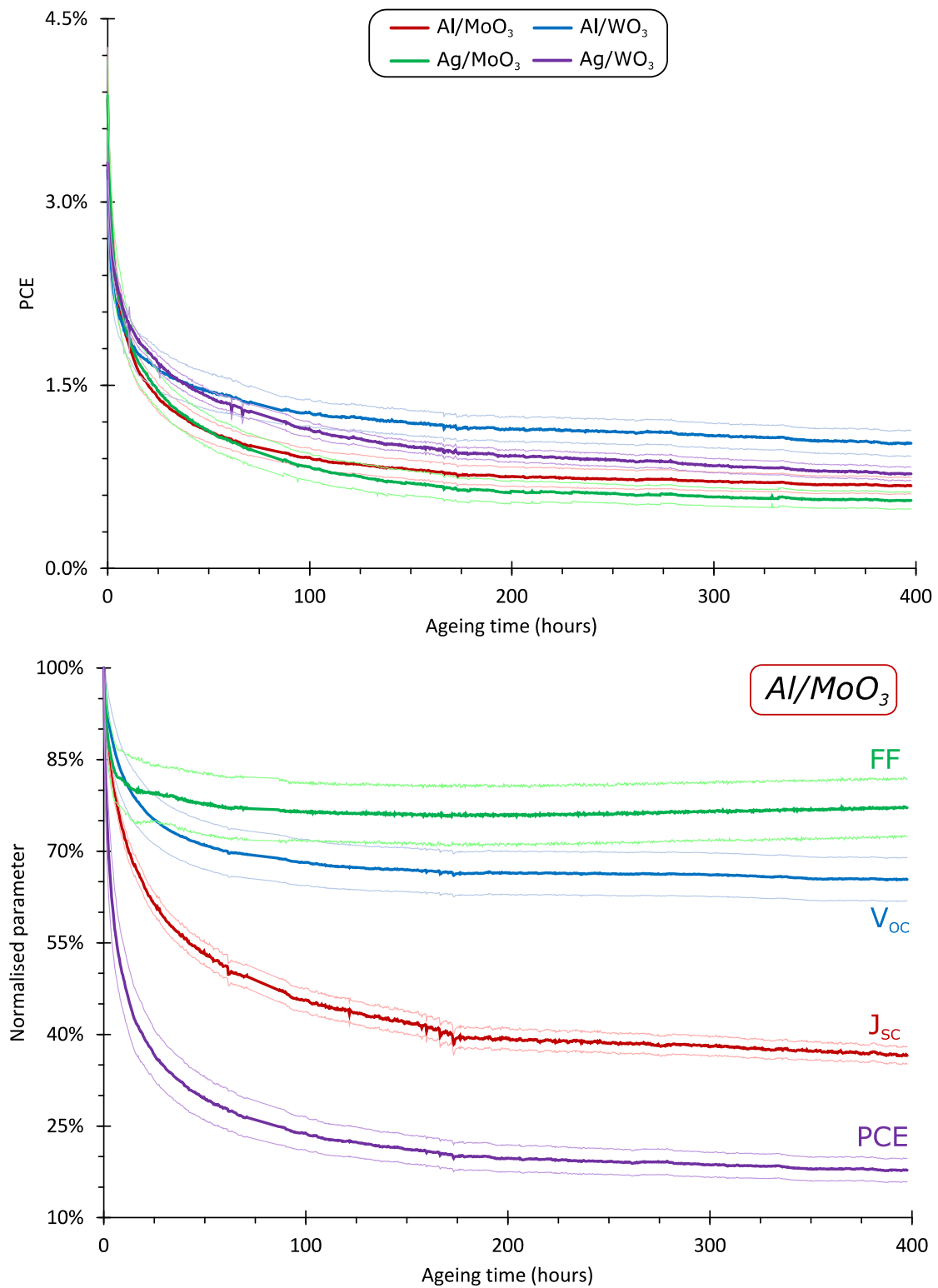


Figure 5.3.1: (top) The evolution of the PCE with photo-aging of inverted OPV devices in a dry synthetic air atmosphere with various combinations of materials as HTLs and top electrodes; and (bottom) the evolution of the normalised photovoltaic parameters of the Al/MoO₃ inverted OPV devices as they are photo-aged in a dry synthetic air atmosphere. Uncertainties, indicated by the lighter-shaded and thinner curves, represent one standard deviation when averaged across ca. 16 devices; the parameters are normalised to their initial values.

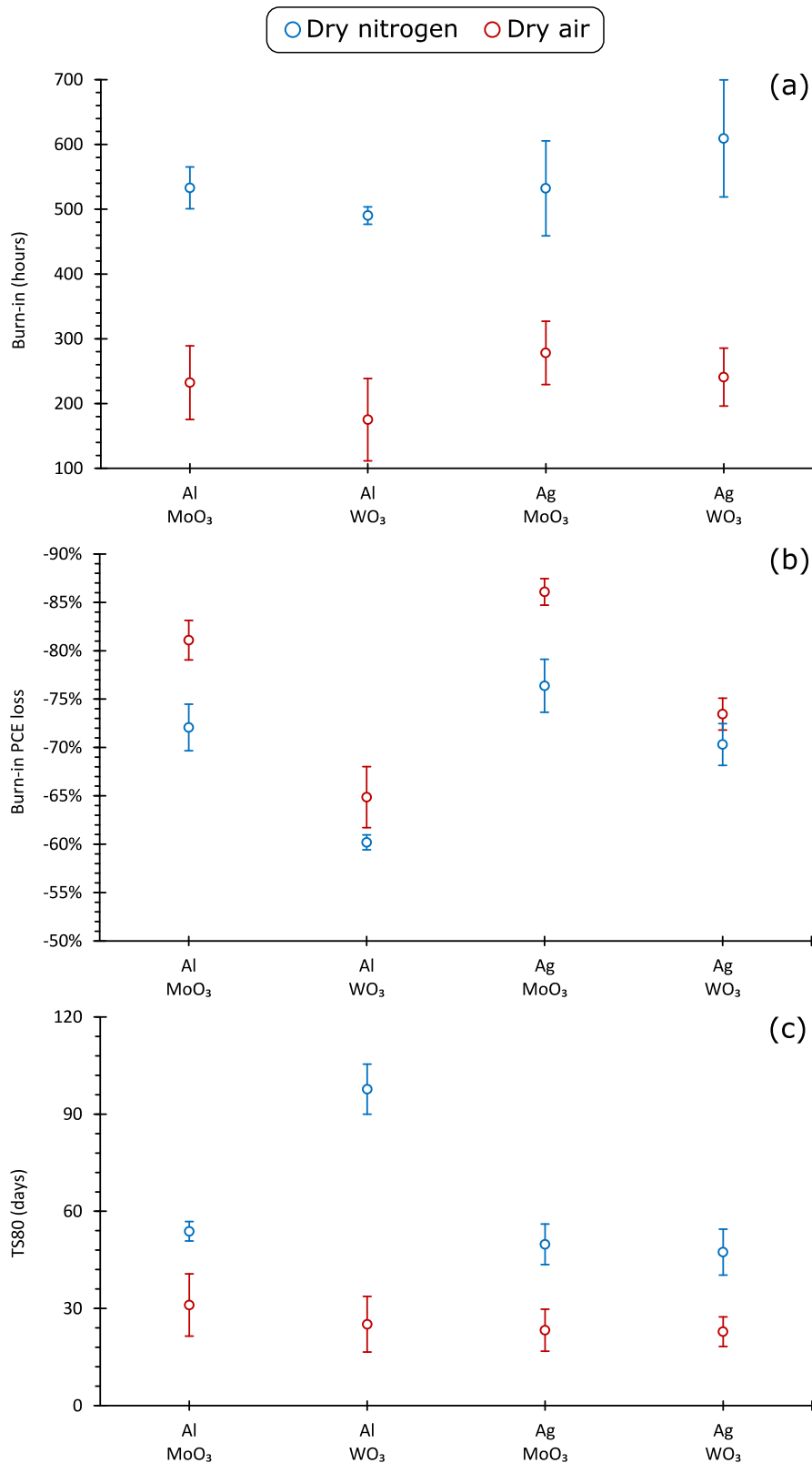


Figure 5.3.2: Variation with HTL/electrode material for: (a) burn in time; (b) proportion of efficiency lost in burn-in; and (c) projected T_{580} in the photo-ageing of inverted OPV devices in dry air and dry nitrogen atmospheres. Uncertainties represent one standard deviation across ca. 12 devices for N_2 and ca. 16 devices for O_2/N_2 . The statistics for the O_2/N_2 experiment were found by fitting the PCE data with the triexponential model (equation 5.2.11). It should be noted that in (b), the burn-in efficiency loss is normalised to the real η_0 and not the η_0 value predicted by the model.

Upon comparison of the bottom of Figure 5.2.10 and Figure 5.3.1, it is evident that all of the principle photovoltaic parameters contribute to the more rapid loss of efficiency in the burn-in for the synthetic air experiment. Furthermore, it is interesting to see that the evolution of the PV parameters decay is the same with all material combinations – indicating that interfacial mechanisms at the hole extraction interface play very little role. As discussed in section 5.2.3, losses in FF and V_{OC} in the burn in are typically associated with an increased prevalence of photo-generated charge traps near either or both of the charge extraction interfaces, which increases the monomolecular recombination rate.^{158,159} This was used to explain the differences in V_{OC} behaviour between different HTL materials in the burn-in, and an increase in the rate of charge trap formation was proposed as an explanation for the faster V_{OC} loss observed when more intense radiation is used to age the devices. As the addition of oxygen to the ageing atmosphere has an effect similar to increasing the intensity of the ageing radiation, it seems likely that the origin of the V_{OC} loss is similar. It has previously been shown by Schafferhans, *et al.* that exposure of P3HT:PC₆₁BM-based OPV devices to oxygen under illumination leads to the formation of deep charge traps in the active layer;¹⁰⁸ consequently, it seems probable that this exposure to oxygen likewise causes faster V_{OC} and FF loss in the burn-in.

The other contributing factor to the faster burn-in is the loss in J_{SC} . While the proportional loss of J_{SC} in the burn-in is similar in both the nitrogen and synthetic air experiments, the rate of loss both during and after burn-in is much higher in the synthetic air experiment, resulting in shorter projected T_{S80} lifetime values. As with the nitrogen experiment (Figure 5.2.10), this was correlated to a cross-spectrum decrease in EQE; however, the proportional loss of EQE was greater in the dry synthetic air experiment, as shown in Figure 5.3.3.

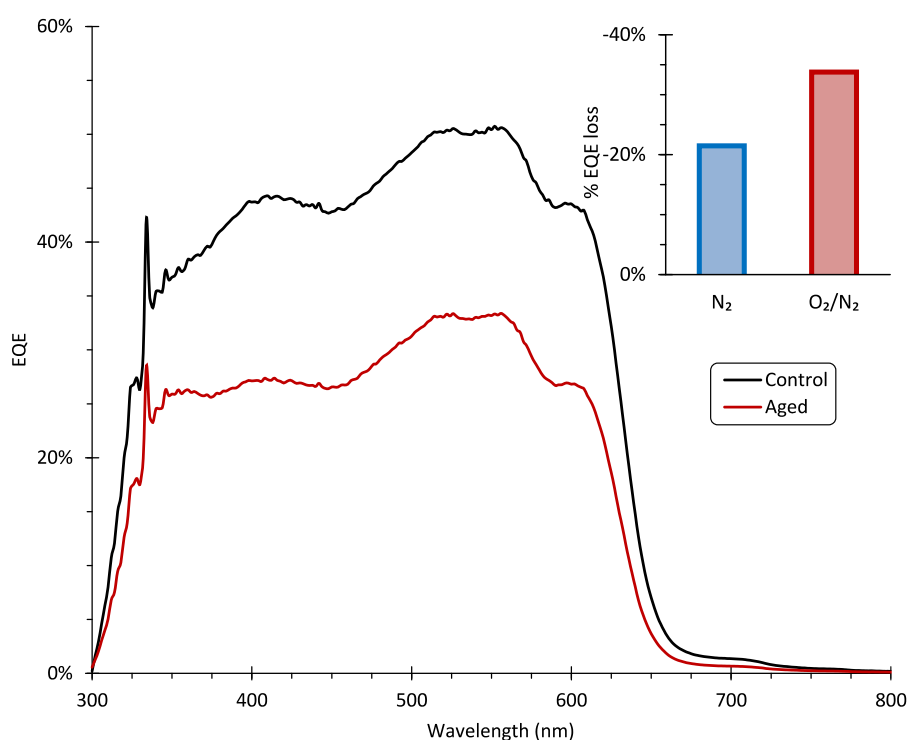


Figure 5.3.3: EQE data obtained from unaged control and photo-aged (400 hours, O_2/N_2 atmosphere, $800 W m^{-2}$) Al/MoO₃ inverted OPV devices; and (inset) a comparison of proportional EQE loss of the dry nitrogen and dry synthetic air experiments. Proportional EQE loss is calculated as the difference in EQE at 520 nm between the aged and control samples as a percentage of the EQE of the control. The aged and control curves in the main plot are representative of several devices measured in this experiment.

It should be noted that the degradation mechanisms observed in the nitrogen experiment are most likely still present in the synthetic air experiment. With respect to the accelerated J_{SC} loss in the burn-in, the mechanisms identified in section 5.2.3 are unlikely to be accelerated by the presence of oxygen. There is a possibility that instead of promoting the dimerisation of the fullerenes, which was the mechanism that J_{SC} loss in the nitrogen experiment was attributed to¹⁶⁶ (see section 5.2.3), oxygen acts to form bridges between the fullerenes. This has been previously observed to take place when fullerenes are exposed to oxygen, and is thought to proceed via a [2+2] cycloaddition mechanism.²⁰⁴ It is unclear if this would have the same effect as fullerene dimerisation upon the J_{SC} , but it would seem probable. There is some evidence that this may be occurring in this experiment, as there is a slight decline in the 400 nm band in the EQE between the control sample and the sample photoaged in an oxygen atmosphere (Figure 5.3.3), and this band is associated with the presence of PC₆₁BM aggregates.²⁰⁵

It is probable that an additional mechanism is present that accelerates J_{SC} loss in the burn-in. The most likely source is photobleaching of the active layer through photooxidation. This mechanism is well documented in P3HT active layers, in which oxygen attacks the side-chains of the polymer, resulting in the formation of radicals that propagate throughout the chain and fragment it.⁶⁷ As discussed in Chapter 2, fragmentation of the conjugated backbone of the P3HT removes its ability to absorb light, thereby lowering J_{SC} .^{65,67} Some evidence for this can be found in the EQE data (Figure 5.3.3), in which the samples exhibit a greater cross-spectrum reduction in EQE than their counterparts in the nitrogen experiment, similar to the changes in absorption spectra observed in photooxidation studies of conjugated polymers (Figure 2.3.3).^{65,67} The loss of EQE is not as pronounced as the absorption losses in the studies cited in Chapter 2; however, it is likely that the photooxidation in this experiment is limited by the rate at which oxygen can diffuse through and around the top electrode into the device rather than the kinetics of the reaction itself. The effect of electrode thickness on the rate of J_{SC} loss upon photo-ageing has already been investigated by *Lloyd et al.*, and their results are consistent with the slower degradation rate observed in these experiments.²⁰⁶

A further effect that was observed during the synthetic air experiment was the increase in leakage current that was observed as the experiment progressed (Figure 5.3.4). This was not observed in the dry nitrogen or humid nitrogen (*vide infra*) experiments, but was observed with all material combinations in the synthetic air study, suggesting that the phenomenon is associated with one or more parts of the device common to all the samples: the active layer, ETL, or transparent electrode.

An increase in the leakage current of the devices signifies a decline in the diode function of the device, i.e. its ability to selectively resist a current in reverse bias (shunt resistance). One possible cause of this is doping of the active layer by oxygen. This has been observed by Schafferhans, *et al.* in a study published in *Organic Electronics* in 2010.¹⁰⁸ In their study, the authors observe that oxygen doping of the active layer occurs in both the dark and the light, but is expedited by the presence of light.¹⁰⁸ They go on to show that oxygen doping is also behind the majority of the J_{SC} loss observed in the devices from their study with photo-ageing.¹⁰⁸ It is likely, therefore, that oxygen doping also plays a role in the J_{SC} loss observed in the devices in this experiment; however, as the study by Schafferhans, *et al.* was carried out with the direct architecture, different HTL/ETL and electrode materials, a shorter timescale and higher intensity radiation, caution should be exercised before drawing too many parallels between the two studies.

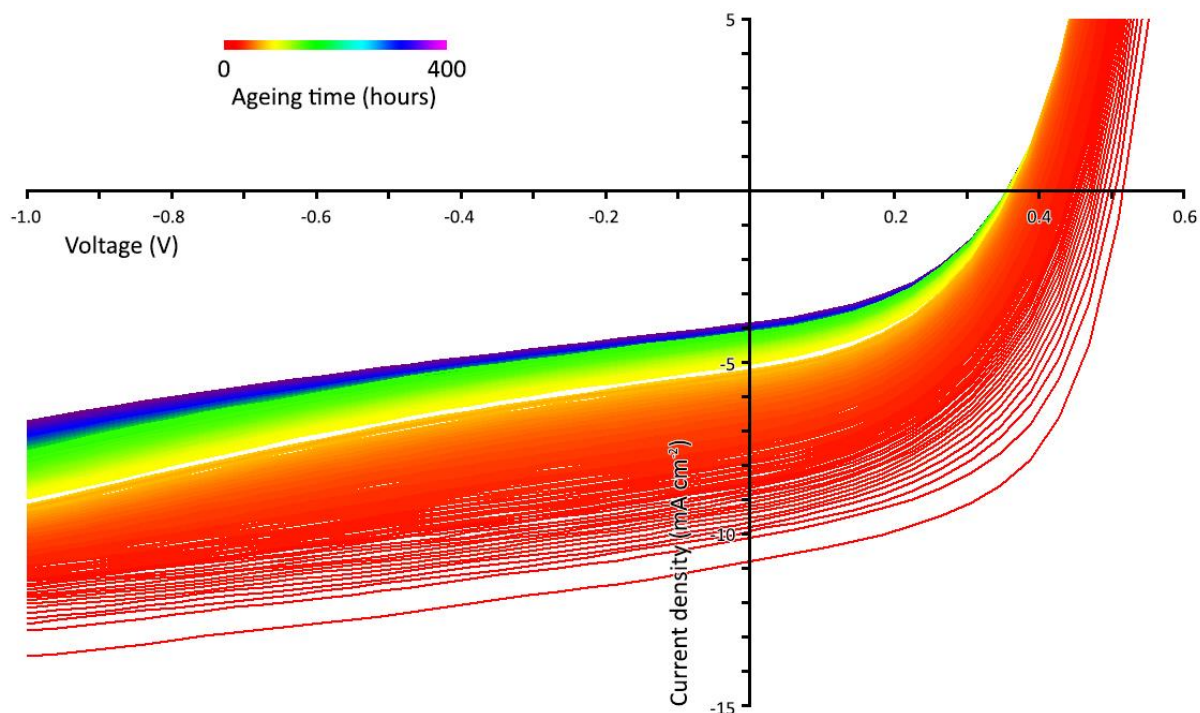


Figure 5.3.4: Evolution of the IV curve of a Al/MoO₃ device as the device is photo-degraded in dry synthetic air at 800 W m⁻². The increase in curvature in the negative bias portion of the curve with ageing indicates an increase in the leakage current/decrease of the shunt resistance of the device.

5.3.2. Degradation in humid nitrogen

In order to observe the effects of humidity on the degradation of OPV devices, the dry nitrogen experiment was repeated with a humid nitrogen atmosphere. All of the material combinations examined in section 5.2 were used in this experiment, but the experiment only ran for 400 hours due to technical challenges with the experiment apparatus. During this time, the samples were kept in a nitrogen (oxygen-free) atmosphere with a relative humidity of between 76% and 77%. The PCE data obtained from the samples in this experiment are shown in Figure 5.3.5.

Due both to the significantly shorter measurement time and to artefacts in the measurements arising from fluctuations in the lamp output, the algorithm in Figure 5.2.2 did not converge when fitting either the biexponential or triexponential model (equations 5.2.7 and 5.2.11 respectively) to the PCE data and, consequently, degradation statistics were not determined for this experiment.

The PCE degradation trends observed with the metal-oxide HTL-containing devices are relatively similar in dry and humid nitrogen atmospheres (cf. Figure 5.2.3 and Figure 5.3.5). It can therefore be surmised that, on this timescale, humidity has little effect on the degradation of the active layer, ETL, or ITO electrode. However, this experiment has only examined the burn-in portion of the degradation curve; it is possible that humidity becomes more important in the longer term degradation of these devices. On the other hand, humidity does have a pronounced effect on the devices with PEDOT:PSS HTLs, as shown in Figure 5.3.6 and Figure 5.3.7.

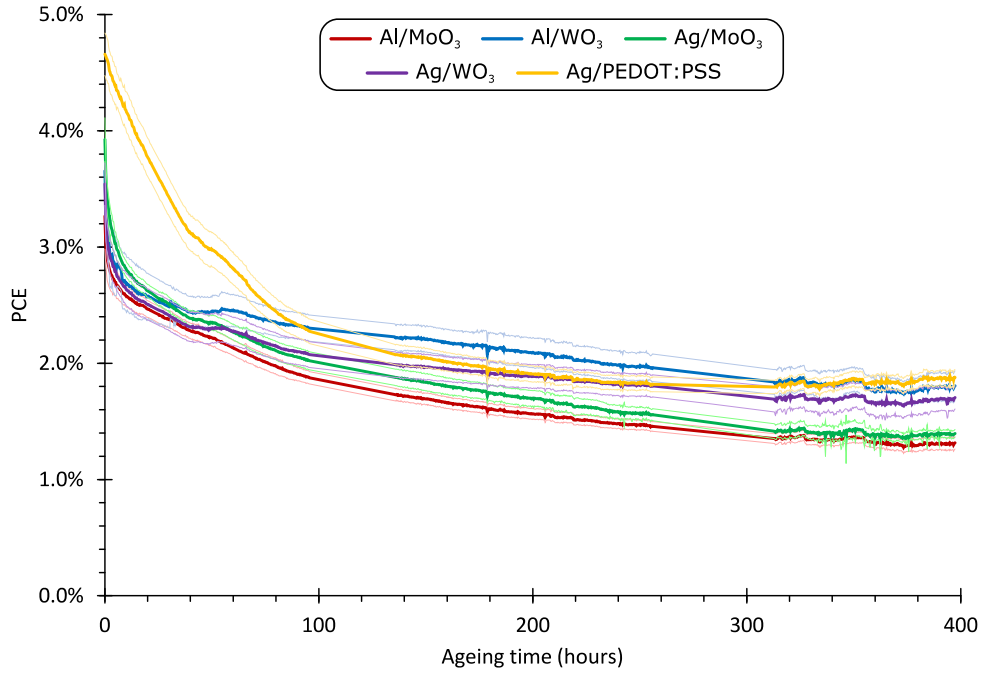


Figure 5.3.5: The evolution of the PCE with photo-ageing of inverted OPV devices in a humid nitrogen atmosphere with various combinations of materials as HTLs and top electrodes. Uncertainties, indicated by the lighter-shaded and thinner curves, represent one standard deviation across ca. 12 devices.

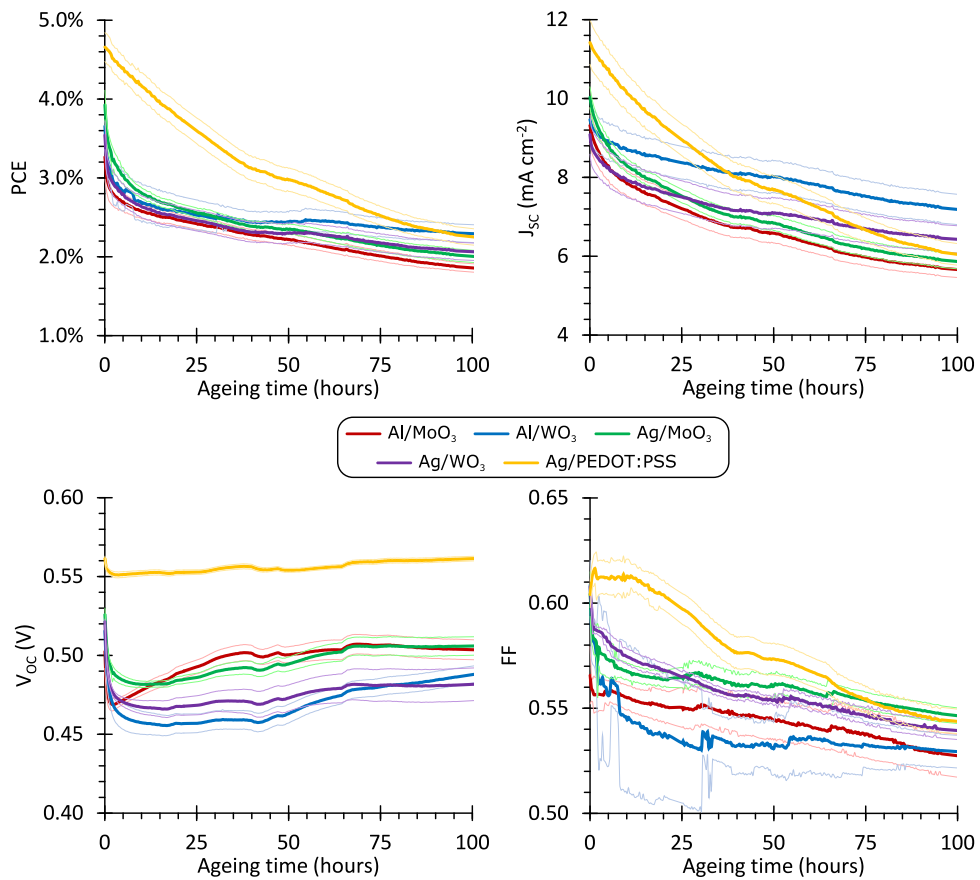


Figure 5.3.6: The evolution of the PV parameters of the OPV samples during the first 100 hours of photoageing under a humid nitrogen atmosphere. Uncertainties represent one standard deviation when averaged across ca. 12 devices.

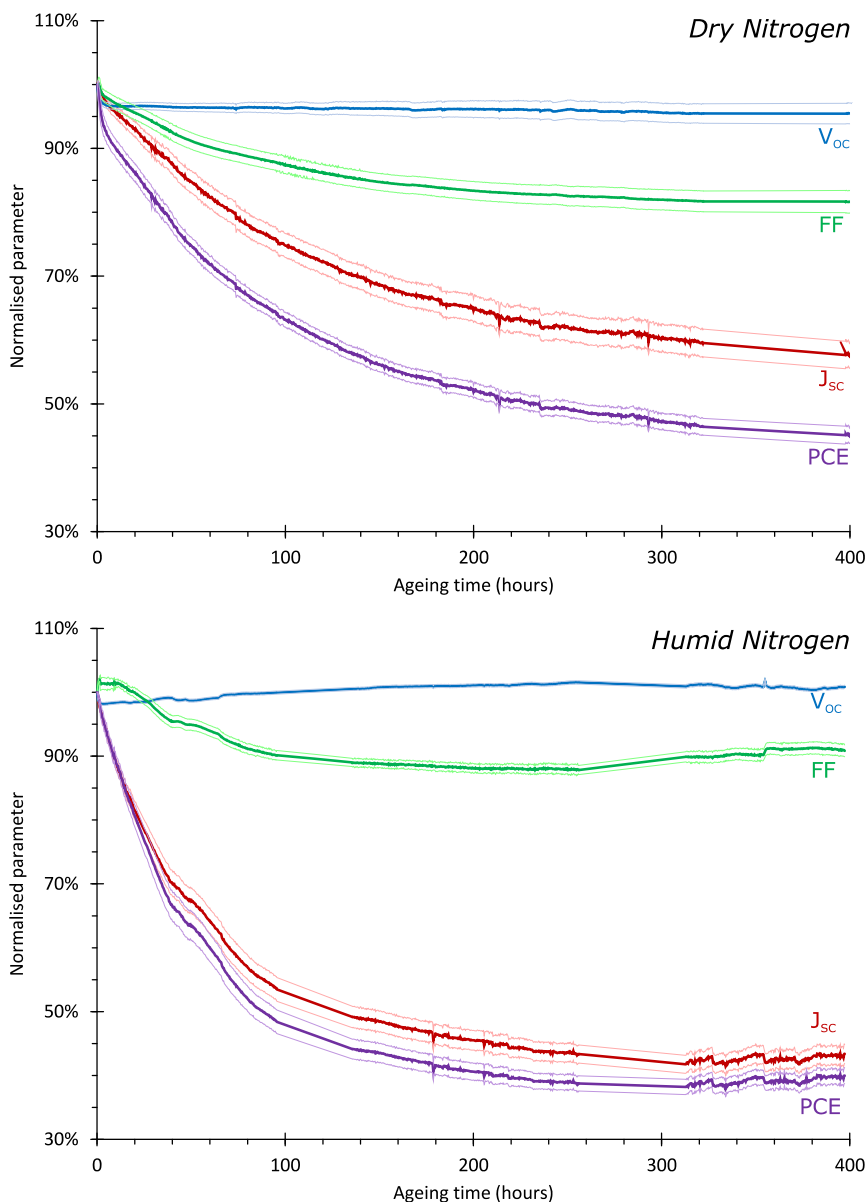


Figure 5.3.7: The evolution of the normalised photovoltaic parameters of the Ag/PEDOT:PSS inverted OPV devices as they were photo-aged in (top) a dry nitrogen atmosphere, and (bottom) a humid nitrogen atmosphere. Uncertainties, indicated by the lighter-shaded and thinner curves, represent one standard deviation when averaged across ca. 12 devices; the parameters are normalised to their initial values.

The presence of humidity correlates to accelerated efficiency loss in the burn-in in the Ag/PEDOT:PSS devices, primarily driven by a sharp decline in J_{sc} . This is in contrast to the rapid degradation of Al/PEDOT:PSS devices observed in Chapter 4, in which J_{sc} loss was preceded by a rapid decline in FF. There, efficiency loss was attributed to the rapid formation of an electrically insulating layer between the HTL and the electrode which would act as a homogeneous charge extraction barrier across the area of the electrode.¹³⁴ This mechanism was characterised by the formation of an inflection point or “S-shape” at the V_{oc} (Figure 4.2.3), which is not seen in this experiment (Figure 5.3.8).

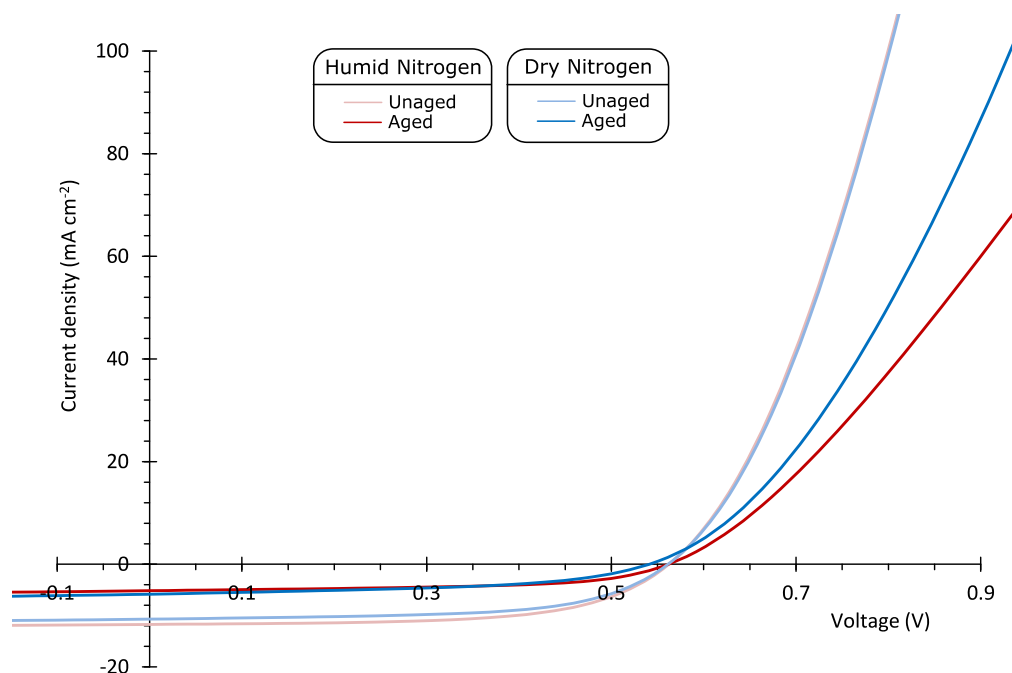


Figure 5.3.8: Effects on the IV curve of a Ag/PEDOT:PSS device as the device undergoes 400 hours of photodegradation in either humid nitrogen (76% RH - red) or dry nitrogen (blue). The decrease of slope in the forward bias, positive current region indicates a substantial increase in the series resistance of the device, which is more pronounced in the sample aged in humid nitrogen.

In addition to the decline in J_{SC} , a significant increase in the series resistance is observed in the Ag/PEDOT:PSS devices (Figure 5.3.8). For a similar ageing time, the increase in the series resistance of a device that was photoaged in a humid nitrogen atmosphere is significantly greater than the increase observed in a device aged in dry nitrogen. This additional increase in series resistance due to the humidity could be caused by a reduction in the conductivity of the PEDOT:PSS due to absorption of water from the chamber atmosphere. The hygroscopicity of PEDOT:PSS is well documented, as is the tendency for thin films of PEDOT:PSS to increase in sheet resistance upon exposure to humidity.^{130,138} The structure of a PEDOT:PSS film is granular, with the PEDOT being more concentrated in the core of the grains and the PSS more concentrated at the grain boundaries.¹⁵⁴ Binding between the grains occurs primarily through a network of hydrogen bonding.¹⁵⁴ When the film absorbs water, the water disrupts the hydrogen bonding between grains and causes them to separate, resulting in the formation of large electrically-insulating regions in the structure.¹⁵⁴ Over time, this has the dual effect of both decreasing the cohesive strength of the film¹⁵⁴ and increasing its series resistance.¹³⁸ This could also partially explain the more rapid loss of J_{SC} with humidity; however, it is also possible that this is due to degradation of the active layer by the increasingly acidic PSS component of the PEDOT:PSS HTL, as this component can be extremely corrosive in humid atmospheres and has even been demonstrated to etch ITO in direct devices under similar conditions.¹⁴⁰

5.4. Summary

In this chapter, the results of several experiments examining the photodegradation of inverted OPV devices were discussed. These experiments were carried out in a custom-built chamber in which 64

devices of varying materials composition could be constantly monitored while being photo-aged in different atmospheres.

The photodegradation behaviour of the devices mimicked the archetypal burn-in/linear behaviour commonly observed in OPV devices aged in laboratory conditions. It was decided that an all-exponential model would be a better choice to model this behaviour than an exponential-linear model as the long term degradation behaviour of the samples would be more likely to exhibit exponential character than linear character. Some material combinations exhibited a two-stage burn-in, with an initial rapid exponential decay followed by a slower exponential efficiency loss until the transition to the post burn-in period. In order to model this early degradation behaviour, a modification to the biexponential model was made to accommodate the initial rapid efficiency loss in which an extra exponential term was added. Using the biexponential and triexponential models, an algorithm was developed to automatically fit these models to the degradation data in order to determine the duration and efficiency loss in the burn-in and the projected lifetime of the devices.

In the photodegradation experiments carried out under nitrogen, a number of differences between the different materials used at the hole extraction interface were observed. In particular, it was noted that devices containing PEDOT:PSS HTLs and silver electrodes had significantly shorter and less severe burn-ins, and that devices with WO_3 HTLs and aluminium top electrodes have estimated lifetimes roughly twice that of the other material combinations. In general, it was observed that the burn-in periods of the devices in this experiment were significantly longer and more severe than in other literature examples.¹³¹ It was concluded that this was caused by the lower intensity of the radiation used for ageing and the increased near-UV component of the radiation as compared to an AM1.5G spectrum.

It was also observed that during the burn-in, the devices exhibited unusual V_{oc} behaviour that was highly dependent on the materials used in the device and the ageing radiation intensity. In particular, the devices exhibited two stages of V_{oc} loss, separated by a brief recovery period. The first stage showed dependence on the HTL material, with MoO_3 -containing devices exhibiting a stronger V_{oc} drop, while the second stage showed dependence on the metal electrode, with silver-containing devices exhibiting a greater V_{oc} loss. As V_{oc} loss is frequently associated with interfacial trapping, it was proposed that these two stages of V_{oc} loss arise from two distinct sets of charge traps: one that forms due to interaction between the light and the HTL material, the other due to the silver electrode. A possible explanation for the second stage of V_{oc} loss is the diffusion of silver into the device, which was observed in thermal degradation study.

The projected lifetimes (post burn-in) of the devices when photoaged in an inert atmosphere were significantly shorter than literature examples of similar experiments.¹⁵⁷ It was noted that the devices in this experiment experienced faster than usual V_{oc} loss following the burn-in and that this was only weakly dependent on the materials used for the HTL or top electrode. Based on unpublished experiments conducted by colleagues in the Organic Electronics group at the University of Bordeaux, it was proposed that this V_{oc} loss is due to the action of the ZnO ETL which, when exposed to near-UV radiation, has been shown to lower the V_{oc} of the device over time.²⁰² This phenomenon (and the increased severity of the burn-in) would likely be avoided completely if the near-UV component of the ageing radiation were filtered out. It was also observed that the devices with a PEDOT:PSS HTL experienced a pronounced increase in series resistance over time that is likely a

consequence of the corrosiveness of the PSS and its interaction with either the silver electrode or the active layer.

The effects of oxygen exposure during aging were shown to significantly impact every aspect of the ageing of the devices: the burn-in both increases in severity and decreases in duration, while the projected lifetimes of the devices decreased by up to 75%. This is proposed to be mostly a consequence of photooxidation of the active layer. This phenomenon has been repeatedly observed in previous studies, and mechanisms for the photo-degradation of P3HT active layers are well understood. Unlike oxygen, humidity had no significant effect on the degradation of the devices with metal-oxide HTLs in the timescale that was studied (400h); however, it had a significant impact on the burn-in of the PEDOT:PSS-containing devices. PEDOT:PSS is known to be highly hygroscopic, so this result is likely due to the absorption of water from the chamber atmosphere causing both an increase in the series resistance of the layer and an increase in its corrosiveness.

These experiments, like those detailed in Chapter 4, have further emphasised the importance of materials choice when designing OPV to match the operating conditions that they will encounter. They highlighted the fact that a device architecture can be stable under one condition, but not necessarily under another. For instance, Ag/PEDOT:PSS devices were shown to be very stable under thermal stress, and when aged under illumination in an inert atmosphere. However when illumination is combined with humidity, the stability of the Ag/PEDOT:PSS device is decreased dramatically. Likewise, it was shown that a good choice in HTL and metal electrode can significantly increase the projected lifetime of a device when the device is aged in inert conditions; however, when the device is exposed to oxygen, the active layer becomes the limiting factor. Therefore, it is evident that any discussion of designing devices that will cope with real-world operating conditions must go beyond simply trying to block extrinsic degradation stimuli through encapsulation and filtration; it is essential to also consider the inherent stability of the device to these stimuli and how this can be improved through the use of appropriate materials in the devices' fabrication.

6.1. General conclusions

This study has employed a range of characterisation techniques to study the role that the use of different materials at the hole extraction interface in inverted OPV devices has in the devices' resilience to degradation stimuli.

The first part of the study dealt with the effects of thermal ageing of P3HT:PC₆₁BM OPV devices and showed that the devices' degradation shows significant variation when different materials are used for the HTL (MoO₃, WO₃, or PEDOT:PSS) and metal electrode (silver or aluminium). All the devices exhibited J_{SC} loss with thermal ageing which was attributed to thermally-induced phase separation and crystalline domain growth. This J_{SC} loss was not observed in samples that used PCDTBT:PC₇₁BM active layers, most likely because PCDTBT has a higher T_g and does not facilitate mass-transport as well as P3HT, thus preventing domain growth. The use of PEDOT:PSS HTLs and aluminium electrodes together in a device was found to lead to extremely rapid degradation of the device due to corrosion of the electrode by the PEDOT:PSS and the formation of an insulating oxide. Some of the devices exhibited an additional degradation mechanism to the J_{SC} loss, which was primarily driven by losses in V_{OC} and FF . This mechanism was only observed in devices with MoO₃ HTLs and silver electrode, and not in any other combination of materials. The material dependence of this behaviour, and the fact that it is driven by V_{OC} and FF loss would be consistent with the formation of charge traps in the active layer, caused by the diffusion of species from the hole extraction interface. This was supported by observations in a thermal degradation study of devices with PCDTBT:PC₇₁BM active layers, in which the same loss of V_{OC} was observed in Ag/MoO₃ devices, but took place over a much longer timescale – consistent with the high T_g of the PCDTBT limiting the rate of diffusion into the active layer.

Following the device degradation study, a physical characterisation study was carried out in order to correlate the observed changes in the PV parameters of the devices with thermal ageing (particularly the V_{OC} and FF loss observed in the Ag/MoO₃ samples) to physical changes in the devices. RBS analysis revealed that the silver samples exhibit substantial changes in their elemental profile with thermal ageing, while the aluminium samples exhibited no change. These changes could not be correlated to any previously-observed changes in the PV parameters of the OPV devices, in particular the V_{OC}/FF -driven mechanism observed in Ag/MoO₃ devices as the elemental profile changes are observed with both MoO₃ and WO₃ HTLs. The changes in elemental profile are more pronounced in samples containing WO₃, so much so that significant quantities of tungsten can even be detected at the surfaces of the samples after thermal ageing. Further analysis of the RBS data, and subsequent AFM measurements revealed that an increase in the roughness of the samples was responsible for many of the observed changes in elemental profile (although diffusion could not be entirely ruled out as also taking place), and that this roughness increase was more severe when WO₃ HTLs were used. The presence of tungsten at the surface of the aged samples in the RBS experiments, and the surface

morphology of the samples was suggestive that the silver electrode was dewetting from the HTL, to the extent that HTL was being exposed in places. To test the effect this might have upon the performance of a device with thermal ageing, an experiment was carried out in which devices with silver electrodes of varying thicknesses were thermally aged. It was found that devices with very thin electrodes experienced catastrophic failure due to a dramatic increase in the series resistance of the device, which occurred much faster in the devices with WO_3 HTLs than those with MoO_3 HTLs. Subsequent AFM analysis revealed that this was due to the silver electrode forming isolated “islands” as it de-wetted from the HTL, removing its ability to extract a current from the device.

In order to understand how the physical changes and changes in PV parameters related to changes in the mechanical stability of the devices, a fracture analysis study was carried out on thermally-aged inverted OPV samples with MoO_3 or WO_3 HTLs, and aluminium or silver top electrodes. All of the samples fractured at the HTL/active layer interface prior to ageing, and the adhesion of this interface increased with all material combinations after one week of thermal ageing. The increase in adhesion was greatest in the aluminium-containing samples, to the extent that it increased beyond the cohesion strength of the BHJ active layer, causing the fracture path to shift from the HTL/active layer interface to within the active layer. The increase in adhesion observed in the silver samples was not as great as what was observed with the aluminium samples, so the fracture path remained at the HTL/active layer interface. As the silver samples were aged further, the fracture path moved to within the active layer, without showing significant variation in fracture energy – indicating that the cohesion of the active layer has declined – likely a consequence of thermally-induced phase separation, and therefore related to the J_{sc} loss observed with thermal ageing. The fractured samples were analysed by XPS depth profiling, which revealed that a significant degree of intermixing occurs in the silver samples with one week of thermal ageing, which is likely the reason for the observed increase in adhesion. A change in the surface potential energy of the fractured surface was observed with one week of thermal ageing, which is consistent with a change in the chemical composition at the interface. The changes in the samples were relatively similar with both HTL materials, so although this shows that species from the top interface are diffusing into the device when silver electrodes are used, this only manifests as a loss of V_{oc} and FF when MoO_3 is used as an HTL material – suggesting that either the diffusing silver chemically interacts with the MoO_3 to form charge traps, or it is the MoO_3 itself that forms charge traps, but it only diffuses into the device when a silver electrode is used.

In the second part of the experiment, a series of photoageing experiments were carried out using a purpose-built ageing chamber. These experiments were carried out to test the role that different HTL (MoO_3 , WO_3 , or PEDOT:PSS) and electrode materials (silver or aluminium) can play in the photostability of devices, both in inert conditions, and in the presence of oxygen and humidity. The first experiment, done under a nitrogen atmosphere, found that the devices fabricated in this study exhibited far longer and more severe burn-ins than are typically observed with devices of this type. By comparing with previously published photostability studies, it was possible to conclude that the increased length of the burn-in was due to the lower intensity of the radiation used, which slowed the generation of charge traps in the active layer, meaning that the V_{oc} declined more slowly than in other studies. Literature sources also suggested that the more severe burn-in, which was driven by a larger than normal loss of J_{sc} , was due to the interaction of UV light with impurities and residual solvent in the active layer, and (to a lesser extent) the presence of more amorphous fullerene domains in the active layer. Some material dependency was observed in this study. In particular,

PEDOT:PSS-containing devices had shorter and less severe burn-ins due to greater V_{OC} stability, while the metal-oxide HTL samples exhibited an initial rapid decline, partial recovery, and then slower decline in V_{OC} with photoageing. The latter phenomenon could be due to the formation of two distinct sets of charge traps, one due to interaction with the HTL (most pronounced with MoO_3) and one due to interaction with the electrode (most pronounced with silver). The decline of V_{OC} also played the main role in determining the rate of efficiency loss post burn-in. The material combination with the longest projected lifetime in these conditions was Ag/WO_3 , and although its projected lifetime of 97.7 ± 7.7 days was approximately twice as long as the other material combinations (due to a slower V_{OC} loss), this is significantly shorter than what has been reported in other studies (between 2.8 and 3.8 years).¹⁵⁷ The proposed reason for this is that some of the literature studies conduct their ageing experiments without a UV component in the radiation source, and unpublished results from Drs Giorgio Mattana and Sylvain Chambon at the University of Bordeaux suggest that ZnO ETLs (which were used in all the samples) can accelerate V_{OC} loss with UV exposure.²⁰² In the devices containing PEDOT:PSS, this was accompanied by an increase in the series resistance, which was thought to be due to corrosion of the silver electrode by the acidic PSS component, leading to the formation of a layer of less-conductive Ag_xO .

The effects of oxygen and humidity upon the photodegradation of the devices were also examined. Oxygen had a significant impact on the degradation of the devices, removing all material dependency, shortening and intensifying their burn-ins, and drastically shortening their projected lifetimes. The changes in the burn-in arose from faster declines in J_{SC} , V_{OC} , and FF . The faster losses of V_{OC} and FF are likely a consequence of the formation of additional charge traps by oxygen that ingresses into the device. The faster decline in the J_{SC} in both the burn-in and post burn-in periods is most likely a consequence of photooxidative bleaching of the active layer, removing its ability to absorb radiation, and ultimately shortening the projected lifetimes of the devices.⁶⁷ This J_{sc} loss is coupled with an increase in the leakage current of the device, which was not observed in the nitrogen experiment and may be due to doping of the active layer by oxygen.¹⁰⁸ In comparison, humidity had remarkably little effect on the early stages of photoageing of the inverted OPV devices, except with the samples that incorporated a PEDOT:PSS HTL. These samples exhibited a significantly accelerated and intensified burn-in, which was primarily driven by declines in the J_{SC} and increases in the series resistance. It was proposed that the latter is due to the absorption of water from the atmosphere by the PEDOT:PSS layer, disrupting its hydrogen bonding network and increasing its sheet resistance, as has been observed in thin PEDOT:PSS films previously.¹⁵⁴ The added water increases the acidity of the PSS component, so it is possibly that this acts to corrode the active layer, leading to the accelerated loss of J_{SC} .

This study has demonstrated the presence of several, previously un-reported degradation mechanisms in inverted OPV solar cells, as well as examining the interrelationship between the use of different materials at the hole collecting interface, and the stability of the device towards different degradation stimuli. It is not the conclusion of this study that one particular material is “bad” or “good” when it comes to its application in OPV. Rather, the design of an OPV solar cell must match the materials to be used with the environment to which the device is to be exposed. Such considerations must include, for example, the quality of encapsulation, whether the device will be exposed to high temperatures or significant quantities of UV radiation, whether thin electrodes are required for transparency, and whether the device will be subjected to mechanical stress. The answers to these (and other) questions can be used to select materials that are appropriate to the

application that the device is being designed for, and thereby maximise its potential lifetime. Matching materials to applications to maximise lifetime will be of utmost importance in working towards the goal of 10 year's lifetime and in the large-scale commercialisation of OPV technology.

6.2. Avenues for future research

One thing that is always true of research is that it is never finished, there are always things left to investigate. This section details a few areas where this work can be carried on, or that may be of interest to other researchers.

With respect to the ageing chamber constructed for this study, there is certainly scope for future experiments using this apparatus. This may include a longer humidity experiment than the one carried out in this study so that the effects of humidity on the estimated lifetime of the devices can be quantified. Further experiments could include using UV filters to confirm the role that UV radiation plays in the ageing of the devices, or testing devices fabricated from higher-efficiency polymers like PCDTBT. The chamber was designed to be as flexible as possible, to accommodate a range of different experiments and upgrades. This might include the ability to age the devices at P_{max} or J_{SC} , rather than at V_{oc} as they are now, or including a Peltier element to actively control the sample temperature, or even the testing of whole OPV modules rather than individual devices.

With respect to studying the role that material choice plays in device lifetime, there is much left to study. This work was limited to a relatively small number of materials (three HTLs and two electrodes), but this represents a small fraction of the different materials that have been documented in functional OPV devices. Replacing ITO with another transparent conductor has been a priority for the OPV research community for many years now, and although many solutions have been proposed, only a few have been tested for the role they play in device stability. Carrying out thermal degradation and photodegradation studies of devices incorporating, for example, graphene electrodes, carbon nanotube composite electrodes, or silver nanowire electrodes should be a priority for researchers in these areas. The silver nanowire electrodes' resilience to thermal degradation could be of great interest given the tendency silver has demonstrated in this study towards dewetting from metal-oxide HTLs and diffusing into the device. There is also a range of HTL and ETL materials to be examined (including new materials in this application like self-assembled monolayers) and the role that different processing techniques can have in determining the stability of a device (for instance, solution processed WO_3 vs. evaporated). While some of the issues preventing device lifetimes from reaching 10 years can be ameliorated through good encapsulation strategies, encapsulation costs can be significantly lowered if the devices are designed to be more inherently stable to extrinsic degradation stimuli.

Finally, one of the most promising areas of OPV research being pursued in order to raise the efficiency of OPV devices is that of non-fullerene acceptor species. In spite of all the interest in this subject, relatively little information exists about the stability of devices that incorporate these compounds. It is unclear how morphologically stable a BHJ incorporating a non-fullerene acceptor would be when thermally aged, although this would likely be determined by how the solubility of the acceptor in the donor compares with its fullerene counterparts. Fullerene acceptors can have a stabilising effect on an active layer undergoing photooxidation due to their radical scavenging properties, so would non-fullerene acceptors have the same effect? Under illumination fullerene

acceptors can dimerise during the burn-in, resulting in J_{sc} loss – would non-fullerene acceptors be vulnerable to the same process? These are questions that need to be answered if the potential of non-fullerene acceptors is to be realised.

References

1. Intergovernmental Panel on Climate Change. *Climate Change 2013 -- The Physical Science Basis: Working Group I Contribution to the Fifth Assessment Report of the Intergovernmental Panel on Climate Change*. (Cambridge University Press, 2014). at <<https://books.google.fr/books?id=jn4mCAAQBAJ>>
2. Tripathi, A. K., Roberts, C. D. & Eagle, R. A. Coupling of CO₂ and Ice Sheet Stability Over Major Climate Transitions of the Last 20 Million Years. *Science (80-.)*. **326**, 1394–1397 (2009).
3. Kelley, C. P., Mohtadi, S., Cane, M. A., Seager, R. & Kushnir, Y. Climate change in the Fertile Crescent and implications of the recent Syrian drought. *Proc. Natl. Acad. Sci.* **112**, 3241–3246 (2015).
4. COP21 | United nations conference on climate change. at <<http://www.cop21.gouv.fr/en/>>
5. Bloomberg New Energy Finance. *New Energy Outlook 2016*. (2016).
6. Oil Prices Have Hit a 10-Year Low. They're Not Going to Stay There. *Foreign Policy* (2016). at <<http://foreignpolicy.com/2016/01/06/oil-prices-have-hit-a-10-year-low-theyre-not-going-to-stay-there/>>
7. Yergin, D. *The Prize: The Epic Quest for Oil, Money & Power*. (Free Press, 2011). at <<https://books.google.fr/books?id=WiUTwBTux2oC>>
8. Africa's new breed of solar energy entrepreneurs. *BBC News* (2015). at <<http://www.bbc.com/news/business-30805419>>
9. Becquerel, A. E. Mémoire sur les effets électriques produits sous l'influence des rayons solaires. *Comptes Rendus des Séances Hebd.* **9**, 561–567 (1839).
10. This Month in Physics History. *APS News* **18**, 2 (2009).
11. Green, M. A., Emery, K., Hishikawa, Y., Warta, W. & Dunlop, E. D. Solar cell efficiency tables (version 47). *Prog. Photovoltaics Res. Appl.* **24**, 3–11 (2016).
12. *Stability and Degradation of Organic and Polymer Solar Cells*. (John Wiley & Sons, Ltd, 2012). doi:10.1002/9781119942436
13. Shirakawa, H., Louis, E. J., MacDiarmid, A. G., Chiang, C. K. & Heeger, A. J. Synthesis of electrically conducting organic polymers: halogen derivatives of polyacetylene, (CH) x. *J. Chem. Soc. Chem. Commun.* 578 (1977). doi:10.1039/c39770000578
14. The Nobel Prize in Chemistry 2000. *Nobelprize.org* at <https://www.nobelprize.org/nobel_prizes/chemistry/laureates/2000/>
15. Krebs, F. C., Espinosa, N., Hösel, M., Søndergaard, R. R. & Jørgensen, M. 25th Anniversary Article: Rise to Power - OPV-Based Solar Parks. *Adv. Mater.* **26**, 29–39 (2014).
16. Berny, S., Blouin, N., Distler, A., Egelhaaf, H.-J., Krompiec, M., Lohr, A., Lozman, O. R., Morse, G. E., Nanson, L., Pron, A., Sauermann, T., Seidler, N., Tierney, S., Tiwana, P., Wagner, M. & Wilson, H. Solar Trees: First Large-Scale Demonstration of Fully Solution Coated, Semitransparent, Flexible Organic Photovoltaic Modules. *Adv. Sci.* **3**, 1500342 (2016).

17. Espinosa, N., García-Valverde, R., Urbina, A. & Krebs, F. C. A life cycle analysis of polymer solar cell modules prepared using roll-to-roll methods under ambient conditions. *Sol. Energy Mater. Sol. Cells* **95**, 1293–1302 (2011).
18. García-Valverde, R., Cherni, J. A. & Urbina, A. Life cycle analysis of organic photovoltaic technologies. *Prog. Photovoltaics Res. Appl.* **18**, 535–558 (2010).
19. Gambhir, A., Sandwell, P. & Nelson, J. The future costs of OPV – A bottom-up model of material and manufacturing costs with uncertainty analysis. *Sol. Energy Mater. Sol. Cells* 1–10 (2016). doi:10.1016/j.solmat.2016.05.056
20. Scharber, M. C. On the Efficiency Limit of Conjugated Polymer:Fullerene-Based Bulk Heterojunction Solar Cells. *Adv. Mater.* **28**, 1994–2001 (2016).
21. Jørgensen, M., Norrman, K., Gevorgyan, S. A., Tromholt, T., Andreasen, B. & Krebs, F. C. Stability of Polymer Solar Cells. *Adv. Mater.* **24**, 580–612 (2012).
22. Reese, M. O., Gevorgyan, S. a., Jørgensen, M., Bundgaard, E., Kurtz, S. R., Ginley, D. S., Olson, D. C., Lloyd, M. T., Morvillo, P., Katz, E. a., Elschner, A., Haillant, O., Currier, T. R., Shrotriya, V., Hermenau, M., Riede, M., R. Kirov, K., Trimmel, G., Rath, T., Inganäs, O., Zhang, F., Andersson, M., Tvingstedt, K., Lira-Cantu, M., Laird, D., McGuinness, C., Gowrisanker, S. (Jimmy), Pannone, M., Xiao, M., Hauch, J., Steim, R., DeLongchamp, D. M., Rösch, R., Hoppe, H., Espinosa, N., Urbina, A., Yaman-Uzunoglu, G., Bonekamp, J.-B., van Breemen, A. J. J. M., Girotto, C., Voroshazi, E. & Krebs, F. C. Consensus stability testing protocols for organic photovoltaic materials and devices. *Sol. Energy Mater. Sol. Cells* **95**, 1253–1267 (2011).
23. Krebs, F., Carle, J., Cruysbagger, N., Andersen, M., Lilliedal, M., Hammond, M. & Hvidt, S. Lifetimes of organic photovoltaics: photochemistry, atmosphere effects and barrier layers in ITO-MEHPPV:PCBM-aluminium devices. *Sol. Energy Mater. Sol. Cells* **86**, 499–516 (2005).
24. Jørgensen, M., Carlé, J. E., Søndergaard, R. R., Lauritzen, M., Dagnæs-Hansen, N. a., Byskov, S. L., Andersen, T. R., Larsen-Olsen, T. T., Böttiger, A. P. L., Andreasen, B., Fu, L., Zuo, L., Liu, Y., Bundgaard, E., Zhan, X., Chen, H. & Krebs, F. C. The state of organic solar cells—A meta analysis. *Sol. Energy Mater. Sol. Cells* **119**, 84–93 (2013).
25. Green, M. A., Emery, K., Hishikawa, Y., Warta, W. & Dunlop, E. D. Solar cell efficiency tables (version 46). *Prog. Photovoltaics Res. Appl.* **23**, 805–812 (2015).
26. Liu, Y., Zhao, J., Li, Z., Mu, C., Ma, W., Hu, H., Jiang, K., Lin, H., Ade, H. & Yan, H. Aggregation and morphology control enables multiple cases of high-efficiency polymer solar cells. *Nat. Commun.* **5**, 5293 (2014).
27. Wantz, G., Derue, L., Dautel, O., Rivaton, A., Hudhomme, P. & Dagrón-Lartigau, C. Stabilizing polymer-based bulk heterojunction solar cells via crosslinking. *Polym. Int.* **63**, 1346–1361 (2014).
28. Rivaton, A., Tournebize, A., Gaume, J., Bussière, P.-O., Gardette, J.-L. & Therias, S. Photostability of organic materials used in polymer solar cells. *Polym. Int.* **63**, 1335–1345 (2014).
29. Luque, A. & Hegedus, S. *Handbook of Photovoltaic Science and Engineering*. (Wiley, 2011). at <<https://books.google.fr/books?id=sLMkCsde1u4C>>
30. Jørgensen, M., Norrman, K. & Krebs, F. C. Stability/degradation of polymer solar cells. *Sol. Energy Mater. Sol. Cells* **92**, 686–714 (2008).

31. Guo, X., Baumgarten, M. & Müllen, K. Designing π -conjugated polymers for organic electronics. *Prog. Polym. Sci.* **38**, 1832–1908 (2013).
32. Blom, P. W. M., Mihailetschi, V. D., Koster, L. J. A. & Markov, D. E. Device Physics of Polymer:Fullerene Bulk Heterojunction Solar Cells. *Adv. Mater.* **19**, 1551–1566 (2007).
33. Mayer, A. C., Scully, S. R., Hardin, B. E., Rowell, M. W. & McGehee, M. D. Polymer-based solar cells. *Mater. Today* **10**, 28–33 (2007).
34. Knupfer, M. Exciton binding energies in organic semiconductors. *Appl. Phys. A* **77**, 623–626 (2003).
35. Tang, C. W. Two-layer organic photovoltaic cell. *Appl. Phys. Lett.* **48**, 183 (1986).
36. Goh, C., Scully, S. R. & McGehee, M. D. Effects of molecular interface modification in hybrid organic-inorganic photovoltaic cells. *J. Appl. Phys.* **101**, 114503 (2007).
37. Shaw, P. E., Ruseckas, A. & Samuel, I. D. W. Exciton Diffusion Measurements in Poly(3-hexylthiophene). *Adv. Mater.* **20**, 3516–3520 (2008).
38. Lin, Y. & Zhan, X. Non-fullerene acceptors for organic photovoltaics: an emerging horizon. *Mater. Horizons* **1**, 470 (2014).
39. Yu, G., Gao, J., Hummelen, J. C., Wudl, F. & Heeger, A. J. Polymer Photovoltaic Cells: Enhanced Efficiencies via a Network of Internal Donor-Acceptor Heterojunctions. *Science (80-.)*. **270**, 1789–1791 (1995).
40. Vongsaysy, U., Pavageau, B., Wantz, G., Bassani, D. M., Servant, L. & Aziz, H. Guiding the Selection of Processing Additives for Increasing the Efficiency of Bulk Heterojunction Polymeric Solar Cells. *Adv. Energy Mater.* **4**, (2014).
41. Verploegen, E., Mondal, R., Bettinger, C. J., Sok, S., Toney, M. F. & Bao, Z. Effects of Thermal Annealing Upon the Morphology of Polymer-Fullerene Blends. *Adv. Funct. Mater.* **20**, 3519–3529 (2010).
42. Chen, H., Hu, S., Zang, H., Hu, B. & Dadmun, M. Precise Structural Development and its Correlation to Function in Conjugated Polymer: Fullerene Thin Films by Controlled Solvent Annealing. *Adv. Funct. Mater.* **23**, 1701–1710 (2013).
43. Lin, Y., Li, Y. & Zhan, X. Small molecule semiconductors for high-efficiency organic photovoltaics. *Chem. Soc. Rev.* **41**, 4245 (2012).
44. Scharber, M. C., Mühlbacher, D., Koppe, M., Denk, P., Waldauf, C., Heeger, A. J. & Brabec, C. J. Design Rules for Donors in Bulk-Heterojunction Solar Cells—Towards 10 % Energy-Conversion Efficiency. *Adv. Mater.* **18**, 789–794 (2006).
45. Nielsen, C. B., Holliday, S., Chen, H.-Y., Cryer, S. J. & McCulloch, I. Non-Fullerene Electron Acceptors for Use in Organic Solar Cells. *Acc. Chem. Res.* **48**, 2803–2812 (2015).
46. Holliday, S., Ashraf, R. S., Wadsworth, A., Baran, D., Yousaf, S. A., Nielsen, C. B., Tan, C.-H., Dimitrov, S. D., Shang, Z., Gasparini, N., Alamoudi, M., Laquai, F., Brabec, C. J., Salleo, A., Durrant, J. R. & McCulloch, I. High-efficiency and air-stable P3HT-based polymer solar cells with a new non-fullerene acceptor. *Nat. Commun.* **7**, 11585 (2016).
47. Proctor, C. M., Kuik, M. & Nguyen, T.-Q. Charge carrier recombination in organic solar cells. *Prog. Polym. Sci.* **38**, 1941–1960 (2013).

48. Moulé, A. J., Bonekamp, J. B. & Meerholz, K. The effect of active layer thickness and composition on the performance of bulk-heterojunction solar cells. *J. Appl. Phys.* **100**, 94503 (2006).
49. Zeng, L., Tang, C. W. & Chen, S. H. Effects of active layer thickness and thermal annealing on polythiophene: Fullerene bulk heterojunction photovoltaic devices. *Appl. Phys. Lett.* **97**, 53305 (2010).
50. Ratcliff, E. L., Zacher, B. & Armstrong, N. R. Selective Interlayers and Contacts in Organic Photovoltaic Cells. *J. Phys. Chem. Lett.* **2**, 1337–1350 (2011).
51. Lai, T.-H., Tsang, S.-W., Manders, J. R., Chen, S. & So, F. Properties of interlayer for organic photovoltaics. *Mater. Today* **16**, 424–432 (2013).
52. Courtright, B. A. E. & Jenekhe, S. A. Polyethylenimine Interfacial Layers in Inverted Organic Photovoltaic Devices: Effects of Ethoxylation and Molecular Weight on Efficiency and Temporal Stability. *ACS Appl. Mater. Interfaces* **7**, 26167–26175 (2015).
53. Steim, R., Kogler, F. R. & Brabec, C. J. Interface materials for organic solar cells. *J. Mater. Chem.* **20**, 2499 (2010).
54. Mazzi, K. a. & Luscombe, C. K. The future of organic photovoltaics. *Chem. Soc. Rev.* **44**, 78–90 (2015).
55. Candelise, C., Winkler, M. & Gross, R. Implications for CdTe and CIGS technologies production costs of indium and tellurium scarcity. *Prog. Photovoltaics Res. Appl.* **20**, 816–831 (2012).
56. Langley, D., Giusti, G., Mayousse, C., Celle, C., Bellet, D. & Simonato, J.-P. Flexible transparent conductive materials based on silver nanowire networks: a review. *Nanotechnology* **24**, 452001 (2013).
57. Park, H., Rowehl, J. A., Kim, K. K., Bulovic, V. & Kong, J. Doped graphene electrodes for organic solar cells. *Nanotechnology* **21**, 505204 (2010).
58. Barnes, T. M., Bergeson, J. D., Tenent, R. C., Larsen, B. A., Teeter, G., Jones, K. M., Blackburn, J. L. & van de Lagemaat, J. Carbon nanotube network electrodes enabling efficient organic solar cells without a hole transport layer. *Appl. Phys. Lett.* **96**, 243309 (2010).
59. Vosgueritchian, M., Lipomi, D. J. & Bao, Z. Highly Conductive and Transparent PEDOT:PSS Films with a Fluorosurfactant for Stretchable and Flexible Transparent Electrodes. *Adv. Funct. Mater.* **22**, 421–428 (2012).
60. Ding, Z., Stoichkov, V., Horie, M., Brousseau, E. & Kettle, J. Spray coated silver nanowires as transparent electrodes in OPVs for Building Integrated Photovoltaics applications. *Sol. Energy Mater. Sol. Cells* **157**, 305–311 (2016).
61. Weinberger, B. R., Akhtar, M. & Gau, S. C. Polyacetylene photovoltaic devices. *Synth. Met.* **4**, 187–197 (1982).
62. Wang, N., Tong, X., Burlingame, Q., Yu, J. & Forrest, S. R. Photodegradation of small-molecule organic photovoltaics. *Sol. Energy Mater. Sol. Cells* **125**, 170–175 (2014).
63. Norrman, K., Alstrup, J., Jørgensen, M. & Krebs, F. C. Lifetimes of organic photovoltaics: photooxidative degradation of a model compound. *Surf. Interface Anal.* **38**, 1302–1310 (2006).
64. Chambon, S., Rivaton, A., Gardette, J.-L., Firon, M. & Lutsen, L. Aging of a donor conjugated

- polymer: Photochemical studies of the degradation of poly[2-methoxy-5-(3',7'-dimethyloctyloxy)-1,4-phenylenevinylene]. *J. Polym. Sci. Part A Polym. Chem.* **45**, 317–331 (2007).
65. Tournebize, A., Bussière, P.-O., Wong-Wah-Chung, P., Thérias, S., Rivaton, A., Gardette, J.-L., Beaupré, S. & Leclerc, M. Impact of UV-Visible Light on the Morphological and Photochemical Behavior of a Low-Bandgap Poly(2,7-Carbazole) Derivative for Use in High-Performance Solar Cells. *Adv. Energy Mater.* **3**, 478–487 (2013).
 66. Dang, M. T., Hirsch, L. & Wantz, G. P3HT:PCBM, Best Seller in Polymer Photovoltaic Research. *Adv. Mater.* **23**, 3597–3602 (2011).
 67. Manceau, M., Rivaton, A., Gardette, J.-L., Guillerez, S. & Lemaître, N. The mechanism of photo- and thermooxidation of poly(3-hexylthiophene) (P3HT) reconsidered. *Polym. Degrad. Stab.* **94**, 898–907 (2009).
 68. Abdou, M. S. A. & Holdcroft, S. Solid-state photochemistry of π -conjugated poly(3-alkylthiophenes). *Can. J. Chem.* **73**, 1893–1901 (1995).
 69. Mei, J. & Bao, Z. Side Chain Engineering in Solution-Processable Conjugated Polymers. *Chem. Mater.* **26**, 604–615 (2014).
 70. Nelson, J. Polymer:fullerene bulk heterojunction solar cells. *Mater. Today* **14**, 462–470 (2011).
 71. Mühlbacher, D., Scharber, M., Morana, M., Zhu, Z., Waller, D., Gaudiana, R. & Brabec, C. High Photovoltaic Performance of a Low-Bandgap Polymer. *Adv. Mater.* **18**, 2884–2889 (2006).
 72. Park, S. H., Roy, A., Beaupré, S., Cho, S., Coates, N., Moon, J. S., Moses, D., Leclerc, M., Lee, K. & Heeger, A. J. Bulk heterojunction solar cells with internal quantum efficiency approaching 100%. *Nat. Photonics* **3**, 297–302 (2009).
 73. Fraga Domínguez, I., Topham, P. D., Bussière, P.-O., Bégué, D. & Rivaton, A. Unravelling the Photodegradation Mechanisms of a Low Bandgap Polymer by Combining Experimental and Modeling Approaches. *J. Phys. Chem. C* **119**, 2166–2176 (2015).
 74. Turkovic, V., Engmann, S., Tsierkezos, N., Hoppe, H., Madsen, M., Rubahn, H.-G., Ritter, U. & Gobsch, G. Long-term stabilization of organic solar cells using UV absorbers. *J. Phys. D: Appl. Phys.* **49**, 125604 (2016).
 75. Neugebauer, H., Brabec, C., Hummelen, J. C. & Sariciftci, N. S. Stability and photodegradation mechanisms of conjugated polymer/fullerene plastic solar cells. *Sol. Energy Mater. Sol. Cells* **61**, 35–42 (2000).
 76. Chambon, S., Rivaton, A., Gardette, J.-L. & Firon, M. Photo- and thermal degradation of MDMO-PPV:PCBM blends. *Sol. Energy Mater. Sol. Cells* **91**, 394–398 (2007).
 77. Hoke, E. T., Sachs-Quintana, I. T., Lloyd, M. T., Kauvar, I., Mateker, W. R., Nardes, A. M., Peters, C. H., Kopidakis, N. & McGehee, M. D. The Role of Electron Affinity in Determining Whether Fullerenes Catalyze or Inhibit Photooxidation of Polymers for Solar Cells. *Adv. Energy Mater.* **2**, 1351–1357 (2012).
 78. Ashcroft, N. W. & Mermin, N. D. *Solid State Physics*. (Harcourt College Publishers, 1976). at <<http://books.google.co.nz/books?id=FRZRAAAAMAAJ>>
 79. Lilley, J. *Nuclear Physics: Principles and Applications*. (John Wiley & Sons, 2006).

80. Kittel, C. *Introduction to solid state physics*. (Wiley, 2005). at <<http://books.google.co.nz/books?id=kym4QgAACAAJ>>
81. Mikhnenko, O. V, Blom, P. W. M. & Nguyen, T.-Q. Exciton diffusion in organic semiconductors. *Energy Environ. Sci.* **8**, 1867–1888 (2015).
82. Street, R. A. Electronic Structure and Properties of Organic Bulk-Heterojunction Interfaces. *Adv. Mater.* **28**, 3814–3830 (2016).
83. Xu, G., Lu, N., Wang, W., Gao, N., Ji, Z., Li, L. & Liu, M. Universal description of exciton diffusion length in organic photovoltaic cell. *Org. Electron.* **23**, 53–56 (2015).
84. Chen, H., Hegde, R., Browning, J. & Dadmun, M. D. The miscibility and depth profile of PCBM in P3HT: thermodynamic information to improve organic photovoltaics. *Phys. Chem. Chem. Phys.* **14**, 5635 (2012).
85. Derue, L., Dautel, O., Tournebize, A., Drees, M., Pan, H., Berthumeyrie, S., Pavageau, B., Cloutet, E., Chambon, S., Hirsch, L., Rivaton, A., Hudhomme, P., Facchetti, A. & Wantz, G. Thermal stabilisation of polymer-fullerene bulk heterojunction morphology for efficient photovoltaic solar cells. *Adv. Mater.* 5831–5838 (2014). doi:10.1002/adma.201401062
86. Yang, X., Van Duren, J. K. J., Janssen, R. A. J., Michels, M. A. J. & Loos, J. Morphology and thermal stability of the active layer in poly(p-phenylenevinylene)/methanofullerene plastic photovoltaic devices. *Macromolecules* **37**, 2151–2158 (2004).
87. Karagiannidis, P. G., Georgiou, D., Pitsalidis, C., Laskarakis, A. & Logothetidis, S. Evolution of vertical phase separation in P3HT:PCBM thin films induced by thermal annealing. *Mater. Chem. Phys.* **129**, 1207–1213 (2011).
88. Eisele, U. *Introduction to Polymer Physics*. (Springer Berlin Heidelberg, 2012). at <<https://books.google.fr/books?id=manoCAAAQBAJ>>
89. Bertho, S., Haeldermans, I., Swinnen, A., Moons, W., Martens, T., Lutsen, L., Vanderzande, D., Manca, J., Senes, A. & Bonfiglio, A. Influence of thermal ageing on the stability of polymer bulk heterojunction solar cells. *Sol. Energy Mater. Sol. Cells* **91**, 385–389 (2007).
90. Zhao, J., Swinnen, A., Van Assche, G., Manca, J., Vanderzande, D. & Mele, B. Van. Phase Diagram of P3HT/PCBM Blends and Its Implication for the Stability of Morphology. *J. Phys. Chem. B* **113**, 1587–1591 (2009).
91. Schaffer, C. J., Palumbiny, C. M., Niedermeier, M. A., Burger, C., Santoro, G., Roth, S. V. & Müller-Buschbaum, P. Morphological Degradation in Low Bandgap Polymer Solar Cells - An In Operando Study. *Adv. Energy Mater.* 1600712 (2016). doi:10.1002/aenm.201600712
92. Wang, T., Pearson, A. J., Dunbar, A. D. F., Staniec, P. A., Watters, D. C., Yi, H., Ryan, A. J., Jones, R. A. L., Iraqi, A. & Lidzey, D. G. Correlating Structure with Function in Thermally Annealed PCDTBT:PC70BM Photovoltaic Blends. *Adv. Funct. Mater.* **22**, 1399–1408 (2012).
93. Staniec, P. A., Parnell, A. J., Dunbar, A. D. F., Yi, H., Pearson, A. J., Wang, T., Hopkinson, P. E., Kinane, C., Dalgliesh, R. M., Donald, A. M., Ryan, A. J., Iraqi, A., Jones, R. A. L. & Lidzey, D. G. The Nanoscale Morphology of a PCDTBT:PCBM Photovoltaic Blend. *Adv. Energy Mater.* **1**, 499–504 (2011).
94. Cho, S., Seo, J. H., Park, S. H., Beaupré, S., Leclerc, M. & Heeger, A. J. A Thermally Stable Semiconducting Polymer. *Adv. Mater.* **22**, 1253–1257 (2010).

95. Wang, D. H., Kim, J. K., Seo, J. H., Park, O. O. & Park, J. H. Stability comparison: A PCDTBT/PC71BM bulk-heterojunction versus a P3HT/PC71BM bulk-heterojunction. *Sol. Energy Mater. Sol. Cells* **101**, 249–255 (2012).
96. Derue, L., Dautel, O., Tournebize, A., Drees, M., Pan, H., Berthumeyrie, S., Pavageau, B., Cloutet, E., Chambon, S., Hirsch, L., Rivaton, A., Hudhomme, P., Facchetti, A. & Wantz, G. Thermal Stabilisation of Polymer-Fullerene Bulk Heterojunction Morphology for Efficient Photovoltaic Solar Cells. *Adv. Mater.* **26**, 5831–5838 (2014).
97. Vongsaysy, U., Bassani, D. M., Servant, L., Pavageau, B., Wantz, G. & Aziz, H. Formulation strategies for optimizing the morphology of polymeric bulk heterojunction organic solar cells: a brief review. *J. Photonics Energy* **4**, 40998 (2014).
98. Derue, L., Lecourtier, C., Gorisse, T., Hirsch, L., Dautel, O. & Wantz, G. A solvent additive to enhance the efficiency and the thermal stability of polymer:fullerene solar cells. *RSC Adv.* **5**, 3840–3843 (2015).
99. Tournebize, A., Rivaton, A., Gardette, J.-L., Lombard, C., Pépin-Donat, B., Beaupré, S. & Leclerc, M. How Photoinduced Crosslinking Under Operating Conditions Can Reduce PCDTBT-Based Solar Cell Efficiency and then Stabilize It. *Adv. Energy Mater.* **4**, 1301530 (2014).
100. Proctor, C. M., Kuik, M. & Nguyen, T.-Q. Charge carrier recombination in organic solar cells. *Prog. Polym. Sci.* **38**, 1941–1960 (2013).
101. Cowan, S. R., Banerji, N., Leong, W. L. & Heeger, A. J. Charge Formation, Recombination, and Sweep-Out Dynamics in Organic Solar Cells. *Adv. Funct. Mater.* **22**, 1116–1128 (2012).
102. Langevin, P. Recombination et mobilités des ions dans les gaz. *Ann. Chim. Phys.* **28**, 433–530 (1903).
103. Deibel, C., Wagenpohl, A. & Dyakonov, V. Influence of charge carrier mobility on the performance of organic solar cells. *Phys. status solidi - Rapid Res. Lett.* **2**, 175–177 (2008).
104. Coropceanu, V., Cornil, J., da Silva Filho, D. A., Olivier, Y., Silbey, R. & Brédas, J.-L. Charge Transport in Organic Semiconductors. *Chem. Rev.* **107**, 926–952 (2007).
105. Clarke, T. M., Peet, J., Nattestad, A., Drolet, N., Dennler, G., Lungenschmied, C., Leclerc, M. & Mozer, A. J. Charge carrier mobility, bimolecular recombination and trapping in polycarbazole copolymer:fullerene (PCDTBT:PCBM) bulk heterojunction solar cells. *Org. Electron.* **13**, 2639–2646 (2012).
106. Mihailetschi, V. D., Xie, H. X., de Boer, B., Koster, L. J. A. & Blom, P. W. M. Charge Transport and Photocurrent Generation in Poly(3-hexylthiophene): Methanofullerene Bulk-Heterojunction Solar Cells. *Adv. Funct. Mater.* **16**, 699–708 (2006).
107. Liao, H.-H., Yang, C.-M., Liu, C.-C., Horng, S.-F., Meng, H.-F. & Shy, J.-T. Dynamics and reversibility of oxygen doping and de-doping for conjugated polymer. *J. Appl. Phys.* **103**, 104506 (2008).
108. Schafferhans, J., Baumann, A., Wagenpohl, A., Deibel, C. & Dyakonov, V. Oxygen doping of P3HT:PCBM blends: Influence on trap states, charge carrier mobility and solar cell performance. *Org. Electron.* **11**, 1693–1700 (2010).
109. Parnell, A. J., Dunbar, A. D. F., Pearson, A. J., Staniec, P. A., Dennison, A. J. C., Hamamatsu, H., Skoda, M. W. A., Lidzey, D. G. & Jones, R. A. L. Depletion of PCBM at the Cathode Interface in

- P3HT/PCBM Thin Films as Quantified via Neutron Reflectivity Measurements. *Adv. Mater.* **22**, 2444–2447 (2010).
110. Orimo, A., Masuda, K., Honda, S., Benten, H., Ito, S., Ohkita, H. & Tsuji, H. Surface segregation at the aluminum interface of poly(3-hexylthiophene)/fullerene solar cells. *Appl. Phys. Lett.* **96**, 43305 (2010).
 111. Kuik, M., Koster, L. J. A., Wetzelaer, G. A. H. & Blom, P. W. M. Trap-Assisted Recombination in Disordered Organic Semiconductors. *Phys. Rev. Lett.* **107**, 256805 (2011).
 112. Mandoc, M. M., Kooistra, F. B., Hummelen, J. C., de Boer, B. & Blom, P. W. M. Effect of traps on the performance of bulk heterojunction organic solar cells. *Appl. Phys. Lett.* **91**, 263505 (2007).
 113. Leong, W. L., Welch, G. C., Kaake, L. G., Takacs, C. J., Sun, Y., Bazan, G. C. & Heeger, A. J. Role of trace impurities in the photovoltaic performance of solution processed small-molecule bulk heterojunction solar cells. *Chem. Sci.* **3**, 2103 (2012).
 114. Rauh, D., Deibel, C. & Dyakonov, V. Charge Density Dependent Nongeminate Recombination in Organic Bulk Heterojunction Solar Cells. *Adv. Funct. Mater.* **22**, 3371–3377 (2012).
 115. Cowan, S. R., Leong, W. L., Banerji, N., Dennler, G. & Heeger, A. J. Identifying a Threshold Impurity Level for Organic Solar Cells: Enhanced First-Order Recombination Via Well-Defined PC84BM Traps in Organic Bulk Heterojunction Solar Cells. *Adv. Funct. Mater.* **21**, 3083–3092 (2011).
 116. Kim, Y., Cook, S., Tuladhar, S. M., Choulis, S. A., Nelson, J., Durrant, J. R., Bradley, D. D. C., Giles, M., McCulloch, I., Ha, C.-S. & Ree, M. A strong regioregularity effect in self-organizing conjugated polymer films and high-efficiency polythiophene:fullerene solar cells. *Nat. Mater.* **5**, 197–203 (2006).
 117. Menon, A., Dong, H., Niazimbetova, Z. I., Rothberg, L. J. & Galvin, M. E. Polydispersity Effects on Conjugated Polymer Light-Emitting Diodes. *Chem. Mater.* **14**, 3668–3675 (2002).
 118. Ballantyne, A. M., Chen, L., Dane, J., Hammant, T., Braun, F. M., Heeney, M., Duffy, W., McCulloch, I., Bradley, D. D. C. & Nelson, J. The Effect of Poly(3-hexylthiophene) Molecular Weight on Charge Transport and the Performance of Polymer:Fullerene Solar Cells. *Adv. Funct. Mater.* **18**, 2373–2380 (2008).
 119. Heumueller, T., Burke, T. M., Mateker, W. R., Sachs-Quintana, I. T., Vandewal, K., Brabec, C. J. & McGehee, M. D. Disorder-Induced Open-Circuit Voltage Losses in Organic Solar Cells During Photoinduced Burn-In. *Adv. Energy Mater.* **5**, 1500111 (2015).
 120. Kyaw, A. K. K., Wang, D. H., Luo, C., Cao, Y., Nguyen, T. Q., Bazan, G. C. & Heeger, A. J. Effects of solvent additives on morphology, charge generation, transport, and recombination in solution-processed small-molecule solar cells. *Adv. Energy Mater.* **4**, 1–9 (2014).
 121. Chambon, S., Derue, L., Lahaye, M., Pavageau, B., Hirsch, L. & Wantz, G. MoO₃ Thickness, Thermal Annealing and Solvent Annealing Effects on Inverted and Direct Polymer Photovoltaic Solar Cells. *Materials (Basel)*. **5**, 2521–2536 (2012).
 122. Dupont, S. R., Voroshazi, E., Nordlund, D. & Dauskardt, R. H. Morphology and interdiffusion control to improve adhesion and cohesion properties in inverted polymer solar cells. *Sol. Energy Mater. Sol. Cells* **132**, 443–449 (2015).

123. Kaake, L., Dang, X.-D., Leong, W. L., Zhang, Y., Heeger, A. & Nguyen, T.-Q. Effects of Impurities on Operational Mechanism of Organic Bulk Heterojunction Solar Cells. *Adv. Mater.* **25**, 1706–1712 (2013).
124. Chambon, S., Rivaton, A., Gardette, J.-L. & Firon, M. Reactive intermediates in the initiation step of the photo-oxidation of MDMO-PPV. *J. Polym. Sci. Part A Polym. Chem.* **47**, 6044–6052 (2009).
125. Seemann, A., Sauermann, T., Lungenschmied, C., Armbruster, O., Bauer, S., Egelhaaf, H.-J. & Hauch, J. Reversible and irreversible degradation of organic solar cell performance by oxygen. *Sol. Energy* **85**, 1238–1249 (2011).
126. Goldmann, C., Gundlach, D. J. & Batlogg, B. Evidence of water-related discrete trap state formation in pentacene single-crystal field-effect transistors. *Appl. Phys. Lett.* **88**, 63501 (2006).
127. Gu, G. & Kane, M. G. Moisture induced electron traps and hysteresis in pentacene-based organic thin-film transistors. *Appl. Phys. Lett.* **92**, 53305 (2008).
128. Spanggaard, H. & Krebs, F. C. A brief history of the development of organic and polymeric photovoltaics. *Sol. Energy Mater. Sol. Cells* **83**, 125–146 (2004).
129. Eo, Y. S., Rhee, H. W., Chin, B. D. & Yu, J.-W. Influence of metal cathode for organic photovoltaic device performance. *Synth. Met.* **159**, 1910–1913 (2009).
130. Norrman, K., Gevorgyan, S. A. & Krebs, F. C. Water-Induced Degradation of Polymer Solar Cells Studied by H 2 18 O Labeling. *ACS Appl. Mater. Interfaces* **1**, 102–112 (2009).
131. Voroshazi, E., Verreet, B., Aernouts, T. & Heremans, P. Long-term operational lifetime and degradation analysis of P3HT:PCBM photovoltaic cells. *Sol. Energy Mater. Sol. Cells* **95**, 1303–1307 (2011).
132. Glatthaar, M., Riede, M., Keegan, N., Sylvester-Hvid, K., Zimmermann, B., Niggemann, M., Hinsch, A. & Gombert, A. Efficiency limiting factors of organic bulk heterojunction solar cells identified by electrical impedance spectroscopy. *Sol. Energy Mater. Sol. Cells* **91**, 390–393 (2007).
133. Voroshazi, E., Verreet, B., Buri, A., Müller, R., Di Nuzzo, D. & Heremans, P. Influence of cathode oxidation via the hole extraction layer in polymer:fullerene solar cells. *Org. Electron.* **12**, 736–744 (2011).
134. Züfle, S., Neukom, M. T., Altazin, S., Zinggeler, M., Chrapa, M., Offermans, T. & Ruhstaller, B. An Effective Area Approach to Model Lateral Degradation in Organic Solar Cells. *Adv. Energy Mater.* **5**, 1500835 (2015).
135. Lechêne, B., Leroy, J., Tosoni, O., de Bettignies, R. & Perrier, G. Origin of the S-Shape upon Aging in Standard Organic Solar Cells with Zinc Oxide as Transport Layer. *J. Phys. Chem. C* **118**, 20132–20136 (2014).
136. Po, R., Carbonera, C., Bernardi, A. & Camaioni, N. The role of buffer layers in polymer solar cells. *Energy Environ. Sci.* **4**, 285–310 (2011).
137. Po, R., Carbonera, C., Bernardi, A., Tinti, F. & Camaioni, N. Polymer- and carbon-based electrodes for polymer solar cells: Toward low-cost, continuous fabrication over large area. *Sol. Energy Mater. Sol. Cells* **100**, 97–114 (2012).

138. Kawano, K., Pacios, R., Poplavskyy, D., Nelson, J., Bradley, D. D. C. & Durrant, J. R. Degradation of organic solar cells due to air exposure. *Sol. Energy Mater. Sol. Cells* **90**, 3520–3530 (2006).
139. Norrman, K., Larsen, N. B. & Krebs, F. C. Lifetimes of organic photovoltaics: Combining chemical and physical characterisation techniques to study degradation mechanisms. *Sol. Energy Mater. Sol. Cells* **90**, 2793–2814 (2006).
140. Krebs, F. C. & Norrman, K. Analysis of the failure mechanism for a stable organic photovoltaic during 10 000 h of testing. *Prog. Photovoltaics Res. Appl.* **15**, 697–712 (2007).
141. Hofmann, A. I., Smaal, W. T. T., Mumtaz, M., Katsigiannopoulos, D., Brochon, C., Schütze, F., Hild, O. R., Cloutet, E. & Hadziioannou, G. An Alternative Anionic Polyelectrolyte for Aqueous PEDOT Dispersions: Toward Printable Transparent Electrodes. *Angew. Chemie - Int. Ed.* **54**, 8506–8510 (2015).
142. White, M. S., Olson, D. C., Shaheen, S. E., Kopidakis, N. & Ginley, D. S. Inverted bulk-heterojunction organic photovoltaic device using a solution-derived ZnO underlayer. *Appl. Phys. Lett.* **89**, 143517 (2006).
143. Şahin, Y., Alem, S., De Bettignies, R. & Nunzi, J. M. Development of air stable polymer solar cells using an inverted gold on top anode structure. *Thin Solid Films* **476**, 340–343 (2005).
144. Li, G., Chu, C. W., Shrotriya, V., Huang, J. & Yang, Y. Efficient inverted polymer solar cells. *Appl. Phys. Lett.* **88**, 3–6 (2006).
145. Lee, K., Kim, J. Y., Park, S. H., Kim, S. H., Cho, S. & Heeger, A. J. Air-Stable Polymer Electronic Devices. *Adv. Mater.* **19**, 2445–2449 (2007).
146. Sun, Y., Takacs, C. J., Cowan, S. R., Seo, J. H., Gong, X., Roy, A. & Heeger, A. J. Efficient, Air-Stable Bulk Heterojunction Polymer Solar Cells Using MoOx as the Anode Interfacial Layer. *Adv. Mater.* **23**, 2226–2230 (2011).
147. Lloyd, M. T., Olson, D. C., Lu, P., Fang, E., Moore, D. L., White, M. S., Reese, M. O., Ginley, D. S. & Hsu, J. W. P. Impact of contact evolution on the shelf life of organic solar cells. *J. Mater. Chem.* **19**, 7638 (2009).
148. Mateker, W. R., Sachs-Quintana, I. T., Burkhard, G. F., Cheacharoen, R. & McGehee, M. D. Minimal Long-Term Intrinsic Degradation Observed in a Polymer Solar Cell Illuminated in an Oxygen-Free Environment. *Chem. Mater.* **27**, 404–407 (2015).
149. Voroshazi, E., Cardinaletti, I., Uytterhoeven, G., Li, S., Empl, M., Aernouts, T. & Rand, B. P. Role of electron-and hole-collecting buffer layers on the stability of inverted polymer: Fullerene photovoltaic devices. *IEEE J. Photovoltaics* **4**, 265–270 (2014).
150. Wang, Q., Williams, G. & Aziz, H. Photo-degradation of the indium tin oxide (ITO)/organic interface in organic optoelectronic devices and a new outlook on the role of ITO surface treatments and interfacial layers in improving device stability. *Org. Electron.* **13**, 2075–2082 (2012).
151. Wang, Q., Williams, G., Tsui, T. & Aziz, H. Photochemical deterioration of the organic/metal contacts in organic optoelectronic devices. *J. Appl. Phys.* **112**, 64502 (2012).
152. Wang, Q. & Aziz, H. Poor photo-stability of the organic/LiF/Al contact in organic optoelectronic devices. *Org. Electron.* **12**, 1571–1575 (2011).

153. Williams, G., Wang, Q. & Aziz, H. The Photo-Stability of Polymer Solar Cells: Contact Photo-Degradation and the Benefits of Interfacial Layers. *Adv. Funct. Mater.* **23**, 2239–2247 (2013).
154. Dupont, S. R., Novoa, F., Voroshazi, E. & Dauskardt, R. H. Decohesion Kinetics of PEDOT:PSS Conducting Polymer Films. *Adv. Funct. Mater.* **24**, 1325–1332 (2014).
155. Dupont, S. R., Oliver, M., Krebs, F. C. & Dauskardt, R. H. Interlayer adhesion in roll-to-roll processed flexible inverted polymer solar cells. *Sol. Energy Mater. Sol. Cells* **97**, 171–175 (2012).
156. Roesch, R., Faber, T., von Hauff, E., Brown, T. M., Lira-Cantu, M. & Hoppe, H. Procedures and Practices for Evaluating Thin-Film Solar Cell Stability. *Adv. Energy Mater.* **5**, 1501407 (2015).
157. Peters, C. H., Sachs-Quintana, I. T., Kastrop, J. P., Beaupré, S., Leclerc, M. & McGehee, M. D. High efficiency polymer solar cells with long operating lifetimes. *Adv. Energy Mater.* **1**, 491–494 (2011).
158. Voroshazi, E., Cardinaletti, I., Conard, T. & Rand, B. P. Light-Induced Degradation of Polymer:Fullerene Photovoltaic Devices: An Intrinsic or Material-Dependent Failure Mechanism? *Adv. Energy Mater.* **4**, 1400848 (2014).
159. Peters, C. H., Sachs-Quintana, I. T., Mateker, W. R., Heumueller, T., Rivnay, J., Noriega, R., Beiley, Z. M., Hoke, E. T., Salleo, A. & McGehee, M. D. The Mechanism of Burn-in Loss in a High Efficiency Polymer Solar Cell. *Adv. Mater.* **24**, 663–668 (2012).
160. Rösch, R., Tanenbaum, D. M., Jørgensen, M., Seeland, M., Bärenklau, M., Hermenau, M., Voroshazi, E., Lloyd, M. T., Galagan, Y., Zimmermann, B., Würfel, U., Hösel, M., Dam, H. F., Gevorgyan, S. A., Kudret, S., Maes, W., Lutsen, L., Vanderzande, D., Andriessen, R., Teran-Escobar, G., Lira-Cantu, M., Rivaton, A., Uzunoğlu, G. Y., Germack, D., Andreasen, B., Madsen, M. V., Norrman, K., Hoppe, H. & Krebs, F. C. Investigation of the degradation mechanisms of a variety of organic photovoltaic devices by combination of imaging techniques—the ISOS-3 inter-laboratory collaboration. *Energy Environ. Sci.* **5**, 6521 (2012).
161. Tong, X., Wang, N., Slootsky, M., Yu, J. & Forrest, S. R. Intrinsic burn-in efficiency loss of small-molecule organic photovoltaic cells due to exciton-induced trap formation. *Sol. Energy Mater. Sol. Cells* **118**, 116–123 (2013).
162. Reese, M. O., Morfa, A. J., White, M. S., Kopidakis, N., Shaheen, S. E., Rumbles, G. & Ginley, D. S. Pathways for the degradation of organic photovoltaic P3HT:PCBM based devices. *Sol. Energy Mater. Sol. Cells* **92**, 746–752 (2008).
163. Kawano, K. & Adachi, C. Reduced initial degradation of bulk heterojunction organic solar cells by incorporation of stacked fullerene and lithium fluoride interlayers. *Appl. Phys. Lett.* **96**, 1–4 (2010).
164. Kawano, K. & Adachi, C. Evaluating Carrier Accumulation in Degraded Bulk Heterojunction Organic Solar Cells by a Thermally Stimulated Current Technique. *Adv. Funct. Mater.* **19**, 3934–3940 (2009).
165. Balcaen, V., Rolston, N., Dupont, S. R., Voroshazi, E. & Dauskardt, R. H. Thermal cycling effect on mechanical integrity of inverted polymer solar cells. *Sol. Energy Mater. Sol. Cells* **143**, 418–423 (2015).
166. Heumueller, T., Mateker, W. R., Distler, A., Fritze, U. F., Cheacharoen, R., Nguyen, W. H., Biele, M., Salvador, M., von Delius, M., Egelhaaf, H.-J., McGehee, M. D. & Brabec, C. J.

- Morphological and electrical control of fullerene dimerization determines organic photovoltaic stability. *Energy Environ. Sci.* **9**, 247–256 (2016).
167. Gevorgyan, S. a., Madsen, M. V., Dam, H. F., Jørgensen, M., Fell, C. J., Anderson, K. F., Duck, B. C., Mescheloff, A., Katz, E. a., Elschner, A., Roesch, R., Hoppe, H., Hermenau, M., Riede, M. & Krebs, F. C. Interlaboratory outdoor stability studies of flexible roll-to-roll coated organic photovoltaic modules: Stability over 10,000h. *Sol. Energy Mater. Sol. Cells* **116**, 187–196 (2013).
 168. Cros, S., de Bettignies, R., Berson, S., Bailly, S., Maise, P., Lemaitre, N. & Guillerez, S. Definition of encapsulation barrier requirements: A method applied to organic solar cells. *Sol. Energy Mater. Sol. Cells* **95**, S65–S69 (2011).
 169. Hösel, M., Søndergaard, R. R., Jørgensen, M. & Krebs, F. C. Comparison of UV-Curing, Hotmelt, and Pressure Sensitive Adhesive as Roll-to-Roll Encapsulation Methods for Polymer Solar Cells. *Adv. Eng. Mater.* **15**, 1068–1075 (2013).
 170. Tipnis, R., Bernkopf, J., Jia, S., Krieg, J., Li, S., Storch, M. & Laird, D. Large-area organic photovoltaic module-Fabrication and performance. *Sol. Energy Mater. Sol. Cells* **93**, 442–446 (2009).
 171. Park, J.-S., Chae, H., Chung, H. K. & Lee, S. I. Thin film encapsulation for flexible AM-OLED: a review. *Semicond. Sci. Technol.* **26**, 34001 (2011).
 172. Tanenbaum, D. M., Dam, H. F., Rösch, R., Jørgensen, M., Hoppe, H. & Krebs, F. C. Edge sealing for low cost stability enhancement of roll-to-roll processed flexible polymer solar cell modules. *Sol. Energy Mater. Sol. Cells* **97**, 157–163 (2012).
 173. Ahmad, J., Bazaka, K., Anderson, L. J., White, R. D. & Jacob, M. V. Materials and methods for encapsulation of OPV: A review. *Renew. Sustain. Energy Rev.* **27**, 104–117 (2013).
 174. Krebs, F. C., Tromholt, T. & Jørgensen, M. Upscaling of polymer solar cell fabrication using full roll-to-roll processing. *Nanoscale* **2**, 873 (2010).
 175. Li, G., Yao, Y., Yang, H., Shrotriya, V., Yang, G. & Yang, Y. ‘Solvent Annealing’ Effect in Polymer Solar Cells Based on Poly(3-hexylthiophene) and Methanofullerenes. *Adv. Funct. Mater.* **17**, 1636–1644 (2007).
 176. Manor, A., Katz, E. a., Tromholt, T. & Krebs, F. C. Enhancing functionality of ZnO hole blocking layer in organic photovoltaics. *Sol. Energy Mater. Sol. Cells* **98**, 491–493 (2012).
 177. Destouesse, E., Chambon, S., Courtel, S., Hirsch, L. & Wantz, G. Solution-Processed Small-Molecule Bulk Heterojunctions: Leakage Currents and the Dewetting Issue for Inverted Solar Cells. *ACS Appl. Mater. Interfaces* **7**, 24663–24669 (2015).
 178. *Borate Glasses*. (Springer US, 1978). doi:10.1007/978-1-4684-3357-9
 179. *ASTM G173-03(2012), Standard Tables for Reference Solar Spectral Irradiances: Direct Normal and Hemispherical on 37° Tilted Surface*. (ASTM International, 2012). doi:10.1520/G0173-03R12.2
 180. Pickett, J. E. & Sargent, J. R. Sample temperatures during outdoor and laboratory weathering exposures. *Polym. Degrad. Stab.* **94**, 189–195 (2009).
 181. Kumar, A., Sista, S. & Yang, Y. Dipole induced anomalous S-shape I-V curves in polymer solar

- cells. *J. Appl. Phys.* **105**, 94512 (2009).
182. Wagenpfahl, A., Rauh, D., Binder, M., Deibel, C. & Dyakonov, V. S-shaped current-voltage characteristics of organic solar devices. *Phys. Rev. B* **82**, 115306 (2010).
 183. Won Choi, H., Young Kim, S., Kim, K.-B., Tak, Y.-H. & Lee, J.-L. Enhancement of hole injection using O₂ plasma-treated Ag anode for top-emitting organic light-emitting diodes. *Appl. Phys. Lett.* **86**, 12104 (2005).
 184. Kim, J. B., Kim, C. S., Kim, Y. S. & Loo, Y.-L. Oxidation of silver electrodes induces transition from conventional to inverted photovoltaic characteristics in polymer solar cells. *Appl. Phys. Lett.* **95**, 183301 (2009).
 185. Thakur, A. K., Baboz, H., Wantz, G., Hodgkiss, J. & Hirsch, L. Relation between charge carrier density and lifetime in polymer-fullerene solar cells. *J. Appl. Phys.* **112**, 44502 (2012).
 186. Cowan, S. R., Roy, A. & Heeger, A. J. Recombination in polymer-fullerene bulk heterojunction solar cells. *Phys. Rev. B* **82**, 245207 (2010).
 187. Rutherford, E. LXXIX. The scattering of α and β particles by matter and the structure of the atom. *Philos. Mag. Ser. 6* **21**, 669–688 (1911).
 188. Geiger, H. & Marsden, E. LXI. The laws of deflexion of a particles through large angles. *Philos. Mag. Ser. 6* **25**, 604–623 (1913).
 189. Chu, W. K., Mayer, J. W. & Nicolet, M. A. *Backscattering spectrometry*. (Academic Press, 1978).
 190. Anderson, T. L. *Fracture mechanics: fundamentals and applications*. (CRC press, 2005).
 191. Kanninen, M. F. An augmented double cantilever beam model for stud propagation and arrest. *Int. J. Fract.* **9**, 83–92 (1973).
 192. Tummala, N. R., Bruner, C., Risko, C., Brédas, J.-L. & Dauskardt, R. H. Molecular-Scale Understanding of Cohesion and Fracture in P3HT:Fullerene Blends. *ACS Appl. Mater. Interfaces* **7**, 9957–9964 (2015).
 193. Hofmann, S. *Auger- and X-Ray Photoelectron Spectroscopy in Materials Science*. **49**, (Springer Berlin Heidelberg, 2013).
 194. Sadewasser, S. & Glatzel, T. *Kelvin Probe Force Microscopy*. **48**, (Springer Berlin Heidelberg, 2012).
 195. Kelvin. Contact electricity of metals. *Philos. Mag. Ser. 5* **46**, 82–120 (1898).
 196. Xu, W., Song, H., Yan, D., Zhu, H., Wang, Y., Xu, S., Bai, X., Dong, B. & Liu, Y. YVO₄:Eu³⁺,Bi³⁺ UV to visible conversion nano-films used for organic photovoltaic solar cells. *J. Mater. Chem.* **21**, 12331 (2011).
 197. Gevorgyan, S. A., Espinosa, N., Ciammaruchi, L., Roth, B., Livi, F., Tsopanidis, S., Züfle, S., Queirós, S., Gregori, A., Benatto, G. A. dos R., Corazza, M., Madsen, M. V., Hösel, M., Beliatas, M. J., Larsen-Olsen, T. T., Pastorelli, F., Castro, A., Mingorance, A., Lenzi, V., Fluhr, D., Roesch, R., Maria Duarte Ramos, M., Savva, A., Hoppe, H., Marques, L. S. A., Burgués, I., Georgiou, E., Serrano-Luján, L. & Krebs, F. C. Baselines for Lifetime of Organic Solar Cells. *Adv. Energy Mater.* 1600910 (2016). doi:10.1002/aenm.201600910
 198. Steinfeld, J. I., Francisco, J. S. & Hase, W. L. *Chemical Kinetics and Dynamics*. (Prentice Hall,

- 1999). at <<https://books.google.fr/books?id=I1jwAAAAMAAJ>>
199. NREL Reference Solar Spectral Irradiance: Air Mass 1.5. at <<http://rredc.nrel.gov/solar/spectra/am1.5/>>
 200. Pearson, A. J., Hopkinson, P. E., Couderc, E., Domanski, K., Abdi-Jalebi, M. & Greenham, N. C. Critical light instability in CB/DIO processed PBDTTT-EFT:PC71BM organic photovoltaic devices. *Org. Electron. physics, Mater. Appl.* **30**, 225–236 (2016).
 201. Hintz, H., Sessler, C., Peisert, H., Egelhaaf, H.-J. & Chassé, T. Wavelength-Dependent Pathways of Poly-3-hexylthiophene Photo-Oxidation. *Chem. Mater.* **24**, 2739–2743 (2012).
 202. Mattana, G. & Chambon, S. *Unpublished results.* (IMS Laboratory - University of Bordeaux, 2016).
 203. Gao, X.-Y., Feng, H.-L., Ma, J.-M., Zhang, Z.-Y., Lu, J.-X., Chen, Y.-S., Yang, S.-E. & Gu, J.-H. Analysis of the dielectric constants of the Ag₂O film by spectroscopic ellipsometry and single-oscillator model. *Phys. B Condens. Matter* **405**, 1922–1926 (2010).
 204. Taylor, R., Barrow, M. P. & Drewello, T. C60 degrades to C1200. *Chem. Commun.* 2497–2498 (1998). doi:10.1039/a806726k
 205. Sutti, S., Williams, G. & Aziz, H. Role of the donor material and the donor–acceptor mixing ratio in increasing the efficiency of Schottky junction organic solar cells. *Org. Electron.* **14**, 2392–2400 (2013).
 206. Lloyd, M. T., Olson, D. C., Berry, J. J., Kopidakis, N., Reese, M. O., Steirer, K. X. & Ginley, D. S. Enhanced lifetime in unencapsulated organic photovoltaics with air stable electrodes. in *2010 35th IEEE Photovolt. Spec. Conf.* 001060–001063 (IEEE, 2010). doi:10.1109/PVSC.2010.5614676

A

Appendix A

Transportation of fracture analysis samples

As the samples were fabricated at the University of Bordeaux in France, but were to be analysed at Stanford University in the United States, some logistical challenges had to be overcome in order to carry out this research, i.e. how to transport 32 large glass samples over 9000 km in an inert atmosphere without breaking the substrates or scratching the surface. In order to protect the samples from mechanical damage, a series of purpose-built plastic boxes were fabricated by 3D printing (3D Systems Cube), with the design shown in Figure A.1. Once the samples were placed in the boxes and the boxes were closed, the boxes were placed in two layers of thick plastic bags which were heat sealed while in the glovebox. These bags were sufficient to maintain the oxygen and water-free atmosphere around the samples until they were transferred to a glovebox with an inert atmosphere at Stanford.

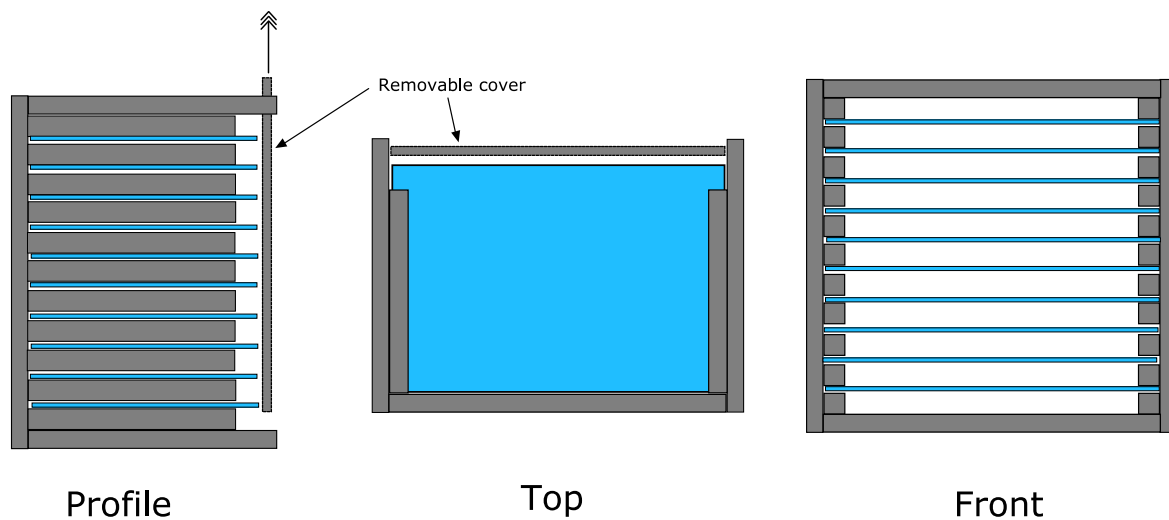


Figure A.1: Cutaway schematics of the plastic boxes fabricated to transport the fracture analysis samples safely to the United States.

B

Appendix B

XPS survey scans of fractured samples

This appendix contains the XPS survey scan data measured from the samples that fractured at the HTL/active layer interface in the fracture analysis experiment. The fracture path was determined visually for those samples that fractured within the BHJ.

B.1. Unaged control samples

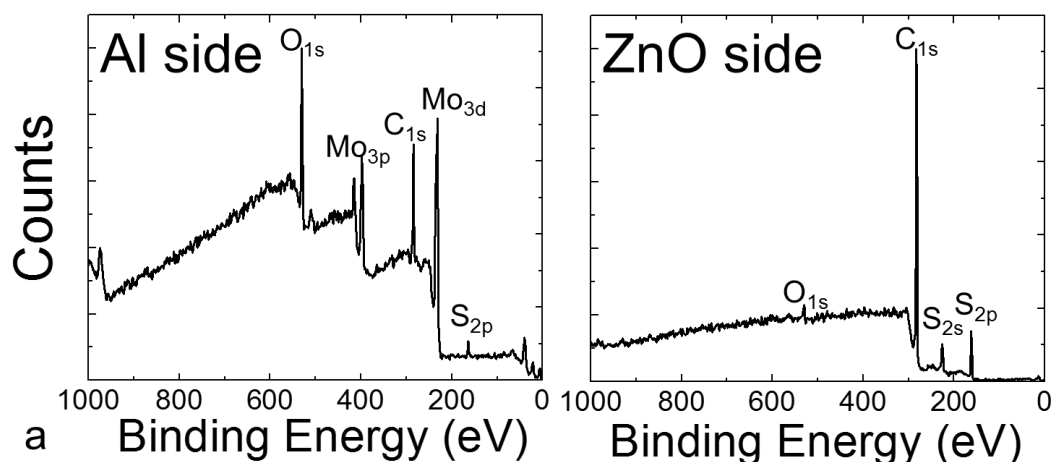


Figure B.1.1: The XPS survey scans measured from the fractured control Al/MoO₃ sample. The metal side is shown on the left and the ZnO side on the right. Data measured and figures prepared by Nicholas Rolston.

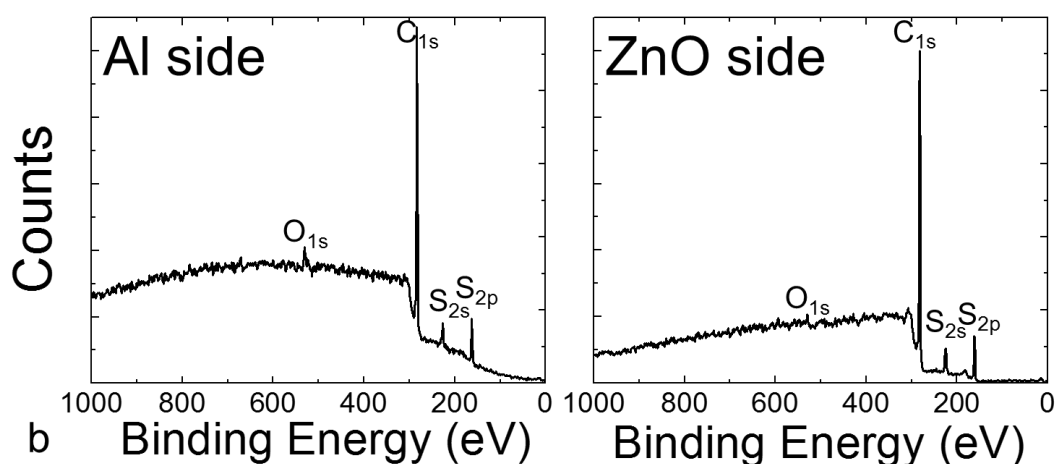


Figure B.1.2: The XPS survey scans measured from the fractured control Al/WO₃ sample. The metal side is shown on the left and the ZnO side on the right. Data measured and figures prepared by Nicholas Rolston.

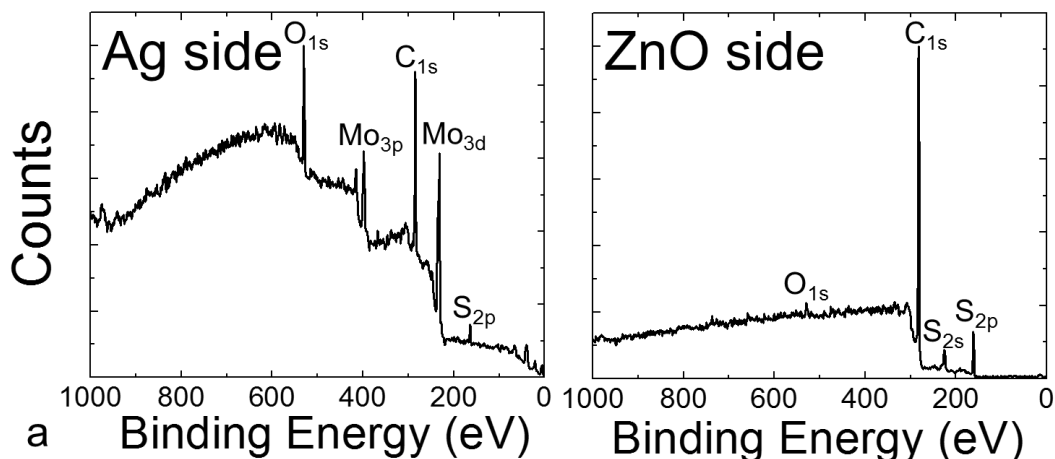


Figure B.1.3: The XPS survey scans measured from the fractured control Ag/MoO₃ sample. The metal side is shown on the left and the ZnO side on the right. Data measured and figures prepared by Nicholas Rolston.

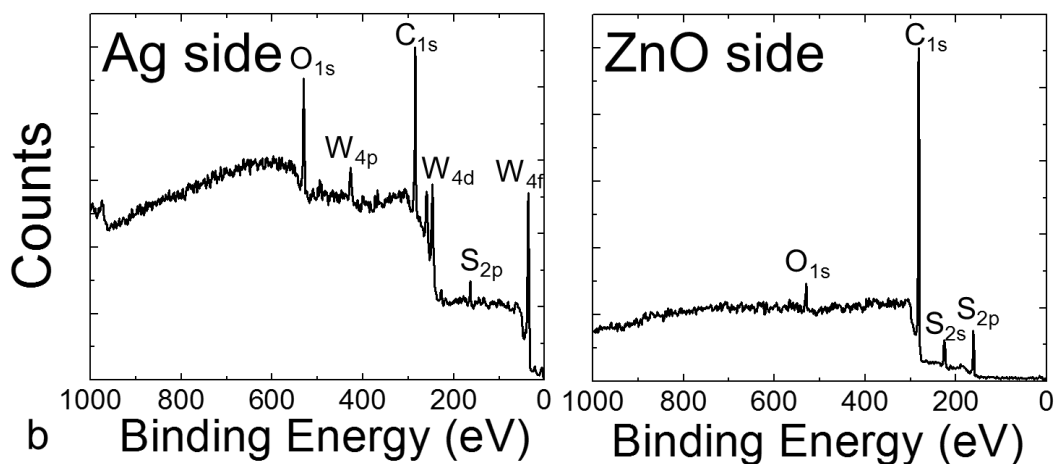


Figure B.1.4: The XPS survey scans measured from the fractured control Ag/WO₃ sample. The metal side is shown on the left and the ZnO side on the right. Data measured and figures prepared by Nicholas Rolston.

B.2. Samples aged one week

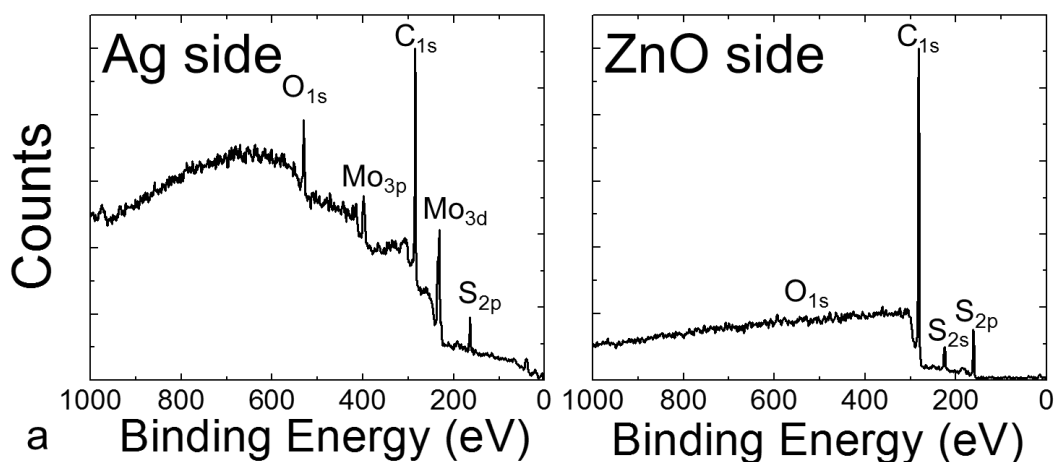


Figure B.2.1: The XPS survey scans measured from the fractured Ag/MoO₃ sample that was aged one week. The metal side is shown on the left and the ZnO side on the right. Data measured and figures prepared by Nicholas Rolston.

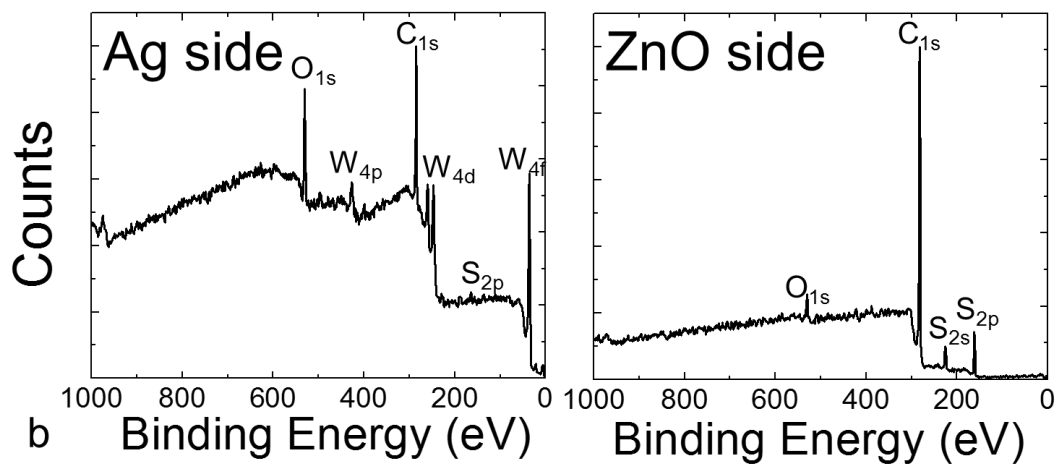


Figure B.2.2: The XPS survey scans measured from the fractured Ag/WO₃ sample that was aged one week. The metal side is shown on the left and the ZnO side on the right. Data measured and figures prepared by Nicholas Rolston.